Departament d'Enginyeria Electrònica

UNIVERSITAT POLITÈCNICA DE CATALUNYA

Institut d'Estudis Espacials de Catalunya (IEEC)
Institut de Ciències de l'Espai (CSIC)

IEEC **CSIC**
Consejo Superior de Investigaciones Científicas

Design and assessment of a low-frequency magnetic measurement system for eLISA

by

Ignacio Mateos Martín

A thesis submitted for the degree of Doctor

Advisors:
Prof. Juan Ramos Castro
Prof. Alberto Lobo Gutiérrez

Barcelona, 2015

To my parents and to the memory of Alberto Lobo,
who also made everything possible.

"Paréceme, Sancho, que no hay refrán que no sea verdadero,
porque todos son sentencias sacadas de la mesma experiencia,
madre de las ciencias todas, especialmente aquel que dice:
Donde una puerta se cierra, otra se abre."

"... y basta también que un hombre honrado
haya dado noticia destas discretas locuras ..."

El Ingenioso Hidalgo Don Quixote de la Mancha,
Miguel de Cervantes Saavedra.

Contents

CONTENTS

iv

Acknowledgements

No es mi intención alargarme demasiado con el listado de las muchas personalidades que me han acompañado durante esta etapa del doctorado, pero claro está, tampoco sería justo quedarse corto. "En las cortesías antes se ha de pecar por carta de más que de menos", que dijo el renombrado escritor.

Primero en la lista y con letras de oro, el insigne Alberto Lobo, supervisor y principal artífice de esta tesis. En su ausencia no ha sido fácil mantener la ilusión, pero haber tenido la oportunidad de compartir los primeros años juntos ha sido todo un lujazo, y la finalización de esta tesis es mi humilde homenaje póstumo. El desarrollo de este trabajo tampoco hubiera sido posible sin la batuta de Juan Ramos. La libertad que me dio para ir tomando decisiones resultaba menos arriesgada sabiendo que su ojo experto revisaba los detalles. Gracias Juan por hacer todo el proceso tan fluido.

Estoy en deuda con el excelente grupo de Astronomía Gravitacional/LISA -con unas cervezas lo apañamos-, Carlos, Víctor, Lluis, Miquel, Ivan, Ferran, Daniel y Francisco. Cada uno de ellos es una pieza clave dentro de este puzle de ciencia, tecnología y burocracia. Acordarme también de los antiguos miembros que dejaron huella en su paso. Gracias Pep, Marc, Nikos, Rubén, Aleix, Priscilla y Xevi. Y que no falten en estas lineas el Sr. Guerrero, junto con las *jefas* del IEEC, Anna, Eva y Pilar.

Special thanks go to the people that helped me wrap up this thesis, Pepe Morales, Maria Garoffolo, Bill Weber, Pep Sanjuán, Carlos Sopuerta, Debora Gaseni, Paco Peña, Joan Sanz, and Luis Arnedo. I am also very grateful to the members of the Budker Group from the Physics Department for their support and hospitality during my stay at the University of California at Berkeley.

Saliendo del ambiente académico y barriendo ya para casa, gracias a mis hermanos, Nico y Marisa, con los que compartí piso en Barcelona, lejos del pueblo. Años que disfrutamos de grandes homenajes en forma de copiosas comidas, de esas que te acortan la vida pero que te alargan la sonrisa. A mi tía Charo y mi her-

Acknowledgements

manita Alejandra, las más grandes de todo Jerez -me perdonen las demás-. Y como no podía ser menos, a mis padres, Carmen y Paco. Mi motivación por estudiar ha estado siempre ligada a vuestra ilusión y apoyo incondicional. Este doctorado es por vosotros, ¡padres!.

Ya para rematar, si hay alguien que ha sufrido -y reído- las aventuras y desventuras de esta tesis, esa es Antonia. Mil gracias por convertir esta a veces rutinaria andanza del doctorado en algo tan divertido. Cuando imagino que habrá después de estas lineas que ya terminan, sólo puedo pensar en muchos años de risas y más risas contigo.

<div align="right">

Barcelona, September of 2015

</div>

List of Figures

List of Tables

List of Acronyms

ADC	Analog-to-digital Converter
AI	Atom Interferometer
AM	Amplitude-modulated
AMR	Anisotropic Magnetoresistance
AOM	Acousto-optic Modulator
ASD	Amplitude Spectral Density
ASW	Application Software
BEC	Bose-Einstein Condensation
BS	Beam Splitter
BSW	Boot Software
CNES	Centre National d'Études Spatiales
COC	Certificate of Calibration
CSAM	Chip-scale Atom Magnetometer
CSIC	Consejo Superior de Investigaciones Científicas
DAC	Digital-to-analog Converter
DAU	Data Acquisition Unit
DAVLL	Dichroic-atomic-vapor Laser Lock
DDS	Data and Diagnostics Subsystem
DFACS	Drag Free Attitude Control System
DFB	Distributed-feedback Laser
DMM	Digital Multimeter
DMU	Data Management Unit

DPU	Data Processing Unit
E^{2}PROM	Electrically Erasable Programmable Read-only Memory
EH	Electrode Housing
eLISA	evolved Laser Interferometer Space Antenna
EM	Engineering Model
ENBW	Equivalent Noise Bandwidth
EPTA	European Pulsar Timing Array
ESA	European Space Agency
ESTEC	European Space Research and Technology Centre
FEE	Front-end Electronics
FM	Flight Model
FM BB	Frequency-modulated Bell-Bloom
GMI	Giant Magneto-impedance
GMR	Giant Magnetoresistance
GNSS-R	Global Navigation Satellite System Reflectometry
GRS	Gravitational Reference Sensor
GW	Gravitational Wave
I^{2}C	Inter-integrated Circuit
IABG	Industrieanlagen-Betriebsgesellschaft mbH
IA	Instrumentation Amplifier
ICE	Institut de Ciències de l'Espai
IEEC	Institut d'Estudis Espacials de Catalunya
IS	Inertial Sensor
LCA	LTP Core Assembly
LEO	Low Earth Orbit
LIGO	Laser Interferometer Gravitational-wave Observatory
LISA	Laser Interferometer Space Antenna
LPF	LISA Pathfinder
LSB	Least Significant Bit

LSD	Least Significant Digit
LSF	Least Squares Fitting
LTP	LISA Technology Package
MCF	Mobile Coil Facility
MI	Magneto-impedance
NASA	National Aeronautics and Space Administration
NMOR	Nonlinear Magneto-optical Rotation
NTC	Negative Temperature Coefficient
OBC	On-board Computer
OMS	Optical Metrology System
OSTT	On-station Thermal Test
PCB	Printed Circuit Board
PCU	Power Control Unit
PDU	Power Distribution Unit
PSD	Power Spectral Density
PTA	Pulsar Timing Array
PPTA	Parkes Pulsar Timing Array
RF	Radio Frequency
RTI	Referred to the Input
SC	Spacecraft
SPI	Serial Peripheral Interface
SQUID	Superconducting Quantum Interference Devices
STE-QUEST	Space-time Explorer and Quantum Equivalence Principle Space Test
TBD	To Be Designed
TC	Temperature Coefficient
TIA	Transimpedance Amplifier
TM	Test Mass
TM$_1$	Test Mass 1
TM$_2$	Test Mass 2

List of Acronyms

TMR	Tunneling Magnetoresistance
TRL	Technology Readiness Level
UB	Universitat de Barcelona
uC	Microcontroller
UC	University of California
UPC	Universitat Politècnica de Catalunya
VE	Vacuum Enclosure

Chapter 1

Introduction

The primary purpose of this thesis is the design, development and validation of a system capable of measuring magnetic fields with low-noise conditions at sub-millihertz frequencies. Such an instrument is conceived as a part of a space mission concept for a gravitational-wave observatory called eLISA (evolved Laser Interferometer Space Antenna). In addition, the work of this thesis is also well-suited for use in magnetically sensitive fundamental physics experiments requiring long integration time, such as high-precision measurement of the weak equivalence principle. Within this context, the baseline design of the instrument is also foreseen to monitor the environmental magnetic field in a proposed mission concept involving space atom-interferometric measurements, known as STE-QUEST (Space-Time Explorer and Quantum Equivalence Principle Space Test).

Before going into the details of the magnetic measurement system, we put the work of the thesis into context and introduce the primary goals of the eLISA and STE-QUEST mission concepts. On the one hand, a brief overview about gravitational wave nature and its detection is given. We also describe the reasons to perform magnetic field measurements in the eLISA spacecraft. Moreover, a general outlook about the eLISA technology demonstrator, the LISA Pathfinder, is given. On the other hand, a brief introduction on the weak equivalence principle is offered and the space-based test using a dual species atom interferometry is explained. Finally, we discuss the need of the magnetic field monitoring subsystem as part of the STE-QUEST payload.

1.1 Gravitational wave astronomy

A compelling indirect proof of the existence of gravitational waves (GWs) was carried out by Russell A. Hulse and Joseph H. Taylor via the decay of the orbital period of the binary pulsar PSR 1913+16 [82]. The results proved that the system is losing energy at a rate in excellent agreement with the predictions of Einstein's General

Relativity, assuming the reason for the energy lost is the emission of gravitational waves due to the motion of the binary system [177]. The discovery, awarded with the 1993 Nobel Prize in Physics, opened up the study of relativistic gravitation for the last few decades, when potential advances in ground- and space-based GW observatories have aimed for direct detection along a wide range of frequencies. Nowadays, thanks to the latest technological developments, a new era of gravitational wave astronomy is expected for the near future, opening a new window to revolutionize our understanding of the Universe.

1.1.1   Measurable emissions of gravitational waves

According to the general theory of relativity [56], gravitational waves are small ripples in the spacetime geometry that travel away from their source at the speed of light. They have two polarization states that provoke freely falling bodies to expand in one direction, while squeezing in the perpendicular direction to the previous one. These polarizations, which are transverse to the wave's propagation direction, are usually denoted as plus polarization "+" and cross polarization "×". Their effects on a ring of free falling masses are shown in Figure 1.1.
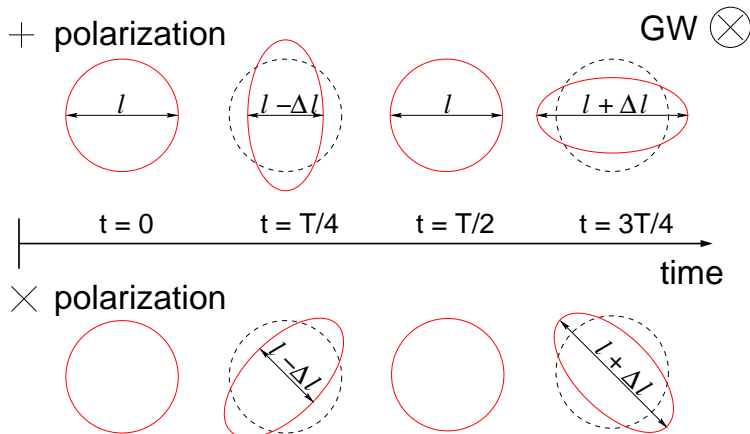
Figure 1.1:   Polarizations of a gravitational wave. Effect of a GW on free falling bodies disposed in a circle for the plus and cross polarization. The propagation of the GW is perpendicular to the plane of the circles. The dashed circles indicate the initial position of the bodies.

The amplitude of a GW is usually characterized by the strain h, given by

$$h = 2\frac{\Delta l}{l}, \tag{1.1}$$

which is provided by the measurable relative change Δl caused by a GW in the initial arm length l between the masses. Hence, the obvious solution is to extend the arm

length in order to observe larger relative changes. However, the weak interaction of the gravitational radiation with matter makes it difficult to detect them, since the relative change in the distance between the bodies is very tiny. In the quadrupole approximation [168], the order of magnitude of the strain h of the gravitational radiation far from the source can be estimated as

$$h \simeq \frac{2G}{c^4} \frac{\dddot{I}_{ij}}{d},$$

(1.2)

where $\dddot{I}_{ij}$ is the reduced quadrupole moment, d is the distance from the source, G is the gravitational constant, and c is the speed of light. The small factor $G/c^4 = 8.2 \cdot 10^{-45}$ s^2 m^{-1} kg^{-1} gives an idea of the challenge of detecting GWs. The feeble strength of gravity entails that detectable signals for the current observatories must be produced by the most violent astrophysical events in the Universe, such as coalescence of black holes, supernova core collapse of massive stars, or remnants of the Big Bang. As an example, for energetic phenomena, such as inspiraling binary neutron stars of $1.2 \, \mathrm{M}_\odot$ at 100 Mpc, the value for the strain h is estimated on the order of $\sim 10^{-23}$ [163, 26]. This small number only generates shifts of $5 \cdot 10^{-21}$ m between two test masses separated by 1 km.

The GW sources radiate in a wide spectrum, which is usually categorized into four different bandwidths: the *ultra low frequency* band (10^{-18} Hz to 10^{-13} Hz); the *very low frequency* band (10^{-9} Hz to 10^{-7} Hz); the *low frequency* band (10^{-5} Hz to 10^{-1} Hz); and the *high frequency* band (1 Hz to 10^4 Hz) [81]. In particular, the low-frequency gravitational radiation between 10^{-4} Hz and 1 Hz is intended for space-borne mission concepts, such as the evolved Laser Interferometer Space Antenna (eLISA). Figure 1.2 shows the sources of gravitational waves within the eLISA bandwidth compared to on-ground detectors.

Several experimental approaches have been developed for the detection of GWs during the last decades. After the pioneer resonant-mass detector implemented by J. Weber in the sixties [187, 188], subsequents improvements of the original Weber bars have been developed [58, 18, 74, 19, 31, 8]. The physical principle is based on cylindrical or, more recently, spherical bodies, which enter into resonance when they are excited by a passing GW at the oscillation frequency. An important disadvantage is the limited detection bandwidth between tens and hundreds of hertz at the kilohertz frequency range. Nowadays, resonant detectors are still awaiting for direct GW detection coming from extremely energetic short bursts with low event rate, such as AURIGA [194] and NAUTILUS [20] in Italy.

In the mid 1970's, an alternative concept using laser interferometer devices began to develop. The main advantage over the resonant-mass detector is the sensitivity enhancement along a wider bandwidth, covering a broader range of GW sources. This approach is based on the Michelson-type configuration [131], where a coherent laser beam is split into two arms, bounced off by two reflective test masses (mirrors),
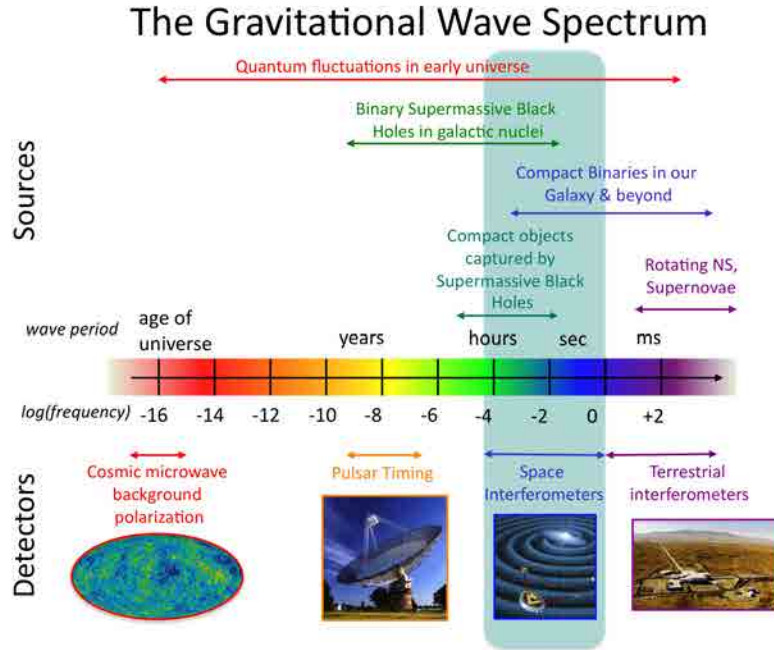
Figure 1.2: Gravitational-wave spectrum. Gravitational sources and detecting methods along the range of radiation frequencies. Credit: NASA.[1]

and then recombined prior to the photodiode detection. Figure 1.3 shows the differential displacement between the optical arms induced by a "+" polarization wave that arrives perpendicular to the detector's plane. The optical path length changes are then measured by the light phase differences in the interference pattern over time. Hence, the modulated light power measured by the photodiode at the interferometer output is given by [26]

$$P(t) = P_0 \sin^2 \left[\frac{2\pi}{\lambda}(L_1 - L_2) + \frac{2\pi}{\lambda} h(t) L \right], \qquad (1.3)$$

where P_0 is the laser power, λ is the laser wavelength, and L is the mean of the arm lengths L_1 and L_2. The second term of the equation $(2\pi h(t)L/\lambda)$ is the phase difference $\Delta\phi(t)$ in response to an incident GW.

The major noise sources which limit the sensitivity of ground-based interferometric detectors result from the photon shot noise, radiation pressure noise, standard quantum limit, thermal noise, seismic noise and gravity gradient noise [155]. In order to reach the sensitivity needed to detect for GWs, several adaptations of the original

---

[1] http://science.gsfc.nasa.gov/663/research/
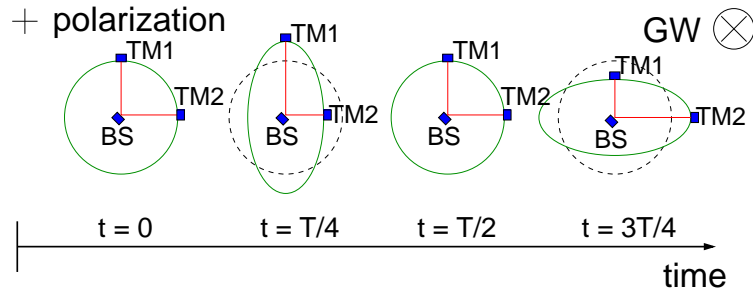
Figure 1.3: Laser interferometer approach. Changes in the distance between two bodies (TM1 and TM2) with respect the beam splitter (BS) when a GW transverses the detector.

design have been implemented in the current interferometer detectors. Along this line, the power- and signal-recycled Michelson interferometer helps to suppress the shot noise and increase the signal-to-noise ratio within a determined bandwidth or for some specific sources [110, 128]. For optimization purposes, Fabry-Perot cavities maximize the integration time between each optical arm and the GW [5, 2, 43]. Another important arrangement to increase the spatial and temporal stability of the laser and minimize laser beam jitter is achieved by placing an input mode cleaner right after the laser source [15]. A schematic diagram of the aforementioned techniques is shown is Figure 1.4.
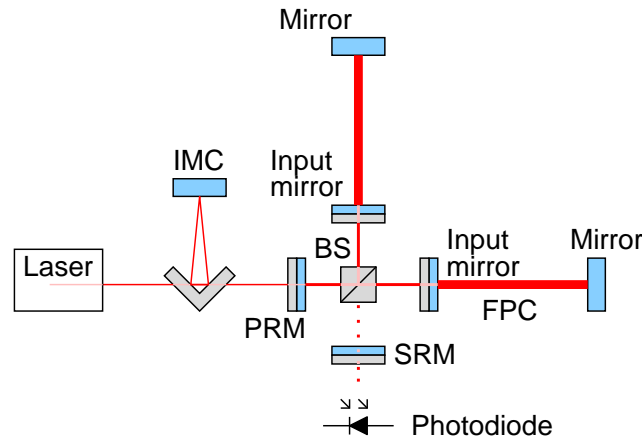
Figure 1.4: Schematic diagram of a power- and signal-recycled Michelson interferometer using Fabry-Perot cavities (FPC) and input mode cleaner (IMC). BS, beam splitter; PRM, power recycling mirror; SRM, signal recycling mirror.

Much work has been done on the different ground-based interferometric detectors located around the globe. They can be categorized in three types: first-generation detectors, which traditionally have been operated and involved in scientific observations; second-generation detectors, which are currently under way; and third gener-

ation detectors, which are new infrastructures under conceptual design study. The main first-generation detectors are LIGO [1] in USA (two at Hanford and one at Livingston), Virgo [3] in Italy, GEO600 [68] in Germany, and TAMA300 [116] in Japan. The successors of those detectors are Advanced LIGO (aLIGO) [71], Advanced Virgo [4], GEO-HF [189], and KAGRA [172]. Finally, the underground Einstein Telescope (ET) is a proposed third-generation detector with ten times better strain sensitivity than advanced detectors up to an extended low frequency limit of 1 Hz [162]. Below this frequency, seismic noise and arm length limit the low-frequency performance of the terrestrial detectors. Therefore, a dedicated space-borne mission based on the eLISA concept is crucial to observe the rich GW spectrum between 0.1 mHz and 1 Hz. An overview of this mission is given in Section 1.1.2.

A pulsar timing array (PTA) is an alternative approach used to search GWs with a frequency from 10^{-9} Hz to 10^{-5} Hz, mostly expected to be emitted by super massive black holes binaries. The detection concept is based on the radio telescope measurements of the pulse arrival times emitted by millisecond pulsars. The regular pulsar arrival times might undergo correlated changes produced by the influence of passing GWs along the region between Earth and the pulsars. Currently, the three main PTAs under operation are the European Pulsar Timing Array (EPTA) [94], the North American Nanohertz Observatory for Gravitational Waves (NANOGrav) [127], and the Parkes Pulsar Timing Array (PPTA) [75]. These three projects form the International Pulsar Timing Array collaboration. The future radio telescope project called Square Kilometre Array (SKA) [98] is planned to achieve sensitivities with at least an order of magnitude improvement in the gravitational wave strain amplitude compared with any other radio instrument.

Recent proposals for GW detection using atom-based interferometry have been studied during the last years [67, 76, 52]. In this detection strategy, cold atom clouds are used as inertial test masses instead of the reflective bodies used in conventional laser interferometry. Although further work is required to overcome some complex aspects in the design [28], the overall maturity of the technology is increasing quickly and is expected to be a powerful technique for future GW detection.

The comparison between the sensitivity curves of some of the most relevant detectors mentioned above is shown in Figure 1.5 along with the detectable GW sources.

1.1.2 An overview of the eLISA mission concept

eLISA is a space-based observatory proposed as a ESA large (L-class) space mission and conceived to directly detect low-frequency gravitational radiation between 0.1 mHz and 1 Hz [57].[2] This bandwidth, which is not observable from Earth, is expected to reveal some of the most exciting GW sources, such as massive black holes

---

[2]In October 2013, the *Gravitational Universe* was selected by ESA as the science theme for the next L3 mission.
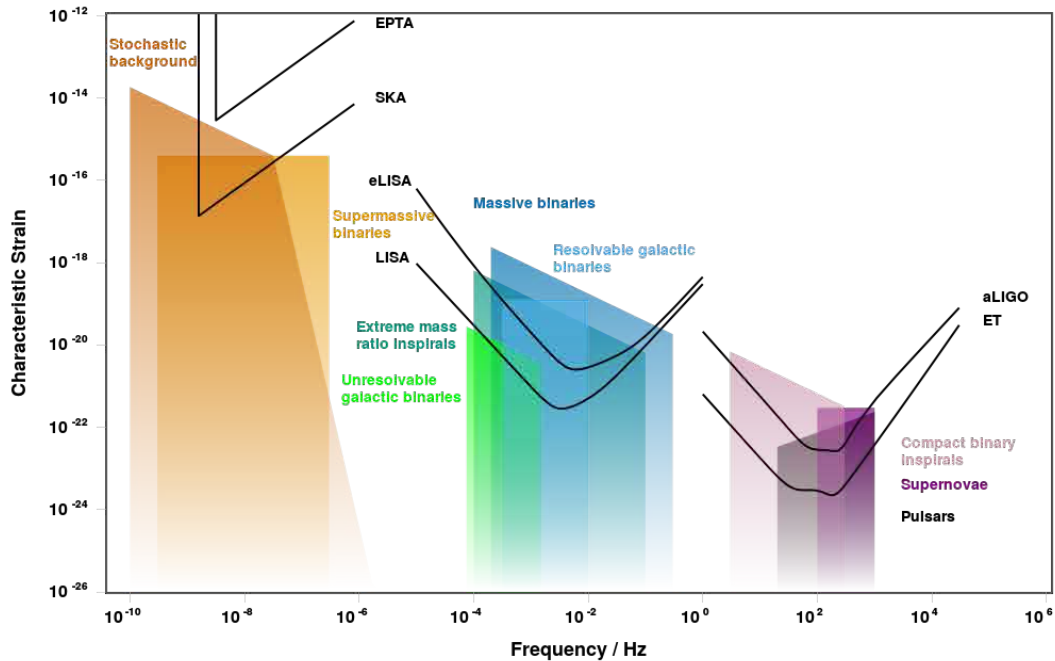
Figure 1.5: Characteristic strain curves for a variety of detectors and potential signals [133].

coalescence, compact binaries, and extreme mass ratio inspirals. Its current design is a reduced version of the generic LISA concept [27], which was a joint ESA-NASA project with decades of assessment and development study. Most of the technology is transfered directly from LISA although due to cost reduction, some valuable variations were adopted (see Table 1.1). As shown in Figure 1.6 , eLISA will be made up by three drag-free spacecraft (one "mother" and two "daughters") in a one-million-kilometer side equilateral triangle. Each side forms a two-link interferometer between freely floating test masses (TMs) that act as the geodesic reference mirrors for the gravitational wave measurement. The spacecraft constellation will follow a heliocentric orbit, at a distance of 1 AU from the sun (between 10° and 30° behind the Earth) and on a plane of the constellation tilted by 60° with respect to the ecliptic. The present design scheme makes it possible to maintain a near-equilateral triangular geometry along the mission lifetime without the need for station keeping. However, the inter-spacecraft distance will vary due to the gravitational disturbances of the Solar system on the spacecraft. These changes, in the order of 2% of the nominal arm length, are expected to occur in long time scales of months, i.e, outside of the frequency band of interest for eLISA (time scales of hours). Therefore, the precise interferometer measurements along the eLISA bandwidth can be separated from the slower drifts in the nominal arm length over the duration of the mission.

Table 1.1: Main parameters comparison between the LISA and eLISA.

	LISA	eLISA
Spacecraft	3 identical	1 Mother and 2 Daughters
Arm length	$5 \cdot 10^6$ km 6 laser links	$1 \cdot 10^6$ km 4 laser links
Laser power	2 W	2 W
Incident light power	370 pW	710 pW
Laser wavelength	1064 nm	1064 nm
Telescope	⌀40 cm	⌀20 cm
Orbit	Heliocentric 20° behind Earth	Heliocentric 10° to 30° behind Earth
Mission duration	5 years nominal 10 years extended	2 years nominal 5 years extended
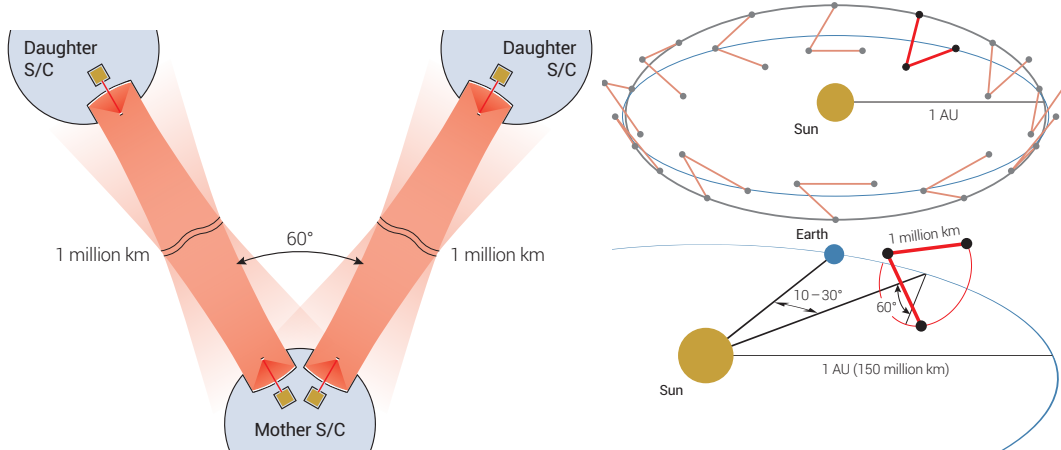
Figure 1.6: Left: the Mother spacecraft is optically linked with the two Daughters spacecraft for the current eLISA configuration. Top right: annual evolution of the three spacecraft orbit. The trajectory of one of the spacecraft (gray line) is represented together with the Earth orbit (blue line). Bottom right: current eLISA flight configuration trailing the Earth.

As shown in Figure 1.7, the major systems involved in the eLISA payload include the gravitational reference sensor (GRS), the drag-free control and the optical metrology system (OMS). There is one payload at the end of each arm forming the link with another spacecraft, i.e, two identical units on the mother spacecraft and one on each daughter spacecraft. In the following lines, a brief overview of these elements is given.

Gravitational reference sensor and drag-free control

The GRS monitors the motion in all six degrees of freedom between the spacecraft and the TM, a 46 mm-side cube made of gold-platinum. The instrument uses surrounding capacitive displacement sensors reaching a sensitivity up to the $\mathrm{nm\,Hz}^{-1/2}$ level. This signal, together with the more precise interferometry readout, is used to perform the drag-free control loop and angular alignment by means of an array of micro-Newton spacecraft thrusters. The drag compensation system keeps the TM shielded from the non-gravitational sources within the required free-fall conditions along the sensitive axis (interferometric axes). Additionally for keeping the TM centered, the housing includes electrostatic actuators that can apply forces on the non-sensitive degrees of freedom of the TM. Apart from this, the GRS also contains a caging mechanism to block the TM position during launch, and a UV system for photoelectric discharge of the TM in the course of science operation.
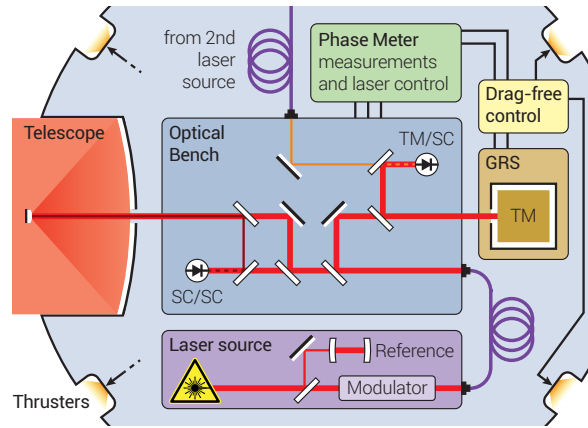
Figure 1.7: Main components of the eLISA payload: the gravitational reference sensor (GRS) enclosing the TM, the optical metrology system, and the drag free and attitude control system (DFACS).

Optical metrology system

The OMS plays the very important role of quantifying the relative displacement between the two test masses. For noise cancellation purpose, a combination of interferometric readouts is used by measuring not only the distance between spacecraft, but also between the TM and their spacecraft. Due to the large arm length the collimated light sent out from the remote spacecraft is expanded and needs to be collected by a local optical telescope. Hence, from a 2 W laser source (at 1064 nm wavelength) transmitted at the distant spacecraft, only an incoming light power of 710 pW is received after traveling through the inter-spacecraft distance. This small fraction can not be simply reflected again to the remote spacecraft; therefore, apart

from the master laser, the other optical links are frequency locked between them. The received light from the far spacecraft is combined with a local laser at similar frequency (but not equal) to generate a heterodyne signal at MHz frequencies (beat note at the difference frequency), which is detected by a photodiode as shown in Figure 1.7. The changes between the TM distances caused by a GW shift the phase of the laser light so that it is conserved in the heterodyne signal. After this, a phase meter system based on a phase-locked loop (PLL) acquires the science readout with μrad Hz$^{-1/2}$ level within the measurement band.

1.1.3 Magnetic field effects in eLISA

As aforementioned, due to the extremely low amplitude of gravitational waves, the TMs have to be shielded from non-gravitational forces, which would disturb their pure geodesic motion. Consequently, environmental conditions around the TMs need to be under stringent control; otherwise the different noise disturbances would conceal the GW signal. The LISA noise requirement in terms of free-fall accuracy $S_{\delta a,\text{LISA}}^{1/2}$ (m s^{-2} Hz$^{-1/2}$) in the frequency band between $0.1\,\text{mHz} \leq \omega/2\pi \leq 100\,\text{mHz}$ is plotted in Figure 1.8. At frequencies below 1 mHz, the noise estimation is dominated by a residual acceleration noise of $3\,\text{fm s}^{-2}\text{Hz}^{-1/2}$ per test mass, which is mainly caused by the drag-free control and environmental effects, e.g., thermal, magnetic and random charging fluctuations [11]. Among them, one of the main contributors to the total acceleration noise budget is the surrounding magnetic field in the spacecraft, created by the interplanetary magnetic field, electronic units and other components such as the micro-thrusters, batteries, solar panel cells, etc. These produce dc and fluctuating magnetic fields and gradients which must be kept below certain values in order to ensure proper science operation of the GW observatory. The magnetic field and magnetic field gradient cause a non-gravitational force and torque on the TM due to its non-zero magnetization $\mathbf{M}$ and susceptibility χ. This spurious force $\mathbf{F}$ and torque $\mathbf{N}$ on the TM volume V induced by a magnetic disturbance is given by

$$\mathbf{F} = \left\langle \left[\left(\mathbf{M} + \frac{\chi}{\mu_0} \mathbf{B} \right) \cdot \boldsymbol{\nabla} \right] \mathbf{B} \right\rangle V \tag{1.4}$$

and

$$\mathbf{N} = \langle \mathbf{M} \times \mathbf{B} + \mathbf{r} \times [(\mathbf{M} \cdot \boldsymbol{\nabla}) \, \mathbf{B}] \rangle V, \tag{1.5}$$

where $\mu_0 = 4\pi \cdot 10^{-7}\,\text{m kg s}^{-2}\,\text{A}^{-2}$, $\mathbf{r}$ is the vector distance to the center of the TM and $\langle \cdots \rangle$ denotes TM volume average of the enclosed quantity. The force fluctuations are estimated by

$$\delta F = \frac{\chi V}{\mu_0} \langle \delta \mathbf{B} \cdot \boldsymbol{\nabla} B \rangle + V \langle \mathbf{M} \cdot \delta(\boldsymbol{\nabla} B) \rangle + \frac{\chi V}{\mu_0} \langle \mathbf{B} \cdot \delta(\boldsymbol{\nabla} B) \rangle + \frac{\chi V}{\mu_0} \langle \delta \mathbf{B} \cdot \delta(\boldsymbol{\nabla} B) \rangle. \tag{1.6}$$

10

This leads to keeping the dc and slow time-varying magnetic fields and gradients below certain values in order to ensure proper science operation of the GW observatory.[3] The quadratic coupling of the last term of the equation may be relevant in the presence of ac magnetic fields with close frequencies, which can cause a low-frequency fluctuation component due to the down-conversion of the high-frequency magnetic signals [184, 179, 59, 60]. A smaller contribution is due to the Lorentz force produced by the interaction between the charged TM moving through the fluctuating interplanetary magnetic field [14].
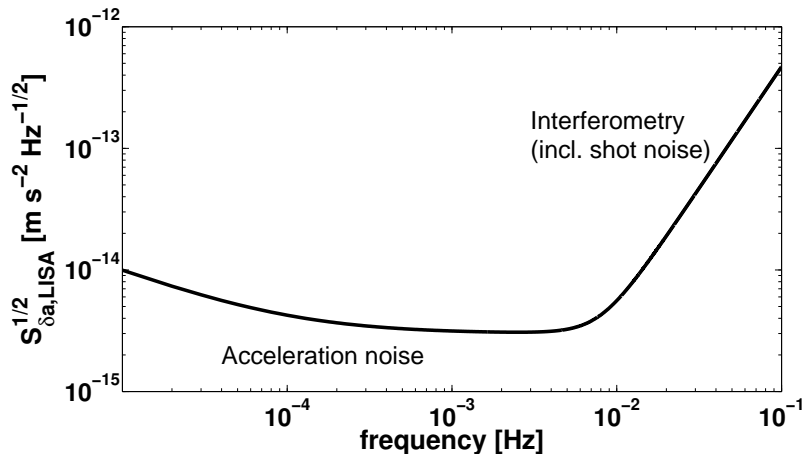
Figure 1.8: LISA noise requirement plotted as amplitude spectral density (ASD) of the differential acceleration of the test masses.

The magnetic properties of the TMs ($\mathbf{M}$ and χ) are known due to several on-ground and in-flight experiments [47]. However, the magnetic field environment ($\mathbf{B}$ and $\boldsymbol{\nabla}\mathbf{B}$) at the TM locations needs to be carefully evaluated and suppressed from the main data stream during the mission. To that end, eLISA will have a set of magnetic sensors placed in key locations, with the purpose of discerning the low-frequency magnetic noise contributions from the overall acceleration noise budget.

1.1.4 The route to eLISA: LISA Pathfinder

Due to the the cutting-edge technology behind eLISA, and given that some hardware can not be fully tested on ground, a dedicated technology demonstrator satellite was developed to pave the way for eLISA. This technological mission adopted within the ESA program is LISA Pathfinder. The basic concept is to mimic one of the eLISA arms within a single spacecraft, shrinking the optical link between test masses from

---

[3]Fluctuations of the magnetic moment density of the TM are not expected due to the extremely stable thermal conditions prevailing inside the GRS [108].

$1 \cdot 10^6$ km to around $30\,\mathrm{cm}$. The main objective is ultimately the very high precision with which test masses must be set in geodesic motion inside the spacecraft, with a reduced acceleration noise budget compared to eLISA of

$$S_{\delta a,\mathrm{LPF}}^{1/2}(\omega) \leq 3 \times 10^{-14} \left[1 + \left(\frac{\omega/2\pi}{3\ \mathrm{mHz}} \right)^2 \right] \mathrm{m\,s^{-2}\,Hz^{-1/2}} \qquad (1.7)$$

in the frequency band between 1 mHz and 30 mHz [183]. This means that also the lower end of the eLISA measurement band (0.1 mHz) has been relaxed.

LISA Pathfinder contains two payloads: the LISA technology package (LTP) provided by ESA, and the disturbance reduction system (DRS) from the NASA contribution. The LTP determines the relative position and rotation of both free-falling test masses by laser interferometry [12], while the DRS supplies an additional colloid thruster and control system [61]. In the same way as for eLISA, the mayor subsystems on board the LTP include the optical metrology subsystem (OMS), the gravitational reference sensor (GRS), the drag-free attitude control system (DFACS), and the data and diagnostics subsystem (DDS). Most of these subsystems are very similar to those for eLISA, in particular, the GRS will be mainly the same. A drawing of the LTP is displayed in Figure 1.9, which shows the optical bench interferometer and the GRS vacuum chambers containing the TMs.
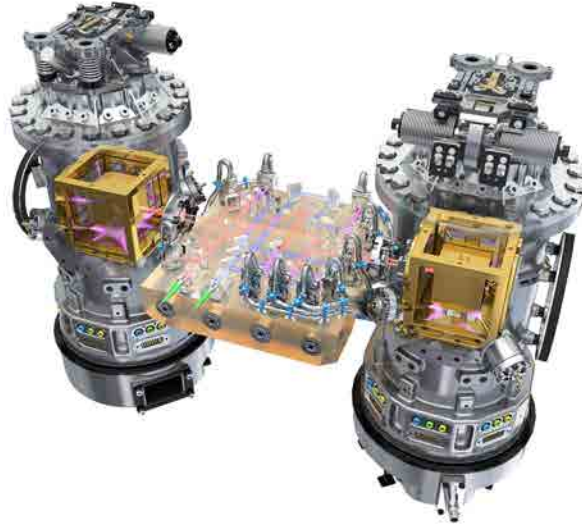
Figure 1.9: Artist impression of the LISA Technology Package. Each of the vacuum enclosures (the two silvery cylindrical towers) encloses one TM at its center (gold cube), which are linked via the optical bench. Credit: ESA/medialab.

The OMS measures not only the relative displacement between the TMs, but also the distance of one of the TMs (TM1) with respect to the spacecraft. More details can

be found in [21]. Regarding the drag-free subsystem, there are two control loops: the drag-free loop and the electrostatic suspension loop. The former keeps the spacecraft centered with respect to the TM1 by means of micro-Newton thrusters. The second control loop acts via the surrounding electrodes on the second test mass (TM2) to keep a fixed distance with the remaining TM and prevent the TM2 from colliding with the wall of the electrode housing. Consequently, these control loops maintain a drag-free operation of the first TM, while ensuring a quasi-free fall trajectory for the second test mass.
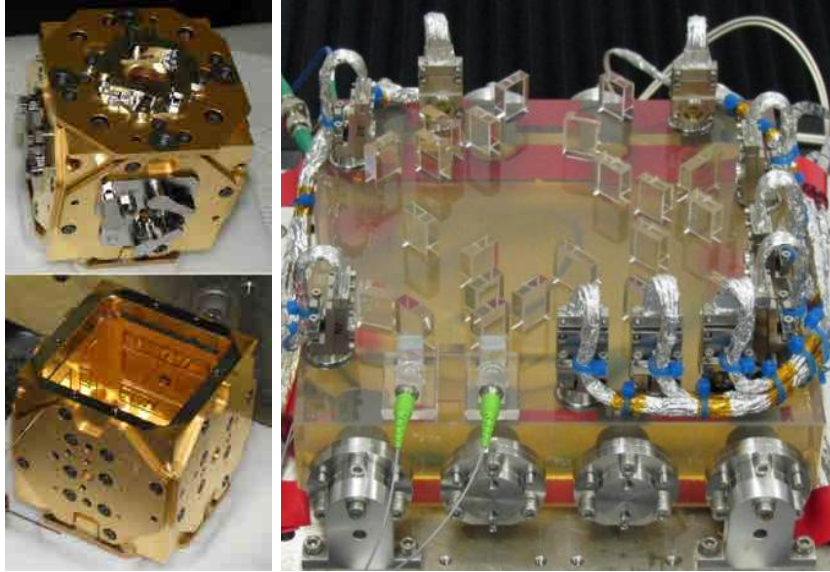
Figure 1.10: Left: electrode housing of the GRS. Credit: eLISA Consortium. Right: flight optical bench before integration into the LTP. The optical beams are applied into the optical bench by means of the fiber injector (green connectors). Credit: University of Glasgow and University of Birmingham.

The last of the subsystem mentioned above is the DDS, which has the crucial function of distinguishing between various sources of noise that directly affect the main scientific measurement of the mission, i.e. the interferometer phase readout. The estimation of the effects of each independent disturbance on the parasitic acceleration noise is obtained by dedicated flight experiments, where the DDS plays a very important role. More specifically, the DDS will provide the necessary instrumentation to monitor and characterize the effect of thermal, magnetic and charged particle environment inside the spacecraft [37]. Once the relationship between induced perturbations and interferometer readings is estimated, the excess noise on the interferometer readings can be established by monitoring each independent source of disturbance. The DDS is composed of a number of sensors (magnetometer, thermistors, and a particle detector) and actuators (coils and heaters) called diagnostic

items:

- **Thermal diagnostics**: An array of 24 thermistors and 14 calibration heaters is attached in key points of the LTP, which are the inertial sensors, the optical bench and the suspension struts. The sensors monitor the stable thermal environment with a sensitivity better than $10^{-5}\,\mathrm{K\,Hz}^{-1/2}$ along the measurement bandwidth [160]. The purpose is to translate temperature information into test mass acceleration noise. This relationship is obtained by applying high signal-to-noise ratio thermal signals by means of the calibration heaters [141].

- **Radiation monitor**: The particle detector samples the flux of charged particles that hit the LISA Pathfinder spacecraft, some of which will eventually reach the TMs and generate charge depositions in them. Average charging rates can be established by thorough measuring over long periods of time provided by the inertial sensor, but temporal fluctuations of the galactic cosmic ray (GCR) flux and solar energetic particle (SEP) events contaminate the scientific data. Thus, the radiation monitor is used to correlate the incident radiation and the TM charging. The minimization of this TM charging noise can be accomplished by either matching charging and discharging rates, or through post-processing of the radiation monitor data.

- **Magnetic diagnostics**: As previously mentioned, due to the residual magnetic properties of the TM, the magnetic field and magnetic field gradient in the TM region result in acceleration fluctuations. Like in the thermal diagnostics subsystem, a set of sensors and actuators, magnetometers and induction coils in this case, is used to determine the transfer function relating the magnetic forces and the effect on the motion of the test masses. The instrumentation required for the magnetic measurements is part of this thesis and it is explained in detail in Chapter 2.

A magnetic diagnostics subsystem fulfilling the LISA Pathfinder and the more demanding eLISA conditions would also be appropriate for use in magnetically sensitive fundamental physics experiments requiring long integration time, such as high-precision measurements of the weak equivalence principle using space atom interferometry in STE-QUEST [9]. Therefore, the work presented in this thesis has been also proposed beyond the scope of eLISA as part of the magnetic field monitoring system within the STE-QUEST atom interferometer (AI) payload. An overview about the main concept on the test planned for STE-QUEST is given in the next section.

1.2   Testing the weak equivalence principle

The weak equivalence principle (WEP), also known as universality of free fall (UFF), is a key concept of general relativity grounded on the identity between the inertial

and the gravitational mass. The principle states that if any uncharged test body is placed at an initial event in space-time and given an initial velocity there, then its subsequent trajectory will be independent of its internal structure and composition. The WEP can be tested by measuring the differential acceleration between two different bodies freely falling in the same gravitational field, and their deviations can be assessed by the Eötvös ratio as

$$\eta_{\text{AB}} = 2\frac{a_{\text{A}} - a_{\text{B}}}{a_{\text{A}} + a_{\text{B}}} = 2\frac{(m_{\text{g}}/m_{\text{i}})_{\text{A}} - (m_{\text{g}}/m_{\text{i}})_{\text{B}}}{(m_{\text{g}}/m_{\text{i}})_{\text{A}} + (m_{\text{g}}/m_{\text{i}})_{\text{B}}}, \tag{1.8}$$

where a_{A} and a_{B} are the accelerations of the test masses A and B, m_{g} is the gravitational mass and m_{i} is the inertial mass. Hence, the nonzero value of η_{AB} implies the violation of the WEP. The study of possible quantified violations can give relevant information for the better understanding of the fundamental force of nature or the relationship of gravity with other fundamental interaction theories, such as string theory or canonical quantum gravity [95, 91].

The WEP deviations have been tested in a large number of experiments at different levels of accuracy by using macroscopic bodies or coherent matter waves. Table 1.2 shows a comparison between various current and future tests referenced to the Earth's gravitational field. As it happens when terrestrial GW detectors are used, the sensitivity of ground WEP tests is limited by several inherent effects, as for example, gravity gradients, environmental disturbances, short free fall evolution times, and smaller variations of gravitational potential. For this reason, space-based tests utilizing macroscopic test bodies, as the Microscope experiment (ESA-CNES), or quantum matter, as the STE-QUEST mission concept, represent a significant improvement over the best current on-ground tests. In the following section, the performance of the atom interferometry payload required for the WEP test in STE-QUEST is outlined.

1.2.1 An overview of the STE-QUEST mission concept

STE-QUEST (Space-time Explorer and Quantum Equivalence Principle Space Test) is a M5 candidate mission proposed to ESA within its Cosmic Vision program. Its primary scientific goal consists in quantifying the universality of the free propagation of matter waves in the Earth's gravitation field to an uncertainty in the Eötvös parameter better than $2 \cdot 10^{-15}$ [173]. The planned payload for the test of the WEP comprises a dual species differential atom interferometer using Potassium and Rubidium isotopes. The choice of ^{41}K and ^{87}Rb is mainly motivated by previous experience for atomic sample preparation and cooling techniques [156, 158, 165]. These two atomic clouds are condensed to a quantum degenerate state (Bose-Einstein condensate – BEC) in order to reduce systematic effects and guarantee high contrast, thanks to the long coherence length and the low expansion rates of the ensembles [63].

Table 1.2: Present and upcoming on-ground and space WEP tests. Grey rows indicate the experiments using macroscopic test masses. The best present measurement is $1.8 \cdot 10^{-13}$ [164].

	Experiment	η	Elements
	Torsion balance [164]	$(0.3 \pm 1.8) \cdot 10^{-13}$	Ti, Be
On-ground	AI/FG5 [146]	$(7 \pm 7) \cdot 10^{-9}$	Cs, corner cube
	Dual AI (Garching) [63]	$(1.2 \pm 1.7) \cdot 10^{-7}$	^{85}Rb, ^{87}Rb
	Dual AI (ONERA) [32]	$(1.2 \pm 3.2) \cdot 10^{-7}$	^{85}Rb, ^{87}Rb
	Dual AI (Firenze)[176]	$(0.2 \pm 1.6) \cdot 10^{-7}$	^{87}Sr, ^{88}Sr
	Dual AI (Hanover)* [165]	10^{-9}	^{87}Rb, ^{39}K
	Dual AI (Berkeley)* [70]	10^{-14}	^{6}Li, ^{7}Li
	Dual AI (Stanford)* [51]	$10^{-15}/10^{-16}$	^{85}Rb, ^{87}Rb
Space	STE-QUEST* [9]	10^{-15}	^{41}K, ^{87}Rb
	MICROSCOPE* [178]	10^{-15}	Pt, Ti
	STEP* [143]	10^{-18}	Pt, Ir, Nb, Be
	Galileo Galilei* [140]	10^{-17}	TBD

*Upcoming WEP experiments.

With the considered approach, the AI performance requires a sensitivity to differential acceleration better than $1 \cdot 10^{-11}/\tau^{1/2}\,\mathrm{m\,s^{-2}}$, for an integration time τ between $20\,\mathrm{s}$ and $3.5 \cdot 10^{6}\,\mathrm{s}$.

A highly elliptical Earth orbit (10.6 h period) is needed to ensure large gravitational accelerations during the perigee passage in order to maximize the signal-to-noise ratio of a possible violation signal from the interferometer readouts. The rest of the orbit, after the perigee phase, is employed for validation and calibration plans of the instrument. The target uncertainty in the Eötvös ratio at the $2 \cdot 10^{-15}$ level is achieved after an integration time of about 1.2 years for 3 years of routine science operation. Figure 1.11 shows the spacecraft trajectory, which has an altitude of 2500 km at perigee and 33600 km at apogee.

The atom interferometer makes use of the atom-light interaction by applying a sequence of three laser pulses ($\pi/2 - \pi - \pi/2$) for coherently split, reflect, and recombine the atomic wave packets. The instrument utilizes a double-diffraction scheme, which transfers a symmetric momentum splitting of $4\hbar k$, for the effective wave vector k and Planck's constant $\hbar$, while the internal states along its two arms are the same [101, 53]. This scheme makes it possible to reduce phase shifts couplings, such as homogeneous magnetic fields or off-resonant light fields. Although the matter waves travel with the same internal state during the free evolution time of the interferometer sequence, a state labeling appears in the output ports which enables the measurement of the phase shift by state selective fluorescence technique. Neglecting non-inertial contributions, the difference in phase at the end of the inter-
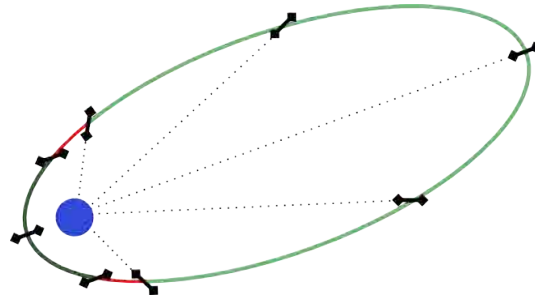
Figure 1.11: Elliptical geosynchronous transfer orbit for STE-QUEST spacecraft. AI measurements are taken during the perigee passes (dark green line), where the sensitive axis of the AI is pointed towards the spacecraft-Earth direction (black symbols). Along the red lines the spacecraft changes the orientation required for the different operation phases [9].

ferometer pulse sequence scales as $\phi_{\mathrm{a}} = \vec{k} \cdot \vec{a} T^2$, where $\vec{k}$ is the effective wave vector, $\vec{a}$ the relative acceleration, and T the free evolution time between the laser pulses. The beam splitter is oriented in the instrument sensitive axis $\vec{k} \| \vec{a}$. Figure 1.12 shows an interferometer geometry similar to a Mach-Zehnder one in combination with a double diffraction beam splitting technique.
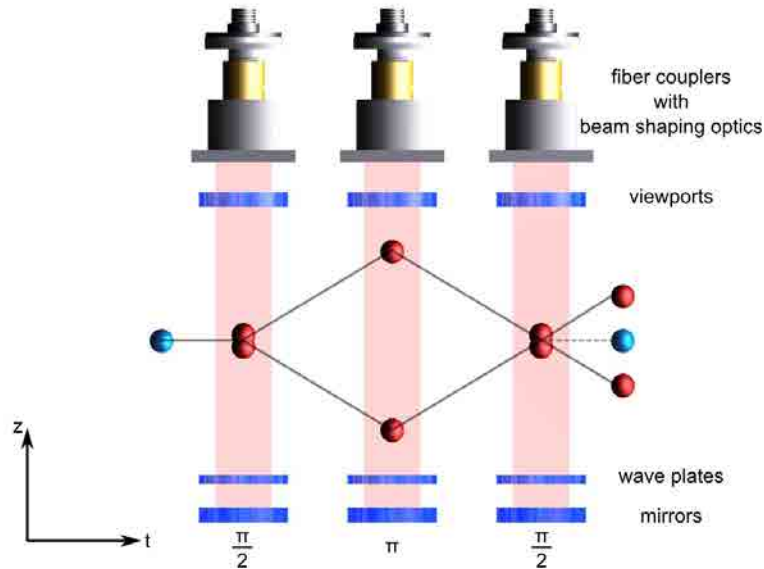
Figure 1.12: Temporal sequence of the Mach-Zehnder AI with double diffraction. The laser pulses symmetrically split, reflect, and recombine the atoms trajectories. The blue and red circles indicate the two hyperfine levels of the atoms. The two pairs of symmetrical light fields have orthogonal linear polarization due to the $\lambda/4$ wave plate response, thus creating the counter propagation beams [9].

17

The scientific AI payload is divided into three main functional systems based on a modular design: the Physics Package, the Laser System, and the Electronics Package [166]. Inside the Physics Package, the two Bose-Einstein condensation (BEC) wave packets are generated and manipulated by using different elements, such as magnetic, optical and chip traps (Figure 1.13). The preparation period lasts less than 10 s. At this point the interferometer sequence is started by the Raman probe lasers, followed by the fluorescence detection sequence through the charge-coupled device (CCD) readouts. Besides, the Physics Package provides the vacuum and magnetic environment (set of Helmholtz coils and mu-metal shielding) required for the complete experimental cycle.
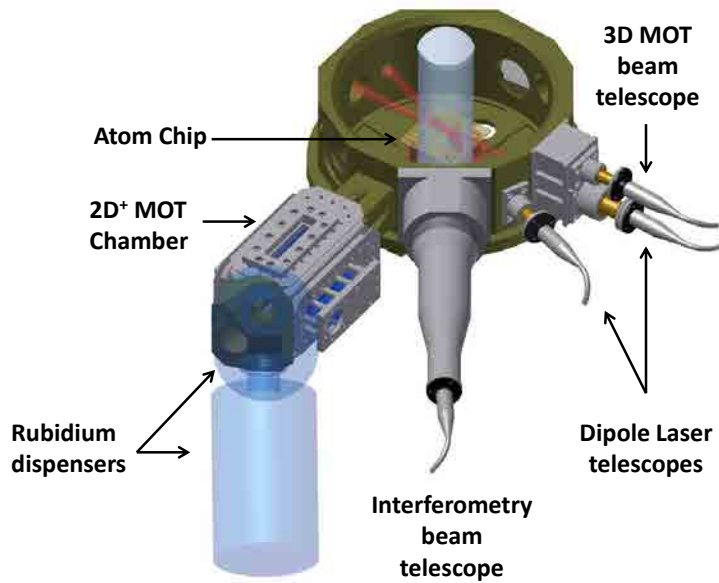
Figure 1.13: Main subsystems of the Physics Package. The 2D$^+$-MOT chamber captures and cools down the two isotopes released from the dispensers. Atoms are pushed, loaded and pre-evaporated into the atom chip. The dipole laser finalizes the evaporation process and reaches the two BECs. Finally, the Raman beams (light blue beam in the drawing) probe the two samples and the interrogation sequence starts.

The Laser System includes the light sources connected to the Physics Package for cooling, trapping, preparation, coherent manipulation, and detection of the atomic population. Additionally, it contains the switching and distribution module, which manages the complex arrangement of the laser lights according to the steps of the experiment. Finally, the Electronics Package consists of various functional electronic units in charge of driving the magnetic fields, radio-frequency signals, laser control loops and high voltage supplies. Moreover, each of these subsystems are monitored and commanded by the data management unit (DMU), which is also the interface to the on board computer (OBC) of the spacecraft.

1.2.2   Magnetic field effects in STE-QUEST

Apart from the intrinsic noise performance of the on-board instrumentation, some specific effects related to the spacecraft environment can induce a spurious differential acceleration, which would obscure a possible WEP violation signal. Hence, the achievement of STE-QUEST is directly related to the proper identification and suppression of these contributions below the targeted differential acceleration sensitivity of $1 \cdot 10^{-11} \mathrm{m\,s^{-2}\,\tau^{-1/2}}$. One of the main error sources in the output signal comes from the magnetic field gradients.
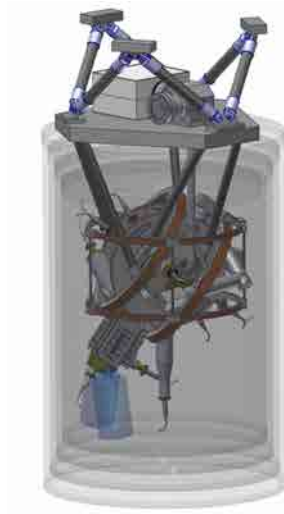
Figure 1.14: Mu-metal shielding surrounding the Physics Package. The vacuum pump on the top is placed outside the magnetic shield due to its ferromagnetic components.

During the interferometry process, the influence of the temporal magnetic field fluctuations is minimized by preparing both atom species in the state $m_F = 0$. In this way, the linear Zeeman shift does not play any role. However, the quadratic Zeeman effect is still coupled to the applied bias field, which is necessary to define the axis of the spin polarization for the atoms. Hence, the phase response of the interferometer due to the lack of homogeneity of the magnetic field can be written as

$$\phi = \int_{-\infty}^{+\infty} g(t) 2\pi \alpha B(t)^2 dt, \tag{1.9}$$

where $g(t)$ is the sensitive function [99], α is the coefficients for the quadratic Zeeman shifts, and B is the amplitude of the magnetic field. Since the quadratic Zeeman coefficients are different for each atom species, the stray magnetic fields have to be suppressed below a certain level compatible with the targeted measurement accuracy.

For the more demanding constraints in the current design, the magnetic field gradient in a reduced volume above the atom chip should be less than $0.4\,\mathrm{nT\,m^{-1}}$ [190].

In order to meet the magnetic requirement stated above, a four-layer mu-metal shielding encloses the Physics Package as shown in Figure 1.14. In addition to passive shielding, the baseline design of STE-QUEST also foresees active magnetic compensation of slowly varying external fields ($< 0.1\,\mathrm{Hz}$). Tiny magnetic sensors and compensation coils wound around the shield will help to attenuate the external magnetic drifts within a continuous closed-loop mode. The size of the magnetometer is determined by the air gap between the subsequent shield layers (13 mm in the baseline design). A similar active compensation method was applied in the design of the cold atom space clock PHARAO [97].

1.3   Objectives and structure of the thesis

Among the different sensors required for the aforementioned space missions, magnetometers are necessary devices to monitor the slow drifts of the environmental magnetic field. The present work of this thesis is mainly focused on the design and development of a system capable of monitoring magnetic fields with low-noise conditions at sub-millihertz frequencies. Different magnetic sensing technologies (fluxgate, anisotropic magnetoresistance, and atomic magnetometer), together with dedicated electronic noise reduction techniques, are studied in order to assess if they can be used for space missions demanding low-frequency requirements, such as the eLISA concept. The design of the magnetic sensing in eLISA is previously addressed in the development and validation of the magnetic diagnostic subsystem of LISA Pathfinder, also part of this thesis. We remark that eLISA is a demanding mission in terms of low-noise/low-frequency requirements, which limit the performance of the on-board instrumentation. This means that a system fulfilling the eLISA low-frequency noise requirements will also be suitable for other missions such, as STE-QUEST. Moreover, these missions require the careful control of the local magnetic environment generated by the spacecraft. The reason is that the main on-board instrument can only operate successfully and achieve its performance if the magnetic environment, including that generated by the spacecraft itself, is sufficiently benign. Therefore, this work also involves the investigation of the magnetic characteristics of the magnetometer and its possible impact on the scientific experiment. Finally, another potential problem in LISA Pathfinder is the accuracy of the magnetic field estimation from the magnetometer to the region of interest. A robust interpolation method based on an new magnetometer array configuration is presented in this work. Although other topics are covered, the objectives mentioned here are considered amongst the most challenging problems in this thesis. In order to find a solution along this lines, the following aspects are addressed in the next chapters.

20

Chapter 2 describes the design and validation of the magnetic diagnostics unit on board LISA Pathfinder. This subsystem consists of a set of fluxgate magnetometer and induction coils with the ultimate purpose of determining the magnetic force noise contribution. The experience obtained with the development of the magnetic diagnostics for LISA Pathfinder helped us to interpret the critical points of the system. Thus, a much more solid option must be considered for eLISA, due to the fact that its requirements are more demanding than in LISA Pathfinder.

In **Chapter 3**, the proposed design of the magnetic field monitoring for the eLISA mission concept is described. Previous studies have demonstrated that anisotropic magnetoresistances do not achieve the required sensitivities for eLISA at 1 mHz. Besides, their behavior at lower frequencies (0.1 mHz) has been hardly explored before. The aim of this chapter is to design and characterize a magnetic system based on anisotropic magnetoresistances with appropriate noise reduction techniques in the sub-millihertz frequency range. In this chapter we present the dedicated research in order to evaluate if anisotropic magnetoresistances are useful for eLISA in terms of stability.

eLISA-like space missions require careful consideration regarding the magnetic contamination caused by the spacecraft's sources. With respect to this, AMR uses a physical principle different from fluxgate magnetometers, although both principles include a magnetic core as a sensor head. Therefore, the magnetic properties of the device and its impact on the magnetic environment need to be investigated and quantified. On the whole, the objective of **Chapter 4** is to assess the contribution of the magnetic effects caused by the AMR sensor array on the total acceleration noise budget.

By design, the magnetometers cannot be physically placed at the site of the TM, which is the region where we aim to monitor the field. Then, since direct measurements in the TM location are not available, an interpolation method needs to be implemented. In **Chapter 5** we evaluate the accuracy of the magnetic field map reconstruction at the test mass with the currently conceived instrumental layouts. The robustness of the interpolation method is evaluated under different magnetic scenarios and takes into account common sources of errors in the measurement system.

In **Chapter 6** an experiment with a novel magnetic sensing technology based on alkali-vapor cell is developed and characterized. One remarkable advantage in atom magnetometers is that the sensor readings are related to fundamental physical constants. As a result, in principle the technology might be less susceptible to low-frequency changes. Even so, in practical situations there are external elements that can deteriorate the noise performance along the eLISA bandwidth. A tabletop optical setup is built with the purpose of evaluating if the magnetometer is suitable for low-frequency noise applications like the eLISA concept.

Finally, the main conclusions of the thesis and the future work to be undertaken are discussed in **Chapter 7**. Supplementary information to the main outcomes of

the study is included in several appendices at the end of the thesis.

Chapter 2

Magnetic Diagnostics Subsystem for LISA Pathfinder

The problem of magnetic sensing in eLISA has naturally been addressed first in its technology demonstrator, LISA Pathfinder. This chapter describes the main characteristics of the magnetic diagnostics subsystem for the LISA Pathfinder Technology Package (LTP). This magnetic diagnostics module consists of two main parts, the magnetic measurement subsystem and the on-board instrumentation for magnetic field generation. We present the instrumentation and some of the different tests carried out to validate the hardware according to the mission requirements. We also describe the principal drawbacks that came up during the development of the subsystem. Our experience with LISA Pathfinder's magnetic instrumentation serves us as the starting point for its counterpart in the eLISA mission, and also for other space applications beyond the scope of eLISA, such as STE-QUEST.

2.1 Magnetic measurement subsystem

Apart from the strict size, weight and power restrictions required in the design of the on-board instrumentation for LISA Pathfinder, one of the most relevant constraints is the long-term stability, which limits the noise performance at low frequencies. Hence, the magnetic measurement subsystem needs to confirm the fulfillment of the dc magnetic requirement and the fluctuations at the location of the TM shown in table 2.1 [183, 180].

The estimated magnetic fluctuations in the spacecraft set the limit of noise level for the magnetic sensors and the associated readout electronics. That is, the noise of the subsystem should be at least an order of magnitude less noisy than the maximum estimated magnetic fluctuations. As a result, the magnetic measurement subsystem must comply with a noise figure of

$$S_{B,\text{system}}^{1/2} \leq 10\,\text{nT}\,\text{Hz}^{-1/2}, \ 1\,\text{mHz} \leq \frac{\omega}{2\pi} \leq 30\,\text{mHz}. \tag{2.1}$$

The noise performance along the measurement bandwidth is the most important characteristic to be studied since the milli-hertz range is hardly explored and on rare occasions specified by the manufacturers of sensors and electronics components. Apart from this, among different requirements, the subsystem is requested to have a field measurement range of $\pm 60\,\mu\text{T}$ and an uncertainty better than 1% for end of scale [183, 88].

Table 2.1: dc requirements and estimated fluctuations in the TM locations for LISA Pathfinder.

dc requirement	ASD estimation
$\lvert \mathbf{B}_{\text{bg}} \rvert \leq 10\ \mu\text{T}$	$S_{\mathbf{B}}^{1/2}(\omega) \leq 100\,\text{nT}\,\text{Hz}^{-1/2}$
$\lvert \boldsymbol{\nabla} B_{\text{bg},x} \rvert \leq 5\sqrt{3}\,\mu\text{T}\,\text{m}^{-1}$	$S_{\nabla B_x}^{1/2}(\omega) \leq 250\sqrt{3}\ \text{nT}\,\text{m}^{-1}\,\text{Hz}^{-1/2}$

2.1.1 Magnetic sensors

Magnetometers for LISA Pathfinder have been selected among space qualified fluxgate devices. Fluxgate technology was chosen on grounds of its excellent sensitivity, low noise and long heritage in space applications, where it has been the preferred solution in the past decades. The sensor head of a typical fluxgate sensor uses a sense winding (pickup coil) surrounding a inner excitation coil that is usually wound around two halves of a high magnetic permeability core (Vacquier-type core in this case [147]), which is periodically driven into saturation. If there is no external magnetic field, the opposite drive currents for each core half cancel out the total flux and compensate part of the odd harmonics sensed by the pickup coil. In the presence of any external magnetic field, the second harmonic of the driving frequency induced in the sense winding is used as a measure of the magnetic field. Based on Faradays's induction law, the even harmonic portion of the pickup coil voltage is given by

$$V_{\text{o}} = V_{\text{p}} \left(\frac{N_{\text{s}}}{N_{\text{p}}} \right)^2 \mu_{\text{a}} \frac{\mu_{\text{d}}'}{\mu_{\text{d}}^2} H_{\text{s}} \tag{2.2}$$

where V_{p} is the driving voltage, N_{p} and N_{s} is the number of turns of the driving (primary) and sense (secondary) windings, μ_{d} is the differential permeability dB/dH, μ_{d}' is the second order derivative d^2B/dH^2, and $\mu_{\text{a}} = \mu_{\text{d}}/(1 + K\mu_{\text{d}})$ is the apparent permeability of the core to the signal field H_{s} with a core demagnetization factor of K [66].
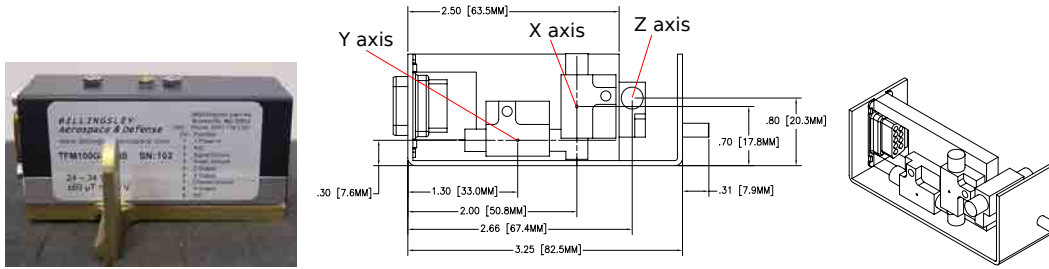
Figure 2.1: Left: engineering model of the Billingsley triaxial fluxgate magnetometer selected for LISA Pathfinder. Center and right: mechanical drawing of the inner sensor heads (X, Y and Z axis).

The selected space qualified magnetometer (TFM100G4) is an *ultra-miniature* triaxial fluxgate device designed for high reliability by Billingsley [30]. However, in spite of being a small sensor within the variety of the low-noise fluxgate family, the magnetometer is still bulky ($94 \, \text{cm}^3$) (see Figure 2.1), has large ferromagnetic sensor heads ($\sim 2 \, \text{cm}$ long), and the power consumption of each triaxial magnetometer is $\simeq 0.8 \, \text{W}$. These reasons led to the placing of only four triaxial sensors at somewhat large distances from the TMs ($\geq 18.85 \, \text{cm}$) in order to avoid back-action disturbances [13]. The locations of the magnetometers in the LISA Pathfinder payload is listed in Table 2.2 and illustrated in Figure 2.2.

Table 2.2: Location of the magnetometers and TMs for a fixed reference frame in the spacecraft. x-axis connects both TM centers and y-axis points towards the solar array (vertical axis). Units are in meters.

Item		**x**	**y**	**z**
	1	-0.0758	0.3694	0.532
	2	0.0758	-0.3694	0.532
Magnetometer	3	-0.3765	0	0.532
	4	0.3765	0	0.532
Test mass	1	-0.1880	0	0.532
	2	0.1880	0	0.532

Some specifications of the fluxgate magnetometer are displayed in Table 2.3. The principal characteristics of the fluxgate magnetometer within the LISA Pathfinder terms are: (i) discrimination, which is related to the noise and resolution; (ii) repeatability for long-term measurements, where thermal dependences are crucial; and (iii) accuracy of the measured value along with the offset and linearity.

25
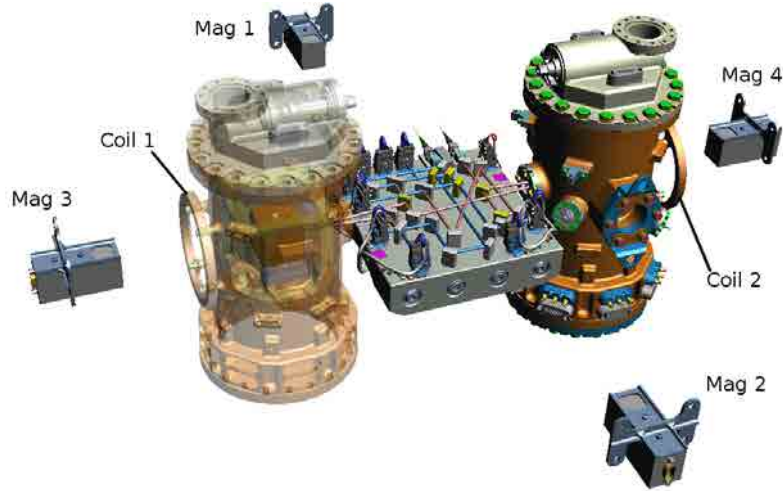
Figure 2.2: The payload of LISA Pathfinder with the four triaxial fluxgate magnetometers. Each of the electrode housings (cubic structures) inside the vacuum enclosure (the two cylindrical towers) encloses one TM at its center (solid gold cube).

Table 2.3: Specifications of the magnetic measurement subsystem for LISA Pathfinder (sensor model: Billingsley TFM100G4).

Parameter	Value
Field range (B_{range})	$\pm 60\,\mu\mathrm{T}$
Temperature coefficient (TC)	$1.2\,\mathrm{nT/K}$ $(0.002\%\,\mathrm{FS/K})$
Noise density ($S_{\mathrm{B}}^{1/2}$)	$< 100\,\mathrm{pT}/\sqrt{\mathrm{Hz}}$ @ 1 Hz
Input current (I_{supply})	$< 60\,\mathrm{mA}$
Input voltage (V_{supply})	$24 - 34\,\mathrm{V}$
Linearity (LSF)	0.015%
Sensitivity	$166.7\,\mu\mathrm{V/nT}$
Offset voltage	$< 25\,\mathrm{mV}\,(150\,\mathrm{nT})$
Bandwidth	$3.5\,\mathrm{kHz}$
Operating temperature	$-55^{\mathrm{o}}\mathrm{C}$ to $+85^{\mathrm{o}}\mathrm{C}$
Susceptibility to perming	$\pm 20\,\mathrm{nT}$ shift with $0.5\,\mathrm{mT}$
Axial alignment	$< 1^{\mathrm{o}}$
Weight	101 g

2.1.2 Signal processing circuit

The main parts of the electronics of the feedback-type fluxgate magnetometer used for LISA Pathfinder are shown in Figure 2.3. In the analog scheme, an oscillator produces a waveform at frequency $f_{\mathrm{d}} = 15\,\mathrm{kHz}$ as the excitation signal of the core

driver. Besides, another waveform at twice the excitation frequency is generated for the reference of the phase synchronous detector. The amplitude of the excitation current produced by the driver must be large enough to lead the whole sensor core into deep saturation so that the noise and perming effects of the magnetometer are reduced [170]. These electronics circuits should have low second harmonic distortion since it can conceal the sensor output signal. After this, the even harmonics of the drive frequency sensed by the pickup coil are amplified by a resonant circuit together with an ac-coupled amplifier, demodulated by a phase sensitive detector, and integrated. Then, the dc output of the integrator is sent to the pickup coil as the feedback of the close-loop control with the purpose of enlarging the limited linear range by canceling the field seen by the sensor core. The voltage across the feedback resistor (V_{fb}) measured by a differential amplifier is proportional to the detected magnetic field

$$B = \frac{V_{\mathrm{fb}}}{R_{\mathrm{fb}}} K_{\mathrm{coil}}, \tag{2.3}$$

where R_{fb} is the feedback resistance and K_{coil} is the current-to-field ratio of the pickup coil. Finally, the signal is low-pass filtered and quantized by an analog-to-digital converter (ADC) within the data acquisition unit (DAU), which is part of the data management unit (DMU).
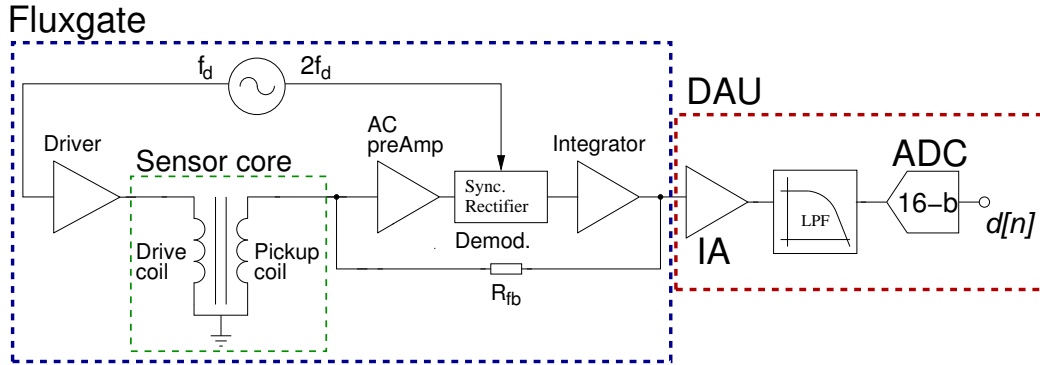
Figure 2.3: Block diagram of the analog signal conditioning circuit for the fluxgate magnetometer.

2.1.3 Performance tests

The qualification of flight hardware for space missions has a rigorous technology roadmap to be pursued before final acceptance. Regarding the magnetic diagnostics, the validation of the magnetometer performance, which is part of this thesis, has passed extensive testing according to the science requirements and top-level architecture definition [183], aimed to ensure their functionalities during mission operations.

In the following paragraphs, some of the results obtained for the most relevant test campaigns of the magnetic measurement subsystem are described. The magnetic items include both engineering and flight models of the magnetometers together with the electronics of the DMU related to the data acquisition of the magnetic diagnostics [102, 103, 106, 118].

Noise performance

The effective noise of fluxgate-type magnetometers may be partially caused by several major contributions, such as the difficulty of magnetization of small volumes inside the ferromagnetic core [170], material and geometry of the sensor core [148, 44], temperature dependence, long-term stability, thermal/mechanical stresses, characteristics of the excitation field, and many other [139, 138, 149, 126]. At low frequencies, although it is well known that the noise in fluxgate magnetometers is subject to $1/f$ type power spectrum, the noise specifications of sensors and electronics reported in the recent literature rarely cover such low frequencies as required in LISA Pathfinder. The behavior of the low-frequency power spectral density can be approximated by

$$S_B(f) = S_{\text{wn}} \left(1 + \frac{f_c}{f^\alpha} \right), \tag{2.4}$$

where S_{wn} is the white noise of the sensor, the corner frequency f_c tends to be higher than $1\,\text{Hz}$ and α is typically around 1. The last two terms are of critical importance along the milli-hertz range in our application. Alternatively, the instrument noise can be described by the root-mean square (rms) noise power, which is obtained by integrating the power spectral density over a given bandwidth from f_{H} to f_{L}. As a result, for $\alpha = 1$ the mean-square noise is given by

$$B_{\text{n,rms}}^2 = \int_{f_{\text{L}}}^{f_{\text{H}}} S_B(f)df = S_{\text{wn}} \left(f_{\text{H}} - f_{\text{L}} + f_c \ln \frac{f_{\text{H}}}{f_{\text{L}}} \right). \tag{2.5}$$

For spectra at frequencies below $1\,\text{Hz}$, the model prediction of the noise is based on the semi-empirical Eq. (2.4) and can only be solved approximately. Hence, a test campaign was envisaged in order to characterize the low-frequency noise, and in accordance with Eq. (2.1), verify that the system (magnetometer together with its associated electronics) is capable of discerning magnetic fluctuations of $10\,\text{nT}\,\text{Hz}^{-1/2}$ down to $1\,\text{mHz}$.

The stability of the external ambient field during the experiment is subject to the Earth's magnetic field variations and the environmental perturbations caused by equipments and ferromagnetic materials. Therefore, due to the fact that the amplitude spectrum of the environmental magnetic fields in the laboratory is around $200\,\text{nT}\,\text{Hz}^{-1/2}$ at $1\,\text{mHz}$ (see Figure 2.4), the measurements of the sensor noise need to be performed in appropriate conditions of magnetic cleanliness. These variations
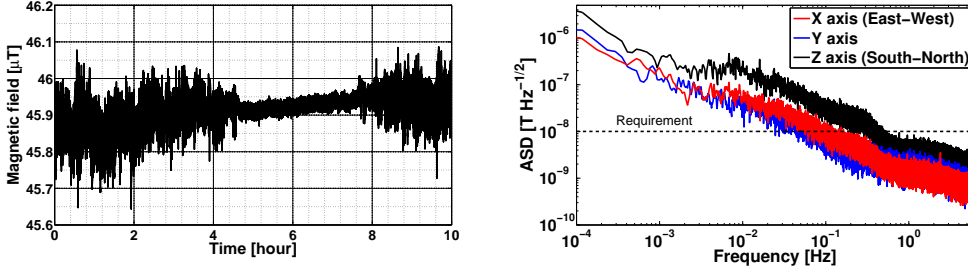
Figure 2.4: Temporal evolution (left) and amplitude spectral density (right) of the environmental magnetic field at the IEEC lab.

have to be reduced to a value lower than $1\,\mathrm{nT\,Hz}^{-1/2}$ at $1\,\mathrm{mHz}$ in order to discriminate between noise of the system and true environmental fluctuations. In other words, the external ambient field is required to be shielded at a level better than $46\,\mathrm{dB}$, which is easily obtained by means of a passive enclosure of a high-permeability material [175, 152]. The shielding factor is given by

$$A_{\mathrm{db}} = 20\log_{10}\frac{B_{\mathrm{out}}}{B_{\mathrm{in}}} \tag{2.6}$$

where B_{out} is the external magnetic field before placing the shield, and B_{in} is the residual field inside the shielding due to B_{out}. Thus, the magnetometer under test was placed inside a three-layer cylindrical shield of mu-metal (nickel-iron alloy) to screen out the slow drift of the environmental magnetic field (see Figure 2.5), mainly due to the inverse power-law frequency dependence of the Earth's magnetic field [42]. Various noise measurements were taken with the magnetic shielding placed in the center of a three-axis Helmholtz coil system in order to achieve higher attenuation. The intention is that the set of coils compensate the environmental field by generating an opposite field to that one seen in the surrounding area of the mu-metal enclosure. However, compensation fields are not necessary for noise performance because of the ample attenuation ratio of the passive mu-metal shielding (approximately 64 dB at room temperature in an Earth field of $50\,\mu\mathrm{T}$ [112]). All the runs have consisted in measurements of at least five hours, which is enough to estimate the amplitude spectral density (ASD) at $1\,\mathrm{mHz}$. Besides, the data were analyzed after the system was warmed up in order to avoid extra noise due to thermal dependences.

The procedure to determine the noise performance of the system was split into two parts; the noise measurements of (i) the sensor itself, and (ii) the circuits of the DAU included in the DMU. The ASDs of these measurements shown in Figure 2.6 indicate that the requirement is met along the measurement bandwidth. As expected, the noise of the electronics involved in the magnetic subsystem of the DAU limits the performance, in particular the main contribution is introduced by the transition noise of the ADC

29

Figure 2.5: Photographs of the experimental setup for the noise performance test of the magnetic measurement subsystem. Top left: flight model magnetometer fixed to the aluminum support before placing inside the shielding. Top right: setup configuration for the noise measurement of the flight model magnetometer. Bottom left: noise performance test of the magnetic data acquisition unit integrated in the flight model DMU. Bottom right: idem as the plot in top right picture for the engineering model magnetometer. In this case, the magnetometer under test is inside the shielding and an additional magnetometer measures the environmental magnetic field in the lab.

$$S_{B,\text{ADC}}^{1/2} = \sigma_{\text{ADC}} \frac{\text{FS}}{2^N} \frac{1}{s\sqrt{f_{\text{s,ADC}}/2}}, \tag{2.7}$$

where $\sigma_{\text{ADC}} = 1.3\,\text{LSB}$ (least significant bit) is the transition noise in rms of the ADC at worst case, $\text{FS} = 20\,(\pm 10\,\text{V})$ is the full-scale analog input range, $N = 16$ is the number of bits, $f_{\text{s,ADC}} = 3\,\text{Hz}$ is the sampling frequency, and $s = 166.7\,\mu\text{V/nT}$ is the magnetometer sensitivity. This leads to a noise level of $1.9\,\text{nT}\,\text{Hz}^{-1/2}$, in agreement with the one obtained experimentally for both DAUs in Fig 2.6.[1] This noise floor, which exceeds the noise level measured by the magnetometer, is limited via the sampling frequency imposed by the spacecraft telemetry [159]. Regarding the

---

[1]The ADC quantization noise $(\text{FS}/(2^n s(12 f_{\text{s,ADC}}/2)^{1/2}) = 0.4\,\text{nT}\,\text{Hz}^{-1/2})$ is negligible compared to the contribution caused by the ADC rms noise.

sensor noise, the $1/f$ noise of the three curves for each axis scales as $f^{-0.8}$ with the corner frequency around 10 mHz and the low-frequency noise levels are essentially the same ($\simeq 0.8\,\mathrm{nT}\,\mathrm{Hz}^{-1/2}$ at $1\,\mathrm{mHz}$). On the other hand, at higher frequencies the white noise exhibits discrepancies between the different axes by a factor of up to three. A possible reason for such behavior might be the existence of a higher residual field than the expected one due to efficiency loss of the magnetic shielding. However, this possibility seems unlikely since the amplitude attenuation ratio of the shielding should be more than one order of magnitude lower than the one observed in the noise measurements. In order to discard this unforeseen residual fields inside the 3-layer shielding as a possible noise source, another shield assembly of six layers was used to provide a lower field environment, but even so, the noise floor measurements were identical to the previous one. The same behavior took place when the orientation of the magnetometer inside the shielding was changed. Therefore, the noise discrepancies between axes could not be attributed to the magnetic environment. The discrepancies could be caused by extra intrinsic noise on the y-axis of the sensors under test, or by the proximity of the y-axis of the magnetometer to the electronics (see Figure 2.1) that can create some magnetic disturbances.
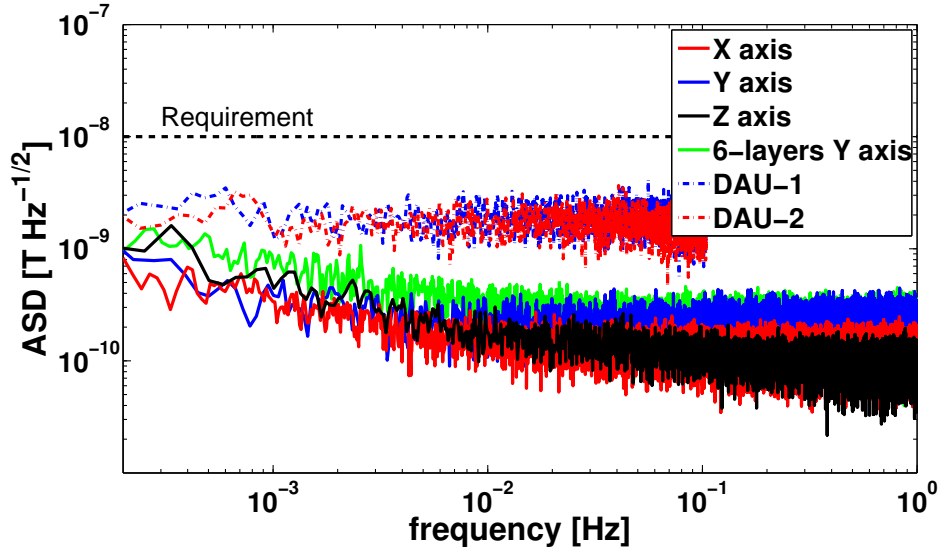
Figure 2.6: Amplitude spectral density of the magnetic measurement subsystem designed for the DDS of the LTP. Solid lines indicate the sensor noise for the three axis and blue/red dashed lines are the ADC noise of the two identical DAUs built in the DMU. All the measurements were performed in a 3-layer shielding except for the solid green trace that used a 6-layer shielding. The purpose was to dismiss unexpected noise contributions caused by unshielded field fluctuations. The black dashed horizontal line indicates the requirement.

On the whole, seven magnetometers (two engineering ones and five flight models) and two DMUs (one engineering one and one flight model) were tested.[2] The results obtained during the activities carried out for noise characterization were reported and the magnetic measurement subsystem validated according to the requirements of the DDS specification [117, 104, 105, 107]. It can be concluded that the magnetic noise of the engineering and flight models of the set of sensors, together with the acquisition system, comfortably meet the requirements in all the desired bandwidth.

Field range and uncertainty

Standard tests were performed to verify that the magnetic measurement system fulfills the design specifications required for the mission. In this particular case we describe the validation of the field measurement range ($\pm 60\,\mu$T) and the uncertainty ($< \pm 1\%$ end of scale) of the system. The measurements were held in a qualified calibration laboratory for magnetic measurements at the Universidad Politécnica de Madrid.

For this setup, the magnetometer was placed in the center of a precision three-axis Helmholtz coils system fed with currents in the range between ± 600 mA at intervals of 50 mA, which is equivalent to $\pm 65.21\,\mu$T and steps of $5.43\,\mu$T.[3] In order to reduce non-orthogonality errors between the magnetometer axes, the sensor position is changed after the sweep for each axis run. First, the magnetometer axis under test is oriented at the East-West coil, and then, the sensor is realigned by getting the maximum magnetometer output for the bias field of the coil. The magnetometer readouts and the current applied to the coils were acquired by means of the DMU and a digital multimeter (DMM), respectively. Figure 2.7 shows the test facility with the experimental setup for the engineering and flight models. In the former, the magnetic subsystem was tested as a whole, while for the flight model, the DMU and magnetometers were verified in separated tests. In this case, the analog inputs of the magnetometers in the DAU were simulated by a programmable power supply in the range between ± 10 V, i.e. $\pm 60\,\mu$T for a sensor sensitivity of $166.7\,\mu$V/nT.

Figure 2.8 shows the averaged values for both implementations (EM and FM) where, as expected, the range of the system covers the values between $\pm 60\,\mu$T. The upper limit is truncated by the bipolar operation of the ADC (from -10 V to 9.9997 V), though it is in compliance with the range considered in the mission specifications. We remark that these tests were performed for every triaxial magnetometer and the twelve analog inputs of both DAUs, and they exhibited the same functioning as shown in Figure 2.8.

For the calculation of the uncertainty, the experimental setup is the same as in

---

[2]During the test with the engineering model of the DMU, only one DAU is included, while in the flight model both identical DAUs are present and tested.

[3]The Helmholtz coil system was calibrated by the Physikalisch-Technische Bundesanstalt (PTB) in Germany. The current-to-field conversion of the coil is $108.69\,\mu$T/A.

Figure 2.7: Test facility for measuring the range and uncertainty of the magnetic measurement subsystem. Left: engineering model test including the DMU and the magnetometer (in the center of the three-axis coil system). Right: test of the flight model DMU using simulated magnetometer readings.
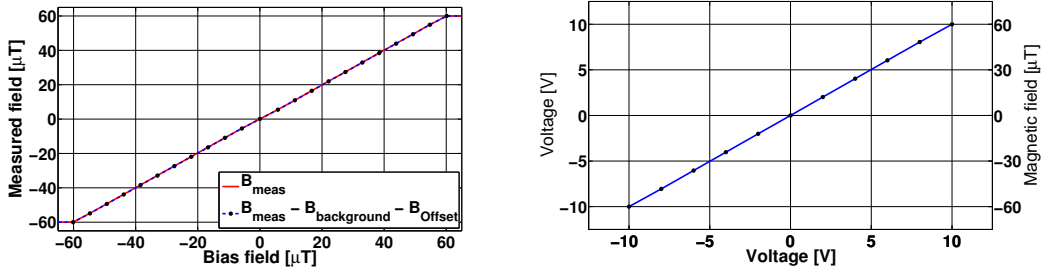
Figure 2.8: Range of the magnetic measurement system of the engineering (left) and flight models (right). Left: the red solid trace shows the magnetometers readings of the DAU as a function of the applied magnetic field. For the blue dash trace, the offset ($B_{\text{offset}} = (B_+ + B_-)/2$) that includes the residual magnetic field and the offset of the system itself have been subtracted.

the magnetic field range test. The magnetic field measurements used are those one closest to the end of scale, and the expanded uncertainty is estimated by

$$U = k \cdot \sqrt{\sigma^2 + \left(\frac{u_1}{\sqrt{3}}\right)^2 + \left(\frac{u_2}{\sqrt{3}}\right)^2 + \left(\frac{u_3}{k'}\right)^2 + \left(\frac{u_4}{k'}\right)^2}, \qquad (2.8)$$

where σ is the standard deviation of the measurement for 300 samples, $u_1 = 1.8\,\text{nT}$ is the resolution of the magnetic measurement system, $u_2 = (0.2\%\,\text{reading} + 7\,\text{LSD}) \cdot 108.69\,\mu\text{T/A}$ is the DMM accuracy, $u_3 = 0.122 \cdot 10^{-3}\,\text{A} \cdot 108.69\,\mu\text{T/A} = 0.01326\,\mu\text{T}$ is the uncertainty provided in the certificate of calibration (COC) of the DMM, $u_4 = 0.08\,\mu\text{T}$ is the uncertainty of the Helmholtz coils system, and k is the coverage

factor. To estimate the expanded uncertainty, the terms u_1 and u_2 are divided by the square root of three assuming uniform distribution, and u_3 and u_4 are divided by the coverage factor indicated in its COC ($k' = 2$). Then, the square root of the sum of terms is multiplied by $k = 2$ in order to increase the level of confidence to approximately 95%. The estimation of the uncertainty is based on the recommendation given in [87].

Table 2.4 shows a summary of the results for the end of scale of the magnetic measurement system. In order to keep the analog inputs away from saturation but close to the full scale, the currents applied to the coil were 550 mA for the X and Z axes and 500 mA for the Y axis. The results obtained during the activities with the engineering and flight models were reported in [104, 105, 107]. Note that the purpose of this test is to verify that the uncertainty of the magnetic measurement achieves the requirements specified for the mission ($< 1\%$ eos). However, the estimated uncertainty is not a definitive value, which can be readily improved by using test measurement instrumentation with better performance, such as a common $6\frac{1}{2}$ digit DMM.

Table 2.4: Summary results for the field uncertainty of the magnetic measurement subsystem.

Axis	I_{coil} [mA]	B_{coil} [μT]	B_{sensor} [μT]	σ [μT]	U [μT]	U [%]	Acceptance $< 1\%$ eos
X	550.3	59.81	58.78	0.052	0.26	0.45	Pass
	-550.3	-59.81	-59.65	0.052	0.26	0.44	
Y	500.35	54.38	55.04	0.069	0.27	0.49	Pass
	-500.35	-54.38	-55.18	0.043	0.24	0.44	
Z	550.3	59.81	59.61	0.042	0.26	0.43	Pass
	-550.3	-59.81	-59.66	0.040	0.25	0.42	

On-station thermal test: magnetic measurements

The LISA Pathfinder satellite was examined in a series of space environment tests conducted at the IABG mbH space simulation/thermal vacuum facilities in Ottobrunn (Germany) [65, 69]. The primary objectives of the On-station thermal test (OSTT) are to prove spacecraft performance under the extreme thermal conditions and to collect data for the thermal model correlation on the LTP core assembly (LCA) level (see Figure 2.9).

In addition to this, the OSTT makes it possible to approve the proper functioning of the magnetic measurement subsystem integrated in the spacecraft and operated under space conditions, i.e., with a nominal vacuum below 10^{-4} Pa and heated up by an array of lamps simulating the solar irradiance perceived by the spacecraft in orbit. However, the Ottobrunn facility is not magnetically shielded. As a result,

Figure 2.9: On-station thermal test campaign. Left: LISA Pathfinder at the IABG mbH facilities during the OSTT test. Right: The spacecraft in front of the space vacuum chamber. Credits: Airbus DS.

the magnetometers monitored the Earth magnetic field during the different thermal runs. Figure 2.10 shows the amplitude spectral density for the twelve data streams of the magnetic measurement system at one of the temperature limits expected during flight, the hot phase at 30.5°C±0.5°C. The environmental magnetic noise curves are compatible with the one measured in our lab in Barcelona (see Figure 2.4). Finally, we conclude that, to some degree, the magnetic measurement subsystem operating in parallel with the other diagnostics and instrumentation of the spacecraft functioned as expected.[4]

2.1.4 Looking into eLISA: main drawbacks of the LISA Pathfinder magnetic measurement subsystem

The fluxgates on-board the LISA Pathfinder spacecraft are comfortably compliant with the requirements specified for the mission. However, as far as eLISA is concerned, a number of further improvements need to be considered, which have derived in the study of alternative technologies to fluxgate magnetometers. Below, some limitations brought on by the voluminous core and performance of the sensor are briefly described.

Sensor size/weight constraints and spatial uncertainty

Space applications have strict requirements in size and weight, and smaller sensors allow more of them to be incorporated in the spacecraft, therefore increasing the accuracy of the magnetic field map reconstruction. At the same time, the deviations

---

[4]The noise performance of the magnetic measurement subsystem can not be tested during the current campaign since the magnetic environment of the spacecraft was not isolated.
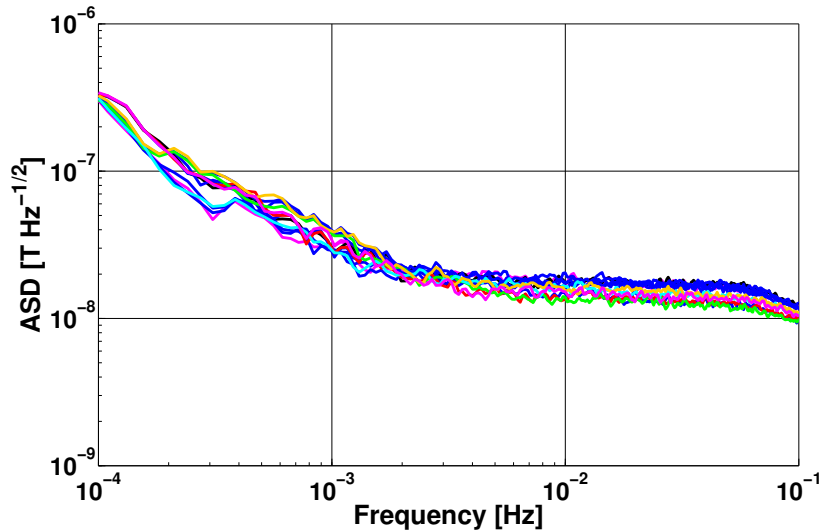
Figure 2.10: Magnetic field fluctuations inside the space vacuum chamber measured by the four triaxial fluxgate magnetometers (12 channels).

from the foreseen position of the sensor head, known as spatial uncertainty, are also decreased with the use of a more compact sensor head.

Noise performance

Fluxgates used in LISA Pathfinder have low noise performance. However, noise curves steeply rise for tinier fluxgate magnetometers [153] and towards lower frequencies. Thus, the development of smaller and yet sensitive magnetometers is a real must for eLISA. Moreover, the measurement bandwidth for eLISA is extended down to 0.1 mHz, which increases the complexity of reaching the suitable noise level at a frequency one order of magnitude lower than that for LISA Pathfinder.

Magnetic-back action

LISA Pathfinder requires detailed knowledge of the local environment generated by the spacecraft due to the sensitivity of the TM displacement because of the magnetic environment. As a result, the magnetic signature of the different magnetic sources on-board the spacecraft, including the magnetometer, was characterized. In particular, the bulky ferromagnetic material contained in the sensor can be critical. In view of this, the magnetic characterization of the device was performed and apportioned by a remnant dipolar magnetic moment of $271 \, \mu\mathrm{Am}^2$ [34]. Consequently, in order to avoid magnetic disturbances on the TM location, fluxgates had to be mounted

far from the TMs (the closest are at 18.85 cm), producing poor results in the determination of the field values at the TM when using classical interpolation methods (see Chapter 5 for more details). On the whole, magnetometers with sufficiently low magnetic back-action effects on the spacecraft environment are required to improve our ability to estimate the magnetic field in eLISA.

Perming effect

All the sensors containing ferromagnetic material, such as fluxgates, can be affected by a residual magnetization of the core when a strong magnetic field is applied. This permanent magnetism on the device, called perming effect, was observed during the vibration test of a fluxgate magnetometer [115], in which the sensor showed a large offset in the x- and z-axis of $-1.8\,\mu$T and $-1.2\,\mu$T respectively [119]. Perming was caused by the strong magnetic fields generated by the shaker's magnet and coil (see Figure 2.11), which increased the zero offset readings of the instrument.

Figure 2.11: Vibration test facility and degaussing process. Left: the flight model fluxgate magnetometer under test is placed on the table structure in front of the shaker system. Right: the magnetometer is fixed onto an aluminum support and placed inside a magnetic shielding for degaussing purpose after the vibration test.

In view of this setback, a degaussing process was undertaken in order to recover the initial offset of the damaged instrument. First, the sensor was fixed inside a three-layer mu-metal chamber equipped with a degaussing coil (see Figure 2.11). Then, an amplitude-modulated alternating magnetic field was applied by the degaussing coil. Basically, the initial amplitude of the bias current was increased up to 10 A (5 mT), and after this, decreased at a rate of $\simeq 0.25$ A/s down to zero current. This procedure was applied in the three axes of the magnetometer. The capability of the method to demagnetize the vibrated magnetometer was proved by taking measurements of

the residual internal magnetic field in the mu-metal chamber.[5] As can be seen in table 2.5, the post-degaussing measurements are reduced by more than one order of magnitude for the magnetized axes X and Z.

Table 2.5: Magnetometer readouts inside the mu-metal chamber before and after degaussing. At the time of this test, SN-01 was the only one vibrated. The data are compared with those taken with other non-vibrated flight (SN-02, SN-03, SN-04) and engineering model (SN-101) magnetometers. These measurements are the residual magnetic field inside the magnetic shielding together with the offset of the sensor ($B_{\text{measured}} = B_{\text{residual}} + B_{\text{offset}}$). Units are in volts.

Axis	SN-01 Before	SN-01 After	SN-02	SN-03	SN-04	SN-101
X	-0.355	-0.019	-0.035	-0.032	-0.032	-0.014
Y	0.054	-0.006	-0.053	-0.043	-0.045	-0.086
Z	-0.204	0.008	-0.029	-0.032	-0.032	- 0.026

To sum up, unexpected offset errors due to the perming effect can lead to inaccuracies between the pre-launch and post-launch magnetic field measurements, which seems to be an usual experience with non-absolute spacecraft magnetometers such as fluxgate [150]. More details about the influence of the offset errors in the estimation of the magnetic field is presented in Section 5.4.3.

2.2 On-board instrumentation for magnetic field generation

As mentioned, the magnetically-induced forces originated by the coupling between the environmental magnetic field and the remnant magnetic characteristics of the TM represent an important contribution to the total noise budget, which can be as high as $40\,\%$, i.e, $1.2 \times 10^{-14}\,\text{m\,s}^{-2}\,\text{Hz}^{-1/2}$ out of $3 \times 10^{-14}\,\text{m\,s}^{-2}\,\text{Hz}^{-1/2}$. In order to estimate and ultimately subtract the magnetic noise and, in addition, to monitor the evolution of the magnetic field with the magnetometers, we also need to determine both the magnetic moments and susceptibilities of the TMs accurately. Thus, the estimation of the magnetic properties must be performed in flight because these characteristics might undergo variations during launch stresses or commissioning operations. For this purpose, the magnetic diagnostics subsystem also contains a dedicated unit that injects controlled magnetic fields with high signal-to-noise ratio by means of two on-board induction coils. The effects of these fields on the TM motion will be detected by the on-board interferometric measurement system. Then, an adequate estimation algorithm is implemented to process this data, determining the magnetic

---

[5]The residual magnetic field inside the shielding, usually $< 0.3\,\mu\text{T}$, depends on the external field strength.

parameters of the TM, and finally accounting for the force noise contribution due to the environmental magnetic field [47, 49, 46].

The science requirements regarding the dc values and stability of the controlled magnetic field and gradient applied to the TMs are summarized in Table 2.6 [183, 88]. In the subsequent sections, the *active* hardware of the magnetic diagnostics module designed for LISA Pathfinder and some of the related test campaigns envisaged to characterize the subsystem are described.

Table 2.6: dc and stability requirements of the controlled magnetic field generation at the location of each TM. The frequency of the applied magnetic field can range from dc to 30 mHz. $B_{x,max}$ is the magnetic field applied at the TM center for a maximum required current of 4 mA.

dc value	Stability $1\,\mathrm{mHz} < \omega/2\pi < 30\,\mathrm{mHz}$
$B_{x,max} = 18\,\mu\mathrm{T}$	$S_{\mathbf{B}}^{1/2}(\omega) \leq 5\,\mathrm{nT}\,\mathrm{Hz}^{-1/2}$
$|\partial B/\partial B_x| > 125\,\mu\mathrm{T}\,\mathrm{m}^{-1}$	$S_{\nabla B_x}^{1/2}(\omega) \leq 12\,\mathrm{nT}\,\mathrm{m}^{-1}\,\mathrm{Hz}^{-1/2}$

2.2.1 Magnetic coils

The on-board coils, placed next to each of the test masses, consist of two circular induction coils made out of a titanium alloy ($\mathrm{Ti_6Al_4V}$), with $N = 2400$ windings of radius $r \simeq 56.5\,\mathrm{mm}$. Ideally, the coils are lined up with the TMs. Consequently, the magnetic field injected along the TM volume keeps axial symmetry with respect to the nominal position.[6] Figure 2.12 shows the complete integration of the coil into the flight model of the LTP, more precisely on the vacuum chamber. As seen also in this figure, the distance along the x-axis between those coils and the closest test masses center is 85.5 mm. More details of the coil positions referred to the coordinate system of the spacecraft are specified in table 2.7.

2.2.2 Controlled current source

The electronics of the controlled current source, which is integrated in the DAU, is designed to generate quantized sinusoidal peak currents up to 4 mA including a configurable dc offset, at any frequency from 1 mHz to 30 mHz, and with an output rate of 1024 samples per cycle. The different stages of the current source are represented as a block diagram in Figure 2.13, where the drawing has been divided

---

[6]The actual alignment between the coils and the test mass reference frame can impact on our ability to compute the magnetic force precisely. The main reasons for possible misalignments are mechanical tolerances and the exact winding accommodation inside the coil structure [134, 135].
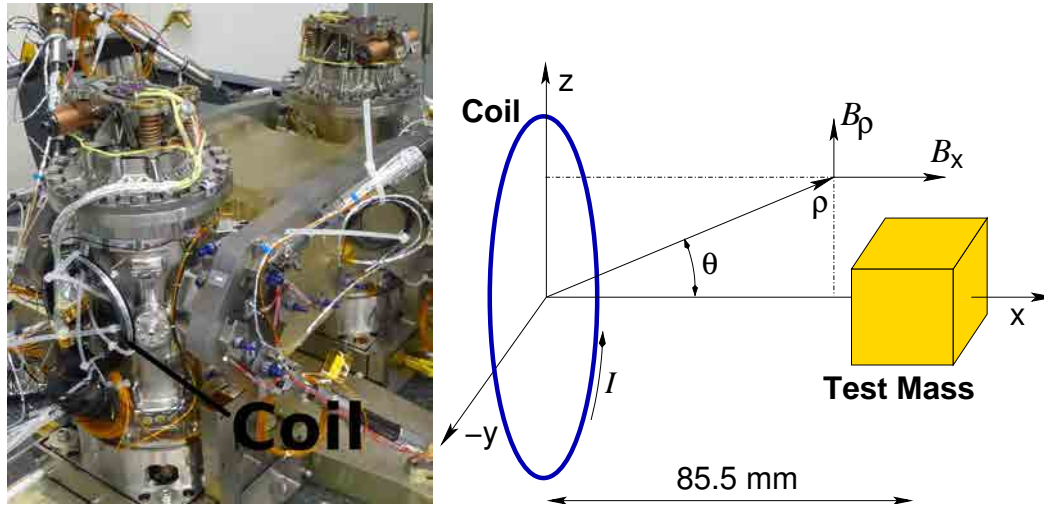
Figure 2.12: Magnetic coil in LISA Pathfinder. Left: coil integrated in the flight model inertial sensor housing. Credits: Airbus DS. Right: geometrical reference frame for the injected magnetic field with its origin at the coil center. Because of the symmetry, the field has only two distinct components, B_x and B_ρ.

Table 2.7: Location of the coils referred to a coordinate system fixed to the spacecraft. TMs locations is indicated in Table 2.2. Units are in meters.

Coils	x	y	z
1	-0.2735	0	0.532
2	0.2735	0	0.532

into two main parts: the digital-to-analog chain and the analog processing circuit. The first part contains two eight-bit digital-to-analog converters (DACs) followed by transresistance amplifiers (I/V) delivering low impedance output operation. The output of the first DAC fixes the reference of the second DAC and thus the peak amplitude of the sinusoidal current applied to the coil. Once the peak value is commanded, the second DAC configured with bipolar operation generate the quantized waveform.[7] In the analog part of the circuit, the bipolar output passes through a low pass-filter with a cut-off frequency of 1 Hz. Then, the voltage waveform is converted to current using an improved Howland current source [62]. Finally, before the electrical current goes to the output, a set of optoelectronic switches is used to configure

---

[7]Some calibration measurements were performed in order to characterize the actual relation between the output current and the digitized values commanded by the DMU (see Appendix A for more details).

the coil connectivity in three possible different states: short-circuit, open-circuit or connected.
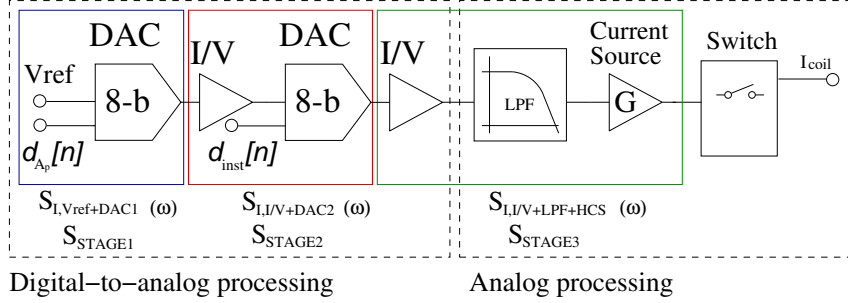
Figure 2.13: Block diagram of the coil's current source.

As mentioned previously, the stability of the magnetic field and the magnetic field gradient applied to the TM must be $S_B^{1/2} \leq 5\,\mathrm{nT\,Hz^{-1/2}}$ and $S_{\nabla B_x}^{1/2} \leq 12\,\mathrm{nT\,m^{-1}\,Hz^{-1/2}}$ between $1\,\mathrm{mHz}$ and $30\,\mathrm{mHz}$ [183]. These numbers define the limits of the current noise level required for the coil source. This requirement has been estimated by means of a simple calculation based on Ampere's Law. Therefore, considering the magnetic field noise requirement and the on-axis distance x between the coil and the TM center, the current spectral density can be expressed as

$$S_I^{1/2} = S_{B_x}^{1/2} \frac{4\pi}{\mu_0 N} \frac{(r^2 + x^2)^{3/2}}{2\pi r^2}. \qquad (2.9)$$

Substituting the setup parameters given in the previous section, the current fluctuation must be lower than $1.12\,\mu\mathrm{A\,Hz^{-1/2}}$. For the case of the magnetic field gradient stability, the maximum noise level of the injected current is estimated by

$$S_I^{1/2} = S_{\partial B_x/\partial x}^{1/2} \frac{2\pi}{\mu_0 N} \frac{(r^2 + x^2)^{5/2}}{3r^2 x}. \qquad (2.10)$$

This leads to current fluctuations of $S_I^{1/2} \leq 110\,\mathrm{nA\,Hz^{-1/2}}$ across the measurement bandwidth. It turns out that the magnetic-field gradient requirement is the more demanding one, which sets the level of noise of the injected intensity for the controlled current source.

Theoretical low-frequency current noise density for dc signals

Before validating the low-frequency noise performance in the lab, the stability of the current source for a dc signal has been determined theoretically. Accordingly, the total noise of the electronics in terms of current spectral density can be expressed as:

$$S_I^{1/2}(I,\omega) \simeq [K_2^2\,H_3^2\,S_{I,\,\text{Stage1}} + H_3^2\,S_{I,\,\text{Stage2}} + S_{I,\,\text{Stage3}}]^{1/2} \qquad (2.11)$$

where $S_{I,\,\text{Stage1}}$ is the power current density of the voltage reference and the first DAC, $S_{I,\,\text{Stage2}}$ is the noise combination considering the transimpedance amplifier and the second DAC, $S_{I,\,\text{Stage3}}$ is the current noise power spectral density for the last stage formed by the second current-to-voltage converter, the low-pass filter and the Howland current source, and K_2 and H_3 are, respectively, the responses of the second and third stages. The design of the current source mainly focuses on the minimization of the low-frequency noise, but also on other constraints such as current amplitude, offset current reduction and desired bandwidth. The details of the noise analysis of the adopted current source are described in Appendix B.

Figure 2.14 shows the noise apportionment for each stage of the whole circuit for a 1 mA dc signal, which is the maximum current value (peak-to-peak current of 2 mA) for the proposed in-flight experiment [47]. The dominant contributions are the Howland current source and the voltage reference (LT1009). Besides, the DAC gets involved in the noise since its output is the linear combination of the selected digitized value and the analog input reference. Therefore, for the worst case, i.e., the full-scale-output of the DAC (digital input $= 255_{\text{dec}}$), the output noise is approximately the contribution due to the voltage reference ($S_{\text{Stage1}}^{1/2} \sim S_{V_{\text{ref}}}^{1/2}$). The estimated values obtained from the noise analysis for the LPF bandwidth are reviewed in Table 2.8.
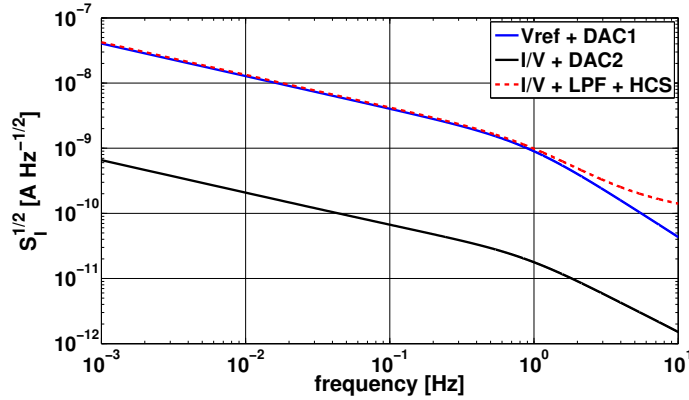
Figure 2.14: Theoretical current spectral density for the different stages of the controlled current source for a dc value of 1mA.

Table 2.8: Summary of the estimated noise level for the controlled current source at LISA Pathfinder frequencies with a constant value of 1 mA. The total noise is calculated as the quadratic sum of each contribution.

Circuit stage	$S_I^{1/2} \left[\mathrm{nA\,Hz}^{-1/2}\right]$	
	@ 1 mHz	@ 30 mHz
Vref + DAC1	40.44	7.38
I/V + DAC2	0.66	0.12
I/V + LPF + HCS	42.30	7.72
Total	58.53	10.69

Theoretical quantized noise of a sinusoidal waveform

As stated above, the second DAC is in charge of generating a sampled sine wave at frequencies between 1 mHz and 30 mHz. Therefore, the quantization error of the sinusoidal signal introduced by the digital-to-analog process can be an important source of noise. The additive noise assuming a uniform quantization and a signal amplitude greater than the resolution Δ_I can be modeled by

$$S_{I,\mathrm{q}}^{1/2} = \frac{\Delta_I}{\sqrt{12 \cdot f_\mathrm{s}}} = \frac{2I_\mathrm{p}}{2^N} \frac{1}{\sqrt{12 \cdot f_\mathrm{s}}} \tag{2.12}$$

where f_s is the sampling frequency, $N = 8$ is the number of bits of the DAC, and I_p is the peak amplitude of the sine wave. In order to generate the waveform, the DMU commands the digital inputs of the DAC at a rate of 1024 samples per cycle. Therefore, the sampling frequencies vary from 1.024 Hz to 30.72 Hz for signals between 1 mHz and 30 mHz, respectively. As a result, during the on-flight experiment the maximum quantization noise of 2.22 μA Hz$^{-1/2}$ is expected for a 1 mHz sinusoidal waveform with and amplitude of 1 mA.

2.2.3 Performance tests

Several test campaigns were carried out in order to assess whether or not the stability of the injected magnetic field is in agreement with the calculations and in compliance with the requirements. The setup utilized to measure these characteristics in the laboratory is shown in Figure 2.15. For the different runs, the coil was fed by the DMU, while the HP3457A multimeter measured the intensity through the coil and the Agilent 34410A acquired the temperature during the test. The validation tests were put into practice for both the engineering and the flight models of the controlled current source of the DMU.
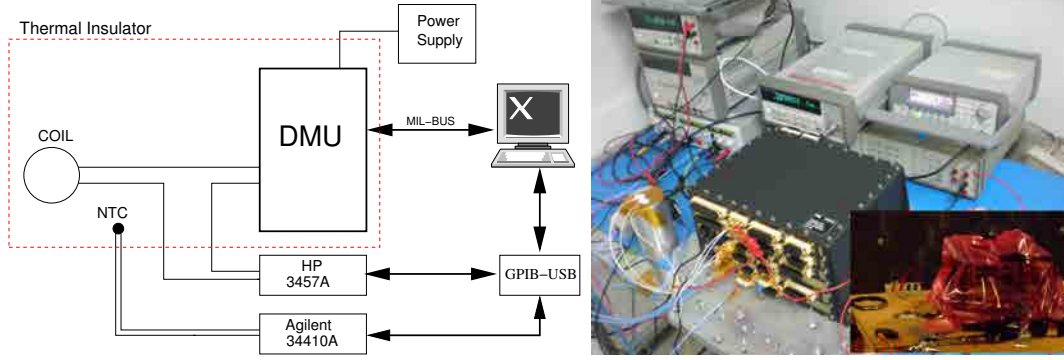
Figure 2.15: Setup for the test campaign of the controlled current source. Right: Clean room facility for the ac current measurements. Lower right-hand corner: Low-temperature fluctuations facility used for the low-frequency noise performance test.

Low-frequency noise of the injected magnetic field and magnetic field gradient

Measuring the stability of the created magnetic field and its gradient, is actually equivalent to measuring the stability of the electric intensity injected by the current source. This is, therefore, an electronic test. The setup was placed inside an anechoic chamber (see Figure 2.15) with a quiet thermal environment with the purpose of reducing temperature effects at low-frequencies. After the warm-up of the hardware, the data were collected during a period of at least 5 hours for currents up to 4 mA.

In Figure 2.16, the noise measurements for dc currents of 1 mA are compared to the theoretical results, where the noise spectral density is perfectly compliant with the mission requirements. Moreover, a good agreement between theoretical predictions and experimental measurements was confirmed. The temperature fluctuations inside the chamber were lower than $50\,\mathrm{mK\,Hz^{-1/2}}$ at 1 mHz. As a result, extra noise due to the thermal dependences is not presented across the LISA Pathfinder bandwidth. See Appendix C for details of the estimation of the thermal coefficient.

The estimation of the off-axis field fluctuations created from the experimental current noise i was calculated from classical expressions [83]. Assuming a coil of radius $a = 56.5\,\mathrm{mm}$, and $N = 2400$ turns, the result can be expressed as

$$B_x(x,\rho) \;=\; \frac{\mu_0}{4\pi}\,\frac{N\pi a^2\,i}{(a\rho)^{3/2}}\,\frac{k}{\pi}\,\left[\frac{1}{2}\,\frac{k^2}{1-k^2}\,E(k)\right] - \frac{\rho}{x}\,B_\rho(x,\rho), \qquad (2.13a)$$

$$B_\rho(x,\rho) \;=\; \frac{\mu_0}{4\pi}\,\frac{N\pi a^2\,i}{(a\rho)^{3/2}}\,\frac{k}{\pi}\,\frac{x}{a}\,\left[-K(k) + \frac{1-k^2/2}{1-k^2}\,E(k)\right], \qquad (2.13b)$$

where
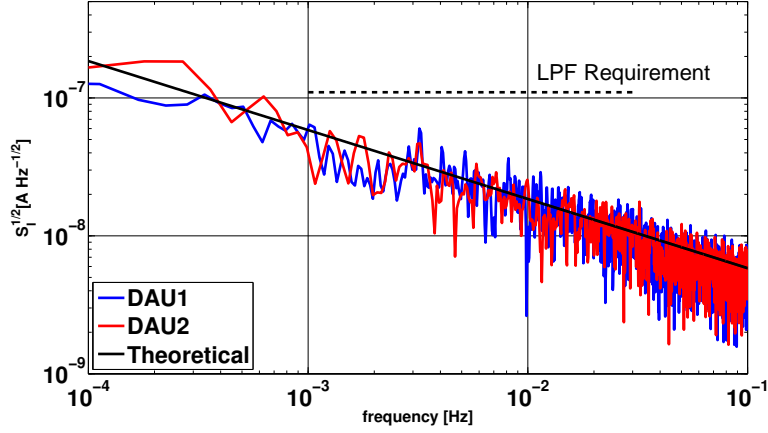
Figure 2.16: Noise measurements for a constant intensity of 1 mA. The two controlled current sources are allocated in both DAUs (DAU1 and DAU2), which are part of the DMU. Theoretical noise (black trace) and requirements (black dashed trace) are also shown.

$$k = \sqrt{\frac{4a\rho}{x^2 + (a + \rho)^2}} \ , \quad \rho^2 = y^2 + z^2, \tag{2.14}$$

and

$$K(k) = \int_0^{\pi/2} (1 - k^2 \sin^2 \phi)^{-1/2} \, d\phi, \qquad E(k) = \int_0^{\pi/2} (1 - k^2 \sin^2 \phi)^{1/2} \, d\phi, \tag{2.15}$$

are elliptic integrals of the first and second kind, respectively. Therefore, according to the noise experimental results, $50 \, \mathrm{nA \, Hz^{-1/2}}$ at $1 \, \mathrm{mHz}$, the map of the field and gradient fluctuations generated by the induction coil within the volume of the TM is shown in Figure 2.17. On the whole, the stability of the magnetic field and the magnetic field gradient applied by the coil to the TM are compliant with the mission requirements, i.e., $S_B^{1/2} \leq 5 \, \mathrm{nT \, Hz^{-1/2}}$ and $S_{\partial B_x/\partial x}^{1/2} \leq 12 \, \mathrm{nT \, m^{-1} \, Hz^{-1/2}}$ between $1 \, \mathrm{mHz}$ and $30 \, \mathrm{mHz}$.

Spectra of quantized sinusoidal waveforms

In this case, the in-band quantization noise when an sinusoidal current is generated by the DAC was measured in the laboratory. As in the previous setup (see Figure 2.15), the coil was connected to the DMU and the current intensity data were taken by using a DMM with a sampling frequency of 40 Hz.
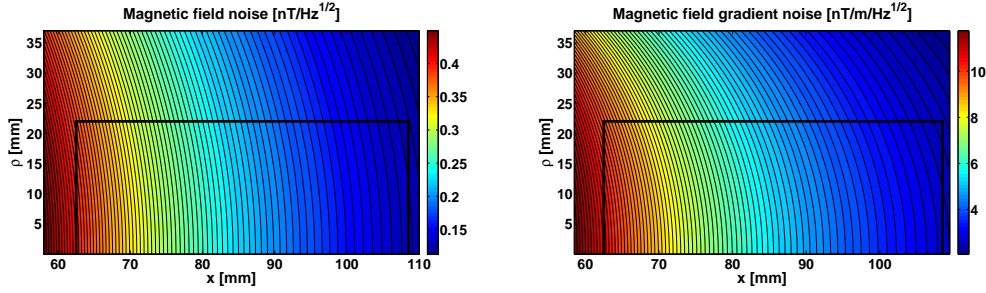
Figure 2.17: Fluctuations of the magnetic field (left) and its gradient (right) across the TM. The black rectangle is one half the area of the TM. Because of the axial symmetry of the field about the x-axis, the other half of the TM was omitted. x is the distance on-axis to the coil center and ρ is the distance to the coil's axis.
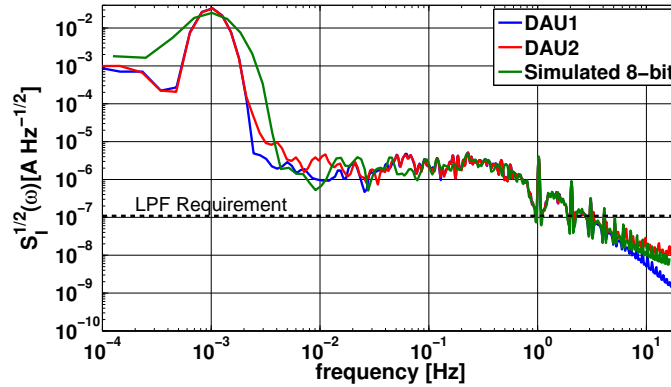
Figure 2.18: Spectra of the quantized sinusoidal signals measured by the flight model DMU (DAU1 and DAU2). The dashed black line represents the current stability requirement.

Figure 2.18 shows the spectra of sine waves of $1\,\mathrm{mA}$ at $1\,\mathrm{mHz}$. The experimental results for both DAUs match the simulated signal constructed by the two eight-bit DACs. As expected, the noise floor due to the quantization effect is above the dc current stability requirement for the mission. However, the high signal-to-noise ratio is still sufficient to allow a good estimate of the magnetic properties of the test masses [49]. The $1\,\mathrm{mHz}$ signal was sampled by the DMU to $1.024\,\mathrm{Hz}$. Consequently, harmonics at this frequency and its multiples appeared due to the sample rate of the signal.

2.2.4 Looking into eLISA: improvements on the on-board instrumentation for magnetic field generation

Further improvements need to be accomplished for the controlled current source for eLISA. However, they are not so critical as in the case of the magnetic measurement subsystem. Once the different electronic noise contributions are disentangled, the main drawbacks can be readily improved with some modifications on the design of the electronics circuits.

Low-frequency noise current source

The instrumentation for the magnetic field generation on board LISA Pathfinder is comfortably compliant with the requirement specified for the mission. However, the low-frequency noise of the present design does not achieve the required performance at the lower end of the eLISA bandwidth, i.e., 0.1 mHz (see Figure 2.16). On account of this, a low-frequency noise study for different current source typologies was performed. The reader can find more details about the noise analysis and measurements in Appendix B and Section 6.3.1. Lastly, the best option for eLISA is the floating-load current source topology, which exhibits a low thermal coefficient and slightly better noise characteristics across the measurement bandwidth. Figure 2.19 shows the current spectral density for the floating-load current source compared to the one used in LISA Pathfinder.
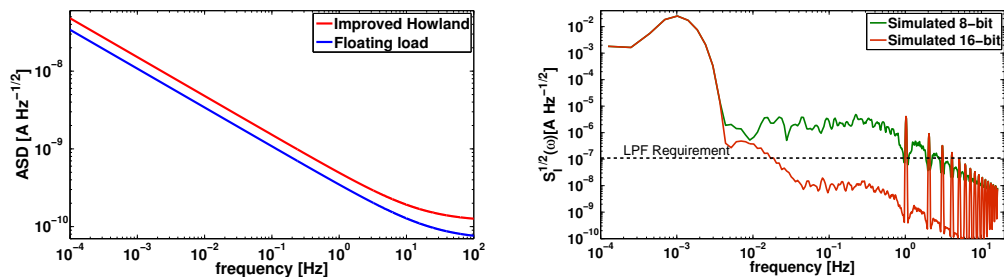
Figure 2.19: Improvements on the controlled current source for eLISA. Left: current spectral density comparison for improved Howland and floating-load current sources with a constant current of 4 mA. Only the voltage reference (LT1009) and the current source typology were considered for the analysis (DACs, I/V converters and low-pass filter were excluded). Right: theoretical estimation of a quantized sinusoidal signal when using a eight-bit DAC (green) or a sixteen-bit DAC (red).

The other important contribution comes from the voltage reference. In this case, the motivation for choosing references with better low-frequency noise characteristics (lower noise floor and $1/f$ corner frequency) would noticeably improve the noise curve.

Quantization noise

The quantization noise is the dominant source when a sinusoidal signal is applied. This contribution is even above the dc current stability requirement. However, its reduction is straightforward by using a DAC with higher resolution in the second stage of the circuit (see Figure 2.13), which is in charge of the sampled waveform. Figure 2.19 shows the spectra comparison of a sine wave of 1 mA at 1 mHz generated for an eight-bit DAC and a sixteen-bit DAC.

Chapter 3

Design of a Magnetic Measurement Subsystem with Magnetoresistances for eLISA

The study presented in this thesis about magnetic sensing with anisotropic magnetoresistive sensors (AMR) shows that the technology is suitable for low-frequency space applications like the eLISA mission. Low noise magnetic measurements at the sub-millihertz frequencies were taken by using different electronic noise reduction techniques in the signal conditioning circuit. We found that conventional modulation techniques reversing the sensor bridge excitation do not reduce the potential $1/f$ noise of the magnetoresistors, so alternative methods such as flipping (sensor magnetization reversal) and electro-magnetic feedback are necessary. In addition, a low-frequency noise analysis of the signal conditioning circuits has been performed in order to identify and minimize the different main contributions from the overall noise. The results for chip-scale magnetoresistances exhibit similar noise along the eLISA bandwidth $(0.1\,\mathrm{mHz} - 1\,\mathrm{Hz})$ to the noise measured by means of the voluminous fluxgate magnetometers used in its precursor LISA Pathfinder mission. The work presented here has been proposed as well as part of the magnetic field monitoring system of the space atom interferometry within the STE-QUEST mission concept [9].

The chapter is organized as follows. Section 3.1 summarizes the state-of-the-art of magnetic sensing technologies. Noise requirement of the system is depicted in Section 3.2. In Sec. 3.3 a brief overview of the noise reduction techniques is explained. In Sec. 3.4 we analyze the noise and thermal contributions of the sensor and signal conditioning circuits to the overall noise. The experimental results are presented in Sec. 3.5, and finally, the main conclusions are drawn in Sec. 3.6.

3.1 State of the art

The survey of magnetic sensors presented herein is grounded on the constraints described in Section 2.1.4 and on the standard requirements for spacecraft-borne magnetometers, such as mass, power, and the effects of the exceptional space environment on the sensor. Table 3.1 shows a summary of cutting-edge commercial-off-the-shelf (COTS) sensors and new prototypes that can be, in principle, available for the design.

Table 3.1: State of the art of miniaturized magnetic sensors suitable for space applications. Since the low-frequency bandwidth required for eLISA is rarely covered in the literature, noise spectral densities are displayed at $1\,\mathrm{Hz}$.

Sensor	Range $[\mu\mathrm{T}]$	Noise Density $[\mathrm{nT}/\sqrt{\mathrm{Hz}}]$ @ $1\,\mathrm{Hz}$	Sensitivity $[\mathrm{mV\,mT^{-1}}]$	Package size $[\mathrm{mm} \times \mathrm{mm}\ (\times\ \mathrm{mm})]$
PCB-FG	± 50	0.02	120000	$33.5 \times 15.6 \times 0.9$ [84]
MicroFG	± 900	2.48	1089.2	4.65×5.04 [38]
	–	2.6	4.23	2.5×2.5 [109]
AMR	± 200	0.18	160 $(V_\mathrm{b} = 5\,\mathrm{V})$	$4 \times 11.3 \times 1.7$ [174, 77]
GMR	150	3	36 $(V_\mathrm{b} = 1.2\,\mathrm{V})$	$6 \times 4.9 \times 1.37$ [174]
TMR	± 2600	3.8	164 $(V_\mathrm{b} = 3.3\,\mathrm{V})$	$3 \times 3 \times 0.75$ [137]
		0.33		$16 \times 8\varnothing$ [111]
GMI	± 100	0.035	100000	22.5×3 [54]
MI	± 17	0.003	68000 $(V_\mathrm{b} = 3\,\mathrm{V})$	$10 \times 0.8 \times 0.5$ [181]
CSAM	± 20	0.005	2400	$1.7 \times 3.3 \times 4.5$ [169, 86]
	–	0.0002	–	$750\,\mathrm{mm^3}$ [129]

Fluxgate magnetometers were the preferred technology in many satellite missions [7]. However, classical fluxgate sensors are too large and their miniaturization compromise the overall performance. Typically for large enough sensors, $1/f$ noise decreases as much as the square root of the volume assuming additive noise, although this does not apply at very small sizes since an individual contribution can dominate the total noise [79, 151]. Micro-fluxgate magnetometers present encouraging noise performance for chip scale devices ($2.48\,\mathrm{nT\,Hz^{1/2}}$), although not better than AMR of similar size ($0.18\,\mathrm{nT\,Hz^{1/2}}$) [38, 109, 174, 77, 154]. On the contrary, PCB fluxgate achieves similar characteristics in term of noise to the conventional fluxgate ($0.02\,\mathrm{nT\,Hz^{1/2}}$), but they are still too bulky [84].

Magnetoresistance devices, such as AMRs and giant magnetoresistances (GMRs), offer very competitive characteristics when size is a limitation. A more recent technology based on the tunneling magnetoresistance (TMR) effect [132, 64] has higher sensitivity than AMRs and GMR sensors [137]. The main drawback is that the intrinsic noise level of TMRs ($3.8\,\mathrm{nT\,Hz^{1/2}}$) without electronic noise reduction techniques

exceeds that of AMR devices at frequencies around 1 Hz [137].

Excellent performance in terms of noise and sensitivity, which could compete with fluxgate magnetometers, has been achieved with highly sensitive magneto-impedance (MI) and giant magneto-impedance (GMI). Latest research shows that the technology could reach noise level below $40\,\mathrm{pT\,Hz^{-1/2}}$ [54, 181]. However, excess noise caused by the large temperature offset drift (340 nT/K) [113] is critical for applications requiring long integration time, such as eLISA.

As stated along this section, solid state magnetometers exhibit a dominant $1/f$ noise behavior. Regarding this, chip-scale atom magnetometers (CSAM) have an advantage over the aforementioned sensors because they are absolute sensors, i.e., the magnetic field measurement is related to fundamental physical constants [36]. As a result, atomic magnetometers might be more immune to long-term drifts that contribute to the low-frequency noise. Integrated magnetometers based on this technology demonstrates a noise level of $5\,\mathrm{pT\,Hz^{-1/2}}$ at 1 Hz [169].

All in all, AMR is the preferred option as it presents a good trade-off between noise and volume compared to the other technologies [174]. Other important motivation for the choice of an AMR sensor is the previous experience in space qualification test campaigns and in small space missions [50, 130, 157, 33].

3.2 Noise requirement of the magnetic measurement system

The main characteristics of the magnetic measurement system to be addressed were described in Section 2.1.4. Regarding the noise performance for the lower end of the eLISA bandwidth, magnetic field fluctuations across the TM are expected to be dominated by a time-varying interplanetary magnetic field no lower than $100\,\mathrm{nT\,Hz^{-1/2}}$ [167, 25], while the spacecraft's magnetic sources are expected to be the main contributors to the magnetic field gradient fluctuations [80]. Therefore, to be on the safe side, although eLISA requirements at subsystem level and the distribution of the magnetic sources in the spacecraft are still not formally defined, the noise performance of the magnetic measurement system should be at least one order of magnitude less noisy than the expected interplanetary magnetic noise to be measured. This implies a sensitivity in the measurement system of

$$S_{B,\mathrm{system}}^{1/2} \leq 10\,\mathrm{nT\,Hz^{-1/2}}, \ \omega/2\pi = 0.1\,\mathrm{mHz}. \tag{3.1}$$

The reason for using AMR sensors as an alternative to the LISA Pathfinder scheme with fluxgate magnetometers, is the mass, size and power restrictions for space applications [50] (see Figure 3.1). Besides, the AMR-type HMC1001 [77] presents the lowest noise level among different commercial magnetoresistive sensors [174]. Nevertheless, an important disadvantage of the AMR technology is the intrinsic $1/f$ noise that limits its use for low-frequency applications [182]. Extensive research

51

was conducted on this topic at frequencies between $0.1\,\mathrm{Hz}$ and $10\,\mathrm{kHz}$. However, to our knowledge, the noise performance of the sensor and its electronics has not yet been explored in the lower end of the eLISA bandwidth ($0.1\,\mathrm{mHz}$). A recent work has shown a noise level of $\sim 100\,\mathrm{nT}\,\mathrm{Hz}^{-1/2}$ at $1\,\mathrm{mHz}$ [33], which clearly exceeds the value in Eq. (3.1). For these reasons, in this chapter we study the low-frequency noise behavior of a prototype based on magnetoresistive sensors with dedicated noise reduction techniques, which are necessary to achieve the envisaged magnetic noise level for eLISA.[1]

Figure 3.1: Fluxgate magnetometer used in LISA Pathfinder and AMR sensor proposed for eLISA. Size of the AMR is specified in Table 3.1.

3.3   Noise reduction techniques

The intrinsic noise characteristics specified by the manufacturer of the magnetoresistors [77] are non-compliant with the requirements. For this reason, different electronic noise reduction techniques need to be assessed in order to minimize the sensor noise level in the eLISA frequency band. This section describes the methods to be studied.

3.3.1   Flipping

AMR sensors contain a thin film composed of a nickel-iron alloy with magnetic anisotropy. They have a sensitive axis to the magnetic field, the *hard* axis, and another axis aligned with the sensor magnetization called the *easy* axis. Taking advantage of these properties, the flipping technique entails the periodic flip of the internal magnetization of the sensor strips by applying switching field pulses (*set/reset* pulses) generated by a thin film conductor, which is wound around the active area of the sensor [72]. The change of the magnetization direction induces the reversion

---

[1]For a hypothetical more demanding scenario, a parallel study was performed in Chapter 6 using an atomic magnetometer [123].

of the output characteristic; as a result, the sensor output signal is modulated at the frequency of the switched pulses. Then, magnetic field measurements between each *set* and *reset* pulses are taken and subsequently demodulated. This sequence makes it possible to subtract the bridge offset, and its related temperature dependence, since the offset voltage remains unchanged while the sensor output reverses the polarity. Figure 3.2 shows the opposite slopes in the output characteristics after the *set* and *reset* pulses, and the following offset voltage extraction for different bridge voltages. In addition, the main advantage of performing modulation techniques by using flipping pulses is the reduction of the $1/f$ noise within the desired bandwidth. Another advantage is the recovery of the output signal degradation induced from strong external magnetic fields ($> 300\,\mu\text{T}$), which resolves an important drawback of magnetometers that use ferromagnetic core, such as fluxgates.
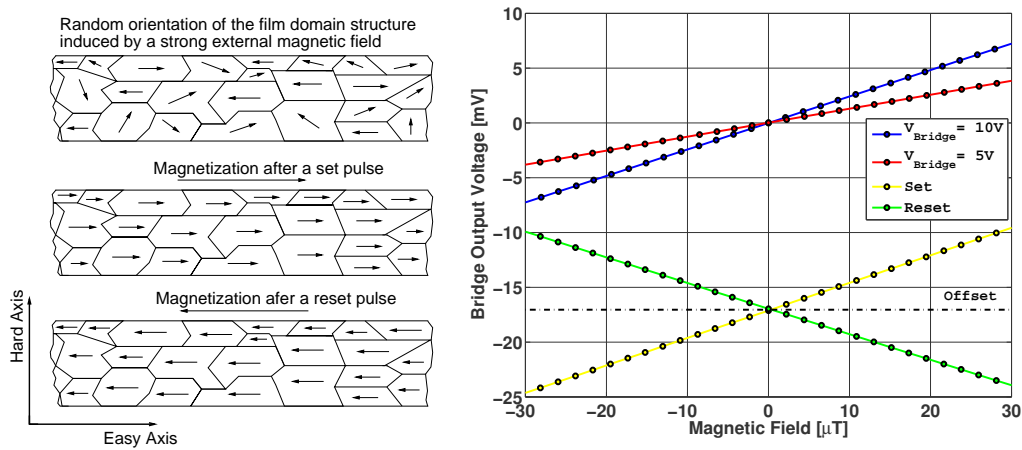
Figure 3.2: Response of the sensor to the flipping technique. Left: magnetic alignment of the permalloy thin film domain structure using *set/reset* pulses. Right: output characteristics as a function of the magnetic field after a *set* (yellow trace) and *reset* (green trace) pulse with $V_{\text{bridge}} = 10\,\text{V}$. Bridge offset extraction is performed for $V_{\text{bridge}} = 10\,\text{V}$ (blue trace) and $V_{\text{bridge}} = 5\,\text{V}$ (red trace).

3.3.2 Electro-magnetic feedback

In order to minimize the coupling between temperature and magnetic field output, the thermal dependence needs to be actively compensated during operation. Since the temperature drifts of the sensor sensitivity show up as a gain error in the measurement, a feedback controller is devoted to maintaining the bridge output close to zero, i.e. in balanced bridge condition, so as to reduce the thermal effects. By using electro-magnetic feedback, an integrated coil involved in the closed-loop controller induces an opposing field to counteract the field component detectable by the

sensor. Then the current flowing through the compensation coil together with the current-to-field conversion of the coil give the magnitude of the magnetic field measurement. This method is particularly useful at low frequencies where temperature drifts become more significant in the overall sensor noise.

3.4 Front-end electronics

The core of the magnetometer consists of a Wheatstone bridge made up of four magnetoresistors with Barber-poler structures for output linearization [73]. Then, the resistance-magnetic field dependence of the AMR can be modeled as

$$R_{\mathrm{AMR}} = R_{\mathrm{b,n}} + \Delta R \frac{B_{\mathrm{m}}}{B_0} \sqrt{1 - \left(\frac{B_{\mathrm{m}}}{B_0}\right)^2}, \tag{3.2}$$

where $R_{\mathrm{b,n}}$ is the nominal resistance of the magnetoresistive element, ΔR is the maximum change of resistance in response to the magnetic field, B_{m} is the measured field (perpendicular to the easy-axis), and B_0 is the total anisotropic field determined by the material and geometry of the sensor. Consequently, the output voltage of the Wheatstone bridge with four identical magnetoresistive elements varying in opposite directions is given by

$$V_{\mathrm{o}} = V_{\mathrm{b}} \frac{\Delta R}{R_{\mathrm{b,n}}} \frac{B_{\mathrm{m}}}{B_0} \sqrt{1 - \left(\frac{B_{\mathrm{m}}}{B_0}\right)^2}, \tag{3.3}$$

where V_{b} is the bridge voltage excitation.[2] Then, the sensitivity $\mathrm{d}V_{\mathrm{o}}/\mathrm{d}B_{\mathrm{m}}$ along the linear behavior of the bridge output characteristics $(B_{\mathrm{m}} < B_0/2)$ is

$$s_{\mathrm{b}} \simeq \frac{\Delta R}{R_{\mathrm{b,n}}} \frac{V_{\mathrm{b}}}{B_0}. \tag{3.4}$$

The second term in Eq. (3.2) is the change of resistance due to the magnetic field

$$\Delta R_{\mathrm{b}} = \Delta R \frac{B_{\mathrm{m}}}{B_0} \sqrt{1 - \left(\frac{B_{\mathrm{m}}}{B_0}\right)^2} \simeq \Delta R \frac{B_{\mathrm{m}}}{B_0}. \tag{3.5}$$

Substituting B_0 from Eq. (3.4) and replacing in Eq. (3.5) gives

$$\Delta R_{\mathrm{b}} = \frac{s_{\mathrm{b}} R_{\mathrm{b,n}} B_{\mathrm{m}}}{V_{\mathrm{b}}} = s_{\mathrm{AMR}} R_{\mathrm{b,n}} B_{\mathrm{m}}, \tag{3.6}$$

where s_{AMR} is the sensitivity of the AMR.

The output signal of the Wheatstone bridge is amplified, low-pass filtered, sampled and digitally demodulated. Figure 3.3 shows the analog signal conditioning circuit for the magnetic field sensing with the flipping method.

---

[2]Reverse diagonals of the resistors bridge have ΔR with opposite sign.
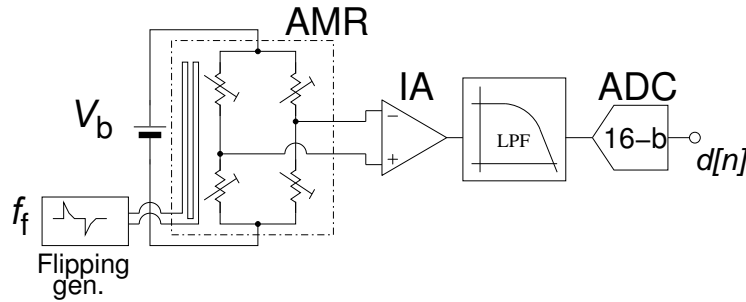
Figure 3.3: Analog signal processing scheme for the flipping method.

The flipping generator circuit performs short *set/reset* pulses ($\tau \simeq 1\,\mu$s) with peaks of 3.3 A along a strap of 1.5 Ω.[3] Although the circuit delivers high current peaks, the duration of the pulses is so short that the energy stemmed from the charged-up capacitor is very small ($E = 0.5\,C\,V^2 = 2.75\,\mu$J for $C = 0.22\,\mu$F). The flipping frequency f_f has been set to 5.5 Hz, enough to reduce the $1/f$ noise of the instrumentation amplifier (IA) by modulating the signal from the magnetometer. The selected modulation frequency is a trade-off among the $1/f$ noise reduction, the effects on the magnetic and thermal disturbances produced by a more periodic switching signal, and the transient response after the pulses. Magnetic field measurements are acquired 10 ms after each *set* and *reset* pulses, so that all the flipping currents have died down below the micro-ampere level, and the low-pass filter settling time has elapsed. Therefore, glitches and transients in the immediate times after the flipping pulses are not seen by the analog-to-digital conversion process.

The analog signal conditioning for electro-magnetic feedback, together with the flipping method, is shown in Figure 3.4. The electro-magnetic feedback circuit is a closed-loop controller, in which a current regulator feeds the compensation coil with the measured magnetic field. In order to force the sensor output signal to zero, which is the remaining error, an integrator is required in the control loop. The measured field magnitude is represented as voltage, which is proportional to the compensation current.

3.4.1 Low-frequency noise analysis

The noise of the system can be split into two different parts, one coming from the intrinsic $1/f$ noise presented in the magnetometer itself and the other one coming from the signal conditioning circuit. In the following lines, we describe the main noise sources in the whole system.

The first stage of the circuit is the magnetic sensor constituted by a magne-

---

[3]The peak current of the *set/reset* pulse can be defined between 2 A and 3 A, which is enough to align the magnetic domains of the magnetoresistive elements along the *easy* axis.
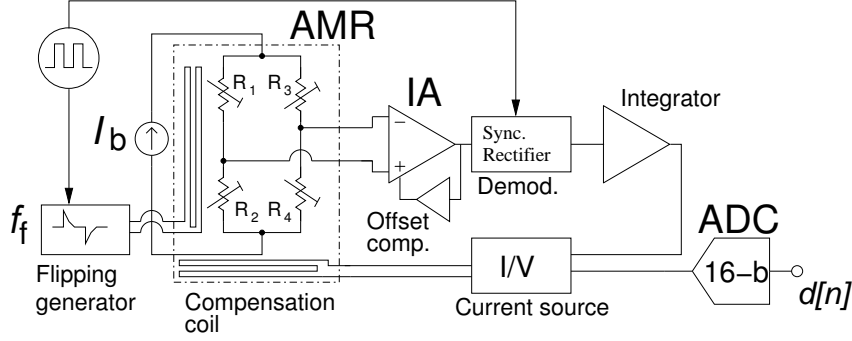
Figure 3.4: Analog signal processing scheme for electro-magnetic feedback together with flipping.

toresistive Wheatstone bridge configuration. The nominal value of the resistors is $R_{b,n} = 850\,\Omega$ and the bridge output sensitivity is $s_b = s_{AMR}V_b = 136\ \mu V\ \mu T^{-1}$, where $s_{AMR} = 32\,\mu V\,V^{-1}\,\mu T^{-1}$ is the AMR sensitivity and $V_b = 4.25$ V is the bridge voltage. Hence, the white-noise floor caused by the Johnson noise of the bridge resistances at 300 K is

$$S_{AMR,\ T}^{1/2} = \sqrt{4k_B T R_{b,n}} = 3.75 \text{ nV Hz}^{-1/2}, \tag{3.7}$$

where k_B is the Boltzmann constant. The voltage noise from the sensor is converted to equivalent magnetic field noise referred to the input dividing by the bridge sensitivity

$$S_{B_{AMR,\ T}}^{1/2} = \frac{S_{AMR,\ T}^{1/2}}{s_{AMR}V_b} = 27.6 \text{ pT Hz}^{-1/2}. \tag{3.8}$$

From this equation and assuming additive noise, the higher the sensor sensitivity or the bridge voltage the lower the equivalent magnetic field noise. At low frequencies, the corner frequency of the $1/f$ noise is around 60 Hz, which leads to a sensor noise level of 21 nT Hz$^{-1/2}$ at 0.1 mHz. So, only the low-frequency contribution from the AMR is sufficient to exceed the requirements given in Eq. (3.1).

As described further on in the text, apart from the intrinsic $1/f$ behavior, the contributions due to the thermal drifts deteriorate the noise performance. In order to overcome these limitations, the scheme shown in Figure 3.4 was implemented. The block diagram considering the most relevant noise sources is given in Figure 3.5, and the closed-loop response of the system is

$$V_o(s) = B_i(s)\frac{K_{eq}H_{int}(s)}{1 + H_{oc}(s) + K_{eq}\cdot K_{coil}\cdot H_{int}(s)}, \tag{3.9}$$

where K_{eq} is the product of the bridge sensitivity s_b and the instrumentation amplifier gain, K_{coil} is the gain of the voltage-to-current converter $(4\,\text{mA V}^{-1})$ multiplied

56

by the compensation coil ratio $(1.96\,\mu\mathrm{T\,mA^{-1}})$, and $H_{\mathrm{int}}(s)$ and $H_{\mathrm{oc}}(s)$ are the transfer functions of the integrator and offset compensation.
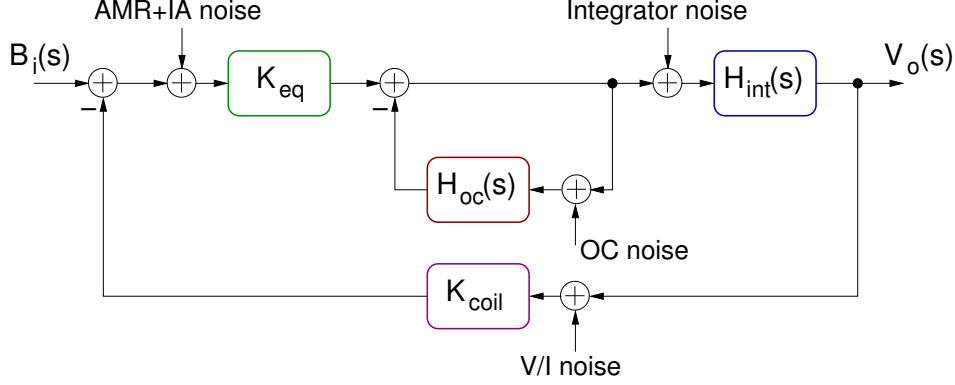
Figure 3.5: Block diagram of the analog signal processing with electro-magnetic feedback.

Concerning the noise contributions of the signal conditioning circuit, the apportionment of the bridge drive circuit is negligible compared with the sensor noise. Besides, *ratiometric measurements* [144] are performed in order to reduce drifts, noise or interference in the analog-to-digital conversion process. Hence, the voltage reference of the analog-to-digital converter (ADC) is also employed to drive the bridge. Afterwards, the bridge output is amplified by a space-qualified low-noise instrumentation amplifier (AD524) with a gain of 100 V $\mathrm{V^{-1}}$. The output noise introduced by this stage considering the closed-loop transfer function (see Figure 3.5) can be modeled as

$$
\begin{aligned}
e_{\mathrm{o,\ IA}}^2 = {} & \left[e_{\mathrm{n,\ IA}}^2 \left(1 + \frac{f_{\mathrm{c},\ e_{\mathrm{n}}}}{f} \right) + i_{\mathrm{n,\ IA}}^2 \left(1 + \frac{f_{\mathrm{c},\ i_{\mathrm{n}}}}{f} \right) R_{\mathrm{b}}^2 \right] \\
& \times \left| \frac{K_{\mathrm{eq}} \cdot H_{\mathrm{int}}}{1 + H_{\mathrm{oc}} + K_{\mathrm{eq}} \cdot K_{\mathrm{coil}} \cdot H_{\mathrm{int}}} \right|^2,
\end{aligned}
\tag{3.10}
$$

where $e_{\mathrm{n,\ IA}} = 7\ \mathrm{nV\ Hz^{-1/2}}$, $i_{\mathrm{n,\ IA}} = 350\ \mathrm{fA\ Hz^{-1/2}}$, $f_{\mathrm{c},\ e_{\mathrm{n}}} = 3\ \mathrm{Hz}$ and $f_{\mathrm{c},\ i_{\mathrm{n}}} = 30\ \mathrm{Hz}$ are the input voltage/current spectral densities and their respective corner frequencies describing the noise characteristic of the IA. The signal from the magnetometer, i.e., the input signal to the amplifier, is modulated by applying flipping pulses. As a result, the noise level of the IA is the one at the frequency of the modulating signal. For the AD524, the equivalent magnetic field noise with a modulating signal of only 5.5 Hz is 64 pT $\mathrm{Hz^{-1/2}}$, thus fully compliant with the system requirements.

The phase sensitive detector is synchronized with the flipping pulses by using an analog switch, which alternates the sign of the unity gain amplifier in order to rectify the modulated signal. The noise contribution for both configurations (inverting and

non-inverting amplifier) are not critical in the overall noise of the signal conditioning circuit. After the rectifier circuit the signal is demodulated and then integrated (see Figure 3.6). The output noise for the integrator is given by

$$
\begin{aligned}
e_{\text{o,Int}}^2 =& \left[(e_n^2 + i_n^2 R_{2,\text{int}}^2 + e_{\text{t2,int}}^2) \left[1 + \left(\frac{f_i}{f} \right)^2 \right] + e_{\text{t1,int}}^2 \left(\frac{f_i}{f} \right)^2 + i_n^2 R_{1,\text{int}}^2 \left(\frac{f_i}{f} \right)^2 \right] \\
& \times \left| \frac{1 + H_{\text{oc}}}{1 + H_{\text{oc}} + K_{\text{eq}} \cdot K_{\text{coil}} \cdot H_{\text{int}}} \right|^2 ,
\end{aligned}
\tag{3.11}
$$

where $f_i = 1/(2\pi R_{1,\text{int}} C_f)$, $e_{\text{t1,int}}$ and $e_{\text{t2,int}}$ is the thermal noise voltage of the resistor $R_{1,\text{int}}$ and $R_{2,\text{int}}$ (both of $10\,\text{k}\Omega$), $e_n^2 = e_{\text{nf}}^2(1 + f_{\text{ce}}/f)$ and $i_n^2 = i_{\text{nf}}^2(1 + f_{\text{ci}}/f)$ are the amplifier input noise in terms of power voltage and power current density. The noise parameters of the op-amp are the noise floor ($e_{\text{nf}} = 3\,\text{nV}\,\text{Hz}^{-1/2}$ and $i_{\text{nf}} = 0.4\,\text{pA}\,\text{Hz}^{-1/2}$) and the corner frequency ($f_{\text{ce}} = 2.7\,\text{Hz}$ and $f_{\text{ci}} = 140\,\text{Hz}$). Hence, the equivalent output noise of the integrator is around 51 pT Hz$^{-1/2}$ at $0.1\,\text{mHz}$.
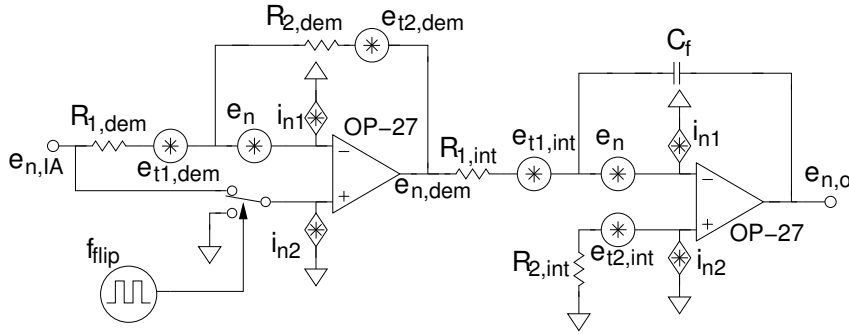
Figure 3.6: Demodulator and integrator circuit with the main contributions considered for the noise estimation.

In addition, an offset compensation integrator is also used between the output and the reference terminal of the AD524 in order to extract the offset of the modulated signal. The noise contribution of this circuit is not critical along the measurement bandwidth since the signal is still modulated at this stage.

The last stages in the closed-loop circuit are the current source to drive the compensation coil and the ADC to measure the output voltage, which is proportional to the measured magnetic field. A floating load topology has been implemented on grounds of its simplicity and low-noise performance. Assuming a typical compensation coil ratio of $0.51\,\text{mA}\,\mu\text{T}^{-1}$, the estimated equivalent magnetic field noise applied by the compensation source is $4\,\text{pT}\,\text{Hz}^{-1/2}$ at $0.1\,\text{mHz}$. This value is negligible compared with the intrinsic noise of the sensor itself (21 nT Hz$^{-1/2}$ at $0.1\,\text{mHz}$,

see Figure 3.7). Regarding the ADC (ADS7809), the manufacturer gives a maximum rms noise of 1.3 LSB (least significant bit). This leads to a spectral noise density of $1.3q/\sqrt{f_s/2} = 1.4\,\mu\text{V}\,\text{Hz}^{-1/2}$ ($11\,\text{pT}\,\text{Hz}^{-1/2}$), where q is the ADC voltage resolution for a 16-bit ADC with a full-scale range of $10\,\text{V}$ ($\pm 5\,\text{V}$). This contribution dominates over the ADC quantization white noise $q/\sqrt{12fs/2} = 0.3\,\mu\text{V}\,\text{Hz}^{-1/2}$ ($2.5\,\text{pT}\,\text{Hz}^{-1/2}$).[4] Since the low-frequency noise characteristics of the ADC are not given by the manufacturer, the corner frequency of the $1/f$ noise were found by experimental fit to the data at $10\,\text{mHz}$.

Figure 3.7 shows the theoretical output spectral noise density for the different stages of the signal conditioning circuit. As expected, the most important contribution at sub-millihertz frequencies is clearly the intrinsic $1/f$ noise of the AMR sensor, which is foreseen to be minimized in the experimental results by the flipping technique. We remark that although the $1/f$ noise of the sensor can be reduced, it cannot be eliminated and is envisaged to continue being the dominant source in the overall noise of the system. In particular, the resistors in the bridge still suffer at long times from a $1/f$ behavior, and the ac modulation of the bridge output does not totally eliminate it. On the other hand, the electronic noise sources from the signal conditioning circuits are well below the magnetic requirement along the measurement bandwidth. This makes it possible to unveil the noise improvement of the sensor itself when utilizing the different noise reduction techniques. The IA, ADC, and Johnson noise of the magnetoresistances can limit the noise performance at frequencies higher than $1\,\text{Hz}$, thus outside the eLISA bandwidth.
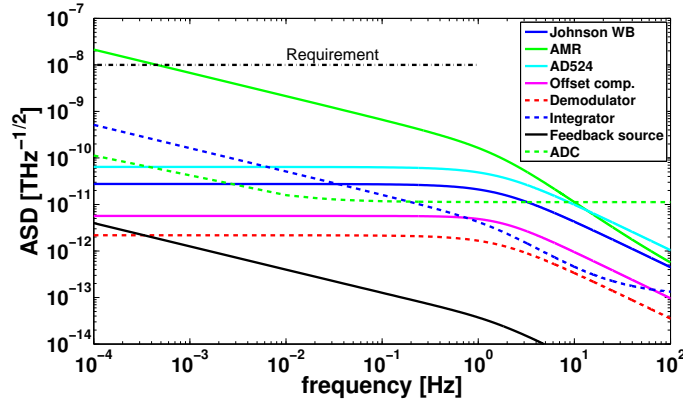
Figure 3.7:   Theoretical equivalent magnetic field noise of the signal conditioning circuit using the flipping technique together with electro-magnetic feedback. Noise contribution of the AMR (green solid trace) shows the intrinsic noise of the sensor without flipping excitation. Its noise reduction due to the modulation technique is estimated experimentally in Sec. 3.5.

---

[4]White noise assumption is true when the quantization error is not correlated to the input signal [29].

3.4.2 Temperature coefficient analysis

The optimization of the thermal dependences in the sensors and the signal conditioning circuit is critical since slow temperature drifts may show up as a low-frequency noise contribution. One of the more sensitive elements to thermal changes is the resistors forming the Wheatstone bridge. Assuming the worst-case condition, the temperature coefficient (TC) of the bridge output voltage is

$$\alpha_{\rm b} \simeq 2V_{\rm b} \left[\frac{R_1 R_2}{(R_1 + R_2)^2} + \frac{R_3 R_4}{(R_3 + R_4)^2} \right] \cdot \alpha_{\rm R,AMR} \tag{3.12}$$

$$= V_{\rm b} \left(1 - \frac{\Delta R_{\rm b}^2}{R^2} \right) \cdot \alpha_{\rm R,AMR} \simeq V_{\rm b} \cdot \alpha_{\rm R,AMR}, \tag{3.13}$$

where $\alpha_{\rm R,AMR} = 0.25\,\%\,{\rm K}^{-1}$ is the TC of the AMR. From Eq. (3.6), the bridge resistances $R_{\rm b,n}$ change by an amount $\Delta R_{\rm b} = s_{\rm AMR} R_{\rm b,n} B_{\rm m} = \pm 1.088\,\Omega$ for a sensor range of $\pm 40\,\mu{\rm T}$. $R_1 = R_4 = R_{\rm b,n} - \Delta R_{\rm b}$ and $R_2 = R_3 = R_{\rm b,n} + \Delta R_{\rm b}$ are the magnetoresistive components shown in Figure 3.4. Therefore, the maximum TC of the Wheatstone bridge is $10.6\,{\rm mV\,K}^{-1}$ and the equivalent magnetic field noise is given by

$$S_{B,\,{\rm WB}}^{1/2}(\omega) = \frac{\alpha_{\rm b}}{s_{\rm AMR} \cdot V_{\rm b}} \cdot S_{T,\,{\rm AMR}}^{1/2}(\omega), \tag{3.14}$$

where $S_{T,\,{\rm AMR}}^{1/2}$ is the thermal fluctuations in the magnetometer location. The thermal environment is not yet determined for eLISA, but the temperature fluctuations inside the satellite are expected to be lower than those required for LISA Pathfinder ($S_{T,\,{\rm LPF}}^{1/2} < 0.1\,{\rm K\,Hz}^{-1/2}$). This leads to an equivalent magnetic field noise of $7.8\,\mu{\rm T\,Hz}^{-1/2}$, which is much larger than the noise level defined in Eq. (3.1). In view of the high thermal dependence of the AMR, flipping and electro-magnetic feedback are used to reduce the thermal drift effects in the sensors.

With the flipping scheme, each magnetic readout is the average difference between two consecutive measurements ($V_{\rm o,\,set}$ and $V_{\rm o,\,reset}$) with opposite polarization

$$V_{\rm o} = \frac{1}{2} \left(V_{\rm o,\,set} - V_{\rm o,\,reset} \right). \tag{3.15}$$

Thus, the effect due to the temperature changes is now given by

$$\alpha_{\rm b} \simeq V_{\rm b} \frac{\Delta R_{\rm b}}{R_{\rm b,n}} \alpha_{\rm R,AMR}, \tag{3.16}$$

where $\alpha_{\rm b}$, assuming the worst-case condition and a full unbalanced Wheatstone bridge (full-scale range), is reduced to $13.6\,\mu{\rm V\,K}^{-1}$ ($0.1\,\mu{\rm T\,K}^{-1}$). Then, the equivalent magnetic field noise given by Eq. (3.14) is $10\,{\rm nT\,Hz}^{-1/2}$, which barely achieves the requirements.

When a constant voltage source feeds the bridge, the temperature dependency of the bridge resistance will vary the bridge output as

$$V_{\mathrm{o}} = \frac{V_{\mathrm{b}}\Delta R_{\mathrm{b}}}{R_{\mathrm{b}}(1 + \alpha_{\mathrm{R,AMR}}T)} \tag{3.17}$$

for a worst-case error. By contrast, temperature sensitivity can be improved by using a constant current source instead, since variations in the resistances are partly compensated with changes in the voltage across the bridge. Then, the sensor output is equivalent to the constant current $V_{\mathrm{o}} = I_{\mathrm{b}}\Delta R_{\mathrm{b}}$ and the thermal stability is improved. Nevertheless, the AMR sensitivity also changes with temperature due to the energy-band structure of the magnetic material [191]. The error due to the temperature dependence of the sensor sensitivity is then $I_{\mathrm{b}}\alpha_{\mathrm{sens}}\Delta R_{\mathrm{b}} = 3.3\,\mu\mathrm{V\,K}^{-1}$ ($24\,\mathrm{nT\,K}^{-1}$), for $\alpha_{\mathrm{sens}} = 0.06\,\%\,\mathrm{K}^{-1}$ and a full-scale range of $\pm 40\,\mu\mathrm{T}$. Thermal fluctuations during laboratory measurements are around $1\,\mathrm{K\,Hz}^{-1/2}$ at $0.1\,\mathrm{mHz}$. Thus, as shown in Figure 3.8, temperature dependences appear as additional noise at low frequencies when using exclusively the flipping technique. As explained before, this effect is reduced by using a negative closed-loop that follows a null ΔR_{b} to keep the bridge balanced. As a result, the gain errors barely affect the measurement.
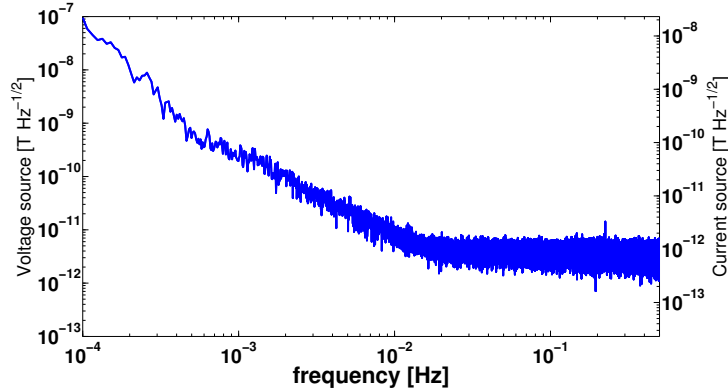
Figure 3.8: Equivalent field noise contribution due to thermal fluctuations in the laboratory using flipping technique at full-scale field range. Thermal contributions were estimated with constant voltage source ($S_B^{1/2} = 0.1 \cdot 10^{-6} \cdot S_{T,\,\mathrm{AMR}}^{1/2}(\omega)$, left vertical axis) and constant current source ($S_B^{1/2} = 24 \cdot 10^{-9} \cdot S_{T,\,\mathrm{AMR}}^{1/2}(\omega)$, right vertical axis) for the bridge excitation (see text for details).

The TCs for the different stages of the circuit are compared in Table 3.2, where thermal drifts of the operational amplifier parameters (bias current, offset current, and offset voltage) can be neglected. On the whole, temperature dependences of the sensor, more precisely the TC of the magnetoresistance and bridge sensitivity, are

the largest thermal contributors of the system. More details about the theoretical analysis of the TCs and errors can be found in Appendix D.

Table 3.2: Temperature coefficients referred to the input for the stages of the electronics in which flipping and electro-magnetic feedback techniques were used. $I_b\Delta R_b$ is the bridge output voltage, $\alpha_R = 0.6\,\mathrm{ppm\,K^{-1}}$, $\alpha_{GIA} = 25\,\mathrm{ppm\,K^{-1}}$, $\alpha_C = 30\,\mathrm{ppm\,K^{-1}}$, and $\alpha_{ADC} = 7\,\mathrm{ppm\,K^{-1}}$.

Source	$TC_{\mathrm{rti}} = k_{\mathrm{TC}}\Delta R_{\mathrm{b,n}}$ [V/K]	k_{TC}
WB resistor (volt. source)	$\alpha_{R,AMR}V_b/R_b\Delta R_b$	1.3×10^{-5}
WB sensitivity	$\alpha_{sens}I_b\Delta R_b$	3.0×10^{-6}
Bias source	$\alpha_R I_b\Delta R_b$	3.0×10^{-9}
IA gain drift	$\alpha_{GIA}I_b\Delta R_b$	1.3×10^{-7}
IA offset compensation	$(\alpha_R^2 + \alpha_C^2)^{1/2}I_b\Delta R_b$	1.5×10^{-7}
Demodulator	$\alpha_R I_b\Delta R_b$	3.0×10^{-9}
Integrator	$(\alpha_R^2 + \alpha_C^2)^{1/2}I_b\Delta R_b$	1.5×10^{-7}
Compensation source	$\alpha_R I_b\Delta R_b$	3.0×10^{-9}
ADC	$\alpha_{ADC}I_b\Delta R_b$	3.5×10^{-8}
Total$_{\mathrm{V-Source}}$	$\sqrt{\Sigma TC_{\mathrm{rti}}^2}$	1.3×10^{-5}
Total$_{\mathrm{I-Source}}$		3.0×10^{-6}

3.5 Results: low-frequency magnetic noise spectral density

3.5.1 Low-frequency noise: stray field measurements

Low-frequency noise measurements for characterizing the system were taken by placing the device inside a three-layer mu-metal shielding. A bias field inside the shielding was not applied for these runs. Therefore, a low residual field around $\sim 20\,\mathrm{nT}$ was measured by the sensor. Lock-in and flipping noise reduction techniques at different modulation frequencies (5.5 and 10 Hz) were carried out by using voltage (5 and 10 V) and current sources (5 mA) to supply the sensor. Figure 3.9 shows the equivalent magnetic field spectral density measured by the system, where ac bridge excitation using lock-in amplification does not improve the potential $1/f$ noise of the magnetoresistors. Nevertheless, the flipping scheme helps to reduce part of it across the desired bandwidth. This contribution cannot be totally mitigated and the

noise measurements still exhibit a dominant $1/f$ behavior coming from the bridge's resistors. Thus, *excess* noise caused by the current that flows across the magnetoresistance bridge could be a significant contribution, which also exhibits a $1/f$ noise power spectrum [136, 78]. Owing to the TC reduction of the sensor, additional improvement in the millihertz bandwidth has been obtained when a low noise current source supplies the bridge instead of a voltage source, showing a similar low-frequency noise to the fluxgate sensor used in LISA Pathfinder. At higher frequencies, the noise level is slightly reduced when flipping frequency and bridge voltage are raised. However, the increase in bridge voltage also implies higher *excess current* noise in the low-frequency band. Besides, more periodic flipping pulses can also induce additional disturbances in the spacecraft's environment. Since our interest is focused on the fluctuations in the low-frequency region, which is the limiting noise factor, flipping pulses at $5.5\,\mathrm{Hz}$ and a dc bridge current of $5\,\mathrm{mA}$ ($V_\mathrm{b} = 4.25\,\mathrm{V}$) are the selected features.
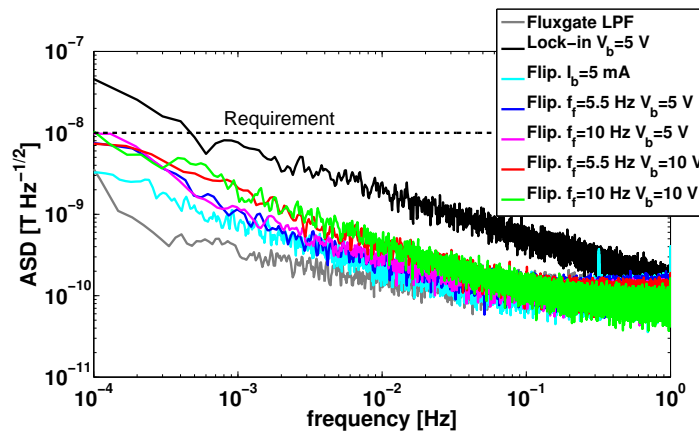
Figure 3.9: Equivalent magnetic field noise density for the engineering model of the fluxgate magnetometer used in LISA Pathfinder (gray trace) and AMR sensor using lock-in amplification and flipping techniques. Measurements have been done driving the AMR sensor with voltage (V_b) and current sources (I_b, cyan trace). Bias field is not applied.

3.5.2 Low-frequency noise under a bias magnetic field

Additional noise in the low frequency band appears as a consequence of the thermal dependence of the sensor coupled with the slow environmental temperature drifts. As shown in Table 3.2 the TC of the system depends on the amount of unbalance of the Wheatstone bridge, i.e., the magnitude of the magnetic field seen by the sensor. For noise investigation, a leading field of $\sim 21\,\mu\mathrm{T}$ with a stability better than $1\,\mathrm{nT}\,\mathrm{Hz}^{-1/2}$ at $0.1\,\mathrm{mHz}$ is applied by a coil inside the magnetic shielding. The purpose is to unbalance the bridge to stress the effect of the gain temperature coefficient of the

sensor and conditioning circuit during the noise measurements. A block diagram of the experimental setup is displayed in Figure 3.10.
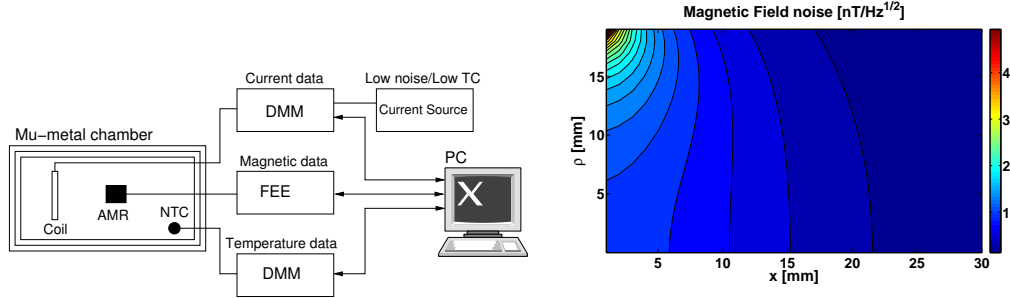
Figure 3.10: Setup for the low-frequency noise measurements under a bias magnetic field. Right: map of the equivalent magnetic field noise at $0.1\,\text{mHz}$ induced by a coil with 1000 windings of radius around 20 mm. The sensor is placed at around $15\,\text{mm}$ from the coil along the x-axis. x and ρ are the distances to the center and to the longitudinal axis of the coil, respectively.

Figure 3.11 shows the noise measurements that were taken by using the flipping technique and electro-magnetic feedback in the presence of a bias field. To begin with, we measured the stability of the current source that generates the bias field and found it suitable to carry out the experiment (see also Figure 3.10). On the one hand, as far as the flipping method is concerned, the equivalent magnetic field noise at $0.1\,\text{mHz}$ increases by an order of magnitude with respect to the previous
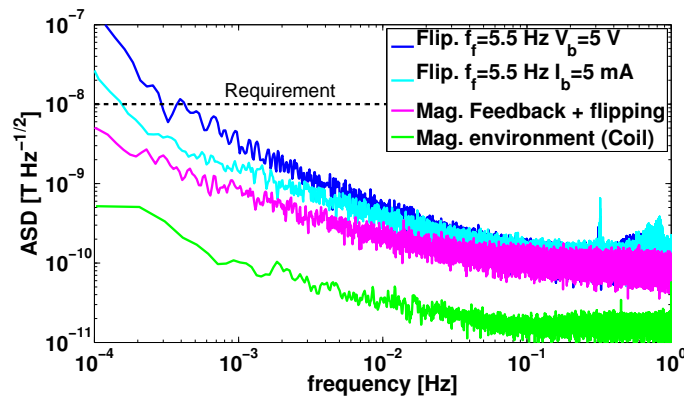
Figure 3.11: Spectral density in terms of equivalent magnetic field using flipping with voltage and current sources and electro-magnetic feedback. The green trace shows magnetic field noise generated by the coil at 15 mm from the sensor. The magnetic noise requirement at 0.1mHz (dashed trace) is achieved by using electro-magnetic feedback (magenta trace). Bias field is $\sim 21\,\mu\text{T}$.

results in Figure 3.9 without a leading field. As expected, the additional noise due to thermal dependence is still more significant when a constant voltage source supplies the bridge. On the other hand, the noise curve for electro-magnetic feedback shows that the effect of the gain temperature coefficient of the sensor is mitigated by the use of a proper closed-loop mode. The noise level achieved is $\simeq 5\,\mathrm{nT\,Hz}^{-1/2}$ at $0.1\,\mathrm{mHz}$, which is below the requirement. Therefore, this compensation method is crucial to maintain long-term stability over temperature, and produces desirable results for measuring magnetic fields at the eLISA frequencies. At higher frequencies, the noise floor is down to $\simeq 100\,\mathrm{pT\,Hz}^{-1/2}$ with the corner frequency at around $0.2\,\mathrm{Hz}$. We remark that the noise floor might be reduced to the Johnson noise of the bridge resistance by increasing the flipping frequency.

3.6 Conclusion

We have presented the low-frequency noise characterization of a magnetic field measuring system based on AMR. Chip-scale magnetoresistive sensors appear as a solution to the disadvantages met when using the bulky fluxgate magnetometers in LISA Pathfinder. Nevertheless, magnetoresistors exhibit higher intrinsic noise characteristics than fluxgate magnetometers. Thus, in order to enhance the noise performance, various methods have been analyzed and tested in the millihertz band. First, flipping techniques help to overcome part of the potential $1/f$ noise, which cannot be avoided with conventional lock-in amplification techniques (ac excitation of the bridge). Secondly, an excess noise below $1\,\mathrm{mHz}$ is exhibited when a magnetic field is applied to the sensor as a result of the temperature dependence of the sensor. A solution is found when using electro-magnetic feedback in the signal conditioning circuit. A closed-loop controller with a compensation coil helps to overcome the thermal dependence and to minimize the additional noise in the bandwidth of interest. With the combination of these methods, the equivalent magnetic noise spectral density is comfortably compliant with the envisaged noise requirement. Therefore, from the achieved noise performance, AMR sensors with dedicated noise reduction techniques are presented as an alternative to the fluxgate sensors used in LISA Pathfinder. With respect to the results published so far, we present a significant improvement of noise performance in the frequency range of the millihertz. Finally, we mention that the technology is likely to be useful beyond the scope of eLISA, especially for space applications like STE-QUEST, with strict restrictions in size, weight, power, and low magnetic noise at low frequencies. Moreover, with the objective of augmenting the technology readiness level (TRL) of the instrument, the magnetic measurement system designed in this chapter has been developed and implemented in a CubeSat (^{3}Cat-2) (See Appendix E for more details).

Chapter 4

Magnetic Back Action Effect of an Anisotropic Magnetoresistance

The environmental stability in eLISA must fulfill stringent requirements regarding the magnetic field and magnetic field gradient in the TM location. eLISA thus requires the careful control, for dc values and low-frequency fluctuations, of the local magnetic environment generated by the spacecraft, and in particular, for the magnetic sources which are closer to the TM. This chapter evaluates the induced forces on the TM due to the magnetic field generated by the AMR magnetometer itself. Section 4.2 gives an overview of the influence of the environmental magnetic field on the TM. In Section 4.3, the magnetic characterization of the magnetic sensor, together with the integrated coils utilized by the electronic noise reduction techniques, is put into practice by using a SQUID magnetometer. In Section 4.4, the magnetic field and the magnetic field gradient in the region occupied by the TM are estimated for the suggested sensor configuration. Then, in Section 4.5 we determine the excess force noise on the TM due to the magnetic contribution of the sensor array. Finally, the conclusions are summarized in Section 4.6.

4.1   Introduction

The fluxgate magnetometers on board LISA Pathfinder somehow need to be kept away from the TMs due to the quantity of ferromagnetic material contained in the core. Otherwise, the magnetic field emitted by the magnetometer can constitute a potential source of disturbance to the noise budget. As a result of the magnetometers location in LISA Pathfinder, the estimation of the magnetic field and gradient in the TM region is very problematic despite the excellent quality of the readout data [16]. For eLISA, the design of an alternative magnetic measuring system able to deal

with these constraints is planned. This implies the magnetic characterization of the new magnetic sensing technology in order to estimate the possible magnetic effect on its environment when the set of sensors is mounted closer to the TM. The magnetic impact caused by the AMR type magnetometers depends not only on the tiny amounts of ferromagnetic material of the sensor head but also on the magnetic field created by the noise reduction techniques explained in Chapter 3. The detailed study of this issue needs to be performed so as to develop criteria for the best choice of the magnetic sensors for eLISA.

4.2 Magnetic contribution to force noise induced by the magnetic sensors

A non-gravitational force can be exerted by the surrounding magnetic field and its gradient when they couple with the magnetic properties of the TM, more precisely magnetization ($\mathbf{M}$) and susceptibility (χ). This spurious force and its fluctuations on the TM volume V are given by Eqs. (1.4) and (1.6). If down-conversion of the high frequency magnetic noise and low-frequency amplitude modulation of ac lines are not considered, second order terms can be neglected and the expression of the temporal force fluctuations is simplified to

$$\delta F = V \langle \mathbf{M} \cdot \delta(\boldsymbol{\nabla} B) \rangle + \frac{\chi V}{\mu_0} \langle \delta \mathbf{B} \cdot \boldsymbol{\nabla} B \rangle + \frac{\chi V}{\mu_0} \langle \mathbf{B} \cdot \delta(\boldsymbol{\nabla} B) \rangle, \qquad (4.1)$$

where $\langle \mathbf{B} \rangle$ and $\langle \boldsymbol{\nabla} B_x \rangle$ are the magnetic field and magnetic field gradient average over the TM volume.[1] Since the vector orientations in the scalar products are unknown, the worst-case estimate of the excess noise in terms of force spectral density along the sensitive x-axis of the experiment, $S_{\delta F_x}^{1/2}$, can be expressed as [161]

$$S_{\delta F_x}^{1/2}(\omega) = V \left[|\langle \mathbf{M} \rangle|^2 S_{\nabla B_x}(\omega) + \left(\frac{\chi V}{\mu_0} |\langle \boldsymbol{\nabla} B_x \rangle| \right)^2 S_{\mathbf{B}}(\omega) \right.$$
$$\left. + \left(\frac{\chi V}{\mu_0} |\langle \mathbf{B} \rangle| \right)^2 S_{\nabla B_x}(\omega) \right]^{1/2}, \qquad (4.2)$$

As a first approximation, we assume that the fluctuating magnetic fields are dominated by the interplanetary magnetic field (see Section 3), and besides, the fluctuations are homogeneous along the volume of the TM. In other words, the fluctuations of the remnant magnetic moment of the sensor, the ones caused by the quantity of

---

[1]It is assumed that the oscillating field is due to varying magnetic moments whose direction is aligned with the relative position vector between source and TM, and also with the sensitive x-axis [186]. This is not reflected in our analysis.

ferromagnetic materials contained in the core, are supposed to be negligible compared with the background field. This is due to the stable thermal conditions inside the LCA. On the other hand, the magnetic field $\mathbf{B}$ when the AMRs are present is the sum of the field generated by the AMRs ($\mathbf{B}_{AMR}$) and the environmental magnetic field ($\mathbf{B}_{bg}$), mostly created by the other spacecraft magnetic sources. These statements are expressed by

$$S_{\mathbf{B}} = S_{\mathbf{B}_{bg}} \quad \text{and} \quad \mathbf{B} = \mathbf{B}_{AMR} + \mathbf{B}_{bg}. \tag{4.3}$$

Based on this assumption, only the last two terms in Eq. (4.2) are sensitive to the magnetic field created by the AMRs. Thus, the excess noise induced by the AMR is due to: (1) the product of the constant field gradient with the environmental field fluctuations; (2) the coupling between the dc magnetic field and the field gradient fluctuations of the environment.

The TM of eLISA will mainly be the same as its counterpart in LISA Pathfinder. The main distinction is aimed at relaxing the environmental requirements on the satellite by lowering the magnetic susceptibility and remnant magnetic moment of the TM [80]. But to be conservative, a worst-case analysis is considered by using the same magnetic properties of the TM as in LISA Pathfinder. In the same way, since the spacecraft's magnetic sources have still not been fully defined for eLISA, the magnetic dc requirements and the estimate of the fluctuations for LISA Pathfinder were adopted for our analysis. The nominal properties of the TM and magnetic background conditions [183] that will be used in Eq. (4.2) are shown in Table 4.1.

Table 4.1: Magnetic properties of the TM, dc requirements and estimated fluctuations in the TM locations for LISA Pathfinder.

TM propts.	dc req.	ASD est.
$\lvert\chi\rvert = 10^{-5}$	$\lvert\mathbf{B}_{bg}\rvert \leq 10~\mu\text{T}$	$S_{\mathbf{B}}^{1/2}(\omega) \leq 100\,\text{nT Hz}^{-1/2}$
$\mathbf{M} = 10^{-4}~\text{A m}^{-1}$	$\lvert\boldsymbol{\nabla} B_{bg,x}\rvert \leq 5\sqrt{3}\,\mu\text{T m}^{-1}$	$S_{\nabla B_x}^{1/2}(\omega) \leq 250\sqrt{3}~\text{nT m}^{-1}\,\text{Hz}^{-1/2}$

Concerning the distribution of the sensor array, the feasible layout may be to place them on the outer face of the vacuum enclosure, symmetrically allocated around the TMs. With this configuration, the nearest distance of each AMR to the TM is about 36 mm, in contrast to the distance of 188 mm for the closest fluxgate sensor in LISA Pathfinder. Therefore, due to the proximity to the TM, the acceleration noise induced by the magnetic characteristic of the AMR magnetometers was quantitatively assessed in Section 4.5 for the configuration displayed in Figure 4.1.

69
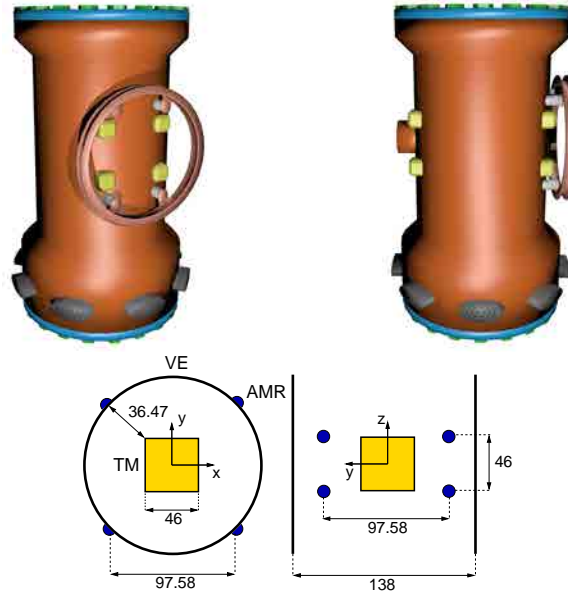
Figure 4.1: AMR magnetometers location. Top: view of the proposed distribution of the AMR sensors (yellow structures) on the vacuum enclosure (cylindrical tower). Bottom: top and front view with distances in mm.

4.3 Magnetic moment measurements of the AMRs

The AMR sensor core comprises a thin permalloy (nickel-iron alloy) film deposited on a silicon substrate and patterned as a resistive strip in a conventional Wheatstone bridge configuration [77]. In spite of the diminutive amount of ferromagnetic materials accommodated in the core, the magnetometer could have a assessable impact if it is attached near the TM. Besides, in view of the magnetic anisotropy of the thin film, the state of the magnetic domains needs to be aligned along the same direction, the easy axis, for the proper functioning of the sensor (see Section 3.3.1). Therefore, the remnant magnetic moment due to the ferromagnetic components of the sensor will be distinctly oriented in a unique direction.

As explained in Chapter 3, the intrinsic $1/f$ noise behavior together with the thermal dependence of the magnetoresistances are the dominant contributions at low frequencies. Hence, several electronic noise reduction techniques were utilized in order to enhance its performance [124]. As a result, the magnetic impact of the sensor depends on the magnetic properties of the sensor itself and the technique used. The technical features that are susceptible to affect the field environment are summarized below.

- Lock-in amplifier: The magnetic impact is merely due to the ferromagnetic

materials contained in the sensors.

- Flipping : Periodic short magnetic pulses with a τ of approximately $1\,\mu$s are applied by a thin film conductor integrated in the sensor. Positive and negative pulses are synchronously applied at 5.5 Hz.

- Electro-magnetic feedback: A built-in coil generates a compensation field to cancel out the field being measured by the sensor.

Due to the lack of specifications, the magnetic moment of the AMR was measured by using two different superconducting quantum interference devices (SQUID), a Quantum Design MPMS XL SQUID at the University of Barcelona and a Superconducting Rock Magnetometer SRM755R (2G Enterprises) at the Institute of Earth Sciences Jaume Almera (CSIC-UB). The former was utilized to obtain the hysteresis curve with respect to an applied external magnetic field, and the latter for direct triaxial measurements with the sensor working under the three aforementioned noise reduction techniques.
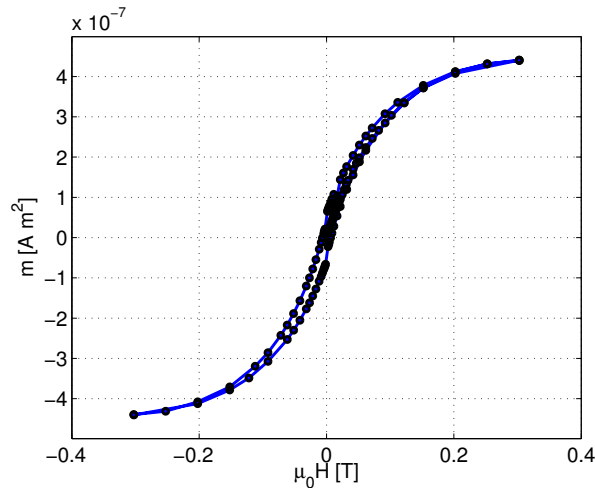
Figure 4.2: Hysteresis curve for the uniaxial magnetoresistance HMC1001. The measurement was performed with the Quantum Design MPMS XL SQUID at 300 K.

While measuring the hysteresis cycle, the size of the sample introduced in the first SQUID is limited by the cross section of the cylindrical holder, a plastic test tube of around 6.5 mm in diameter. As a result, the device can only be placed by aligning the longitudinal axis of the sensor, which is perpendicular to the sensitivity axis, with the longitudinal axis of the holder, i.e, with the direction of the applied field. The result for the hysteresis curve of the HMC1001 uniaxial AMR [30] is displayed in Figure 4.2, where the ferromagnetic behavior is clearly observed. The magnetic response has a saturation magnetic moment of $|\mathbf{m}_{\text{sat}}| \simeq 0.44\,\mu\text{A}\,\text{m}^2$ with

a bias field of $0.3\,\mathrm{T}$, and a remnant magnetic moment of $|\mathbf{m_r}| \simeq 0.05\,\mu\mathrm{A\,m^2}$. These values are considerably small compared to the magnetic properties of the NTC type thermistors in LISA Pathfinder. The saturation and remnant magnetic moment for the NTC sensor is $90\,\mu\mathrm{A\,m^2}$ and $26\,\mu\mathrm{A\,m^2}$, respectively [161]. Apart from this, the NTCs location is more critical since they are attached to the external wall of the electrode housing at only 13 mm of the TM.

With the purpose of knowing about the magnetic impact of the flipping pulses through the set/reset strap (see the figure in Table 4.3), additional magnetic moment data in the three axes have been taken with the SRM755R SQUID when the sensor is working with flipping technique. However, the magnetic moment of the set/reset pulses can not be measured at the fast switching frequency used during operation ($\simeq 5\,\mu\mathrm{s}$ pulse and 0.003% duty cycle) because of the reduced bandwidth of the SQUID. We thus apply small continuous currents instead, and then, the measurements are extrapolated to the actual value of current amplitude generated by the flipping generator circuit (see Figure 3.4). The measurements were taken for the HMC1001 uniaxial and HMC1002 biaxial sensors, but the flipping current was only applied to the former because both share the same electrical performance. The results in Table 4.2 show that the magnetic moment induced by the set/reset coil points to the y direction (m_y column), and therefore the estimated magnetic moment for an instantaneous peak current of $2\,\mathrm{A}$, is lower than $200\,\mu\mathrm{A\,m^2}$.

Table 4.2: Magnetic moment measurements with the SRM755R SQUID. I_{flip} indicates the current applied to the set/reset coil. Right figure: Coordinate axes during the experiment for the uniaxial and biaxial AMRs. Arrows inside the sensors indicate the orientation of the sensitivity axes.

AMR	I_{flip} [mA]	$|\mathbf{m}|$	m_x	m_y	m_z
				$[\mu\mathrm{Am^2}]$	
BiAxial	0	0.018	0.014	-0.010	0.004
Uniaxial	0	0.03	-0.011	0.028	-0.006
	5	0.51	0.027	0.483	0.161
	10	0.968	0.05	0.919	0.30
	15	1.461	0.11	1.386	0.449
	20	1.973	0.10	1.881	0.587

Finally, magnetic moment measurements were also taken by injecting currents to the compensation strap (see the figure in Table 4.3). The maximum field generated by the electro-magnetic feedback into the active area of the AMR is defined by the full scale range of the device. For a feedback current of $40\,\mathrm{mA}$ and a compensation coil ratio of $1.96\,\mu\mathrm{T\,mA^{-1}}$, the measurement range is about $78\,\mu\mathrm{T}$, providing a wide margin for the mission needs. Table 4.3 summarizes the results for the three techniques employed. We remark that for Lock-in amplifier technique, the magnetic

moment displayed in the table corresponds with the remnant magnetic moment $|\mathbf{m}_\mathrm{r}| = 0.05\,\mu\mathrm{A\,m}^2$ in the hysteresis curve. This number is slightly higher than the one obtained when a sweeping field to map out the hysteresis curve is not applied ($\mathbf{m} = 0.03\,\mu\mathrm{A\,m}^2$). The difference is small, but it might be indicative of the deep magnetization of the sensor after being saturated for a strong field of $300\,\mathrm{mT}$.

Table 4.3: Magnetic moment measurements for different electronic noise reduction techniques. Note that the flipping current is a fast peak with a τ of $1\,\mu$s . The right figure shows set/reset and compensation straps where the current is applied according to the method used.

Technique	I_strap [A]	$\lvert \mathbf{m} \rvert$ [$\mu\mathrm{Am}^2$]
Lock-in	-	0.05
Flipping	2	200
	0.01	1.19
	0.02	2.34
Feedback	0.03	3.46
	0.04	4.58
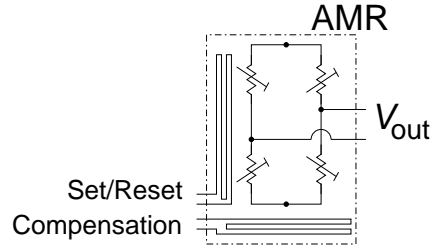
4.4 Magnetic field and magnetic field gradient calculations

The area of the thin permalloy film elements is around $0.9\,\mathrm{mm} \times 1.2\,\mathrm{mm}$, and the closest distance between the magnetometer and the TM for the current layout is $36.47\,\mathrm{mm}$. Consequently, given the small size of the active magnetic area contained in the sensor, the magnetic field and magnetic field gradient created by the AMRs have been estimated by assuming that they behave as magnetic dipoles. Hence, the magnetic field generated by the eight magnetometers at a far enough point $\mathbf{x}$ can be expressed as

$$\mathbf{B}_\mathrm{AMR}(\mathbf{x}) = \frac{\mu_0}{4\pi}\sum_{a=1}^{8}\frac{3(\mathbf{m}_a{\cdot}\mathbf{n}_a)\mathbf{n}_a - \mathbf{m}_a}{|\mathbf{x}-\mathbf{x}_a|^3}, \tag{4.4}$$

where $\mathbf{m}_a$ are the magnetic dipolar moments of the sensors at the points $\mathbf{x}_a$ and $\mathbf{n}_\mathrm{a} = (\mathbf{x}-\mathbf{x}_\mathrm{a})/|\mathbf{x}-\mathbf{x}_\mathrm{a}|$ are the unit vectors directed from $\mathbf{x}_a$ to $\mathbf{x}$. The corresponding expression for the magnetic field gradient is [83]

$$\frac{\partial B_i}{\partial x_j} = \frac{\mu_0}{4\pi}\sum_{a=1}^{8}\frac{3}{|\mathbf{x}-\mathbf{x}_a|^4}[(m_{a,i}n_{a,j} + m_{a,j}n_{a,i}) + (\mathbf{m}_a{\cdot}\mathbf{n}_a)(\delta_{ij} - 5n_{a,i}n_{a,j})], \tag{4.5}$$

where δ_{ij} is Kronecker's delta.

We now proceed to compute the figures derived from the above equations, where the relevant parameter in our estimation is the value of the remnant magnetic moment of the magnetometer. A worst-case scenario is assessed for the maximum dc magnetic field required in the TM location, i.e. $10\,\mu$T (see Table 4.1).[2] Then, for a first case, we assume that the magnetometers on both sides of the TM are measuring an environmental field of $10\,\mu$T. Therefore, an opposite field with the same magnitude is created by each of the chip-scale compensation coils integrated in the AMRs. For the sake of clarity, the field is evaluated in the equatorial plane of the TM (xy-plane for $z = 0$). Besides, the magnetic moment created by the compensation coil ($|\mathbf{m}_{\mathrm{comp}}| = 0.6\,\mu$A m^2) is assumed to be oriented in the z direction (perpendicular to the optical bench plane).[3] Calculations taking into account different orientations of the magnetic moments lead to similar or milder effects, and moreover, the small remnant magnetic moment due to the ferromagnetic properties of the sensor head ($|\mathbf{m}_{\mathrm{comp}}| = 0.05\,\mu$A m^2) can be ignored. Figure 4.3 shows the magnetic field and the magnetic field gradient created by the eight sensors when using electro-magnetic feedback technique for this particular configuration.
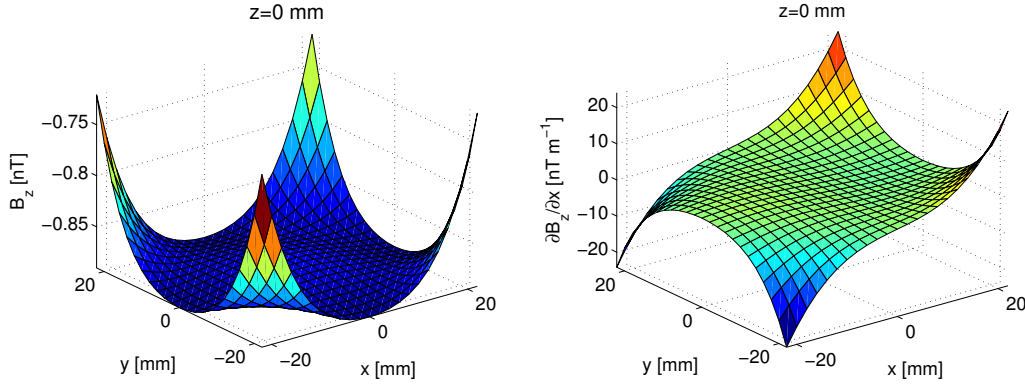
Figure 4.3: z-component of the magnetic field (left) and magnetic field gradient (right) caused by the compensation coil when a background magnetic field of $10\,\mu$T goes homogeneous across the vertical axis of the TM (parallel configuration). Plots are represented in the equatorial plane of the TM (xy-plane for $z = 0$).

An opposite case is studied when a non-homogeneous environmental field goes across the TM. Taking the configuration to the extreme, we assume that the magnetic moment of the magnetometers placed in the opposite side of the TM have opposite directions, i.e., $m_{z,\mathrm{side1}} = 0.6\,\mu$A m^2 and $m_{z,\mathrm{side2}} = -0.6\,\mu$A m^2. We remark

---

[2]This is a requirement for LISA Pathfinder. For eLISA the magnetic cleanliness requirements are not formally defined, but they shall be the same or lower than the LISA Pathfinder ones. Therefore, this is a conservative value for our estimation.

[3]The magnetic moment has been estimated for a feedback current of 5 mA, which is equivalent to a compensated field of $\simeq 10\,\mu$T (see Table 4.3)

that the supposed magnetic arrangement for this configuration is unlikely along the TM volume, since the magnetic field gradient ($\simeq 205\,\mu\text{T}\,\text{m}^{-1}$) would be well over the magnetic cleanliness requirements (see Table 4.1). Therefore, the specified distribution is considered a worst-case estimate. The magnetic field and its gradient for this situation is represented in Figure 4.4.
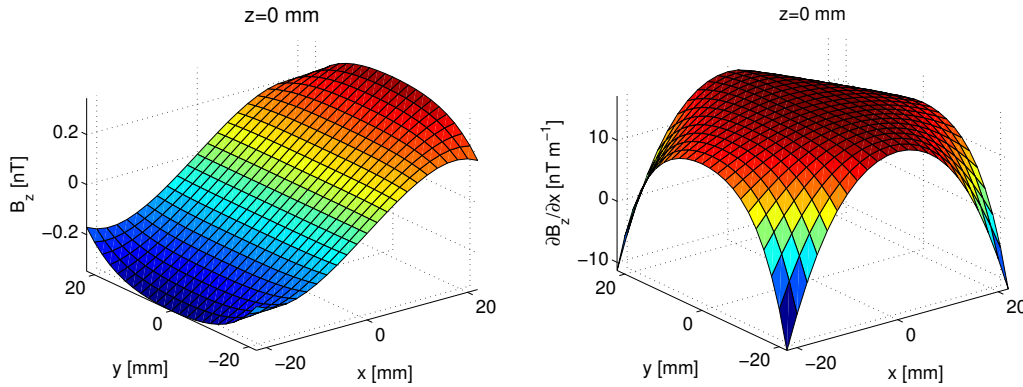
Figure 4.4: z-component of the magnetic field (left) and magnetic field gradient (right) caused by the magnetic moment of the compensation coil oriented along the z-axis, but in antiparallel configuration at the opposite sides of the TM. Plots are represented in the equatorial plane of the TM (xy-plane for $z = 0$).

Before calculating the magnetic noise contribution of the sensor array, we need to estimate the averaged values ($\langle \mathbf{B}_{\text{AMR}} \rangle$ and $\langle \boldsymbol{\nabla} B_{\text{AMR,x}} \rangle$) that will be replaced into Eq. (4.2). The averaged variables are solved by a finite element method using subdivisions of the whole volume of the TM (46 mm × 46 mm × 46 mm) into smaller volumes of $\Delta V = 8\,\text{mm}^3$. Then, the magnetic field and the magnetic field gradient are calculated over the small subdomains by using Eqs. (4.4) and (4.5), and finally the arithmetic means are calculated. The results for the two aforementioned configurations are shown in Table 4.4. Firstly, when all the magnetic moments are in the same direction due to the homogeneous field being measured by the sensors, the magnetic field created by the AMRS on the TM gives the highest mean values, while the magnetic field gradient averages to zero. On the other hand, when the magnetic moments at the different faces of the TM take opposite directions the response is the contrary, the magnetic field on the TM averages to zero and all the magnetic impact is reflected on the magnetic field gradient.

Regarding the magnetic impact caused by the flipping technique, Figure 4.5 shows the short magnetic field pulses averaged over the TM volume for the three-axial magnetometers. The same as in the configuration for a homogeneous field, the magnetic field gradient averages to zero because the magnetic moments of the flipping

Table 4.4: Averaged magnetic field $\langle \mathbf{B}_{\mathrm{AMR}} \rangle$ and magnetic field gradient $\langle \boldsymbol{\nabla} B_{\mathrm{AMR,x}} \rangle$ in the TM created by the proposed sensor configuration using electro-magnetic feedback. The averaged values were calculated for two different arrangements (see text, Figure 4.3 and Figure 4.4 for details).

Magnetic arrag.	$\langle B_x \rangle$	$\langle B_y \rangle$	$\langle B_z \rangle$ [nT]	$\vert \langle \mathbf{B} \rangle \vert$	$\langle \partial B_x / \partial x \rangle$	$\langle \partial B_y / \partial x \rangle$	$\langle \partial B_z / \partial x \rangle$ [nT m^{-1}]	$\vert \langle \boldsymbol{\nabla} B_x \rangle \vert$
Fig. 4.3	0	0	-0.9	**0.9**	0	0	0	0
Fig. 4.4	0	0	0	0	0	0	18.8	**18.8**

pulses are assumed equal in amplitude, orientation and time.[4] In this particular case, the fields created by the tiny set/reset coils need to be applied in the three *easy* axes for the proper functioning of the flipping technique. The maximum instant value appears in the z-component $B_z \simeq -0.3\,\mu\mathrm{T}$, which is caused by a magnetic moment of $200\,\mu\mathrm{A\,m}^2$ (see Table 4.3).

Figure 4.5 also shows the equivalent magnetic field spectral density induced by the flipping pulses on the TM. The magnetic effect of the flipping peaks is more than two orders of magnitude lower than the expected environmental fluctuations in the spacecraft. The peaks in the spectra appear at the flipping frequency (5.5 Hz) and its harmonics, therefore, out of the bandwidth of interest.

It is also worth mentioning that the amplitude modulation of discrete ac magnetic lines can be down-converted into low-frequency acceleration noise [60]. The oscillating field is supposed to be due to the variations of the magnetic moment alignment between the magnetic source and the TM, and also along the x-sensitive axis.[5] However, this lacks importance in our case because the direction of the flipping pulses is fixed by design and it is determined by the integrated set/reset coil.

On the whole, the magnetic field and magnetic field gradient created by the eight magnetometer configuration on the region of the TM are significantly lower than required in Table 4.1. We remark that the magnetic requirements for LISA Pathfinder must be considered as an indicator, so the analysis needs to be verified when the eLISA magnetic requirements are fully defined.

---

[4]The sensors are placed with the same axial configuration and the same current flows through the set/reset straps connected in series for each sensor.

[5]Magnetic fields up to frequencies of 50 kHz were measured for LISA Pathfinder at spacecraft and unit level [186]. ac magnetic measurements are also relevant because high frequency signals can induce low-frequency fluctuations components due to the coupling of the fluctuations of both the magnetic field and the magnetic field gradient (see Eq. (1.6)).

Figure 4.5: Magnetic field averaged over the TM volume induced by the flipping and electro-magnetic feedback techniques. Left: Time-dependent averaged magnetic field caused by the flipping pulses. Note the short duration of the pulse in the zoomed figure. Right: Averaged magnetic field in the case that electro-magnetic feedback is used together with flipping. The small difference between the field components close to zero is caused by the compensation coil when the sensor is measuring a field of $60\,\mu\mathrm{T}$ along the z-axis. Bottom: Noise spectral density of the magnetic field induced by the flipping pulses on the TM. The duration of the simulated pulses for the estimation of the ASD was increased to $60\,\mu\mathrm{s}$.

4.5 Excess noise induced on the TM in the presence of AMRs

As stated before, the force induced on the TM by the eight magnetometers is calculated by means of the magnetic field and magnetic field gradient obtained in the previous section. Moreover, the environmental requirements and magnetic properties of the TM in Table 4.1 are also used.

The force noise estimate is summarized in Table 4.5 assuming a worst possible scenario, which arises from the alignment of the sensors' magnetic moment along the z-axis. Parallel or anti-parallel configuration in opposite face of the TM give comparable effects. The excess noise, Δ in the table, is the relative difference between the total noise including the magnetic contribution of the AMRs ($S_{\mathrm{total,\,AMR}}$) and the noise in the absence of AMR (S_{ref}), which is expressed as

77

$$\Delta = \frac{S_{\text{total, AMR}}^{1/2} - S_{\text{ref}}^{1/2}}{S_{\text{ref}}^{1/2}}. \tag{4.6}$$

As expected from the field calculations, the magnetic contribution of the eight AMR sensors on the total noise budget can be considered negligible. The magnetic impact due to the magnetic properties of the sensor can be ignored compared to the one caused by the compensation coil when a $10\,\mu\text{T}$ field is being measured by the sensors. The same thing happens with the set/reset coil when comparing its magnetic impact to the environmental magnetic fluctuations.

Table 4.5: Summary of results in terms of force noise for an array of 8 AMRs. $\mathbf{m}_{10\,\mu\text{T}}$ and $\mathbf{m}_{80\,\mu\text{T}}$ are the magnetic moments of the compensation coil when the magnetometer measures a magnetic field of $10\,\mu\text{T}$ and $78\,\mu\text{T}$, respectively. Force units are in $\text{fN}\,\text{Hz}^{-1/2}$.

Term	No AMRs	$\|\mathbf{m}_{10\,\mu\text{T}}\|$ $0.6\,\mu\text{A}\,\text{m}^2$	$\|\mathbf{m}_{78\,\mu\text{T}}\|$ $4.58\,\mu\text{A}\,\text{m}^2$
$V\|\langle\mathbf{M}\rangle\|S_{\nabla B_x}^{1/2}(\omega)$	4.215	4.215	4.215
$\frac{\chi V}{\mu_0}\|\langle\boldsymbol{\nabla}B_x\rangle\|S_B^{1/2}(\omega)$	0.671	0.671	0.671
$\frac{\chi V}{\mu_0}\|\langle\mathbf{B}\rangle\|S_{\nabla B}^{1/2}(\omega)$	3.354	3.354	3.356
$S_{\text{total}}^{1/2}(\omega)$	5.428	5.428	5.430
Δ	—	0%	0.03%

4.6 Conclusion

Due to the demanding end-to-end magnetic environment control in eLISA, magnetic moment measurements of the magnetoresitive sensors were carried out to quantify the force excess noise on the TM. The magnetic impact depends on the dedicated noise reduction techniques used in the signal conditioning circuit, i.e, lock-in amplifier, flipping technique, or electro-magnetic feedback. One of the main advantages of AMR technology is its tiny size. Consequently, at least eight magnetometers per TM can be attached to the outside wall of the vacuum enclosure without the risk of back-action effects. The results shows that for the three techniques and their combination, such as flipping together with magnetic feedback, the magnetic noise they induce is mostly negligible. For this reason, the proximity of the magnetometers to the TM does not constitute a problem for the magnetic performance and does not degrade the force noise budget of the mission.

It is worth mentioning that the magnetic impact of the AMRs cannot be fully assessed without precise knowledge of the environmental field in the satellite. Moreover, the magnetic requirements and estimations in eLISA are still not fully specified.

It is therefore desirable to obtain this information to the best possible extent for a more solid estimation. Nevertheless, the results based on the LISA Pathfinder experiments provide relevant information and encouraging results, which are able to deal with the magnetic cleanliness constraints even in the worst cases.

Chapter 5

Interpolation of the Magnetic Field at Test Masses in eLISA

A feasible design for a magnetic diagnostics subsystem for eLISA will be based on that of its precursor mission, LISA Pathfinder. Previous experience indicates that magnetic field estimation at the positions of the test masses has certain complications. This is due to two reasons. The first one is that magnetometers usually back-act due to their measurement principles (i.e., they also create their own magnetic fields), while the second reason is that the sensors selected for LISA Pathfinder have a large size, which conflicts with space resolution and with the possibility of having a sufficient number of them to properly map the magnetic field around the test masses. However, high-sensitivity and small-size sensors that significantly mitigate the two aforementioned limitations exist, and have been proposed in order to overcome these problems. Here we perform a quantitative analysis of the new magnetic system, as it is currently conceived, and assess the feasibility of selecting these sensors in the final configuration of the magnetic diagnostics.

5.1   Introduction

The ongoing research concerning the possible design of a magnetic diagnostics subsystem for eLISA is based on the experience with its precursor mission, LISA Pathfinder, in which high-performance fluxgate magnetometers were chosen because of their sensitivity and availability for space applications [13, 49]. However, these sensors are bulky ($94\,cm^3$) and have a large ferromagnetic sensor head ($\sim 2\,cm$ long). These reasons led to the placing of only four triaxial sensors at somewhat large distances from the TMs ($\geq 18.85\,cm$) to avoid back-action disturbances. Besides, the size of the sensor head also conflicts with space resolution, which might be another source of error in the determination of the magnetic field. A view of the magnetometer location in the LISA Pathfinder payload is shown in Figure 2.2.

We stress that, unlike critical drag-free technology that needs from the in-flight experiments to be fully proved, the feasibility of the magnetic measurement system can be verified in depth from the analysis of the ground test campaigns. On the basis of the previous analysis for LISA Pathfinder, the selected arrangement of magnetic sensors resulted in an unsatisfactory estimation of the magnetic field in the TM region after using classical interpolation methods. Accordingly, alternative approaches needed to be adopted. In particular, an interpolation scheme based on neural networks needed to be developed [48]. For the case of eLISA, a more robust method to reconstruct the magnetic field at the position of the TMs is foreseen. This requires a sufficient number of smaller magnetometers, which additionally must be placed closer to the TMs. Besides, it is required that back-action effects should be negligible. All this motivated the study of alternatives to fluxgate magnetometers. Specifically, magnetoresistances [124, 120] or chip-scale atomic vapor cell devices [36] (see Chapter 6) have been proposed. These small sensors will significantly mitigate the limitations mentioned above. So, they probably will be chosen to be integrated in the magnetic diagnostics subsystem in eLISA, improving the quality of magnetic field interpolation.

All in all, the LISA Pathfinder magnetic diagnostics is fully integrated in the spacecraft due to launch in 2015, and the mission operations together with the data analysis are expected to be completed by 2016. Regarding the magnetic interpolation process to be used in LISA Pathfinder, the aforementioned neural networks algorithms is at the present the most promising one, although it is still an ongoing activity [16]. On the other hand, eLISA is currently under the mission concept study and the critical technologies need to be available for the mission concept selection in 2020. Details can be found in [17, 185] regarding the general status of eLISA and its precursor LISA Pathfinder.

In this section we assess the feasibility of using anisotropic magnetoresistance sensors for estimating the magnetic field and its gradient at the location of the TMs. The chapter is organized as follows. In Section 5.2 the theoretical methods for the magnetic field interpolation are explained, while in Section 5.3 the sensor array and the distribution of the magnetic sources are addressed. The results of our analysis are presented in Section 5.4. Finally, we draw our conclusions in Section 5.5.

5.2   Interpolation methods

The magnetic field at the TM location must be inferred according to the information given by the magnetometer readings. We are interested in a robust method that works without previous knowledge of the spacecraft magnetic field environment. The reasons for this choice are that the expected local spacecraft field might be affected by possible changes of the magnetic characteristics of the spacecraft during launch or during the lifetime of the mission, by deviations from the on-ground performance,

and by varying operational modes in the spacecraft. Hence, methods making use of *a priori* knowledge, such as neural networks or Bayesian frameworks that yield remarkable results in similar estimation problems [48, 142, 90, 89], will not be considered here. Instead, in this work we adopt as our interpolation tool the multipole expansion technique based only on the magnetometer readouts. The results obtained using this method are then compared with other theoretical approaches, such as the Taylor series and the distance weighting interpolating methods. In the following sections we briefly describe the interpolation methods employed for this study.

5.2.1 Multipole expansion

Since the magnetic sources in the spacecraft are located far from the origin of the coordinate system (chosen at the center of the TM) and assuming the material inside the vacuum enclosure is basically non-magnetic, the magnetic field in this region can be considered to be essentially a *vacuum* field. This means

$$\boldsymbol{\nabla} \times \mathbf{B} = \boldsymbol{\nabla} \cdot \mathbf{B} = 0, \tag{5.1}$$

which follows that

$$\mathbf{B}(\mathbf{x}) = \boldsymbol{\nabla}\Psi(\mathbf{x}) \quad \text{and} \quad \boldsymbol{\nabla}^2\Psi(\mathbf{x}) = 0, \tag{5.2}$$

where $\Psi(\mathbf{x})$ is a scalar function. Hence, the estimated magnetic field $\mathbf{B}_{\mathrm{e}}$ obtained employing an array of N sensors can be written as the general solution to Laplace's equation centered at the TM, which can be expressed in terms of an expansion in spherical harmonics:

$$\mathbf{B}_{\mathrm{e}}(\mathbf{x}) = \sum_{l=1}^{L} \sum_{m=-l}^{l} M_{lm}(t)\, \boldsymbol{\nabla}[r^l\, Y_{lm}(\mathbf{n})], \tag{5.3}$$

where $r \equiv |\mathbf{x}|$ and $\mathbf{n} \equiv \mathbf{x}/r$ are the spherical coordinates of the field at $\mathbf{x}$. M_{lm} and Y_{lm} are the multipole coefficients and the standard spherical harmonics of degree l and order m, respectively [83].

The accuracy of the estimation of the magnetic field is given by the order of the expansion, which depends on the number of multipole coefficients that can be computed. Specifically, the accuracy of the interpolation is given by the number of known magnetic field measurements at the boundary of the volume where the field equations are considered. In our case these measurements are provided by the number of magnetometers placed in the spacecraft. Table 5.1 shows the minimum number of magnetometers required to model the magnetic field with a second, third and fourth order multipole expansion.

Table 5.1: Order of the multipole expansion, number of multipole coefficients and number of needed magnetometers. The number of triaxial magnetometers (last column) necessary to achieve the desired order satisfies the condition $3 \cdot N \geq L(L+2)$.

Expansion order L	Equivalent multipole	# of M_{lm} coefficients $L(L+2)$	# of triaxial magnetometers N
2	Quadrupole	8	3
3	Octupole	15	5
4	Hexadecapole	24	8

The coefficients M_{lm} are found by minimizing the equation $\partial \varepsilon^2 / \partial M_{lm} = 0$, where the square error is defined as

$$\varepsilon^2(M_{lm}) = \sum_{s=1}^{N} |\mathbf{B}_{\mathrm{m}}(\mathbf{x}_s) - \mathbf{B}_{\mathrm{e}}(\mathbf{x}_s)|^2 , \tag{5.4}$$

$\mathbf{B}_{\mathrm{m}}$ is the readout of the triaxial magnetometer, and N is the total number of magnetometers. This is done by employing a least-squares method. Once the system of equations is solved, the computed coefficients M_{lm} can be inserted into equation (5.3), replacing the magnetometer's position, $\mathbf{x}_s$, by the TM position, $\mathbf{x}_{\mathrm{TM}}$, to finally obtain the value of the interpolated field at the TM location.

5.2.2 Taylor series

The magnetic field at the TM position inferred from the readings of the magnetometers can also be approximated by a Taylor expansion. As in the case in which the multipole expansion is employed, the order of the Taylor series is determined by the number of magnetometer data channels. In this case the magnetic field at the position of the TMs can be approximated by the following expression:

$$\mathbf{B}_{\mathrm{m}}(\mathbf{x}_s) = \mathbf{B}_{\mathrm{e}}(\mathbf{x}_{\mathrm{TM}}) + \sum_{n=1}^{L} \sum_{i=1}^{3} \frac{\partial^n \mathbf{B}_{\mathrm{e}}(\mathbf{x}_{\mathrm{TM}})}{\partial x_i} \frac{(x_{s,i} - x_{\mathrm{TM},i})^n}{n!}, \tag{5.5}$$

where the origin of coordinates is defined at the center of the respective TM ($\mathbf{x}_{\mathrm{TM}}$), and $\mathbf{x}_s$ are the magnetometer locations. $\mathbf{B}_{\mathrm{e}}(\mathbf{x}_{\mathrm{TM}})$ and $\partial^n \mathbf{B}_{\mathrm{e}}(\mathbf{x}_{\mathrm{TM}})/\partial x_i$ are calculated considering that the magnetic field around the TM has both zero divergence and curl, i.e. the magnetic field gradient tensor $\nabla^n \mathbf{B}$ is a symmetric traceless matrix. Thus, only a total of 5 independent components needs to be computed.

5.2.3 Distance weighting

This method consists in computing the field as a weighted sum of the different magnetometer readings. The calculation is performed as follows:

$$\mathbf{B}_{\mathrm{e}} = \sum_{s=1}^{N} a_s \mathbf{B}_{\mathrm{m}}(\mathbf{x}_s), \tag{5.6}$$

where $\mathbf{B}_{\mathrm{m}}(\mathbf{x}_s)$ are the readouts of the magnetometers. The weighting factors a_s are given by:

$$a_s = \frac{1/r_s^n}{\sum_{i=1}^{N} 1/r_i^n}, \tag{5.7}$$

where n specifies the order of the interpolation and r_i are the distances between the point at which the field must be estimated and the specified magnetometer.

5.3 Magnetic sources and sensor layout

We first note that the interplanetary dc field is expected to be more than one order of magnitude weaker than the sources of the magnetic field present inside the spacecraft [167]. By design, there are not any sources of magnetic field inside the vacuum enclosure cylinder. Since the distribution of the different subsystems in eLISA is not fully defined yet, the distribution of the magnetic sources in the spacecraft is not known. However, in order to provide a realistic scenario to assess the performance of our proposed interpolation methods, we have made the following assumptions. We first assume that the magnitude and location of the magnetic sources are the ones measured for LISA Pathfinder (see Appendix F for details). Moreover, we also assume that the sources of magnetic field can be modeled as point magnetic dipoles. With these premises, a batch of 10^3 different magnetic realizations is generated using the fixed locations and magnitudes of the magnetic field of the sources, but with orientations randomly drawn according to normal distributions for each of the components.

The adequate location and number of magnetometers stem from a trade-off between the accuracy of the reconstruction of the magnetic field map and the magnetic disturbances generated by the magnetometer itself on the TM region. In order to quantify the effect of the sensors, the magnetic moment of an AMR was measured with a Superconducting Quantum Interference Device (SQUID) for different configurations. As explained in Chapter 4, our analysis based on the SQUID measurements shows that symmetrical placements with four and eight sensors are the preferred options in order to minimize the magnetic back-action effects. Moreover, when eight sensors are allocated in a symmetrical configuration on the walls of the vacuum enclosure, their contribution to the magnetic budget is negligible [121]. Figure 5.1
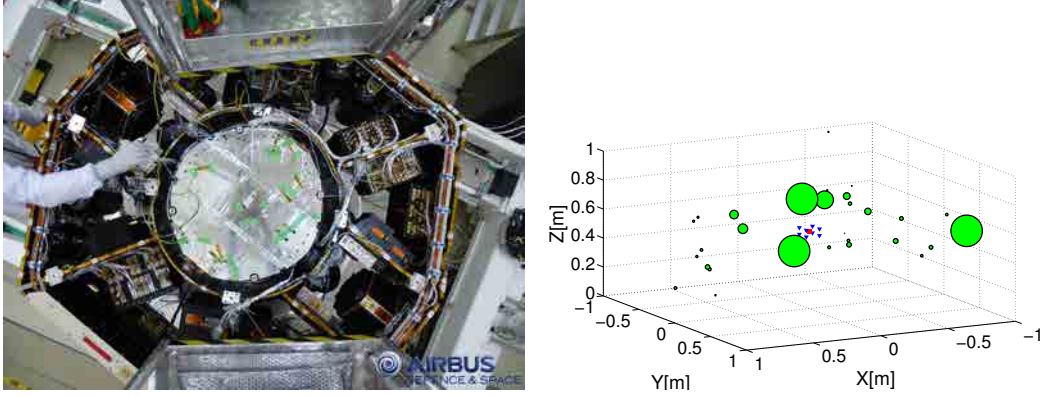
Figure 5.1: Left: flight models units on board the LISA Pathfinder spacecraft. Credits: Airbus DS. Right: a view of the 29 measured dipole magnetic sources (green dots: the size is proportional to their magnetic moment), the test mass (red square) and the eight AMR magnetometers (blue triangles).

displays the distribution of the sources of the magnetic field in the LISA Pathfinder spacecraft and the eight-sensor layout that is being considered in the current analysis for eLISA. The sensor array configuration on the vacuum enclosure is also shown in Figure 4.1. Additionally, a magnetometer's noise floor of $\sim 150\,\text{pT}\,\text{Hz}^{-1/2}$ [120] (see Chapter 3) was considered in the analysis. Accordingly, to mimic the electronic noise of the system, this noise is added to the simulated readouts of the magnetometers.

Finally, in order to assess the performance of each of the interpolating methods, the interpolated magnetic field is compared with the exact one, assuming that the different magnetic sources behave as point dipoles. Then, the total magnetic field generated by the sources can be calculated as

$$\mathbf{B}(\mathbf{x}) = \frac{\mu_0}{4\pi} \sum_{a=1}^{n} \frac{3(\mathbf{m}_a \cdot \mathbf{n}_a)\mathbf{n}_a - \mathbf{m}_a}{|\mathbf{x} - \mathbf{x}_a|^3}, \tag{5.8}$$

where $\mathbf{m}_a$ are the magnetic dipolar moments measured for the different subsystems, $\mathbf{x}_a$ are the source positions, $\mathbf{n}_a$ are the unit vectors directed from $\mathbf{x}_a$ to $\mathbf{x}$, and n is the number of sources. The expression for the magnetic field gradient is given in Eq. (4.5).

5.4   Results

5.4.1   Reconstruction of the magnetic field

As previously stated, to validate the performance of the reconstruction algorithm, a batch of dipoles with randomly generated orientations were simulated and the exact magnetic field for each one of these realizations was compared with the interpolated

results. The left panel of Figure 5.2 shows the x-component of the magnetic field map produced by one of these random configurations. The results are then compared in the right panel with those obtained when using one of our interpolating methods. In this case, the magnetic field reconstructed using multipole expansion. As seen in section 5.2, a multipole expansion based only on eight triaxial magnetometers readings is able to resolve the magnetic field up to the hexadecapole structure, by computing 24 terms in Eq. (5.3). Overall, the interpolated field qualitatively resembles the exact magnetic field, although there are apparent differences far from the positions of the TMs. However, note that the success of the reconstruction method is determined by the accuracy achieved at the region of interest, i.e. at the TM locations. We perform a more quantitative analysis for the three components of the field below.
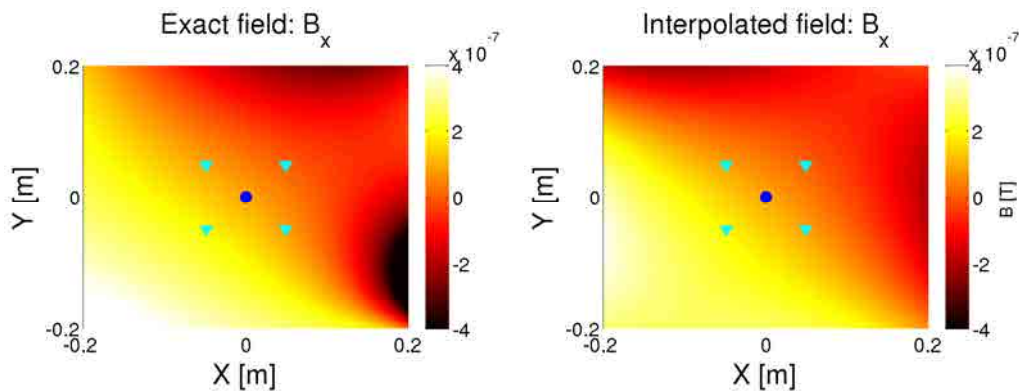
Figure 5.2: Contour plot of the exact (left) and reconstructed (right) magnetic field B_x for a given source dipole configuration using multipole expansion with eight magnetometers. The positions of the eight magnetometers (cyan triangles) and of the test mass (blue circle) are also represented.

The differences (in percentage) between the interpolated field and the source dipole model field are shown in Figure 5.3. Contour plots for the three components and the modulus show the accuracy achieved by the multipole algorithm. As can be seen in this figure, the smallest differences occur in the region enclosed by the magnetometers. Moreover, the accuracy of the interpolating algorithm is good in the central area of the electrode housing, where the TM is located.

To further confirm the validity and general applicability of the multipole expansion, we compared the differences between the interpolated and exact magnetic fields at the position of the TM for three different sensor layouts. Specifically, we first adopted the LISA Pathfinder configuration. In this layout fluxgate magnetometers are used, as depicted in Figure 2.2. In a second step we did the same, but adopting four AMRs placed around the vacuum enclosure at the height of the electrode housing center. Finally, we carried out the same calculation, this time adopting eight AMRs as graphically displayed in Figure 5.1. Average and maximum field errors rel-
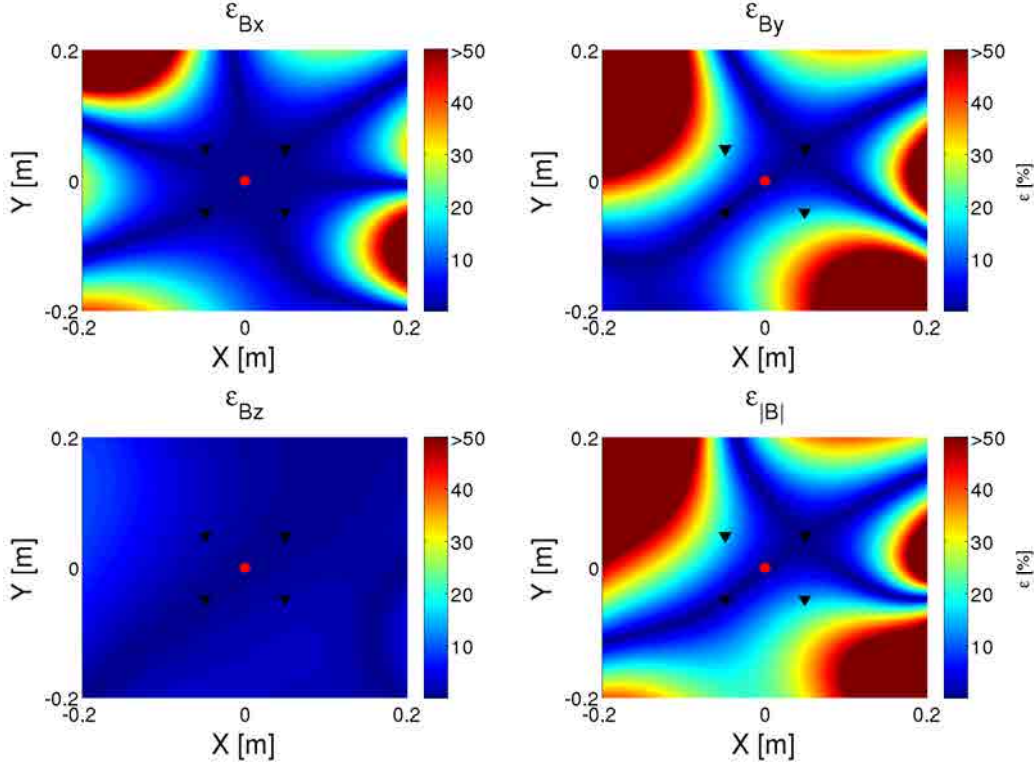
Figure 5.3: Relative errors in the estimation of the magnetic field components and the modulus. To calculate the relative error for each field component, the absolute error is divided by the modulus of the exact value in order to avoid infinities when one of the vector components is close to zero $\varepsilon_{Bx} = (B_{r,x} - B_{e,x})/|\mathbf{B}_r|$.

ative to the modulus ($\overline{\varepsilon}_{|\mathbf{B}|}$ and $\varepsilon_{|\mathbf{B}|,max}$) and to the field components ($\overline{\varepsilon}_{B_i}$) over the 10^3 random runs are shown in table 5.2. In the LISA Pathfinder configuration the accuracy of the reconstructed field at the TM is poor and presents large variations when the multipole expansion is used. In particular, the estimation errors can be as high as 737%. This is the natural consequence of having placed the sensors too far from the center of the TM. Instead, when AMRs are used, the sensors can be placed much closer to the center of the TM, due to their smaller size and intrinsic magnetic moment. The results when the same number of magnetometers is employed show significant improvements, with maximum errors up to 15%. Finally, the estimation errors are reduced by a factor of ~ 6 ($\varepsilon_{|\mathbf{B}|,max} = 2.4\%$) when eight sensors are used. In this case the hexadecapole expansion is employed, and this obviously results in an improved performance of the interpolating algorithm. Last, in Figure 5.4 the distribution of the estimation errors for the randomly simulated cases is shown. This figure clearly shows that the standard deviations are $\leq 1.1\%$ and $\leq 0.18\%$ for the

Table 5.2: Relative errors of the magnetic field estimation at the positions of the TM. $\overline{\varepsilon}_{|\mathbf{B}|}$ and $\overline{\varepsilon}_{B_i}$ are the mean error for a batch of 10^3 randomly orientated magnetic sources relative to the modulus $|\mathbf{B}|$ and to the field component B_i, respectively. The denominator in $\overline{\varepsilon}_{B_i}$ is closer to zero than that of the modulus $\overline{\varepsilon}_{|\mathbf{B}|}$, and this translates in larger errors for the former.

Error	**LPF** (4 Fluxgates)				**eLISA** (4 AMRs)				**eLISA** (8 AMRs)			
[%]	B_x	B_y	B_z	$|\mathbf{B}|$	B_x	B_y	B_z	$|\mathbf{B}|$	B_x	B_y	B_z	$|\mathbf{B}|$
$\overline{\varepsilon}_{|\mathbf{B}|}$	38.2	28.1	20.9	32.5	1.4	1	1.1	1.8	0.1	0.2	0.1	0.1
$\varepsilon_{|\mathbf{B}|,\max}$	737.7	340.3	327.6	803.2	15.0	7.7	14.0	13.3	0.9	2.4	1.4	2.0
$\overline{\varepsilon}_{B_i}$	697.9	202.1	184.5	32.5	13.7	3.8	7.8	1.8	0.6	0.8	5.3	0.1
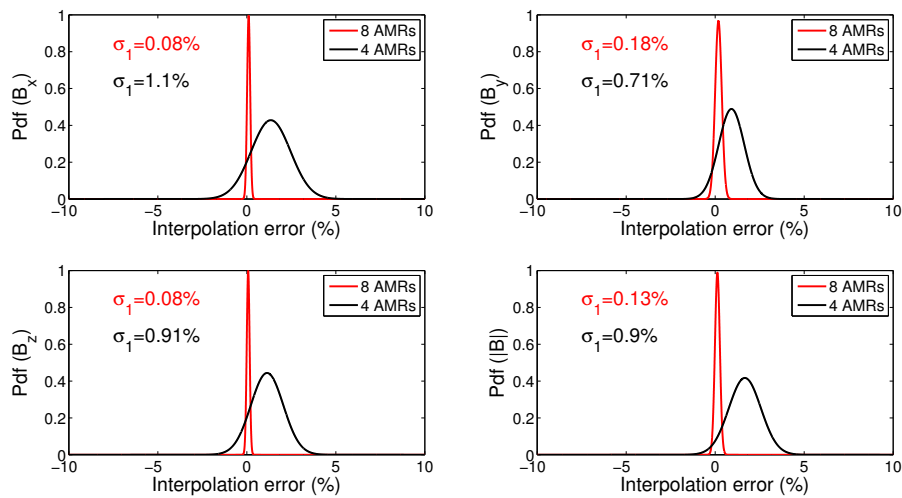
Figure 5.4: Distributions of the relative errors at the TM position for $N = 10^3$ random cases for four (black) and eight (red) AMR sensors.

4-AMR and 8-AMR layouts, respectively. This proves that the averaged estimation errors ($\overline{\varepsilon}_{|\mathbf{B}|} \leq 0.2\%$) are robust and that the performance of the multipole interpolating algorithm is good, providing reliable estimated values of the magnetic field at the location of the TM.

The results described so far were obtained by using the multipole expansion algorithm. However, other interpolation schemes were detailed in Section 5.2, and their performances were compared with that of the multipole expansion in Table 5.3. The order of the interpolation in the distance weighting method is set to $n = 1$. Nevertheless, this choice is not relevant due to the physical symmetry of the sensor placement, i.e., the distances r_s, and consequently the weighting factors a_s, are equivalent for the eight magnetometers. For the Taylor expansion, the second and the higher-order

terms are negligible due to the symmetry of the magnetic distribution. Thus, the Taylor approach mainly estimates the magnetic field as a linear approximation. For this reason, we expect the results of the interpolation to be almost identical to those obtained using the distance weighting method. Table 5.3 shows the accuracies of the estimation of the magnetic field at the position of the TM for the three methods employed in this work. As can be seen, the multipole expansion outperforms by far the rest of the methods described previously.

Table 5.3: Maximum errors of the estimated magnetic field at the position of the TM using different interpolation methods.

Method	$\varepsilon_{|\mathbf{B}|,\max} [\%]$			
	B_x	B_y	B_z	$|\mathbf{B}|$
Distance weighting	8.0	4.0	7.7	7.9
Taylor expansion	8.0	4.0	7.7	7.9
Multipole expansion	0.9	2.4	1.4	2.0

5.4.2 Reconstruction of the magnetic field gradient

Magnetic field gradients also need to be estimated from the readouts of the 8 AMRs. We do this by using the multipole expansion algorithm because, as demonstrated earlier, this interpolating method outperforms the other two methods studied here. For the sake of clarity, only the errors of the gradient interpolation for two components ($\partial B_x/\partial x$ and $\partial B_z/\partial x$) along the spacecraft are shown in Figure 5.5. In this case, minimum errors are also obtained in the center of the TM, though unlike that obtained for the case of the magnetic field, the error increases somewhat faster in the region outside the boundary of the area surrounding the magnetometers. Additionally, relative errors around the TM area are slightly larger than those found for the reconstruction of the magnetic field, although they remain lower than 3%. Figure 5.6 shows the distribution of the estimation errors and standard deviations for five independent components of the gradient matrix $\nabla\mathbf{B}$ at the position of the TM. Inspection of this figure reveals that the multipole expansion scheme is robust. In particular, when this interpolation is used, we obtain not only accurate values of the reconstructed magnetic field, but also of its gradient, with typical accuracies of the order of 2%, and deviations below 2.5% respectively.

5.4.3 Other sources of error

Absolute errors and drifts of the magnetometer readings are relevant to interpolation quality, since the algorithm is entirely based on the magnetometer outputs. Due to the stringent stability requirements for eLISA, drifts of the measurements are not critical. Thus, the analysis is focused on absolute errors. To validate the robustness
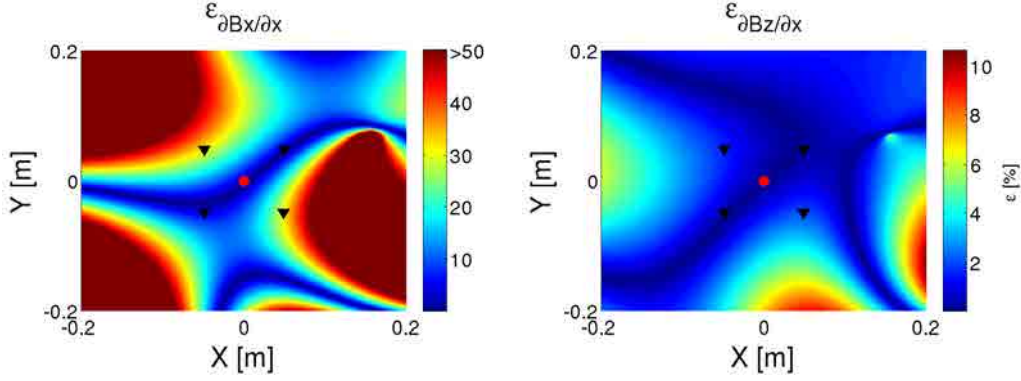
Figure 5.5: Relative errors in the estimation of the magnetic field gradient for a particular source dipole configuration. We only show two components, $\partial B_x/\partial x$ and $\partial B_z/\partial x$. The relative error is computed as $\varepsilon_{\partial B_i/\partial j} = (\partial B_{\mathrm{r},i}/\partial_j - \partial B_{\mathrm{e},i}/\partial_j)/|\partial \mathbf{B}_{\mathrm{r}}/\partial_j|$. Note the different scale for the error bars.
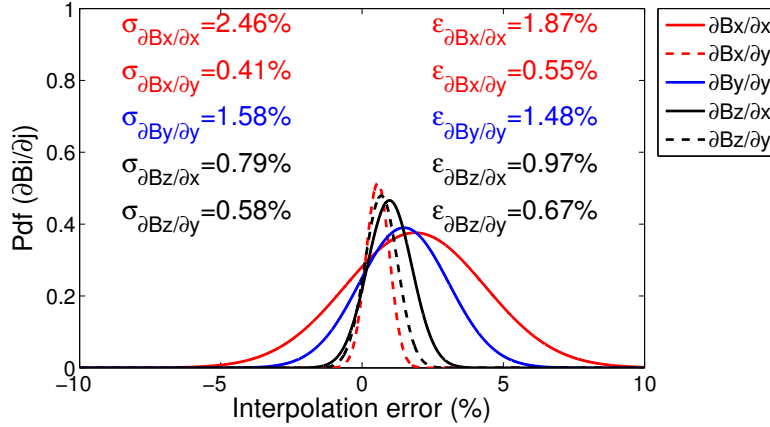
Figure 5.6: Probability density function of the relative errors at the TM position for 10^3 random cases. Five independent terms in the field gradient matrix ($\partial B_x/\partial x$, $\partial B_x/\partial y$, $\partial B_y/\partial y$, $\partial B_z/\partial x$ and $\partial B_z/\partial y$) are considered. Standard deviations and averaged errors relative to the modulus ($|\partial \mathbf{B}/\partial \mathbf{x}|$ and $|\partial \mathbf{B}/\partial \mathbf{y}|$) are shown.

of the system, the performance of the multipole expansion scheme is studied for two common sources of error. Namely, possible offsets in the magnetometer readings and spatial uncertainty — that is, deviations from the nominal position of the sensor core. We analyze their eventual effects separately. Offsets in the magnetometer or in the signal conditioning circuit can be measured on-ground and considered in the analysis. However, unknown magnetometer offsets due to launch stresses can lead to inaccurate field determination [150]. The precision of the position of the sensors may eventually be another source of error that cannot be ignored during the analysis.
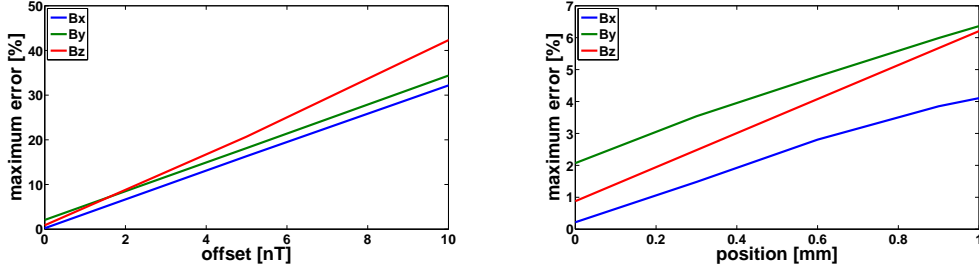
Figure 5.7: Maximum estimation errors of the magnetic field as a function of the offset (left) and spatial uncertainty (right) of the magnetometers.

Spatial uncertainty depends on the size of the sensor head, since smaller heads result in a smaller uncertainty of the precise location of the measurement.

The offsets of the magnetometers can be relevant depending on the measurement technique. In particular, for AMR sensors, flipping signals applied to the sensor help to overcome the offset by reversing the sensor magnetization and modulating the output signal [72]. The changes in the direction of the sensor magnetization lead to inversion of the output characteristics but not the offset, which can be canceled by subtracting the measurements between each flipping pulse. Regarding the spatial uncertainty, the layout of the thin film forming the AMR Wheatstone bridge [77] is deposited by a sputtering process, and has a rough area of $0.9\,\mathrm{mm} \times 1.2\,\mathrm{mm}$. Therefore, a spatial uncertainty smaller than $1\,\mathrm{mm}$ is expected.

The impact of these effects on the accuracy of the multipole expansion algorithm is simulated as follows. First, a $3 \times N$ matrix of offsets is randomly generated according to a uniform distribution with an interval of $[-B_{\mathrm{offset}}, B_{\mathrm{offset}}]$. Secondly, the offset array is added to the $3 \times N$ magnetic channels readings, and finally the magnetic field and errors are estimated. These steps are sequentially repeated for series of 10^3 random offsets with intervals of the same length. A similar procedure is done to assess the robustness of the interpolation to the uncertainty in the location of the sensor heads. The maximum estimation errors as a function of the offset and of the spatial uncertainty are shown in Figure 5.7. As can be observed, the offset of the sensor is more determinant than its spatial resolution. Specifically, for an unpredictable non-measured offset of $10\,\mathrm{nT}$, the maximum estimation error is $\sim 42\%$. These results reflect the relevance of the magnetic sensing technology. Definitely, we stress that appropriate techniques to cancel out the undetermined offset and the use of tiny sensors with accurate spatial resolution are totally necessary.

92

5.5   Conclusion

This new AMR-based sensor arrangement leads to a reliable estimation of the magnetic field and its gradient at the positions of the test masses. Actually, the multipole expansion scheme used in combination with the proposed eight-sensor configuration will represent a reduction of the magnetic field estimation error of more than two orders of magnitude when compared to the solution implemented in LISA Pathfinder (after using the same algorithm). Besides, we have shown that the estimation errors computed for different simulated magnetic scenarios employing the multipole expansion interpolation provides a robust algorithm that does not need any *a priori* knowledge of the magnetic structure in the spacecraft. Also, in addition to these significant advantages, the proposed system has the ability to deliver correct results under unpredictable offsets of the magnetometer readings, and to overcome reasonable imprecisions in the spatial location of the magnetometers. All in all, these improvements in the accuracy of the magnetic field reconstruction are achieved due to the smaller size and lower magnetic back-action of the AMR sensors, which enable more sensors to be placed and for them to be located closer to the TMs. This is a promising result that proves that the use of AMRs combined with the multipole expansion will provide a reliable estimate of the magnetic characteristics at the positions of the test masses of eLISA.

Chapter 6

Low-Frequency Noise Characterization of an Atomic Magnetometer

Noise measurements have been carried out within the LISA bandwidth ($0.1\,\mathrm{mHz}$ - $100\,\mathrm{mHz}$) to characterize an all-optical atomic magnetometer based on nonlinear magneto-optical rotation. This was done in order to assess if the technology can be used for space missions with demanding low-frequency requirements like the eLISA concept. Magnetometry for low-frequency applications is usually limited by $1/f$ noise and thermal drifts, which become the dominant contributions at sub-millihertz frequencies. Magnetic field measurements with atomic magnetometers are not immune to low-frequency fluctuations and significant excess noise may arise due to external elements, such as temperature fluctuations or intrinsic noise in the electronics. In addition, low-frequency drifts in the applied magnetic field have been identified in order to distinguish their noise contribution from that of the sensor. We have found the technology suitable for eLISA in terms of sensitivity, although further work must be done to characterize the low-frequency noise in a miniaturized setup suitable for space missions.

6.1   Introduction

The noise performance of a magnetic measurement system is usually limited by the low-frequency characteristics. Hence, magnetometers and optimized electronics need to be assessed in the LISA bandwidth, since at sub-mHz frequencies, sensor noise is generally dominated by the $1/f$ contribution and thermal drifts. Previous studies on this subject were carried out with magnetoresistance-based magnetometers (see Chapter 3), suggesting the technology as a potential option for eLISA [124, 122]. We are currently investigating sensors based on alkali-vapor cells [36] as an alternative

to fluxgate magnetometers, which are commonly employed in space applications. Alkali-vapor magnetometers are absolute sensors, since the spin-precession frequency is related to the magnitude of the field by fundamental constants. In this regard, they are unlike fluxgates and magnetoresistances, which measure small changes in the field but not its actual value without precise calibration. Therefore, it is plausible that atomic magnetometers might be better for low-frequency applications. Theoretically, their sensing elements are not subject to intrinsic $1/f$ noise, although in practical situations, there are noise sources that might be relevant at very low frequencies:

- Drifts in the power, wavelength, or polarization of the pump and probe lasers. These parameters determine the "light shift", a light-induced shift in the alkali Zeeman energy sublevels which can mimic the effects of an applied magnetic field [125, 41].

- Shifts due to changing cell temperature or alkali-vapor density. Alkali density fluctuations will affect attenuation of the beams within the vapor, affecting the overall light shift.

- Drifts in the phase or duty cycle of the pump laser waveform.

- Intrinsic noise and temperature dependence of the electronics.

- Changes in the stray magnetic field stemmed from the components surrounding the vapor cell.

By definition, the latter is not categorized as magnetometer noise. Nevertheless, it is crucial to disentangle the influence of magnetic-field drifts so that we may study the intrinsic sensor noise. It is important to remark that eLISA is a demanding mission in terms of low-noise/low-frequency concepts. For these reasons, the study below the corner frequency of the $1/f$ noise is critical and it differs from the wide-band applications, where usually only the noise floors are of concern. Some of the estimates we performed are based on the $1/f$ behavior, which is characterized by the white-noise floor and the corner frequency. Other parameters also critical in the low-frequency band, such as ambient temperature fluctuations, are derived from laboratory measurements.

6.1.1 Atomic magnetometry: preferred techniques

Atom-based magnetometers are the most sensitive devices to measure magnetic fields. Furthermore, they do not need the bulky and expensive cryogenic refrigeration required in superconducting quantum interference devices (SQUIDs). The spin-projection-noise-limited sensitivity δB_{SNL} of an atomic magnetometer during a measurement period T is given by

$$\delta B_{\mathrm{SNL}} \simeq \frac{1}{\gamma \sqrt{N\,\tau\,T}}, \tag{6.1}$$

where γ is the gyromagnetic ratio of the atoms and δB_{SNL} scales with the size and temperature of the cell by means of the coherence time τ and the total number of atoms N. Since the fundamental sensitivity limit of atomic magnetometers is much better than the required sensitivity for eLISA, we can trade off sensitivity for size/temperature of the cell, motivating the technology for space missions. Previous results assuming the spin-projection noise as the limiting noise source, suggest that magnetometer containing optimized cells with a size between $1\,\mathrm{cm}$ and $10\,\mu\mathrm{m}$ can reach noise levels around $1\,\mathrm{fT\,Hz^{-1/2}}$ and $10\,\mathrm{pT\,Hz^{-1/2}}$, respectively. The optimal cell temperature may vary from room temperature for the largest cell to $110\,^{\circ}\mathrm{C}$ for the $10\,\mu\mathrm{m}$ cell [171].

Various techniques to measure the Larmor precession frequency Ω_{L} of atomic spins have achieved excellent sensitivities at room temperature, although most of these techniques have been studied at higher frequencies ($\geq 0.1\,\mathrm{Hz}$). Our interest consists in the detection of small magnetic fluctuations in the low-frequency region and at ambient temperature. Hence, based on the experience with the development of the Magnetic Diagnostics for LISA Pathfinder, which was made up by a set of four triaxial fluxgate magnetometers and two coils, the main sensor selection criteria for eLISA are viability for miniaturization, small back-action effect on the spacecraft environment, and low noise in the millihertz region. Regarding the sensor noise, it was defined as $S_{B,\mathrm{system}}^{1/2} \leq 10\,\mathrm{nT\,Hz^{-1/2}}$ at $0.1\,\mathrm{mHz}$ (see Chapter 3). As an alternative in a more demanding scenario, sensor noise and frequency range shall be one order of magnitude lower than the LISA Pathfinder requirement ($10\,\mathrm{nT\,Hz^{-1/2}}$ at $1\,\mathrm{mHz}$). This implies a noise level in the measurement system of

$$S_{B,\mathrm{system}}^{1/2} \leq 1\,\mathrm{nT\,Hz^{-1/2}},\ \omega/2\pi = 0.1\,\mathrm{mHz}. \tag{6.2}$$

Nevertheless, interplanetary magnetic field fluctuations are expected to be at least two order of magnitude higher than this value [167, 25]. Therefore, the noise level defined in Eq. (3.1) is considered sufficient to discern the environmental field fluctuations in the spacecraft.

Chip-scale magnetometers based on magnetic-resonance phenomena can be driven either with radio frequency (RF) fields or with modulated light. A coil-driven magnetometer with micro-fabricated vapor cell has demonstrated noise levels of $5\,\mathrm{pT\,Hz^{-1/2}}$ for a bandwidth from 1 to $100\,\mathrm{Hz}$ [169]. However, the magnetic field created by the RF coils for this method could constitute a potential source of disturbances to the performance of eLISA [121]. A similar noise level has been measured in a frequency-modulated Bell-Bloom magnetometer (FM-BB), using millimeter-scale cells as well [86, 24]. For the two previous arrangements the cell needs to be heated to create sufficient atomic density for the measurement, which could also be detrimental for the quiet thermal environment required in the TM region ($\leq 100\,\mu\mathrm{K\,Hz^{-1/2}}$ at $1\,\mathrm{mHz}$ for LISA Pathfinder) [65]. In this chapter we study the low-frequency noise in a magnetometer prototype based on nonlinear magneto-optical rotation (NMOR)

in a cm-scale cell [6, 35], which retains the all-optical excitation with the advantage that the vapor cell is at room temperature and heaters are not utilized [24]. The principle of operation of the magnetometer is described in Figure 6.1.
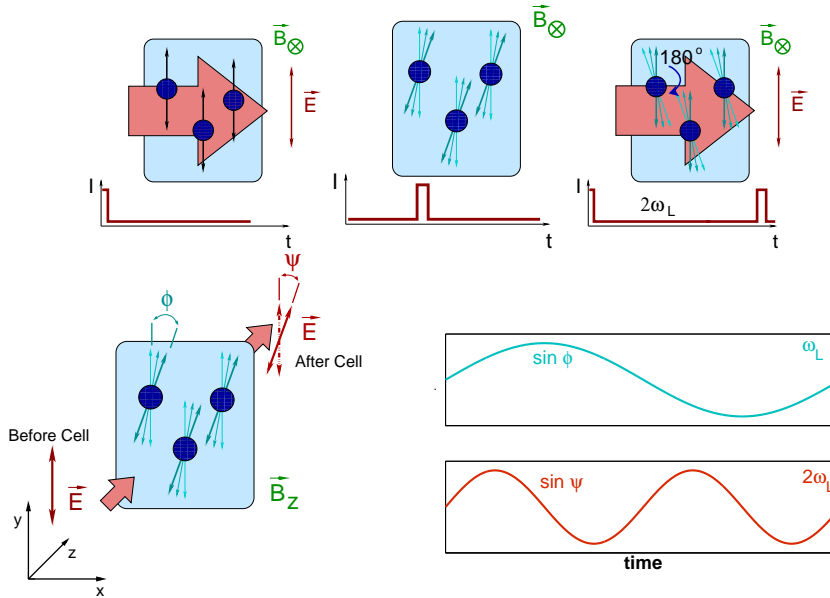
Figure 6.1: Principle of operation of an all-optical atomic magnetometer using nonlinear magneto-optical rotation. The interaction of a polarized laser pulse (pump beam) with a sample of atoms produces an optically anisotropic medium, which is aligned along the electric field of the pump light (top left). The atomic spins precess around the magnetic field changing the optical anisotropy (top center). The pump beam is synchronously applied at the double of the precession frequency ($2\Omega_L$) to reinforce the macroscopic moments oscillations and avoid the fast depolarization rate of the atoms. The pump pulses drive the coherent precession of the atoms about the magnetic field (top right). For the optical detection, a continuous linear polarized laser (probe beam) interacts with the medium and the polarization plane of the probe beam rotates due to the Faraday effect (Bottom left). The maximum rotation occurs when the atomic spins alignment makes 45º with respect to the light polarization (Bottom right).

In Section 6.2 we discuss the test setup using nonlinear magneto-optical rotation with amplitude-modulated light (AM-NMOR). In Section 6.3 we analyze the noise contributions of two important circuits for the magnetic field measurements in the experiment. The experimental results are shown in Section 6.4 and, finally, the main conclusions of the work are summarized in Section 6.5.

6.2   Magnetometer setup using AM-NMOR

The sensor core is a 1 cm diameter and 3 cm long cylindrical antirelaxation-coated cell containing ^{133}Cs atoms (see Figure 6.4). The light of a distributed-feedback (DFB) laser [55] is split into a two-beam arrangement with linearly polarized probe and pump light, and it is frequency stabilized near the D_2 line by means of a dichroic-atomic-vapor laser lock (DAVLL) [193, 93]. The linearly polarized pump beam is square-wave modulated with a 10% duty cycle at a frequency of $\sim 2\Omega_L$ in order to generate atomic alignment [10]. This amplitude modulation is provided by an acousto-optic modulator (AOM) with a RF of 80 MHz such that it drives the coherent precession of the atoms about the external magnetic field to be measured [22]. The continuous probe and modulated pump beam pass through the vapor cell with approximately the same time-averaged light power of $\sim 1\,\mu W$. Finally, the amplitude of the probe optical rotation is measured with a balanced polarimeter at the modulation frequency Ω_m, where the current difference between the two silicon photodiodes (OSD 15-0) is changed to voltage by a transimpedance amplifier (TIA) and is then demodulated with a phase-sensitive detector. The experimental schematic is shown in Figure 6.2.
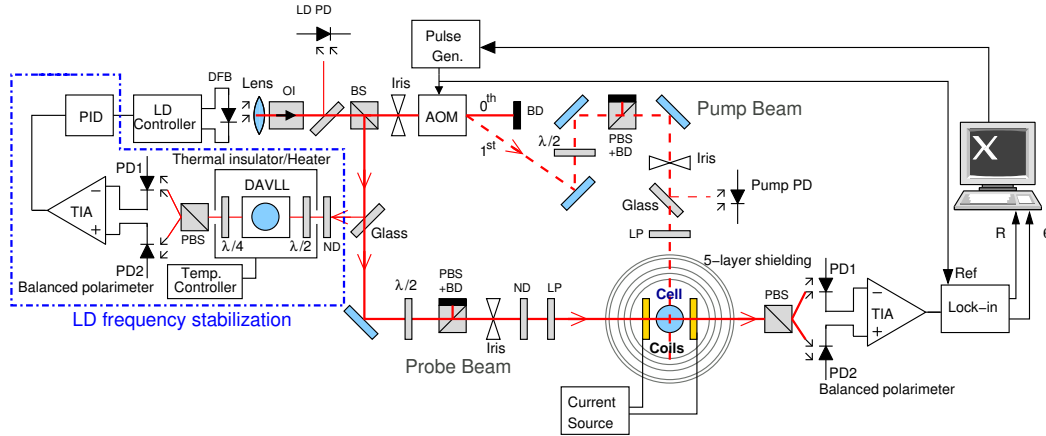
Figure 6.2: Schematic layout for the atomic magnetometer experiment. DFB, distributed feedback laser; OI, optical isolator; (P)BS, (polarizing) beam splitter; AOM, acousto-optic modulator; BD, beam dump; $\lambda/2$, half-wave plate; $\lambda/4$, quarter-wave plate; PD, photodiode; LP, linear polarizer; ND, neutral density filter; DAVLL, dichroic-atomic-vapor laser lock; TIA, transimpedance amplifier.

There are different ways to measure the magnetic-resonance frequency with the same setup: we can map out the whole resonance curve by stepping the modulation frequency, or we can make a single-point measurement of the dispersive trace near the center of the resonance. For the former open-loop method, the dynamic range and the measurement rate are limited by the narrow resonance and the slow scan of the
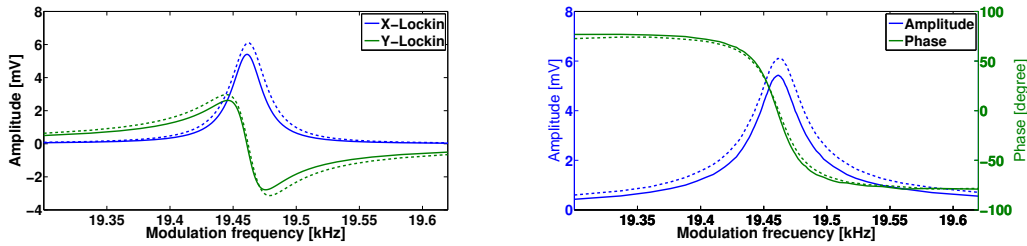
Figure 6.3: Changes in the resonance curve during the long-term measurements. The plots show the outputs of the lock-in amplifier as a function of the modulation frequency, before (dashed line) and after (solid line) a 12-h run. Traces show Lorentzian fits to the data. Left: absorptive (X) and dispersive (Y) components of the magnetic-resonance signal. Right: equivalent amplitude and phase.

resonance curve, respectively. The latter method requires a continuous closed-loop mode to keep the in-phase component locked, i.e., a digital controller that follows the null output of the quadrature component or the equivalent phase signal by tuning the frequency of the pulse generator which drives the modulation. This method of magnetometer operation is also useful to track slow drifts in the measured magnetic field. As can be seen in Figure 6.3, during long-term measurements (~ 12 h), the magnetic-resonance signal used to measure the Larmor frequency shows variations in the amplitude of the in-phase (absorptive) component, as well as the quadrature (dispersive) component obtained from the lock-in amplifier output. Barring fluctuations in the phase of the resonance, the zero-crossing of the dispersive term (at $\Omega_m = 2\Omega_L$) does not shift when either the amplitude or the width of the resonance changes. Such changes can arise from variations in the cell temperature or laser power.

For noise measurements, the Cs cell is placed inside a five-layer mu-metal shielding equipped with a solenoidal coil to apply a bias field along the probe-beam path (see Figure 6.4). An external field is applied to operate the magnetometer at a frequency higher than the linewidth of the resonance, where synchronous optical pumping is employed. Magnetic field fluctuations inside the shield can be caused by the thermal magnetization noise, Johnson noise currents within the magnetic shield itself and unshielded ambient magnetic field fluctuations, but they are not expected to be the dominant source in our measurement ($< 100 \, \text{fT} \, \text{Hz}^{-1/2}$) [36, 100, 92, 192]. One of the critical parts of the setup in the low-frequency band is the stability of the magnetic field created by the coils, which is mostly a requirement on the coil current source. Hence, special care needs to be taken in the design of the current source to prevent it from becoming the dominant noise contribution in the millihertz regime and obscuring the intrinsic noise of the sensor.

In order to address the equivalent magnetic field noise of the magnetometer, we record the setup parameters, namely power, wavelength, current and temperature
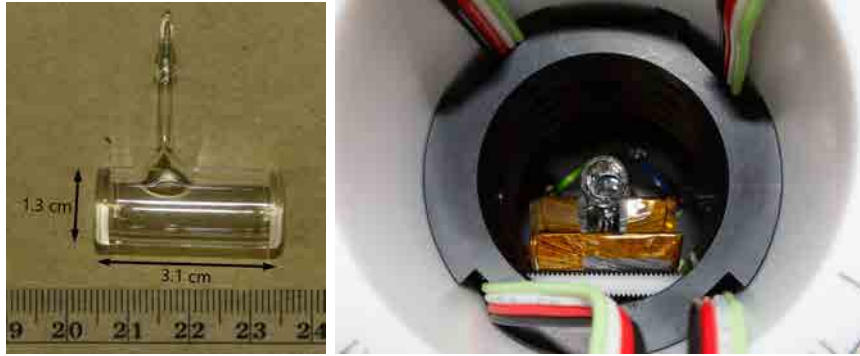
Figure 6.4: Dimensions of the ^{133}Cs cell with antirelaxation coating used in the experiment. Right: Alkali vapor cell allocated inside the five-layer mu-metal shielding.

of the laser diode, power of the pump light, current through the coil, room temperature and magnetic field, polarimeter outputs (single-sided and differential) and lock-in amplifier outputs. These measurements help us disentangle the different contributions in order to study the magnetometer noise, e.g., how the temperature drifts can affect the electronics.

As shown in Figure 6.5, the setup contains table-top optics in order to facilitate the optimization of the different parts and parameters of the experiment. However, future work will include efforts to miniaturize the magnetometer. The miniaturized design can be based on fully-integrated chip-scale magnetometers [169] or microfabricated remote sensor heads coupled to the laser and photodiodes through optical fibers [36]. The evident benefit of the first design is the possibility to include all the components in a single chip. By contrast, the advantage of the latter approach is to keep the cell clear of possible magnetic disturbances caused by the proximity of the laser and electrical connections. Besides, the second design is specially useful when an array of sensors is required since some parts can be shared, as for example the stabilized laser, the AOM and several optical elements.

6.3 Electronic noise contributions

As mentioned in Section 6.1, there are many potential sources of magnetic-resonance frequency drift and intrinsic noise in the magnetometer setup. In this analysis we focus on two circuits that need to be carefully designed in order to minimize their contribution to the resultant total noise. These circuits have been analyzed at two different frequencies. At millihertz scales, an important electronic noise contribution might be attributed to the leading-field current source. At higher frequencies $2\Omega_L$, the noise of the probe-beam polarimeter can dominate the noise floor; which is relevant to making measurements with high signal-to-noise ratio. The DAVLL also uses
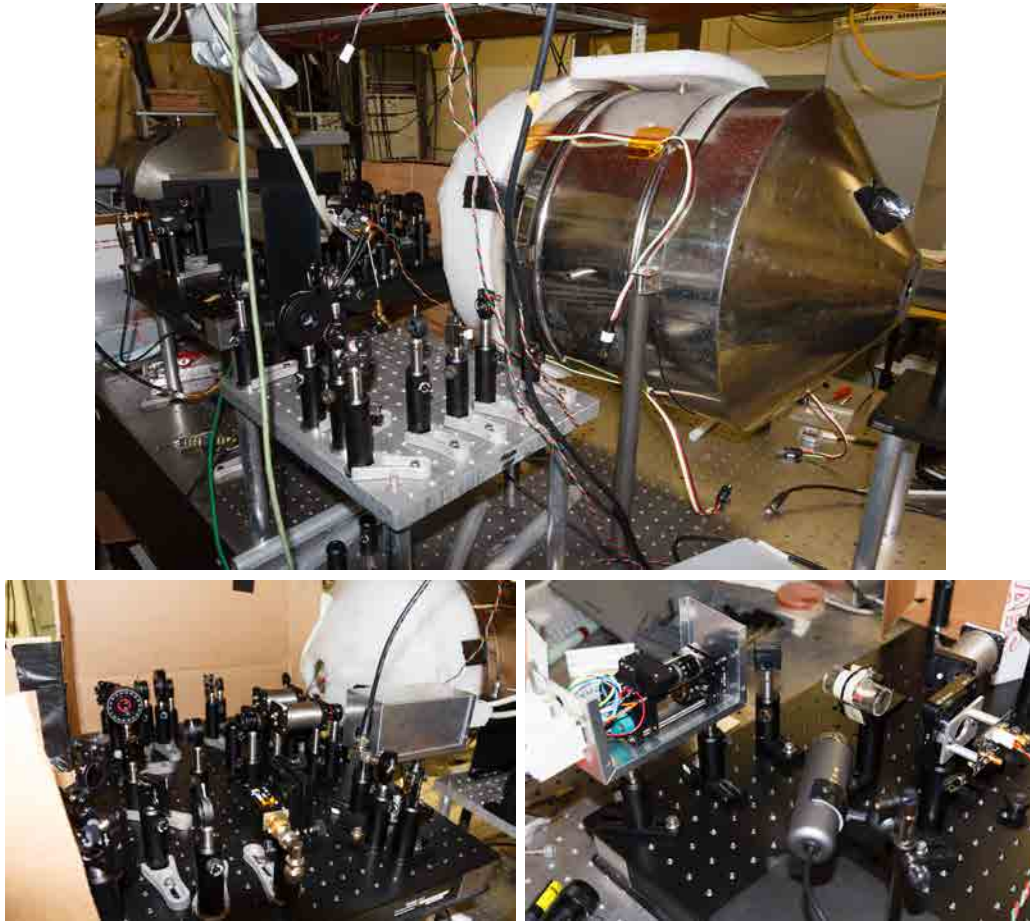
Figure 6.5: Physical implementation of the experimental setup at UC Berkeley. Top and bottom left: overview of the optical setup with the mu-metal shielding. Bottom right: setup for the current and temperature determination of the laser diode in order to obtain the Cs absorption. Cs D_2 line was found at $28.9\,°C$ and $112.5\,mA$ with a peak-to-peak modulated current of $10\,mA$.

a balanced polarimeter to provide an error signal which locks the laser to the atomic resonance. This signal is dc, so slow drifts in the electronic output of the DAVLL polarimeter can cause slow wavelength fluctuations in the laser, thus creating a time-varying light shift within the vapor. We are presently investigating this potential source of magnetometer noise but have reason to believe that it is small compared to the noise contributions studied here because the linearly polarized pump beam contributes a negligible systematic shift to the magnetic-resonance frequency [85]. Other than the two aforementioned circuits, the rest of the electronic boxes shown in Figure 6.2 have been selected from commercial instrumentation.

6.3.1 Equivalent magnetic field noise due to the leading-field current source

Among the different coil current source topologies that have been analyzed for the experiment, the floating-load current source shown in Figure 6.6 has been selected on the grounds of its slightly lower noise and better thermal performance. For the analysis, the noise sources that have been identified in the electronics are the input noise of the operational amplifier, the Johnson noise and the temperature coefficient (TC) in the resistors, as well as thermal dependences of the operational amplifier parameters. The latter are composed of the thermal drift in the bias current $\text{TC}(I_\text{B})$, offset current $\text{TC}(I_\text{OS})$ and offset voltage $\text{TC}(V_\text{OS})$ of the operational amplifier, and they can be neglected since their overall effect is much smaller $(0.03\,\text{pA}\,\text{K}^{-1})$ than the thermal effect of the resistance $(4.3\,\text{nA}\,\text{K}^{-1})$. Hence, the overall power spectral density of the current source S_{I_o} is approximated as

$$S_{I_\text{o}}(\omega) = S_{I_\text{o,noise}}(\omega) + \left(\frac{\partial I_o}{\partial T}\right)^2 S_T(\omega)$$

$$\simeq i_\text{n}^2 + \frac{1}{R_1^2}\left(e_\text{n}^2 + 4k_\text{B}TR_1 + e_\text{n,Vref}^2 + V_\text{ref}^2\alpha^2 S_T\right), \qquad (6.3)$$

where i_n and e_n are the op-amp current and voltage noise spectral densities, $4k_\text{B}R_1T$ is the Johnson noise component, k_B is the Boltzmann constant, $R_1 = 1\,\text{k}\Omega$ is the current source resistance, T is the temperature, $e_\text{n,Vref}$ is the voltage noise of the voltage reference, V_ref is the output of the voltage reference, $\alpha = 0.6\,\text{ppm}\,\text{K}^{-1}$ is the TC of the resistors and S_T is the room temperature fluctuations in power spectral density. All the terms in Eq. (6.3) are frequency dependent except the Johnson noise. Low-frequency noise in the voltage reference and operational amplifier was modeled by the corner frequency at which $1/f$ noise matches the white noise. We used the corner frequency and spectral densities given by the manufacturer, or by experimental data fit. Table 6.1 gives output noise parameters for the op-amp and voltage reference used in the current source.

Table 6.1: Output noise parameters for the components used in the constant current source. Voltage reference (VR) is based on the LTZ1000 Zener reference.

IC	e_n $[\text{nV}/\sqrt{\text{Hz}}]$	f_{c,e_n} $[\text{Hz}]$	i_n $[\text{pA}/\sqrt{\text{Hz}}]$	f_{c,i_n} $[\text{Hz}]$
OP27	3	2.7	0.4	140
VR	46	30	-	-
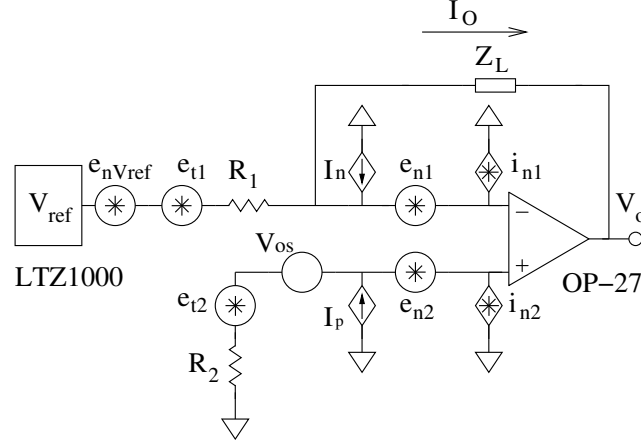
Figure 6.6: Floating-load current source with the main sources considered for noise estimation. Noise parameters for the op-amp and voltage reference are shown in Table 6.1. Manufactures specify $e_n^2 = e_{n1}^2 + e_{n2}^2$ and $i_n = i_{n1} = i_{n2}$.

A current of 7.1 mA is sent through the coil, producing a leading magnetic field of 2.8 μT. For this value of load, Figure 6.7 shows the estimated noise density for the selected floating-load source in comparison with three other classical topologies [62]. Figure 6.8 shows the calculated noise densities obtained for the selected current source, including the contribution due to the thermal fluctuations measured in the laboratory. In the figure, the excess noise due to the thermal dependences of the circuit is significant only below 0.1 mHz, and thus is outside the eLISA bandwidth. The equivalent magnetic field noise is found by multiplying the current noise expressed in Eq. (6.3) by the current-to-field conversion of the coil.

The theoretical noise is 25 nA Hz$^{-1/2}$ at 0.1 mHz, which corresponds to an equivalent magnetic field noise of 10 pT Hz$^{-1/2}$. This is well below the more demanding scenario for the magnetometer noise level in Eq. (6.2). The result implies that the designed current source achieves the performance required for the noise measurements of 0.1 nT Hz$^{-1/2}$ at 0.1 mHz, i.e., to be on the safe side, stability of the applied magnetic field must be at least one order of magnitude less noisy than the limit imposed by the magnetometer requirement or the expected noise of the magnetometer under study. The main source of technical noise in the whole bandwidth is the voltage reference. Hence, making use of low-noise voltage references [39] or batteries [40] will help to improve the noise performance significantly. By eliminating this technical noise, the equivalent magnetic field noise would be reduced to around 6.3 nA Hz$^{-1/2}$ (2.5 pT Hz$^{-1/2}$) at 0.1 mHz without any thermal insulator or active temperature controller.
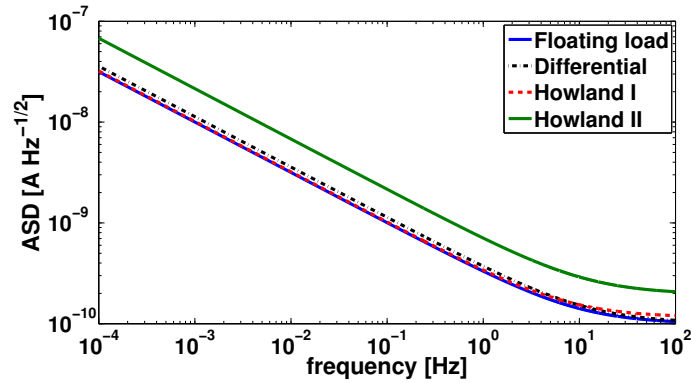
Figure 6.7: Current spectral density for floating-load, differential, classical Howland and improved Howland current sources (See Appendix B for more details). The voltage reference dominates the noise in the measurement bandwidth.
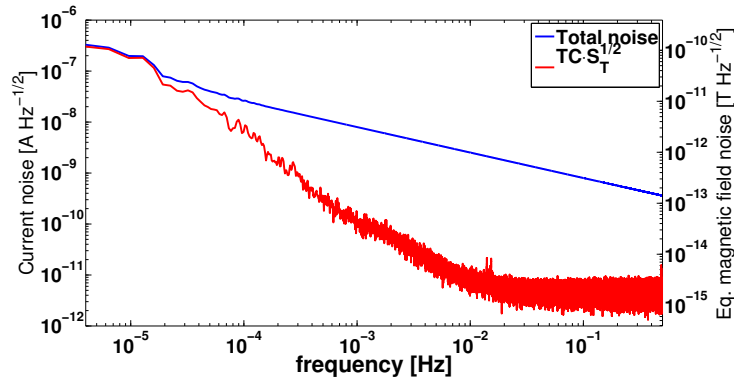
Figure 6.8: Current and magnetic field spectral densities for the floating-load current source (blue) and thermal contribution due to the current source's TC (red). Equivalent magnetic field noise is obtained for a current-to-field ratio of $\sim 392\,\text{nT/mA}$.

6.3.2   Polarimeter noise analysis

The polarimeter circuit is a two-stage amplifier formed by a conventional TIA topology and a non-inverting amplifier in the second stage. The differential signal resulting from the rotation of the light polarization, that is, the difference of the current from two photodiodes, is converted to voltage with a sensitivity of $11\,\text{mV/nA}$. The differential photocurrent induced by the probe rotation is modulated at $2\Omega_{\text{L}}$, so it is the noise floor of the polarimeter at this frequency which determines the magnetometer's sensitivity. This frequency can range from the $\sim$Hz scale to hundreds of kHz at Earth's field. For the eLISA mission the magnetic-resonance frequency will possibly

105

be around hundreds of Hz, although the information available so far is not definitive and a wider range needs to be considered. In any case, the low-frequency analysis is important to study the corner frequency of the $1/f$ noise, since it could be within the bandwidth of modulation.

The polarimeter circuit including the same intrinsic noise sources as in Section 6.3.1 is shown in Figure 6.9. The expected noise for the two stages of the circuit can be computed from Eq. (6.4) and Eq. (6.5).
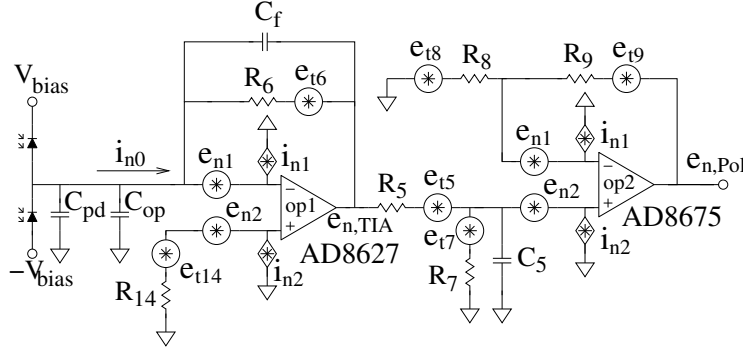
Figure 6.9: TIA and second amplifier stage implementation including the noise sources considered for the analysis.

$$e_{n,TIA}^2 \simeq e_{R_6,t}^2 + i_{n,op1}^2 |Z_f|^2 + \tag{6.4}$$
$$+ \left(e_{n,op1}^2 + e_{R_{14},t}^2 \right) \frac{1 + (2\pi f R_6 C_T)^2}{1 + (2\pi f R_6 C_f)^2}$$
$$e_{n,Ninv}^2 = e_{R_8,t}^2 \frac{R_9^2}{R_8^2} + e_{R_9,t}^2 + i_{n,op2}^2 R_9^2 + \left(1 + \frac{R_9}{R_8} \right)^2$$
$$\times \left[e_{R_7,t}^2 + e_{R_5,t}^2 + e_{n,op2}^2 + i_{n,op2}^2 \left(\frac{R_5 R_7}{R_5 + R_7} \right)^2 \right] \tag{6.5}$$

where $e_{n,op1}$, $i_{n,op1}$, $e_{n,op2}$, $i_{n,op2}$ are the noise properties of the operational amplifier for the first and second stage, $e_{R,t}$ is the thermal noise in the resistor, $e_{n,TIA}$ is the voltage noise at the output of the TIA, $e_{n,Ninv}$ is the voltage noise at the output of the non-inverting amplifier, Z_f is the feedback impedance and C_T is the total circuit capacitance, considering feedback capacitance $C_f = 7\,pF$, op-amp input capacitance $C_{op} = 7.9\,pF$ and photodiode capacitance $C_{pd} = 120\,pF$. Noise gain due to the photodiode's shunt resistor ($50\,M\Omega$) has been considered negligible, in the same way as the noise contribution due to thermal drifts. In order to ensure loop stability and limit gain peaking or oscillations, the feedback capacitor was chosen large enough to get overcompensation; its drawback is the bandwidth reduction ($\sim 78\,kHz$), which is

not an issue for the measurement ($\Omega_\mathrm{m} = 19.45\,\mathrm{kHz}$). The sensitivity of the polarimeter is set by $R_6 = 1\,\mathrm{M\Omega}$, $R_8 = 1.1\,\mathrm{k\Omega}$ and $R_9 = 11\,\mathrm{k\Omega}$ and the total output noise (excluding temperature fluctuations which are considered further on in the text) is

$$
e_{\mathrm{n,Pol}}^2 = e_{\mathrm{n,TIA}}^2 \left(1 + \frac{R_9}{R_8} \right)^2 + e_{\mathrm{n,Ninv}}^2. \tag{6.6}
$$

The polarimeter noise in Figure 6.10 was quantified in terms of current spectral density in order to directly compare to the photocurrent shot noise for a $1\,\mu\mathrm{W}$ beam at $\lambda = 852\,\mathrm{nm}$. The shot noise becomes

$$
i_{\mathrm{sn}} = \rho \sqrt{2 E_{\mathrm{ph}} \left(P_{\mathrm{PD1}} + P_{\mathrm{PD2}} \right)} \tag{6.7}
$$

$$
= \rho \sqrt{2 \frac{hc}{\lambda} P_{\mathrm{DC}}} = 0.375\,\mathrm{pA\,Hz^{-1/2}}
$$

assuming that the silicon photodiode responsivity is $\rho = 0.55\,\mathrm{A\,W^{-1}}$ and that the sum of the received signal power at each photodiode (P_{PD1} and P_{PD2}) equals the total incident light power of the probe beam (P_{DC}). The calculated noise density contributions referred to the input show that the op-amp voltage noise of the TIA is the main contributor at low frequencies and over $10\,\mathrm{kHz}$ (see Table 6.2 for the op-amp characteristics). The high-frequency effect is due to the response of $C_{\mathrm{op}} + C_{\mathrm{pd}}$, where the gain peaking takes effect and is leveled off by the feedback capacitance C_{f} (Figure 6.12, solid red line). At frequencies between $1\,\mathrm{Hz}$ and $10\,\mathrm{kHz}$, the shot-noise level plays the main role in the total spectral noise density, followed by the contribution of the Johnson noise of the large TIA's feedback resistor.

Table 6.2: Output noise characteristics for the op-amps used in the polarimeter. Corner frequency f_c for the op-amp current noise is estimated according to the white noise specified by the manufacturer.

IC	e_n [nV/$\sqrt{\mathrm{Hz}}$]	$f_{\mathrm{c,}e_\mathrm{n}}$ [Hz]	i_n [pA/$\sqrt{\mathrm{Hz}}$]	$f_{\mathrm{c,}i_\mathrm{n}}$ [Hz]
AD8627	17.5	59	0.004	200
AD8675	2.8	6	0.3	2
OPA124	8	848	0.0008	1.75

As in Section 6.3.1, the calculated contribution to the overall temperature dependence of the circuit due to the TC of the resistors is much greater than that due to the drift of the bias/offset current and offset voltage ($\simeq 0.08\,\mu\mathrm{VK^{-1}}$). Therefore, ignoring thermal drifts in the input-referred errors of the operational amplifier, the temperature dependence of the polarimeter is
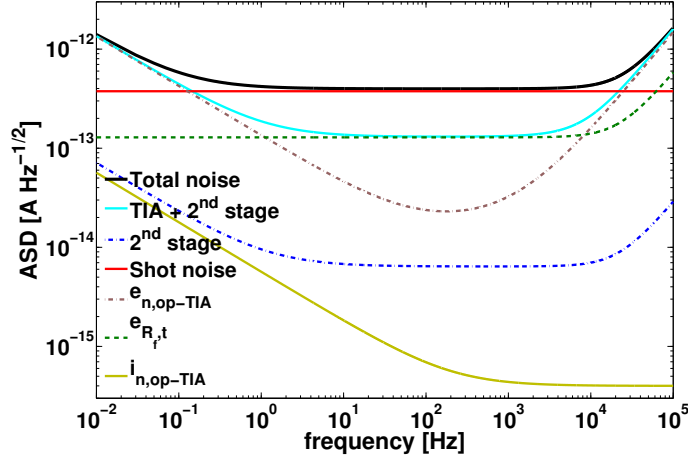
Figure 6.10: Input noise breakdown for the polarimeter. Shot noise of the light and op-amp voltage noise are the most important noise sources. The black trace is the sum of all the noise sources together.

$$\alpha_{\mathrm{Pol}}(T) = \rho P_{\mathrm{DC}} R_6 \sqrt{\alpha_{R6}^2 + 4\alpha_{R,\mathrm{NI}}^2 \left(\frac{R_9}{R_8}\right)^2}, \tag{6.8}$$

where ρ is the photodiode responsivity, P_{DC} is the incident light power, and α_R is $25\,\mathrm{ppm\,K^{-1}}$ and $15\,\mathrm{ppm\,K^{-1}}$ for the resistors of the TIA and the non-inverting amplifier, respectively. Therefore, we obtain that the polarimeter's TC is $166\,\mu\mathrm{V\,K^{-1}}$ ($15\,\mathrm{pA\,K^{-1}}$ or $27\,\mathrm{pW\,K^{-1}}$). Hence, for the thermal environment in eLISA and even in conventional laboratories ($S_{T,\mathrm{lab}}^{1/2} < 1\,\mathrm{mK\,Hz^{-1/2}}$ at $1\,\mathrm{Hz}$), the noise contribution due to the TC of the TIA is considered negligible ($< 15\,\mathrm{fA\,Hz^{-1/2}}$).

In order to reduce the overall noise maintaining the current-to-voltage sensitivity, the second stage could be omitted by increasing the feedback resistor of the TIA. However, for larger values of the feedback resistor, the stray capacitance across the feedback C_{s} has more effect on the bandwidth ($C_{\mathrm{s}} \leq 1\,\mathrm{pF}$ for carefully printed-circuit layout). For that reason, we do not adopt the single TIA option with a higher feedback resistor ($11\,\mathrm{M\Omega}$), though it would be a better option for lower bandwidth applications. As an alternative, a T-network could overcome such drawback, keeping the same value for the largest resistor ($1\,\mathrm{M\Omega}$) and eliminating the need for the non-inverting amplifier. Figure 6.11 shows the circuit for the T-network TIA with the noise sources considered for the analysis. The theoretical voltage noise for this configuration is

$$e_{\mathrm{n,Tnet}}^2 \simeq i_{\mathrm{n,op}}^2 |Z_{\mathrm{f}}|^2 \left| 1 + \frac{R_2}{Z_{\mathrm{f}}} + \frac{R_2}{R_1} \right|^2 + \left(1 + \frac{R_2}{R_1} \right)^2$$
$$\times \left(e_{\mathrm{n,op}}^2 \frac{1 + (2\pi f R C_{\mathrm{T}})^2}{1 + (2\pi f R C_{\mathrm{f}})^2} + e_{R,\mathrm{t}}^2 + e_{R_2,\mathrm{t}}^2 + e_{R_1,\mathrm{t}}^2 \right). \tag{6.9}$$

The approach to minimizing the output noise is limited by the restrictions that the resistors selected for the T-network must: (1) hold the same sensitivity and similar measurement bandwidth as the two-stage configuration, and (2) have a maximum resistance value of $1\,\mathrm{M\Omega}$. The values selected for the T-network are $R = 1\,\mathrm{M\Omega}$, $R_1 = 48.1\,\mathrm{k\Omega}$ and $R_2 = 458.8\,\mathrm{k\Omega}$. The noise spectral densities for the topologies that were analyzed are shown in Figure 6.12, where the results exhibit similar noise for the single-stage amplifier with a T-network and for the two-stage TIA. There is also a compromise between high- and low-frequency noise, and some improvements can be achieved from a trade-off between the input voltage noise and the corner frequency of the op-amp. Figure 6.12 shows the performance comparison of the OPA124 and AD8627, where the high-frequency performance is improved at the expense of having higher $1/f$ noise (see Table 6.2). The noise has been quantified in terms of output voltage spectral density in order to observe the frequency response of the amplifier's voltage noise contribution. The figure shows the pole response caused by the feedback impedance at the beginning of the high-frequency asymptote, $1 + (C_{\mathrm{pd}} + C_{\mathrm{op}})/C_{\mathrm{f}}$, which is the dominant source of noise over $20\,\mathrm{kHz}$. For this particular case, the motivation for choosing better photodiodes like the S1223-01 with smaller C_{pd}, together with op-amps with lower input voltage noise $e_{\mathrm{n,op}}$, would improve the technical noise over $20\,\mathrm{kHz}$, i.e., at fields $\gtrsim 6\,\mu\mathrm{T}$.
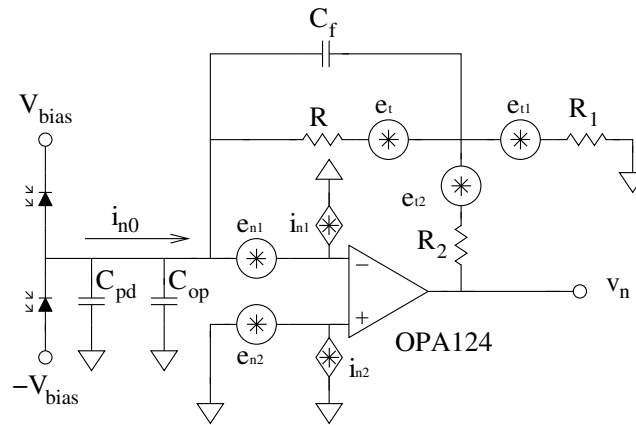
Figure 6.11: T-network TIA implementation with the addition of the noise sources that originate from the op-amp and resistors.
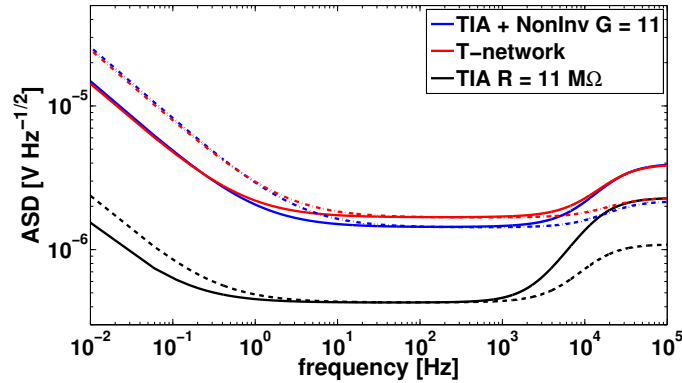
Figure 6.12: Theoretical amplitude spectral densities for a two-stage current-to-voltage amplifier (classical TIA + non-inverting amplifier), TIA with a T-Network in the feedback loop and TIA with a $11\,\mathrm{M\Omega}$ feedback resistor. Noise using the AD8627 is displayed as a solid line and the OPA124 as a dashed line.

For the specific measurements in this experiment, low-frequency contribution caused by the polarimeter circuit is not so critical since the signal is modulated at frequencies where the $1/f$ behavior is mitigated. As seen in Figure 6.12, the corner frequency is around $1.5\,\mathrm{Hz}$, which would be within the zero-field resonance for small magnetic field measurements ($\sim 1\,\mathrm{nT}$). As a result of the estimated spectral density, the low-frequency contribution is not critical for the possible magnetic field environment in eLISA.

In order to confirm the analysis of the circuit, noise measurements were taken between $0.1\,\mathrm{mHz}$ and $10\,\mathrm{Hz}$, where both $1/f$ noise and noise floor are presented. Figure 6.13 shows that the results are in good agreement with the theoretical predictions using the noise sources considered in the circuit. The measured noise floor is around $2.5\,\mu\mathrm{V\,Hz^{-1/2}}$, which corresponds to an equivalent magnetic field noise of $1.5\,\mathrm{pT\,Hz^{-1/2}}$. The polarimeter noise was translated to magnetic field according to the characteristics of the magnetic-resonance curve, i.e., the slope of the absorptive curve gives the relation between amplitude and magnetic-resonance frequency. Given that the magnetic-resonance linewidth is $41.6\,\mathrm{Hz}$ and the peak optical rotation signal is $9.9\,\mathrm{mV}$, the voltage-to-hertz ratio is $0.476\,\mathrm{mV/Hz}$. Another recent magnetometer essentially of the same type but with larger vapor cell and magnetic-resonance linewidth of $2.9\,\mathrm{Hz}$ reaches a noise level of $50\,\mathrm{fT\,Hz^{-1/2}}$ [145].

With the present design, measurements with a signal-to-noise ratio of $70\,\mathrm{dB}$ can be made by using the lock-in amplifier with an equivalent noise bandwidth (ENBW) of $1.25\,\mathrm{Hz}$.
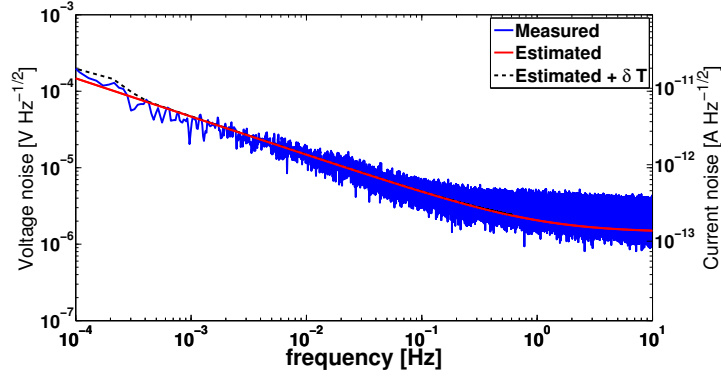
Figure 6.13: Theoretical and measured noise densities of a two-stage current-to-voltage converter.

6.4   Equivalent magnetic field noise measurements

For low-frequency noise characterization of the magnetometer in the laboratory, different runs during periods of at least twelve hours were carried out. The amplitude spectral density for the magnetic noise measurements of the magnetometer is

$$S_{B,\text{system}}^{1/2} = \gamma^{-1} \left(S_{\Omega_\text{m}} + S_{\theta,\Omega_\text{m}} + 2C S_{\Omega_L,\Omega_\text{m}} S_{\Omega_L,\theta} \right)^{1/2}, \tag{6.10}$$

where S_{Ω_m} is the noise power density of the modulation frequency, $S_{\theta,\Omega_\text{m}}$ is the noise power density of the phase fluctuations translated to frequency, γ is the gyromagnetic ratio for ^{133}Cs ($3.5\,\text{Hz}\,\text{nT}^{-1}$) and C is the correlation coefficient for partially correlated signals [136].

The measured equivalent magnetic field noise of the system shown in Figure 6.14 is around $50\,\text{pT}\,\text{Hz}^{-1/2}$ at 0.1 mHz and fulfills the requirement given in Eq. (6.2). The current applied to the coil has also been measured and converted to the equivalent magnetic noise, where, as expected from the estimated value in Section 6.3.1, the noise level is around $8\,\text{pT}\,\text{Hz}^{-1/2}$ at 0.1 mHz. The excess noise observed in the magnetometer at sub-millihertz frequencies is well over the noise applied by the coil. Then, it has been proved that the characterized electronic noise contribution does not limit the performance of the magnetometer at the lower end of the eLISA bandwidth. Now that the main electronic noise sources have been characterized (current source and detector noise), further work can be done in order to unveil the noise limits at low-frequency, such as light shifts induced by the laser light or alkali density fluctuations. At higher frequencies, the magnetometer noise-floor measurement is $\sim 2.5\,\text{pT}\,\text{Hz}^{-1/2}$, which is in agreement with the equivalent magnetic field noise calculated for the polarimeter in Section 6.3.2 (the theoretical estimation considering the polarimeter and the shot noise for $\Omega_\text{m} = 19.45\,\text{kHz}$ is $3\,\text{pT}\,\text{Hz}^{-1/2}$). The main

contributors to the noise floor are the op-amp voltage noise for the first stage of the TIA and the photocurrent shot-noise of the incident light. The theoretical estimation of the additive noise due to the polarimeter, shot-noise, and current source is shown in Figure 6.14 (black trace).
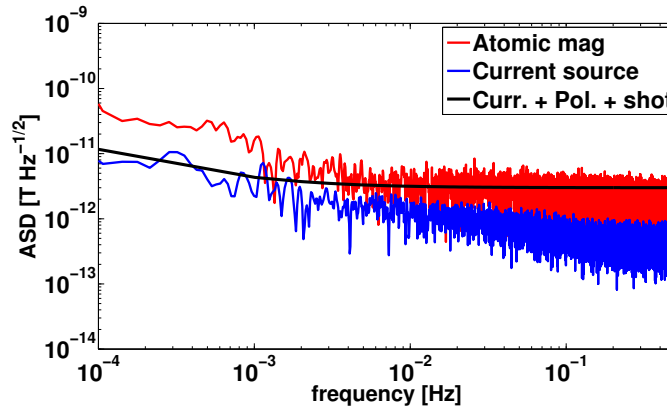
Figure 6.14: Equivalent magnetic field spectral density for the magnetometer (red trace) and equivalent noise applied by the floating-load current source (blue trace). Differences at frequencies higher than 10 mHz between the experimental measurements and the theoretical behavior of the current source (Figure 6.8) are due to the limited resolution of the digital multimeter (Agilent 34461A). The black trace is the sum of the theoretical noise of the current source, the polarimeter and the shot noise at $\Omega_{\mathrm{m}} = 19.45\,\mathrm{kHz}$.

6.5 Conclusion

We presented the noise performance of an atomic magnetometer based on NMOR with modulated light at sub-millihertz frequencies. To quantify and discern electronic contributions from the overall noise measurement, the polarimeter circuit and the current source for the leading field were characterized in terms of their intrinsic noise and thermal dependence. The estimation of the noise of the circuits is in good agreement with the measurements, which are clearly dominated by the electronic $1/f$ noise at lower frequencies and where the thermal effects start to appear below the measurement bandwidth ($< 0.1\,\mathrm{mHz}$). The designed current source creates a quiet magnetic environment which allows us to measure the atom-based sources of drift within the desired bandwidth. In addition, the polarimeter circuit operates below the photon shot-noise level between 1 and 10 kHz; above this frequency range the current-to-voltage converter exhibits gain peaking, which can be readily improved. The magnetometry technique presented herein proves to be a promising technology for eLISA in terms of sensitivity, given the fact that it is well within the eLISA requirement at 0.1 mHz. However, due to the size, weight and power restrictions

for space applications, further work on sensor miniaturization and its effects on the sensitivity and low-frequency drifts should be performed. This work might also be useful in other magnetically sensitive fundamental physics experiments beyond the scope of eLISA, where small sensors with long-integration time are required, such as the search for a permanent electric dipole moment of the neutron [23] and the STE-QUEST mission [9].

Chapter 7

Conclusions and Future Work

The most relevant outcomes and conclusions throughout this dissertation are outlined in this last chapter. We also point out some of the future work and research lines that will be useful not only for the magnetic field monitoring in eLISA-like space missions, but also for the wide field of magnetometry.

7.1 Conclusions

The key aspect of the work described herein is focused on the development of a system capable of monitoring the slow drifts of the environmental magnetic field in eLISA by using chip-scale magnetometers.

The current eLISA magnetic measurement system is based on LISA Pathfinder's, where mature fluxgate technology was selected due to its proven low-noise along the measurement bandwidth ($1\,\mathrm{mHz} \leq \omega/2\pi \leq 30\,\mathrm{mHz}$) and its actual availability for space applications. Different test campaigns were carried out for the validation of the magnetic related passive and active hardware, this is, the magnetic measurement subsystem and the instrumentation for magnetic field generation, respectively. The experience that we gained during the validation of LISA Pathfinder's fluxgates indicates that their use for magnetic field estimation at the TM position presents a few drawbacks driven by the two basic factors that follow.

- Permalloy-core magnetometers are able to disturb their magnetic surroundings due to the employed measurement principle,

- sensors of large size conflict with the possibility of having a sufficient number of them to map the magnetic field properly.

In LISA Pathfinder, these factors limited the total number of triaxial sensors to only four, which moreover had to be placed somewhat far from the TMs ($\geq 18.85\,\mathrm{cm}$). As a consequence, the unsatisfactory quality of the reconstructed field at the TM using

115

classical interpolation methods does not correspond to the the excellent performance of fluxgate. In order to overcome the aforementioned limitations and to ensure a more solid, agreeable approach to the more demanding eLISA objectives, a sufficient number of smaller sensor devices with lower magnetic back-action effects are required. Apart from this, the instrument measurement bandwidth in eLISA is reduced down to 0.1 mHz. One other added difficulty is that the need for using miniaturized sensors also compromises noise performance. These aspects are among the more challenging issues we met in this thesis.

In spite of the dominant $1/f$ noise behavior of chip-scale magnetoresistive sensors, which exceeds the defined requirements, the technology emerges as an alternative to the drawbacks found in the LISA Pathfinder's fluxgate magnetometers. With the purpose of improving the noise characteristics, different electronic techniques were performed in the millihertz band. Among the different noise reduction techniques, the most useful for our particular objective are flipping and electro-magnetic feedback. The former helps to mitigate the $1/f$ contribution, and the latter overcomes the thermal dependence and minimizes the additional noise by means of a closed-loop controller. The achieved noise performance shows significant improvements, which is comfortably compliant with the preliminary mission requirement. Therefore, AMR magnetometers with dedicated noise reduction techniques are revealed as a solution for eLISA in terms of noise. As far as we know, the results presented herein give the best noise characteristics that have been published so far when using AMR in the frequency range of the millihertz. In addition to this, a simplified flight model of the currently proposed magnetic measurement system for eLISA has been integrated in the ^{3}Cat-2 CubeSat (UPC) so as to increase the technology readiness level (TRL) of the instrument.

eLISA-like space missions entail a thorough knowledge of the spacecraft magnetic field since the on-board experiment can only operate propitiously if the magnetic environment achieves the required performance. For this reason, the potential magnetic sources allocated in the spacecraft need to be carefully characterized. In this regard, the same as with the fluxgate device, AMR contains a magnetic core as sensor head. However, for the purpose of maintaining the magnetic cleanliness needed for eLISA, the use of AMRs poses a clear advantage over classical fluxgate magnetometers due to the fact that the amount of ferromagnetic material present in their cores is much smaller. In order to quantify this contribution, magnetic moment measurements of the AMR sensors were taken by using very sensitive SQUID magnetometers. The magnetic impact depends not only on the magnetic properties but also on the noise reduction techniques. The analysis demonstrates that, owing to the inherently low magnetic moment of the AMR and its operation principles, eight magnetometers per TM can be attached in symmetrical configuration to the outside wall of the vacuum enclosure without the risk of back-action effects. For this reason, the proximity of the magnetic sensors to the TM does not present a problem for the magnetic performance and the magnetic noise they induce is mostly negligible.

116

The suggested eight-sensor layout has consistently produced good quality results in estimating the magnetic field and its gradient at the positions of the test masses by using the multipole expansion algorithm. This problem solves one of the key aspects in the LISA Pathfinder's magnetic measurement system, the accuracy of the magnetic field map reconstruction. The results, which do look encouraging, proves mean errors lower than 1% and 2% for the magnetic field and magnetic field gradient, respectively. Hence, the proposed magnetic measurement system for eLISA represents an improvement of the magnetic field estimation error of more than two orders of magnitude compared to the hardware solution implemented in LISA Pathfinder using the same interpolation method. The proposed system has the ability to deliver proper results under different simulated magnetic scenarios, unpredictable offsets of the magnetometer readings, and imprecisions in the spatial location of the magnetometers. Thus, the study demonstrates a robust approach that does not need any *a priori* knowledge of the magnetic structure in the spacecraft. It must be remarked that this improvement has been achieved due to the small size and low magnetic back-action offered by the AMRs, which makes it possible not only to install more sensors but also to place them closer to the TMs. These are remarkable findings that prove that the use of AMRs combined with multipole expansion will yield reliable estimates of the magnetic field map at the test masses location.

Other than the investigation performed with fluxgate and AMR sensors, further research was done with another modern and very promising technology based on nonlinear magneto-optical rotation (NMOR atomic magnetometer). The purpose was to evaluate if the NMOR magnetometer with modulated light was suitable for low-frequency noise applications like the eLISA concept. To quantify and discern the technical noise from the overall noise measurement, the dominant electronics contributions were characterized and minimized. The quiet magnetic environment generated for the sensor noise performance allowed us to measure the atom-based sources of drift within the desired bandwidth. At higher frequencies, the detector noise of our breadboard magnetometer was dominated by the photon shot-noise level between 1 and 10 kHz. We found the technology appropriate for eLISA in terms of sensitivity, given the fact that the noise level at 0.1 mHz was two orders of magnitude lower than for AMR. However, further work must be done on sensor miniaturization and its effects on the sensitivity and low-frequency drifts in order to make the magnetometer compliant with the size restrictions for space missions. As a general outlook, Figure 7.1 shows a comparison of the best results obtained for all the three technologies studied in this thesis.

Finally, we remark that the work described in this thesis is likely to be useful beyond the scope of eLISA, especially for space applications like STE-QUEST, with strict constraints in volume, weight, power, magnetic cleanliness, and low magnetic noise at low frequencies.
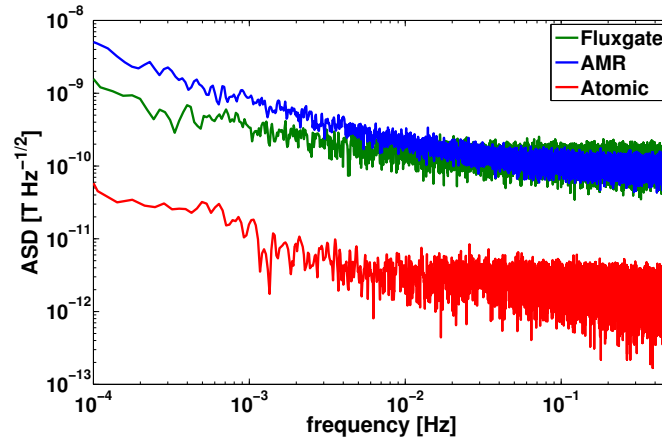
Figure 7.1: Noise comparison between fluxgate, AMR, and atomic sensors.

7.2 Future work

eLISA is currently under the mission concept study and its requirements at the subsystem level are still not fully defined. Besides, LISA Pathfinder will fly at the end of 2015 and the mission operations, expected to be finished by 2016, will obviously provide useful debugging information of the magnetic performance, guiding us towards the requirements needed for eLISA. Therefore, regarding the eLISA magnetic subsystem, our findings look promising, but there is still a lot of work to be done. The technology roadmap to be followed in the future line of work is summed up below.

The technology demonstrator of the eLISA magnetic system embarked in the ³Cat-2 CubeSat is expected to be launched in 2016. Thus, the analysis of the in-flight data will shed light on the effect on the intrinsic noise behavior of the AMR under space environment conditions.

Concerning the atomic magnetometer, the miniaturization of the device and its consequence on the low-frequency noise is a top priority in order to make the technology ready for space applications. The miniaturized design can be based on fully integrated chip-scale magnetometers [169] or microfabricated remote sensor heads coupled to the laser and photodiodes through optical fibers [36]. The evident benefit of the first design is the possibility to include all the components in a single chip. By contrast, the advantage of the latter approach is to keep the cell clear of possible magnetic disturbances caused by electrical connections. Besides, the second design is specially useful when an array of sensors is required since some parts can be shared, such as the stabilized laser, the modulator and some optical elements. In particular, microfabricated remote atomic magnetometers is the preferred option for eLISA

due to the size, weight and power restrictions when an array of magnetometers is required. This technology has no flight heritage as a space science instrument, and one of the motivations of the future work is to increase the TRL of the sensor and verify the scope of its science measurement capability in a space environment. For eLISA, a sensor array configuration combining AMR and compact atomic magnetometers can be investigated. The main advantage of this arrangement is that atomic magnetometers, which are absolute sensors, can be used for in-flight calibration of the AMR sensors.

The negligible contribution of the AMRs on the acceleration noise was calculated on ground of the worst cases magnetic environmental scenario for LISA Pathfinder. We remark that for a better estimate of the magnetic effects, detailed knowledge of the magnetic sources (low-frequency fluctuations, dc, and ac magnetic lines) in the eLISA spacecraft is necessary. It is therefore convenient to procure this data to the best possible extent for a more faithful estimation.

Last but not least, it is worth mentioning that the design of the space atom interferometer in STE-QUEST is currently under study by a European consortium. Thus, the magnetometers distribution of the magnetic field monitoring system will be studied in a more advanced phase of the scientific mission.

Appendix A

Calibration of the LISA Pathfinder Controlled Current Source

This appendix reports on the result obtained during the activities performed in the validation of the controlled current source within the magnetic diagnostics of LISA Pathfinder. The purpose of the test is the on-ground calibration of the current source in order to determine the response of the output current in relation to the coil telecommands.

A.1 Test items

During the test campaign the two data acquisition units (DAUs) of the flight model data management unit (DMU) were validated. Table A.1 shows the items and software versions available for the calibration.

Table A.1: Test items for the calibration of the controlled current source. BSW, boot software; ASW, application software.

Type	Manufacturer	Reference	Code
DMU	NTE/IEEC	L3100-002	FMDMU
BSW	IEEC	1.7	
ASW	IEEC	2.0.090609	

A.2   Coil output current vs sine amplitude telecommand

The test is intended to reproduce the telecommands of the coil wave generation transmitted from the data processing unit (DPU) to the DAU, in particular the telecommands in charge of controlling the amplitude of the sinusoidal signal to be applied to the coil. Table A.2 summarizes the codification of these telecommands packets [114].

Table A.2: Telecommands used for the coil current.

Telecommand	ID Information	Data byte	Current
Coil current	00001000	11111111	Pos. full range
		00000000	Neg. full range
Sine amplitude	00010000	11111111	Pos. full range
		00000000	Zero scale

The DAU was commanded to sweep the sine amplitude from minimum to maximum current intensity values by means of a Python script. The test sequence is shown in Table A.3, where every step of the sweep profile lasted 10 seconds.

Table A.3: Sequence of telecommands sent by the Python script to the DPU.

Coil current	Sine amplitude	Current [mA]
0	255 to 0	-4.2 to 0
255	0 to 255	0 to 4.2

A high stability resistor (1 kΩ, 0.01%, and 6 ppm K^{-1}) was utilized as the load for the current pump. The current measurements through the resistor were taken with an Agilent 34410A digital multimeter with a sampling frequency of 2.44 Hz, and the data were acquired by means of a PC connected via GPIB to the digital multimeter. The test setup is shown in Figure A.1.

A.2.1   Test results

Table A.4 shows a summary of the results for the coil currents that will be used in the magnetic experiment on board the LTP [45]. The current intensity value in each point was averaged with 10 samples.

The uncertainty of the measurements has been inferred by using Eqs. (A.1) and (A.2).

Figure A.1: Setup for the calibration test of the controlled current source of the DMU.

Table A.4: Summary of the calibration for the controlled current source of the flight model DMU. Data bytes of the telecommands are shown in decimal format.

	Sine amplitude ID: 00010000	Coil current ID: 00001000	I_{peak} [mA]	I_{offset} [μA]	$A_{\sin}$ [mA]	U [μA]	U [%]
	30	0	-0.5192	-7.3	0.5119	11.03	2.16
		255	0.5046				
	59	0	-1.013	-10.5	1.0025	13.65	1.36
		255	0.992				
DAU1	88	0	-1.508	-13.5	1.4945	17.13	1.15
		255	1.481				
	118	0	-2.019	-17	2.002	21.18	1.06
		255	1.985				
	30	0	-0.5058	-1.45	0.5044	11.01	2.18
		255	0.5029				
	60	0	-1.004	1.5	1.0055	13.69	1.36
		255	1.007				
DAU2	90	0	-1.501	4	1.505	17.24	1.15
		255	1.509				
	120	0	-1.999	7	2.006	21.24	1.06
		255	2.013				

$$u_c = \sqrt{\left(\frac{u_1}{\sqrt{3}}\right)^2 + \left(\frac{u_2}{\sqrt{3}}\right)^2 + \left(\frac{u_3}{k'}\right)^2 + \sigma^2} \qquad (A.1)$$

$$U = k \cdot u_c \qquad (A.2)$$

where
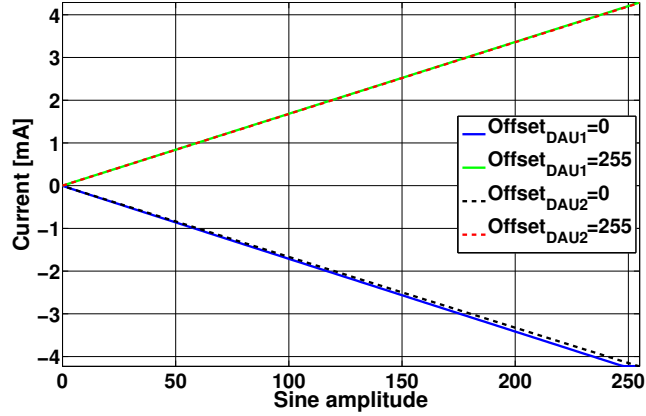
Figure A.2: Coil current sweep. Current as a function of the sine amplitude telecommand.

- u_c is the combined standard uncertainty,

- U is the expanded uncertainty,

- $u_1 = (I_{\max} - I_{\min})/2^8$ is the quantization of the sinusoidal waveform,

- $u_2 = 0.05$ % of reading $+ 0.02$ % of range, which is the accuracy of the digital multimeter,

- $u_3 = 0.00044$ mA is the uncertainty in the certificate of calibration of the multimeter,

- $k = k' = 2$ are the coverage factors,

- σ is the standard deviation of the measurements for 10 samples.

The terms u_1 and u_2 in Eq. (A.1) are divided by the square root of three due to the probability distribution used, and u_3 is divided by the coverage factor indicated in the certificate of calibration of the instrument ($k' = 2$). In Eq. (A.2), the combined standard uncertainty is multiplied by a coverage factor ($k = 2$) in order to estimate the expanded uncertainty, increasing the level of confidence to around 95%. The calculation of the uncertainty is based on the recommendations given in the guide to the expression of uncertainty in measurement [87].

The uncertainty increases with the current source resolution, and the resolution depends on the amplitude of the sinusoidal waveform commanded by the DPU (see Section 2.2). Therefore, the greater the amplitude of the wave, the larger the

124
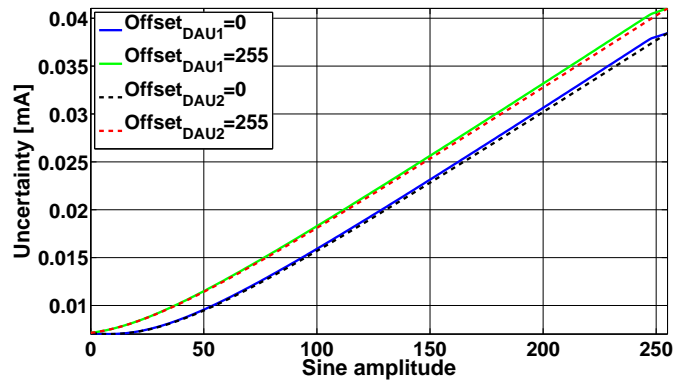
Figure A.3: Uncertainty of the measurement as a function of the sine amplitude telecommand.

uncertainty of the measurement. Figure A.3 shows the response of the uncertainty as a function of the commanded sine amplitude for both DAUs.

Appendix B

Noise Analysis of Current Sources

The low-frequency noise analysis of several typologies of voltage-to-current converters (Howland, improved Howland, floating load, and differential) is assessed in this appendix. The results are also compared with experimental data.

For the design of the current source, we consider an output current of $4\,\mathrm{mA}$ for a load of $1.8\,\mathrm{k\Omega}$. These values are the maximum current defined by requirement and the nominal resistive load of the magnetic coil in LISA Pathfinder. The input voltage of the converter is provided by a precision 10 V voltage reference.

B.1 Howland current source

First, we analyze the noise of two slightly different Howland implementations. These are the classical Howland and the *improved* Howland current pump.

B.1.1 Classical Howland

Figure B.1 shows the noise sources for the classical Howland current pump. This includes the equivalent noise voltage and current sources of the op-amp, and the thermal noise voltage from the resistors. Apart from this, we also consider the noise coming from the voltage reference used as input voltage.

Noise parameters for the op-amp and voltage reference used in the current pump are shown in Table B.1. Notice that manufactures specify the voltage spectral density of the op-amp as $e_\mathrm{n}^2 = e_\mathrm{n1}^2 + e_\mathrm{n2}^2$, and the current noise is $i_\mathrm{n} = i_\mathrm{n1} = i_\mathrm{n2}$. As in the thesis, the low-frequency noise is modeled according to Eq. (B.1)

$$e_n^2(f) = e_{n,wn}^2 \left(1 + \frac{f_{c,e_n}}{f} \right) \tag{B.1}$$

$$i_n^2(f) = i_{n,wn}^2 \left(1 + \frac{f_{c,i_n}}{f} \right) \tag{B.2}$$

where $e_{n,wn}$ and $i_{n,wn}$ are the respective white-noise voltage and white-noise current specifications. f_{c,e_n} and f_{c,i_n} are the corner frequencies of the $1/f$ response at which $e_n^2(f_{c,e_n}) = e_{n,wn}^2$ and $i_n^2(f_{c,i_n}) = i_{n,wn}^2$.

Table B.1: Noise parameters for the operational amplifier (OP27) and the voltage references (REF01 and AD587) used in the analysis. The corner frequencies of the voltage references are fitted by experimental data.

IC	$e_{n,wn}$ $[\mu V\,Hz^{-1/2}]$	f_{c,e_n} [Hz]	$i_{n,wn}$ $[pA\,Hz^{-1/2}]$	f_{c,i_n} [Hz]
OP27	0.003	2.7	0.4	140
REF01	1.7	2.5	-	-
AD587	0.1	35	-	-
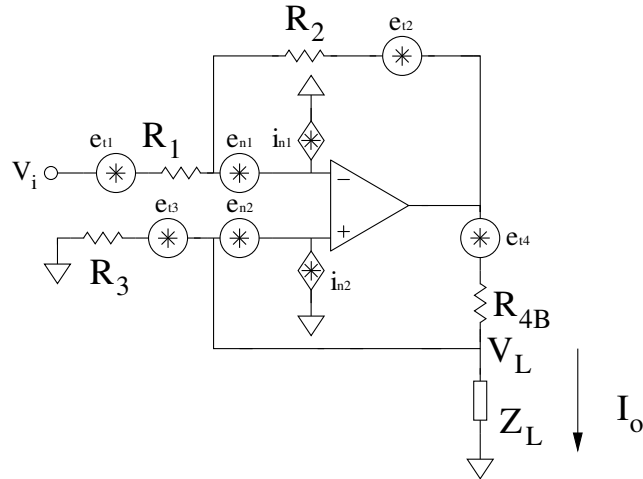
Figure B.1: Classical Howland current pump including the noise sources considered for the analysis.

The different noise sources in Figure B.1 are then referred to the output as

$$i_{n,1}^2 = e_n^2 \left(1 + \frac{R_2}{R_1}\right)^2 \frac{1}{R_4^2}, \tag{B.3}$$

$$i_{n,2}^2 = i_{n1}^2 R_2^2 \frac{1}{R_4^2}, \tag{B.4}$$

$$i_{n,3}^2 = 4k_B T R_1 \left(\frac{R_2}{R_1}\right)^2 \frac{1}{R_4^2}, \tag{B.5}$$

$$i_{n,4}^2 = 4k_B T R_2 \frac{1}{R_4^2}, \tag{B.6}$$

$$i_{n,5}^2 = 4k_B T R_3 \left(1 + \frac{R_2}{R_1}\right)^2 \frac{1}{R_4^2}, \tag{B.7}$$

$$i_{n,6}^2 = 4k_B T \frac{1}{R_4}, \tag{B.8}$$

$$i_{n,7}^2 = e_{nVref}^2 \left(\frac{R_2}{R_1}\right)^2 \frac{1}{R_4^2}, \tag{B.9}$$

$$\tag{B.10}$$

where k_B is the Boltzmann constant, T is the temperature, and $e_{n,Vref}$ is the voltage noise of the voltage reference at the input of the current source. Then, the output noise spectral density of the current source is

$$i_{n,o}^2 = \sum_{k=1}^{7} i_{n,k}^2. \tag{B.11}$$

To achieve the true current-source behavior in this typology the ratio R_2/R_1 must be equal to R_{4B}/R_3. For this condition, the current output does not depend on the load ($I_o = -Vi/R_1$); then, the specifications for the current source mentioned above lead to $R_1 = R_3 = 2.5\,\text{k}\Omega$. For a proper functioning of the circuit, the range of permissible values of the load voltage (V_L) assuming symmetric output saturation (V_{sat}) is given by [62]

$$|V_L| \leq \frac{R_1}{R_1 + R_2} V_{sat}. \tag{B.12}$$

In order to enlarge the range of V_L, which is called voltage compliance, we need $R_2 = R_{4B} \simeq 0.1 R_1 \simeq 195\,\Omega$.

The theoretical and experimental amplitude spectral density for the Howland current source is shown in Figure B.2, where the voltage reference becomes the major contribution. The noise estimation using the voltage reference AD586 instead of REF01 improves the performance a factor of four.
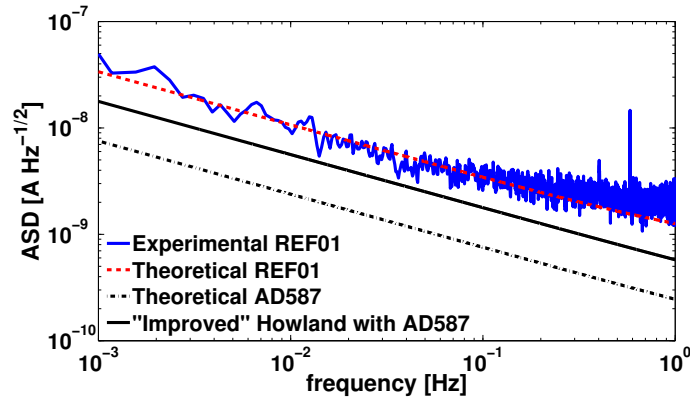
Figure B.2: Noise spectral density for the Howland current source using two different voltage references. Noise curve of the *improved* Howland pump analyzed in Section B.1.2 is also shown.

B.1.2   Improved Howland

For the improved Howland current pump a resistance is included in the positive feedback with the purpose of reducing power consumption. The slight modification is shown in Figure B.3, where the same noise contributions as in the previous case were considered for the analysis.
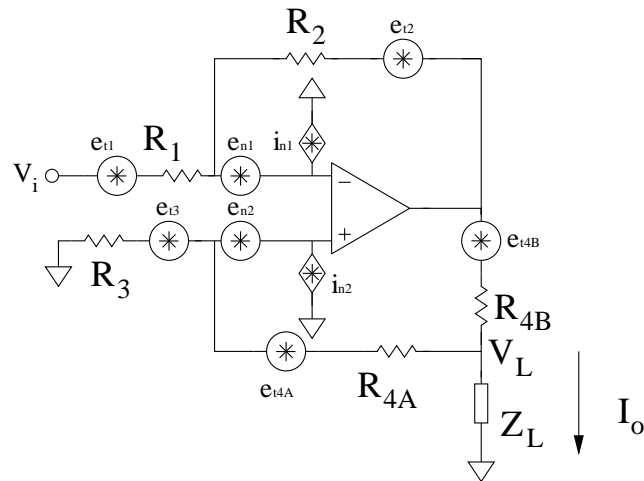
Figure B.3: Noise sources considered for the low-frequency analysis of the improved Howland current pump.

The noise contributions in the improved Howland current pump are referred to the output as

$$i_{n,1}^2 = e_n^2 \left(1 + \frac{R_2}{R_1}\right)^2 \left(\frac{1}{R_{4B}}\right)^2, \tag{B.13}$$

$$i_{n,2}^2 = i_n^2 R_2^2 \frac{1}{R_{4B}^2}, \tag{B.14}$$

$$i_{n,3}^2 = i_n^2 \left(\frac{R_3 R_{4A}}{R_3 + R_{4A}}\right)^2 \left(1 + \frac{R_2}{R_1}\right)^2 \frac{1}{R_{4B}^2}, \tag{B.15}$$

$$i_{n,4}^2 = 4k_B T \frac{R_3 R_{4A}}{R_3 + R_{4A}} \left(1 + \frac{R_2}{R_1}\right)^2 \frac{1}{R_{4B}^2}, \tag{B.16}$$

$$i_{n,5}^2 = 4k_B T R_2 \frac{1}{R_{4B}^2}, \tag{B.17}$$

$$i_{n,6}^2 = 4k_B T R_1 \left(\frac{R_2}{R_1}\right)^2 \frac{1}{R_{4B}^2}, \tag{B.18}$$

$$i_{n,7}^2 = 4k_B T \frac{1}{R_{4B}}, \tag{B.19}$$

$$i_{n,8}^2 = e_{nVref}^2 \left(\frac{R_2}{R_1}\right)^2 \frac{1}{R_{4B}^2}. \tag{B.20}$$

The total output current noise is

$$i_{n,o}^2 = \sum_{k=1}^{8} i_{n,k}^2 \tag{B.21}$$

In the improved Howland, the current-source behavior is achieved when R_2/R_1 matches $(R_{4A} + R_{4B})/R_3$. Then, the output current through the load, assuming R_{4A} much greater than R_{4B}, is given by

$$I_o = -Vi \frac{R_2}{R_1} \frac{1}{R_{4B}}, \tag{B.22}$$

and the voltage compliance can be approximated as

$$|V_L| \leq V_{sat} - \frac{R_2}{R_1} |V_i|. \tag{B.23}$$

The resistor values are solved considering the above-described restrictions and minimizing the total output current noise in Eq. (B.21). The theoretical current spectral density for the improved Howland current source, which is slightly greater than the classical Howland when using the same voltage reference (AD587), is shown in Figure B.2.

B.2 Differential current source

Another simple grounded-load typology of voltage-controlled current source uses a differential amplifier with unity gain. The analyzed circuit with the noise contributions is shown in Figure B.4.
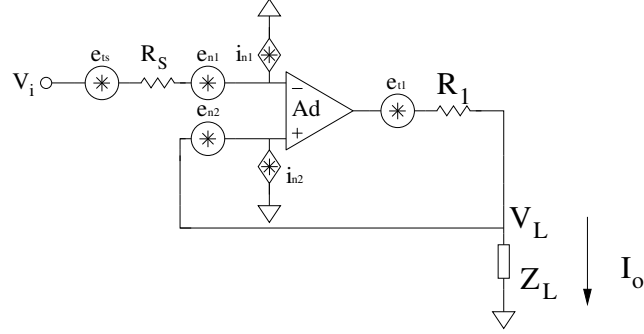
Figure B.4: Differential current pump with the noise sources considered for the analysis.

The noise sources in the differential current pump are then referred to the output as

$$i_{n,1}^2 \quad = \quad e_n^2 \frac{1}{R_1^2}, \tag{B.24}$$

$$i_{n,2}^2 \quad = \quad i_{n1}^2 R_{\rm s}^2 \frac{1}{R_1^2}, \tag{B.25}$$

$$i_{n,3}^2 \quad = \quad i_{n2}^2, \tag{B.26}$$

$$i_{n,4}^2 \quad = \quad 4k_B T R_{\rm s} \frac{1}{R_1^2}, \tag{B.27}$$

$$i_{n,5}^2 \quad = \quad 4k_B T \frac{1}{R_1}, \tag{B.28}$$

$$i_{n,6}^2 \quad = \quad e_{\rm nVref}^2 \frac{1}{R_1^2}, \tag{B.29}$$

$$\tag{B.30}$$

and the total current noise is

$$i_{n,o}^2 = \sum_{k=1}^{6} i_{n,k}^2. \tag{B.31}$$

The circuit was evaluated by using the unity-gain differential amplifier AMP03. Therefore, in view of the noise sources provided by the manufacturer ($e_{\rm n,wn}$ =

$20\,\mathrm{nV\,Hz}^{-1/2}$ and $f_{\mathrm{c,e_n}} \simeq 70\,\mathrm{Hz}$), the analysis is finally done considering the contributions in Figure B.5.
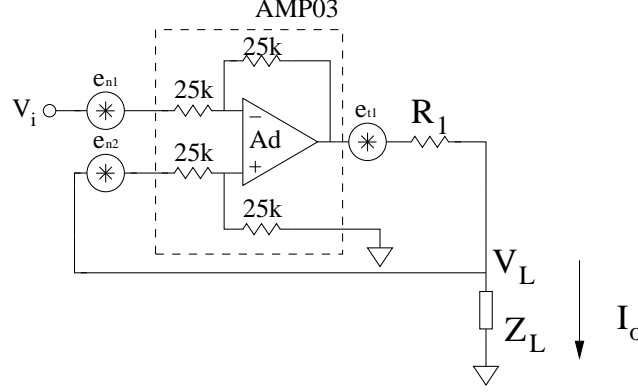
Figure B.5: Noise sources in a differential current source using the AMP03.

$$i_{n,1}^2 = e_n^2 \frac{1}{R_1^2}, \tag{B.32}$$

$$i_{n,2}^2 = 4k_B T \frac{1}{R_1}, \tag{B.33}$$

$$i_{n,3}^2 = e_{\mathrm{nVref}}^2 \frac{1}{R_1^2}, \tag{B.34}$$

then the total power spectral density is

$$i_{\mathrm{n,o}}^2 = \sum_{k=1}^{3} i_{n,k}^2. \tag{B.35}$$

For this typology the load current is defined as

$$I_{\mathrm{o}} = \left. \frac{(A_{\mathrm{d}}-1)V_{\mathrm{L}} - A_{\mathrm{d}} V_{\mathrm{in}}}{R_1} \right|_{A_{\mathrm{d}}=1} = -\frac{V_{\mathrm{in}}}{R_1} \tag{B.36}$$

with a very restrictive voltage compliance of

$$V_{\mathrm{L}} \leq V_{\mathrm{sat}} - I_{\mathrm{o}} R_1. \tag{B.37}$$

Thus, the noise curve of the differential current source for $R_1 = 2.5\,\mathrm{k\Omega}$ is shown in Figure B.6. Experimental results are also compared with the theoretical ones for the voltage reference REF01.
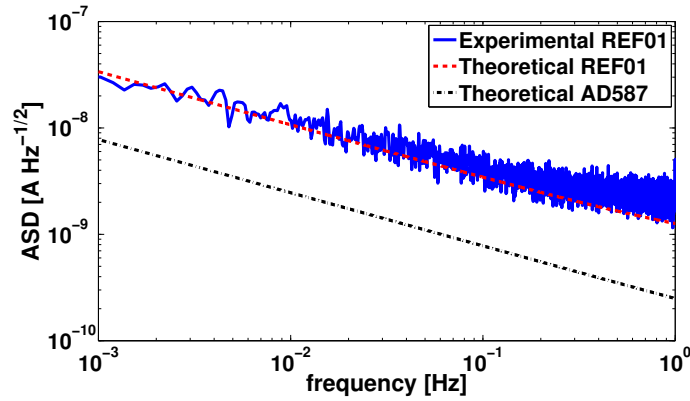
Figure B.6: Theoretical and experimental noise spectral densities for the differential current source.

B.3   Floating load current source

The last typology is a floating-load converter called load-in-the-loop current source, in which the load is the feedback element of the op-amp. For our purpose, none of the coil terminals is required to be committed to ground, so the floating type is a suitable option. Figure B.7 displays the noise sources considered for the current pump.
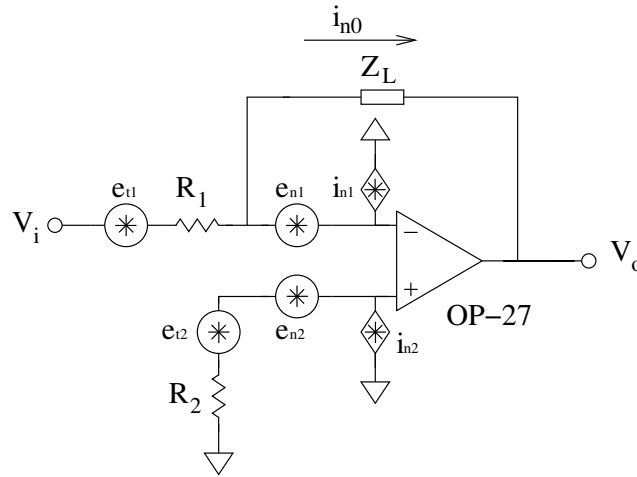
Figure B.7: Noise sources in a floating-load typology.

The noise terms to be taken into account for this floating load configuration are

the following:

$$i_{n,1}^2 = i_{n1}^2, \tag{B.38}$$

$$i_{n,2}^2 = 4k_B T \frac{1}{R_1}, \tag{B.39}$$

$$i_{n,3}^2 = e_n^2 \frac{1}{R_1^2}, \tag{B.40}$$

$$i_{n,4}^2 = e_{\text{nVref}}^2 \frac{1}{R_1^2}, \tag{B.41}$$

and the overall power spectral density of the source is given by

$$i_{\text{n,o}}^2 = \sum_{k=1}^{4} i_{n,k}^2. \tag{B.42}$$

A bias resistor $R_2 = R_1 || R_{\text{L}} \simeq 1\,\text{k}\Omega$ is installed to minimize the effect of the small currents at the input terminals (I_{p} and I_{n}) of the op-amp

$$V_{\text{o}} = I_{\text{p}} R_2 \left(1 + \frac{R_L}{R_1} \right) - I_{\text{n}} R_{\text{L}}. \tag{B.43}$$
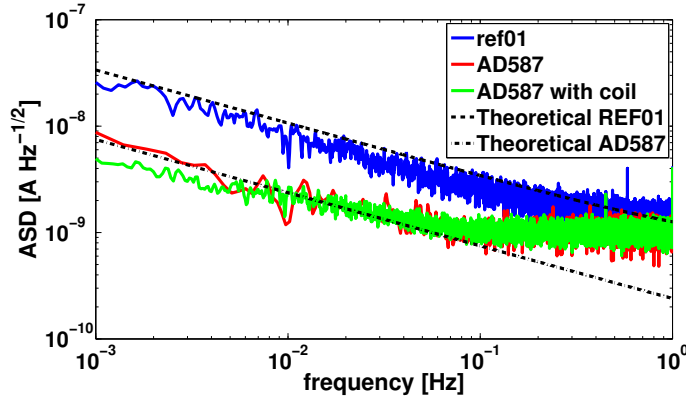
Figure B.8: Theoretical and experimental noise spectral densities for the load-in-the-loop current source with two different voltage references. A high stability resistor was used as load for all the measurements except for the green trace, where the LISA Pathfinder coil was connected instead of the resistor.

The theoretical current spectral density of the load-in-the-loop current source is shown in Figure B.8. Noise measurements were taken for comparison purposes, where the experimental results are in agreement with the one estimated theoretically.

The differences at frequencies higher than $100\,\mathrm{mHz}$ between the measurements and the theoretical estimate are caused by the resolution of the digital multimeter.

Appendix C

Temperature Coefficient of the Improved Howland Pump

This appendix details the estimations of the temperature coefficient of the improved Howland current source used in LISA Pathfinder.

C.1   Improved Howland current source

The analysis is done in the Howland typology shown in Figure B.3. For a practical voltage-to-current converter, the transfer characteristics for an input voltage V_i can be expressed as

$$I_o = AV_i + (1/R_o)V_L, \tag{C.1}$$

where V_L is the output load voltage, A is the gain of the transconductance amplifier in A V^{-1}

$$A = \frac{R_1(R_{4A} + R_{4B}) + R_2 R_{4A}}{R_1 R_{4B}(R_3 + R_{4A})}, \tag{C.2}$$

and $1/R_o$ is the output conductance seen by the load

$$1/R_o = Y_B = \frac{R_2 R_3 - R_1(R_{4A} + R_{4B})}{R_1 R_{4B}(R_3 + R_{4A})}. \tag{C.3}$$

Therefore, for an ideal current-source behavior, I_o has to be independent of V_L, i.e., $R_o = \infty$. This condition is achieved if the resistors are balanced as

$$\frac{R_2}{R_1} = \frac{R_{4A} + R_{4B}}{R_3}. \tag{C.4}$$

If the resistance ratio is unbalanced, an equivalent resistance will appear in parallel with the load and, in consequence, the circuit will not work as a true voltage-to-current converter.

C.2 Temperature coefficient calculation

In practical situations the balance condition of the Howland pump is not achieved due to the temperature coefficients (α) and tolerances (*tol*) of the resistors. According to Eq. (C.4), the worst-case condition is given by

$$\frac{R_2(1+x)}{R_1(1-x)} = \frac{R_{4A}(1-x) + R_{4B}(1-x)}{R_3(1+x)}, \tag{C.5}$$

where

$$x = tol + \alpha\Delta T. \tag{C.6}$$

Substituting the unbalanced resistances of Eq.(C.5) into Eq.(C.3) lead to

$$Y_B = \frac{R_2[(1+x)^2 - (1-x)^2]}{R_{4B}(1-x)^2[R_1(1+x) + R_{4A}(1-x)]}. \tag{C.7}$$

Then, expanding Y_B as a Taylor series, we obtain

$$Y_B \approx \frac{4R_2}{R_{4B}(R_1 + R_{4A})}x + \frac{4R_2(R_1 + 3R_{4A})}{R_{4B}(R_1 + R_{4A})^2}x^2, \tag{C.8}$$

which can be written as

$$Y_B \approx B_B(tol + \alpha\Delta T) + C_B(tol + \alpha\Delta T)^2. \tag{C.9}$$

Our concern is the second term of Eq. (C.1), $Y_B V_L$, in which V_L can be expressed as

$$V_L = I_{o,n}R_L(1 + \beta\Delta T_\beta), \tag{C.10}$$

where $I_{o,n} = V_i R_2/(R_1 R_{4B})$ is the nominal output current for a balanced source, ΔT_β represents changes of temperature at the load position, and R_L and β are the nominal resistance and the temperature coefficient of the load, respectively. Multiplying Eq. (C.10) by Eq. (C.9) we get

$$\begin{aligned} Y_B V_L &= B_B I_{o,n} R_L(1 + \beta\Delta T_\beta)(tol + \alpha\Delta T) + \\ &+ C_B I_{o,n} R_L(1 + \beta\Delta T_\beta)(tol^2 + (\alpha\Delta T)^2 + 2tol\alpha\Delta T). \end{aligned} \tag{C.11}$$

Now, assuming small temperature changes and considering only first-order temperature dependent terms, Eq. (C.11) is simplified as

$$\begin{aligned} Y_B V_L &\approx I_{o,n} R_L \left[\beta(B_B tol + C_B tol^2)\Delta T_\beta + (B_B\alpha + 2C_B\alpha tol)\Delta T\right] \\ &\approx I_{o,n} R_L B_B(\beta tol\Delta T_\beta + \alpha\Delta T). \end{aligned} \tag{C.12}$$

For laboratory conditions, the variations of temperature at the current source location are similar to those one in the load, i.e., $\Delta T \approx \Delta T_\beta$. This leads to

$$Y_{\mathrm{B}} V_L \approx I_{\mathrm{o,n}} R_{\mathrm{L}} B_{\mathrm{B}} (\beta tol + \alpha) \Delta T. \tag{C.13}$$

In the same way as for Y_{B}, the term A in Eq. (C.2) can be expanded as

$$
\begin{aligned}
A &\approx \frac{R_2}{R_1 R_{4\mathrm{B}}} - \frac{R_2 (R_1 - 3R_{4\mathrm{A}})}{R_1 R_{4\mathrm{B}} (R_1 + R_{4\mathrm{A}})} x \\
&\quad + \frac{R_2 (R_1^2 - 2R_1 R_{4\mathrm{A}} + 5R_{4\mathrm{A}}^2)}{R_1 R_{4\mathrm{B}} (R_1 + R_{4\mathrm{A}})^2} x^2 \\
&= A_{\mathrm{A}} + B_{\mathrm{A}} x + C_{\mathrm{A}} x^2.
\end{aligned}
\tag{C.14}
$$

Rearranging with the aforementioned considerations, we have

$$
\begin{aligned}
A V_{\mathrm{i}} &\approx [(B_{\mathrm{A}} + 2C_{\mathrm{A}} tol) \alpha V_i] \Delta T \\
&\approx B_{\mathrm{A}} \alpha V_i \Delta T.
\end{aligned}
\tag{C.15}
$$

Finally, the output current in terms of temperature is

$$I_o \approx [B_{\mathrm{A}} V_i \alpha + I_{\mathrm{o,n}} R_{\mathrm{L}} B_{\mathrm{B}} (\beta tol + \alpha)] \Delta T.$$

Substituting $I_{\mathrm{o,n}} = 4\,\mathrm{mA}$, $R_{\mathrm{L}} = 1.8\,\mathrm{k\Omega}$, $\beta = 4000\,\mathrm{ppm\,K^{-1}}$, $R_1 = R_3 = 100\,\mathrm{k\Omega}$, $R_2 = R_{4\mathrm{A}} + R_{4\mathrm{B}} = 10\,\mathrm{k\Omega} + 267\,\Omega = 10.267\,\mathrm{k\Omega}$, $tol = 1\%$, and $\alpha = 100\,\mathrm{ppm\,K^{-1}}$, the calculated temperature coefficient of the current source is $1.2 \times 10^{-6}\,\mathrm{A\,K^{-1}}$. Consequently, if the required stability of the current source is $110\,\mathrm{nA\,Hz^{-1/2}}$ at $1\,\mathrm{mHz}$, the temperature fluctuations need to be lower than $91\,\mathrm{mK\,Hz^{-1/2}}$ also at $1\,\mathrm{mHz}$.

For satellite conditions, the thermal environment where the current source is located is different than in the load. That is, ΔT, which is outside of the LCA, is much greater than ΔT_B. Taking this into account, the output current is

$$I_o \approx (B_{\mathrm{A}} V_i + I_{\mathrm{o,n}} R_{\mathrm{L}} B_{\mathrm{B}}) \alpha \Delta T.$$

The temperature coefficient for this particular case is $0.8 \times 10^{-6}\,\mathrm{A\,K^{-1}}$. Therefore, the temperature fluctuations in the current source should be lower than $137\,\mathrm{mK\,Hz^{-1/2}}$ at $1\,\mathrm{mHz}$ in order to avoid excess noise due to the thermal contribution.

Appendix D

Errors and Temperature Coefficients of the Magnetic Measurement System with AMRs

We have analyzed a worst-case estimate of the temperature coefficients and errors for the different stages of the magnetic field monitoring system using AMRs. The theoretical expressions and results of the most important error contributions for the proposed instrumentation is given in this appendix. In particular, the temperature coefficient is a relevant parameter in the circuit design since the slow temperature drifts couple to the thermal dependence, thus showing up as low-frequency noise.

D.1   Sensitivity of the AMR Wheatstone bridge

The quantitative analysis was done along the measurement chain described in Chapter 3 (see Figure 3.4), where the contribution of each stage of the signal conditioning circuit is considered individually. These errors are divided into zero and gain errors. The latter, which are more common in our particular case, increase as the Wheatstone bridge gets more unbalanced. However, electro-magnetic feedback technique maintains the output voltage close to the null point (balanced bridge). Therefore, the gain errors barely affect the measurement. On the other hand, part of the zero errors are eliminated by means of the ac modulation when using the flipping technique.

The AMR sensor changes the value of its electrical resistance in response to an applied magnetic field. This resistance-magnetic field dependence can be modeled as in Eq. (3.2). Thus, the output voltage of the four-sensor Wheatstone bridge is given by

$$
\begin{aligned}
V_{\mathrm{o}} &= V_{\mathrm{b}} \left[\frac{R_{\mathrm{b,n}} + \Delta R_{\mathrm{b}}}{2 R_{\mathrm{b,n}}} - \frac{R_{\mathrm{b,n}} - \Delta R_{\mathrm{b}}}{2 R_{\mathrm{b,n}}} \right] = V_{\mathrm{b}} \frac{\Delta R_{\mathrm{b}}}{R_{\mathrm{b,n}}} = I_{\mathrm{b}} \Delta R_{\mathrm{b}} \tag{D.1} \\
&= I_{\mathrm{b}} \Delta R \frac{B_{\mathrm{m}}}{B_0} \sqrt{1 - \left(\frac{B_{\mathrm{m}}}{B_0} \right)^2} \Bigg|_{B_{\mathrm{m}} < B_0/2} \simeq I_{\mathrm{b}} \frac{\Delta R}{B_0} B_{\mathrm{m}},
\end{aligned}
$$

and the sensitivity of the bridge with the magnetic field (s_{b}) is calculated deriving the bridge output voltage

$$
s_{\mathrm{b}} = \frac{\mathrm{d} V_{\mathrm{o}}}{\mathrm{d} B_{\mathrm{m}}} = I_{\mathrm{b}} \frac{\Delta R}{B_0^2} \frac{B_0^2 - 2 B_{\mathrm{m}}^2}{\sqrt{B_0^2 - B_{\mathrm{m}}^2}} \Bigg|_{B_{\mathrm{m}} < B_0/2} \simeq I_{\mathrm{b}} \frac{\Delta R}{B_0}. \tag{D.2}
$$

By definition

$$
s_{\mathrm{b}} \doteq s_{\mathrm{AMR}} V_{\mathrm{b}}, \tag{D.3}
$$

where s_{AMR} is the sensitivity of the AMR. The output of the bridge is then

$$
V_{\mathrm{o}} = s_{\mathrm{AMR}} V_{\mathrm{b}} B_{\mathrm{m}}. \tag{D.4}
$$

Therefore, substituting into Eq. (D.1) we find

$$
\Delta R_{\mathrm{b}} = s_{\mathrm{AMR}} R_{\mathrm{b,n}} B_{\mathrm{m}}. \tag{D.5}
$$

According to the manufacturer, $s_{\mathrm{AMR}} = 32 \, \mu\mathrm{V \, V^{-1} \, \mu T^{-1}}$ and $R_{\mathrm{b,n}} = 850 \, \Omega$ are the typical sensitivity and nominal resistance of the AMR, respectively. In the following sections, each stage of the magnetic measurement system is analyzed separately.

D.2 Errors and temperature coefficients

D.2.1 Bridge current source

The Wheatstone bridge is powered by the current source shown in Figure D.1 with the purpose of minimizing the sensitivity to temperature of the magnetoresistance. In this circuit, the tolerance of the resistors and the operational amplifier non-idealities will affect the bridge voltages and thus the measurement.

Resistors

A gain error is caused by the tolerance of the resistor R_1 contained in the current source circuit. Assuming a worst-case estimate, the error can be calculated as
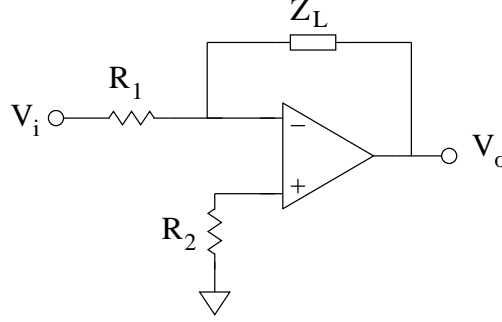
Figure D.1: Current source circuit for the magnetoresistance bridge. Z_L is the equivalent resistance of the AMR Wheatstone bridge.

$$\epsilon_{V,\text{tol s1}} = \frac{V_i}{R_1} \left[\frac{tol}{1 - tol} \right] \Delta R_b \simeq \frac{V_i}{R_1} tol \Delta R_b = I_b tol \Delta R_b, \tag{D.6}$$

where $tol = 0.01\%$ is the resistor tolerance and $I_b = 5\,\text{mA}$ is the bridge current. Therefore, the absolute error is

$$\epsilon_{V,\text{tol s1}} \simeq 5 \times 10^{-7} \cdot \Delta R_b. \tag{D.7}$$

Similarly, the output voltage also depends on the sensitivity of the resistance to temperature. Hence, this error can be expressed in units of V K^{-1} as

$$\epsilon_{V,\text{TC s1}} \simeq I_b \alpha_R \Delta R_b, \tag{D.8}$$

where $\alpha_R = 0.6\,\text{ppm K}^{-1}$ is the resistor temperature coefficient. Substituting into the equation, we obtain

$$\epsilon_{V,\text{TC s1}} \simeq 3 \times 10^{-9} \cdot \Delta R_b. \tag{D.9}$$

We have adopted the above mentioned parameters of the resistances (tol and α_R) along this whole appendix.

Operational Amplifier

The static op-amp limitations such as the input bias current (I_{bias}), the input offset current (I_{OS}), and the input offset voltage (V_{OS}), come into play as

$$\epsilon_{V,\text{op1 s1}} = \left[I_{\text{bias}} \left(\frac{R_2}{R_1} - 1 \right) + \frac{I_{\text{OS}}}{2} \left(\frac{R_2}{R_1} + 1 \right) + \frac{V_{\text{OS}}}{R_1} \right] \Delta R_b. \tag{D.10}$$

For the op-amp OP27G, we have $I_{\text{bias}} = 80\,\text{nA}$, $I_{\text{OS}} = 75\,\text{nA}$, and $V_{\text{OS}} = 100\,\mu\text{V}$. Considering $R_1 = 500\,\Omega$ and $R_2 = 350\,\Omega$, the error is

$$\epsilon_{V,\text{op1 s1}} \simeq 2.4 \times 10^{-7} \cdot \Delta R_\text{b}, \tag{D.11}$$

where the major contributor of the op-amp input-referred errors becomes the offset voltage. All these parameters are temperature-dependent. However, their influences are totally negligible ($\simeq 0.4 \times 10^{-12} \cdot \Delta R_\text{b}$) compared to the temperature coefficient of the resistance. Hence, thermal drifts of the op-amp input-referred errors will not be considered herein.

The open-loop parameters of the op-amp also appear as an error gain in the measurement. Taking into account the dc open-loop gain A_d and the differential input impedance Z_d, the current source output can be expressed as

$$I_\text{b} = \frac{V_\text{i}}{R_1} + \frac{V_\text{o}}{A_\text{d}} \left(\frac{1}{R_1} + \frac{1}{Z_\text{d}} \right) \simeq \frac{1}{R_1} \left(V_\text{i} + \frac{V_\text{b}}{A_\text{d}} \right). \tag{D.12}$$

Therefore, for a maximum bridge voltage the worst case error is

$$\epsilon_{V,\text{op2 s1}} = \frac{V_\text{b,max}}{R_1 A_\text{d}} \cdot \Delta R_\text{b} = \frac{I_\text{b} R_\text{b,max}}{R_1 A_\text{d}} \cdot \Delta R_\text{b}. \tag{D.13}$$

Substituting $R_\text{b,max} = 1.2\,\text{k}\Omega$ and $A_\text{d} = 6 \times 10^5$ for the OP27G into Eq. (D.13), we obtain

$$\epsilon_{V,\text{op2 s1}} \simeq 2 \times 10^{-8} \cdot \Delta R_\text{b}. \tag{D.14}$$

D.2.2 AMR Wheatstone bridge

The tolerance and temperature dependence of the magnetoresistances forming the Wheatstone bridge can show up as an error in the sensor readout. However, if the sensor is supplied with a constant current source and, besides, the flipping technique is used, the effects are mitigated. The output voltage is the average difference between two consecutive measurements ($V_\text{o,set}$ and $V_\text{o,reset}$) with opposite magnetic polarization

$$V_\text{o} = \frac{1}{2} \left(V_\text{o,set} - V_\text{o,reset} \right). \tag{D.15}$$

Therefore, the bridge offset caused by the resistance tolerance can be subtracted since the sensor output reverses the polarity, while the offset keeps unmodified. Nevertheless, the temperature dependence of the sensor continues to affect the magnetometer sensitivity. The error due to this effect in $\text{V}\,\text{K}^{-1}$ becomes

$$\epsilon_{V,\text{TC s2}} \simeq I_\text{b} \alpha_\text{sens} \Delta R_\text{b} = 3 \times 10^{-6} \Delta R_\text{b}, \tag{D.16}$$

for $\alpha_\text{sens} = 0.06\%\,\text{K}^{-1}$.

D.2.3 Instrumentation amplifier

The common-mode voltage signal of the bridge can produce a zero error due to the finite CMRR of the instrumentation amplifier. For the flipping technique, the averaged common-mode voltage at the input of the amplifier is given by

$$V_{\text{c,IA}} \;=\; \frac{V_{\text{b}}}{4}\left(\frac{R_{2,\text{set}}}{R_{1,\text{set}}+R_{2,\text{set}}}+\frac{R_{4,\text{set}}}{R_{3,\text{set}}+R_{4,\text{set}}}\right. \tag{D.17}$$

$$\left.-\frac{R_{2,\text{reset}}}{R_{1,\text{reset}}+R_{2,\text{reset}}}-\frac{R_{4,\text{reset}}}{R_{3,\text{reset}}+R_{4,\text{reset}}}\right) \tag{D.18}$$

where

$$R_{1,\text{set}}=R_{\text{b,n}}-\Delta R_{\text{b}} \qquad R_{1,\text{reset}}=R_{\text{b,n}}+\Delta R_{\text{b}} \tag{D.19}$$

$$R_{2,\text{set}}=R_{\text{b,n}}+\Delta R_{\text{b}} \qquad R_{2,\text{reset}}=R_{\text{b,n}}-\Delta R_{\text{b}} \tag{D.20}$$

$$R_{3,\text{set}}=R_{\text{b,n}}+\Delta R_{\text{b}} \qquad R_{3,\text{reset}}=R_{\text{b,n}}-\Delta R_{\text{b}} \tag{D.21}$$

$$R_{4,\text{set}}=R_{\text{b,n}}-\Delta R_{\text{b}} \qquad R_{4,\text{reset}}=R_{\text{b,n}}+\Delta R_{\text{b}} \tag{D.22}$$

Therefore, the common-mode voltage is canceled out during the modulation process and the zero errors are removed.

On the other hand, the mismatches of the IA internal resistors affect the gain accuracy of the circuit. Hence, the error referred to the input caused by the gain accuracy is given by

$$\epsilon_{\text{V,tol s3}}=I_{\text{b}}\cdot\text{tol}_{\text{G}_{\text{IA}}}\cdot\Delta R_{\text{b}}. \tag{D.23}$$

The gain error given by the manufacturer for the AD524B with a gain of $100\,\text{V V}^{-1}$ is 0.35%, this gives

$$\epsilon_{\text{V,tol s3}}=1.75\times10^{-5}\cdot\Delta R_{\text{b}}. \tag{D.24}$$

In the same way, the error due to the thermal dependence of the IA gain is

$$\epsilon_{\text{V,TC s3}}=I_{\text{b}}\cdot\alpha_{\text{G}_{\text{IA}}}\cdot\Delta R_{\text{b}}, \tag{D.25}$$

substituting $\alpha_{\text{G}_{\text{IA}}}=25\,\text{ppm K}^{-1}$, we get

$$\epsilon_{\text{V,TC s3}}=1.25\times10^{-7}\cdot\Delta R_{\text{b}}. \tag{D.26}$$

D.2.4 Demodulator

The outputs for the two switch states of the synchronous demodulator shown in Figure D.2 are

$$V_{\text{o,no–inv}} \;=\; V_{\text{i,set}}, \tag{D.27}$$

$$V_{\text{o,inv}} \;=\; -\frac{R_2}{R_1}V_{\text{i,reset}}, \tag{D.28}$$

where $V_{\text{o,no–inv}}$ and $V_{\text{o,inv}}$ are the demodulator outputs for the non-inverting and inverting configuration, $V_{\text{i,set}} = V_{\text{i}} + V_{\text{offset}}$, and $V_{\text{i,reset}} = -V_{\text{i}} + V_{\text{offset}}$. Assuming the demodulator output as the averaged difference between two samples for each configuration, we get

$$V_{\text{o}} = \frac{V_{\text{i}}}{2}\left(1 + \frac{R_2}{R_1}\right).$$

(D.29)
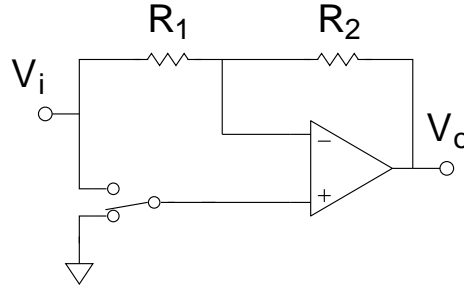
Figure D.2: Synchronous demodulator circuit.

Resistors

For the nominal value of the resistors $R_2 = R_1$, the worst-case error due to the resistors tolerances is referred to the input as

$$\epsilon_{\text{V,tol\,s4}} = V_{\text{i}}\frac{R_2}{R_1}\left[\frac{tol}{1-tol}\right] \simeq V_{\text{i}}\frac{R_2}{R_1}tol = I_{\text{b}}tol\Delta R_{\text{b}},$$

(D.30)

thus

$$\epsilon_{\text{V,tol\,s4}} \simeq 5 \times 10^{-7} \cdot \Delta R_{\text{b}}.$$

(D.31)

In a similar manner, the temperature coefficient of the resistor has an effect on the demodulator output. The error referred to the input can be expressed as

$$\epsilon_{\text{V,TC\,s4}} \simeq I_{\text{b}}\alpha\Delta R_{\text{b}} = 3 \times 10^{-9} \cdot \Delta R_{\text{b}}$$

(D.32)

Operational amplifier: offset voltage, offset current and bias current

Here we consider voltage offset, input bias and offset current of the operational amplifier for the analysis of errors (see Figure D.3). The voltage referred to the input for both switch configuration (inverting and non-inverting configuration) are

$$V_{\text{no–inv}} \;=\; I_{\text{b}}\Delta R_{\text{b}} + \frac{1}{G_{\text{IA}}}\left[V_{\text{offset}}\left(1 + \frac{R_2}{R_1}\right) + \left(I_{\text{bias}} - \frac{I_{\text{OS}}}{2}\right)R_2 \right], \quad \text{(D.33)}$$

$$V_{\text{inv}} \;=\; \frac{R_2}{R_1}I_{\text{b}}\Delta R_{\text{b}} + \frac{1}{G_{\text{IA}}}\left[V_{\text{offset}}\left(1 + \frac{R_2}{R_1}\right) + \left(I_{\text{bias}} - \frac{I_{\text{OS}}}{2}\right)R_2 \right], \text{(D.34)}$$

where G_{IA} is the gain of the instrumentation amplifier. In this case, the offset and bias effects of the op-amp are not canceled out and appear as a *zero* error in the measurement

$$\epsilon_{\text{V,op1 s4}} = \frac{1}{G_{\text{IA}}}\left(2|V_{\text{offset}}| + \left(|I_{\text{bias}}| + \left|\frac{I_{\text{OS}}}{2}\right|\right)R_2 \right). \qquad \text{(D.35)}$$
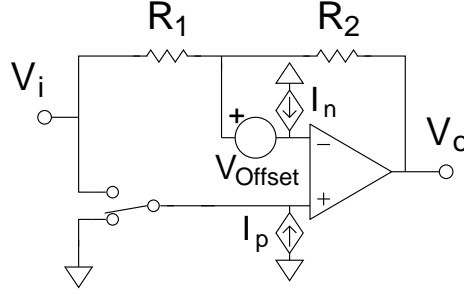
Figure D.3: Demodulator circuit including offset voltage and currents at the input terminals of the op-amp.

Operational amplifier: open loop response

In this section, the differential gain, the common-mode gain, the differential input resistance, and the common-mode input resistance of the op-amp are considered for the error analysis. Figure D.4 shows the equivalent circuit model for the non-inverting amplifier with the errors sources included in the estimate. The gain for this configuration is

$$\frac{V_{\text{o}}}{V_{\text{i}}} = \frac{\left[1 + \frac{R_2}{R_1} + R_2\left(\frac{1}{Z_{\text{d}}} + \frac{1}{Z_{\text{c}}}\right)\right]\frac{1}{2 \cdot CMRR} + 1 + \frac{R_2}{Z_{\text{cm}}}}{1 + \left(1 + \frac{R_2}{R_1}\right)\frac{1}{A_{\text{d}}} + R_2\left(\frac{1}{Z_{\text{d}}} + \frac{1}{Z_{\text{c}}}\right)}. \qquad \text{(D.36)}$$

Hence, for the worst case error we get

$$\epsilon_{\text{no–inv}} \simeq \left(1 + \frac{R_2}{R_1}\right)\left(\left|\frac{1}{CMRR}\right| + \left|\frac{1}{A_{\text{d}}}\right|\right) + \frac{R_2}{Z\text{c}} \qquad \text{(D.37)}$$
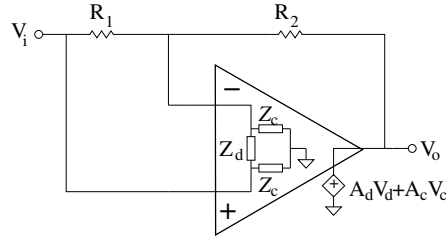
Figure D.4: Operational amplifier with non-inverting configuration including open loop gain and input impedances.

In a similar way, we have calculated the error for the inverting amplifier shown in Figure D.5. For this configuration the effect of the CMRR is negligible and it has not been taken into account.
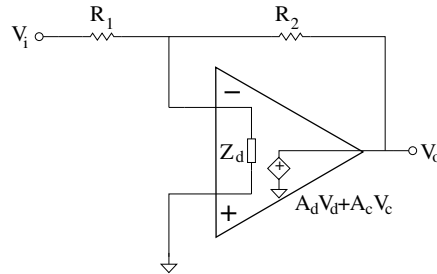
Figure D.5: Operational amplifier with inverting configuration including open loop gain and input impedance.

In this case, the gain of the circuit is

$$\frac{V_\text{o}}{V_\text{i}} = \frac{-A_\text{d}R_2}{R_1(A_\text{d}+1) + R_2 + \frac{R_1 R_2}{Z_\text{d}}}. \tag{D.38}$$

Assuming R_1 is equal to R_2 and Z_d much larger than R_2, the simplified expression for the error is

$$\epsilon_\text{inv} \simeq \frac{\frac{R_2}{R_1}}{1 + \frac{A_\text{d}}{1+\frac{R_2}{R_1}+\frac{R_2}{Z_\text{d}}}} \simeq \frac{2}{A_\text{d}}. \tag{D.39}$$

Substituting $A_\text{d} = 6 \times 10^5$, CMRR = 100 000, $Z_\text{d} = 4\,\text{M}\Omega$, $Z_\text{c} = 2\,\text{G}\Omega$ and $R = 10\,\text{k}\Omega$ into the Eqs. (D.37) and (D.39), the averaged difference error of both configuration is

$$\epsilon_\text{V,op2 s4} \simeq 7.9 \times 10^{-8} \cdot \Delta R_\text{b}. \tag{D.40}$$

D.2.5 Integrator

Figure D.6 shows the integrator circuit that we have considered for the error analysis.
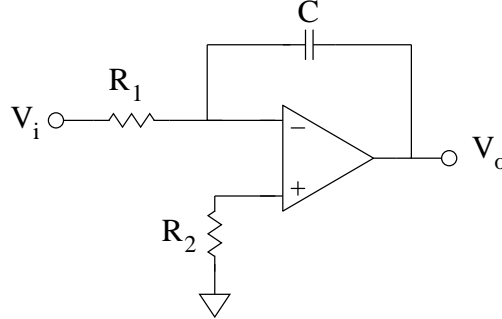
Figure D.6: Integrator circuit.

Resistor and capacitor

The error referred to the input caused by the tolerance of the resistor and the capacitor is given by

$$\epsilon_{V,\text{tol s5}} = \left(tol_R^2 + tol_C^2\right)^{1/2} I_b \Delta R_b, \tag{D.41}$$

where $tol_R = 0.01\%$ is the resistance tolerance and $tol_C = 5\%$ is the capacitor tolerance. The error is then

$$\epsilon_{V,\text{tol s5}} = 2.5 \times 10^{-4} \cdot \Delta R_b. \tag{D.42}$$

In similarity with the previous estimation, the relative error due to the thermal coefficient of the passive components is

$$\epsilon_{V,\text{TC s5}} = \left(\alpha_R^2 + \alpha_C^2\right)^{1/2} I_b \Delta R_b, \tag{D.43}$$

where $\alpha_R = 0.6\,\text{ppm}\,\text{K}^{-1}$ and $\alpha_C = 30\,\text{ppm}\,\text{K}^{-1}$ are the temperature coefficients of the resistor and the capacitor, respectively. Substituting in Eq. (D.43), the error in $\text{V}\,\text{K}^{-1}$ becomes

$$\epsilon_{V,\text{TC s5}} = 1.5 \times 10^{-7} \cdot \Delta R_b. \tag{D.44}$$

Operational amplifier: open loop response

The open loop gain response of an op-amp can be described by

$$A(s) = \frac{A_d}{1 + T_o s}, \tag{D.45}$$

where $1/T_o$ is the dominant-pole frequency.
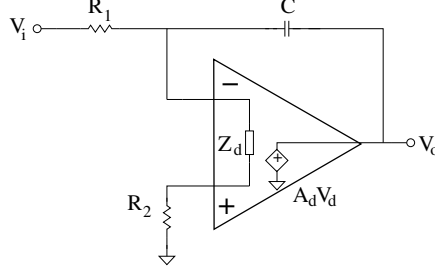
Figure D.7: Integrator circuit including differential input impedance and finite open loop gain.

Considering the open loop gain and the input impedance of the op-amp (see Figure D.7), the gain of the integrator is

$$\frac{V_o(s)}{V_i(s)} = \left[\frac{-1}{R_1 C s} \right] \left[\frac{1}{1 + \left(\frac{1 + T_o s}{A_d} \right) \left(1 + \frac{1}{R_p C s} \right)} \right], \tag{D.46}$$

where R_p is the equivalent of the parallel combination of Z_d and R_1. Due to the large differential gain we can simplified Eq. (D.46) as

$$\frac{V_o(s)}{V_i(s)} = \left[\frac{-1}{R_1 C s} \right] \left[\frac{1}{1 + \frac{s}{\omega_1} + \frac{1}{A_d R_p C s}} \right], \tag{D.47}$$

where $\omega_1 \simeq A_d / T_o$ is the amplifier unity gain bandwidth. Therefore, the low frequency response of an integrator can be estimated as

$$\frac{V_o(s)}{V_i(s)} = \left[\frac{-1}{R_1 C s} \right] \left[\frac{1}{1 + \frac{1}{A_d R_p C s}} \right] = \frac{A_d R_p / R_1}{1 + A_d R_p C s}. \tag{D.48}$$

This equation is analogous to an ideal integrator circuit with a feedback resistor in parallel with the capacitor (see Figure D.8).
The response to a step input whose Laplace transform is V_i/s is substituted in Eq. (D.48)

$$V_o(s) = V_i \frac{A_d R_p}{R_1} \left(\frac{1}{s} - \frac{1}{s + \frac{1}{A_d R_p C}} \right), \tag{D.49}$$
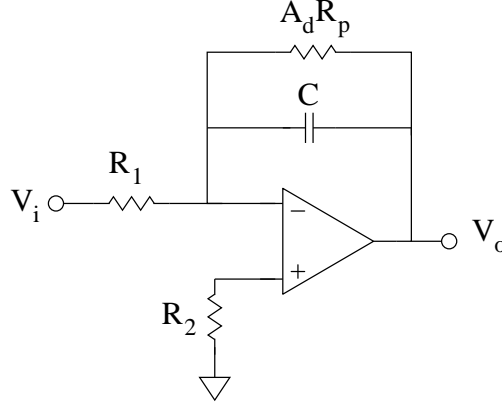
Figure D.8: Equivalent circuit of the integrator for low frequency errors due to finite gain.

and the inverse Laplace transform is

$$V_o(t) = V_i \frac{A_d R_p}{R_1} \left(1 - e^{\frac{-t}{A_d R_p C}} \right). \tag{D.50}$$

Thus, expanding the power series we have

$$V_o(t) \simeq V_i \left[\frac{t}{R_1 C} - \frac{t^2}{2 A_d R_p R_1 C^2} \right], \tag{D.51}$$

where the response of an ideal integrator corresponds to the first term, and the second term is the output error of the integrator. Then, the error is referred to the input as

$$\epsilon_{V,op\ s5} \simeq \frac{t}{2 A_d R_p C} I_b \Delta R_b, \tag{D.52}$$

where $R_1 = 10\,\text{k}\Omega$, $R_p = R_1 // Z_d \simeq 10\,\text{k}\Omega$, $C = 1\,\mu\text{F}$, and $t = 200\,\text{ms}$ is the integration time. Finally, the error is accounted for

$$\epsilon_{V,op\ s5} \simeq 8.3 \times 10^{-8} \cdot \Delta R_b \tag{D.53}$$

We remark that a second integrator between the output and the reference terminal of the IA is used for offset compensation. The errors for this stage are also given by Eqs. (D.43) and (D.52).

D.2.6 Compensation coil current source

The current source in the last stage of the circuit uses the same typology than in Section D.2.1 (see Figure D.1). Hence, the error due to the resistor tolerance can be expressed as

$$\epsilon_{V,\mathrm{tol\,s6}} \simeq 5 \times 10^{-7} \cdot \Delta R_\mathrm{b}, \tag{D.54}$$

and the thermal dependence in $\mathrm{V\,K^{-1}}$ is

$$\epsilon_{V,\mathrm{TC\,s6}} \simeq 3 \times 10^{-9} \cdot \Delta R_\mathrm{b}. \tag{D.55}$$

Operational Amplifier

Taking into account the dc open-loop gain and the differential input impedance, the current output can be expressed as

$$I_{Z_\mathrm{L}} = \frac{V_\mathrm{i}}{R_1} + \frac{V_\mathrm{o}}{A_\mathrm{d}}\left(\frac{1}{R_1} + \frac{1}{Z_\mathrm{d}}\right) \simeq \frac{1}{R_1}\left(V_\mathrm{i} + \frac{V_\mathrm{o}}{A_\mathrm{d}}\right). \tag{D.56}$$

In this case, the output voltage of the circuit is

$$V_\mathrm{o} = -V_\mathrm{i}\frac{A_\mathrm{d}}{1 + \frac{R_1}{Z_\mathrm{d}} + \frac{R_1}{Z_\mathrm{L}}(1 + A_\mathrm{d})} \simeq -V_\mathrm{i}\frac{A_\mathrm{d}}{1 + \frac{R_1}{Z_\mathrm{L}}A_\mathrm{d}}. \tag{D.57}$$

Hence, the error referred to the input is

$$\epsilon_{V,\mathrm{op\,s6}} \simeq -\frac{I_\mathrm{b}}{1 + \frac{R_1}{Z_\mathrm{L}}A_\mathrm{d}}\Delta R_\mathrm{b}. \tag{D.58}$$

Substituting $Z_\mathrm{L} = 3.5\,\Omega$ (max. value), $A_\mathrm{d} = 6\times10^5$, and $R_1 = 500\,\Omega$ into Eq. (D.58), the error is

$$\epsilon_{V,\mathrm{op\,s6}} \simeq -5.8 \times 10^{-11} \cdot \Delta R_\mathrm{b}. \tag{D.59}$$

D.2.7   Analog-to-digital converter

Full scale error

The main error contribution to the dc accuracy of the ADC is the full scale error $(tol_{\mathrm{G_{A/D}}})$. The error referred to the input of the system is

$$\epsilon_{V,\,\mathrm{s7}} = I_\mathrm{b} \cdot \mathrm{tol}_{\mathrm{G_{A/D}}} \cdot \Delta R_\mathrm{b}, \tag{D.60}$$

where the error for $\mathrm{tol}_{\mathrm{G_{A/D}}} = 0.5\%$ is

$$\epsilon_{V,\,\mathrm{s7}} = 2.5 \times 10^{-5} \cdot \Delta R_\mathrm{b}. \tag{D.61}$$

On the other hand, the error caused by the thermal dependence is

$$\epsilon_{V,\mathrm{TC\,s7}} = I_\mathrm{b} \cdot \alpha_{\mathrm{G_{A/D}}} \cdot \Delta R_\mathrm{b}, \tag{D.62}$$

for $\alpha_{\mathrm{G_{A/D}}} = 7\,\mathrm{ppm\,K^{-1}}$ as the temperature coefficient of the ADC, we obtain

$$\epsilon_{V,\mathrm{TC\,s7}} = 3.5 \times 10^{-8} \cdot \Delta R_\mathrm{b}. \tag{D.63}$$

D.3   Total error and temperature coefficient

Table D.1 summarizes the gain errors, zero errors and temperature coefficients for the different circuits contained in the magnetic measurement system.

Table D.1: Errors and temperature coefficients for the stages of the circuit.

Stage	Gain error [V]	Zero error [V]	TC [$\mathrm{V\,K^{-1}}$]
Curr. source res.	$5 \times 10^{-7} \cdot \Delta R_\mathrm{b}$	—	$3 \times 10^{-9} \cdot \Delta R_\mathrm{b}$
Curr. source OP1	$2.4 \times 10^{-7} \cdot \Delta R_\mathrm{b}$	—	—
Curr. source OP2	$2 \times 10^{-8} \cdot \Delta R_\mathrm{b}$	—	—
AMR bridge	—	—	$3 \times 10^{-6} \cdot \Delta R_\mathrm{b}$
IA	$1.75 \times 10^{-5} \cdot \Delta R_\mathrm{b}$	—	$1.25 \times 10^{-7} \cdot \Delta R_\mathrm{b}$
Int. res. (offset comp.)	$2.5 \times 10^{-4} \cdot \Delta R_\mathrm{b}$	—	$1.5 \times 10^{-7} \cdot \Delta R_\mathrm{b}$
Int. OA (offset comp.)	$8.3 \times 10^{-9} \cdot \Delta R_\mathrm{b}$	—	—
Demod. res.	$5 \times 10^{-7} \cdot \Delta R_\mathrm{b}$	—	$3 \times 10^{-9} \cdot \Delta R_\mathrm{b}$
Demod. OP	$7.9 \times 10^{-8} \cdot \Delta R_\mathrm{b}$	1.38×10^{-5}	—
Int. res.	$2.5 \times 10^{-4} \cdot \Delta R_\mathrm{b}$	—	$1.5 \times 10^{-7} \cdot \Delta R_\mathrm{b}$
Int. OA	$8.3 \times 10^{-8} \cdot \Delta R_\mathrm{b}$	—	—
Comp. source res.	$5 \times 10^{-7} \cdot \Delta R_\mathrm{b}$	—	$3 \times 10^{-9} \cdot \Delta R_\mathrm{b}$
Comp. source OA	$5.8 \times 10^{-11} \cdot \Delta R_\mathrm{b}$	—	—
ADC	$2.5 \times 10^{-5} \cdot \Delta R_\mathrm{b}$	—	$3.5 \times 10^{-8} \cdot \Delta R_\mathrm{b}$
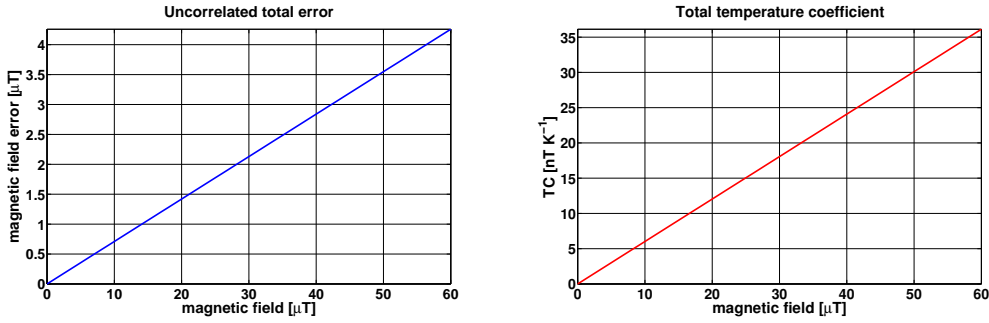
Figure D.9:   Equivalent magnetic error (left) and temperature coefficient (right) of the system as a function of the magnetic field.

Figure D.9 shows the total error and temperature coefficient of the whole circuit as a function of the magnetic field.[1] For a worst-case condition, we added the

---

[1]Null point operation due to the close loop controller is not considered.

different errors and temperature coefficients quadratically assuming them as independent systematic errors. We remark the importance of the electro-magnetic feedback technique in order to minimize the overall error and temperature coefficient of the magnetic measurement system.

Appendix E

Magnetic Measurement System in the ^{3}Cat-2 CubeSat

The ^{3}Cat-2 is a six-unit (6U) CubeSat mission coordinated by the UPC Remote Sensing Laboratory in collaboration with the Institut d'Estudis Espacials de Catalunya (IEEC). The main objective of the ^{3}Cat-2 is the study of ocean altimetry by means of global navigation satellite system reflectometry (GNSS-R). Moreover, the ^{3}Cat-2 is also used for validation of novel technological concepts under operational mission conditions.

The following appendix describes the work done for the CubeSat implementation of a simplified version of the magnetic measurement system designed in Chapter 3.

E.1   Objective

The aim of this work is to serve the ^{3}Cat-2 CubeSat as a platform for in-orbit demonstration of the currently proposed magnetic measurement system for eLISA. This will make it possible to advance the TRL of the instrument. Ideally, eLISA requires a TRL of 5-6 by 2019. This is before the L3 mission concept selection of the ESA science program in 2020.

The main characteristic of our experiment is that the AMR sensors integrated in the payload (eLISA-AMR payload) are magnetically shielded to low-frequency fluctuations by using a mu-metal enclosure. That will make it possible to characterize the low-frequency noise performance of the system under the low Earth orbit (LEO) space environment. Therefore, ^{3}Cat-2 CubeSat will offer the opportunity to measure the capability of the instrument and will guide the progress towards the improved magnetic measurement system for eLISA.

E.2 CubeSat requirements for the eLISA-AMR payload

Low-cost satellites have especially demanding constraints regarding power consumption, physical dimensions, weight, and on-board data handling, which restrict the performance of the on-board instrumentation. Table E.1 shows the principal requirements imposed by the ³Cat-2 project for our electronics board. Thus, the initial design was slightly changed by trading off magnetometer performance for CubeSat requirements.

Table E.1: ³Cat-2 requirements for the eLISA-AMR payload.

Parameter	Value
Power line	+5V
Power consumption	$< 0.5\,\mathrm{W}$ (lowest workable level)
Dimensions	95.89 mm x 90.17 mm x 30 mm
Mass	$\leq 100\,\mathrm{g}$
Temperature range	-40 a $85\,^{\circ}\mathrm{C}$
Maximum continuous operation time per test	3 hours
Bus interface (OBC-payload)	I²C

Moreover, the payload is required to work in autonomous operations. Therefore, a microcontroller (uC) and E²PROM devices were added to the front-end electronics in order to store the data till the request from the on-board computer (OBC).

E.3 Specifications of the eLISA-AMR payload

Due to the strict aforementioned requirements, the most relevant modifications from the original design that affect the performance of the magnetic measurement system are: (i) use of operational amplifiers with lower power consumption, albeit higher noise; (ii) magnetic field range reduction (lower feedback current); and (iii) the three axes of the magnetometer are not powered simultaneously, thus, only data from one axis can be acquired in every run. Besides, we remark that the system can not be characterized at the lower end of the eLISA bandwidth (0.1 mHz) with a maximum of 3 hours of data per run. Consequently, we have to settle for this limitation estimating the noise spectral densities with around ten points at 1 mHz. A brief overview of the principal characteristics of the eLISA-AMR payload is offered below.

Magnetic shielding

The AMR magnetometers were placed inside a small cylindrical enclosure for the purpose of shielding the environmental magnetic field, thus allowing for in-flight low-frequency noise characterization of the magnetometers. The local spacecraft field

will be dominated by the Earth geomagnetic field and the local spacecraft magnetic sources,[1] such as the the magnetic field generated by the active magnetorquer used for attitude control.

The magnetic shield consists of three subsequent mu-metal layers surrounding the sensor head of the magnetometer. The outermost cylinder is a 0.254 mm-thick layer, the centered one has a thickness 0.152 mm, and the innermost shield is a 0.1 mm-thick layer. These three layers are separated by gaps of around 4.5 mm each and assembled to the board by means of a cylindrical aluminum structure that has a diameter of 29 mm and is 38.6-mm-long (see Figure E.1).
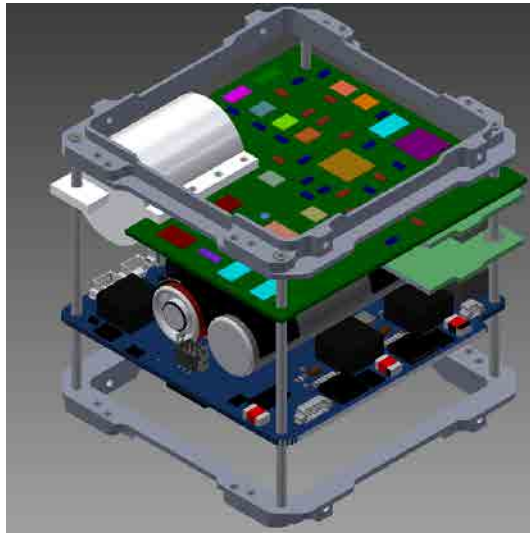
Figure E.1: Drawing of the magnetic measurement system with the mu-metal shield integrated in one standard slot of the CubeSat. For the sake of clarity, only one unit (1U) of the 6U CubeSat is shown. The CubeSat power module (GomSpace/NanoPower P31U) is allocated right under our payload.

Low-frequency noise performance

Low-frequency noise measurements were taken for the three axes of the magnetometer with the small built-in permalloy magnetic shield. As mentioned before, during in-flight mission operations the duration of the runs for the magnetic experiment will be no longer than three hours. Therefore, the noise spectral density will be barely estimated down to 1 mHz. For the lab test, the data were also taken with a short duration of three hours for comparison purposes during the established mission procedures. The equivalent magnetic field noise shown in Figure E.2 is similar to that obtained for the eLISA prototype (see Figure 3.11). As a result, we consider the unit

---

[1]The Earth magnetic field at a LEO altitude of 400 km varies between 25 μT and 50 μT [96].

together with the magnetic shield capable of performing the noise characterization experiment on-board the ³Cat-2 CubeSat.
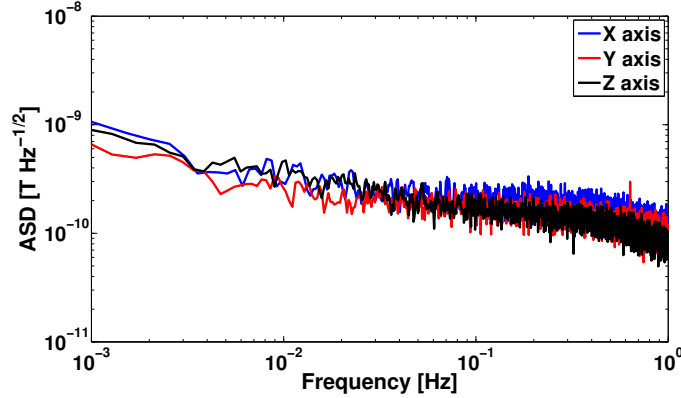
Figure E.2: Equivalent magnetic field spectral densities of the eLISA-AMR payload for 3 h measurements.

More details about the noise performance of the proposed magnetic measurement system for eLISA are described in Chapter 3.

Data storage

The payload employs two serial E²PROM devices summing a total of 256 kB of storage capability, where the synchronous serial communication between the uC and the memories is operated via SPI bus. Once the measurement has been finished, the payload goes into the idle state, switching off the analog signal conditioning circuits (low-power consumption). Then, after receiving the OBC request, the data are sent from the memories to the OBC through the uC using I²C interface . The data rate of the magnetic measurements from the uC to the E²PROM is

$$bitrate = \overbrace{4\,\text{byte}}^{\text{magnetic data}} \cdot 8 \cdot \overbrace{5.5}^{f_\text{s}} = 176\,\text{bps}, \tag{E.1}$$

which results in a maximum storage time of 3 hours and 18 minutes per run.

Sensor head

The sensor head is formed by a uniaxial (HMC1001) and a biaxial AMR (HMC1002). The configuration of the magnetometers was mounted directly on the electronics board together with the analog and digital circuits in order to make the integration easier. The spatial distribution of the sensor head for the triaxial magnetometer is

shown in Figure E.3, where the two devices were placed along their longitudinal axes so as to reduce the diameter of the innermost shield, which is set by the gap between the height of the uniaxial sensor and the inner layer of the magnetic enclosure.
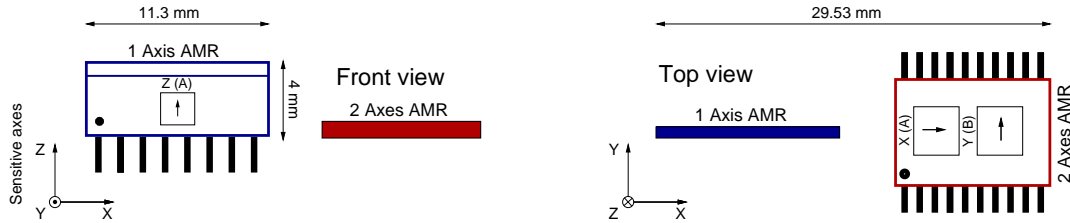
Figure E.3: Spatial distribution of the uniaxial and biaxial AMR magnetometers in the CubeSat. Magnetic sensitive axes are displayed. Front (left) and top (right) view.

Overall specifications

The overall characteristics of the system were assessed and updated during the three development phases, i.e, the prototype, the engineering qualification model and the final flight model. The instrument meets the scientific measurement performance comfortably and the CubeSat requirements specified in Table E.1. The flight model of the board with the magnetic shield is shown in Figure E.4, which has been already integrated in the CubeSat.

Current work is being done on the debugging and validation of the interface software between the payload and the OBC.

Figure E.4: Flight model of the eLISA-AMR payload for the [3]Cat-2 mission. Right: payload integration of the flight model in the CubeSat.

A general outlook of the specifications for the eLISA-AMR payload is given in Table E.2.

Table E.2: Specifications of the magnetic monitoring system for the CubeSat.

Parameter	Symbol	Value
Field range	B_{range}	$\pm 15\,\mu\mathrm{T}$[a]
RTI temperature coefficient (Sensor + FEE)	TC_{rti}	$3 \cdot 10^{-6}\Delta R_{\mathrm{b,n}}\,\mathrm{V/K}$
Noise density	$S_{\mathrm{B}}^{1/2}$	$0.14\,\mathrm{nT\,Hz^{-1/2}}$ at 1 Hz $1\,\mathrm{nT\,Hz^{-1/2}}$ at 1 mHz
Input current	I_{bridge}	5 mA
Input voltage	V_{bridge}	4.25 V[b]
Linearity error		0.1% FS
Sensitivity	s_{AMR}	$254.5\,\mathrm{mV}/\mu\mathrm{T}$[c]
ADC resolution	ΔB_{ADC}	0.6 nT
Equivalent resolution	$\Delta B_{\mathrm{eq.}}$	0.01 nT[d]
Bandwidth	BW	2.75 Hz
AMR operating temperature		-55ºC to +150ºC
Spatial resolution		< 1 mm
Power consumption	P_{max}	0.32 W
	P_{nominal}	0.26 W
	P_{standby}	0.025 W
Weight		76.6 g

[a]Range limited by the output current of the op-amp.

[b]For a typical bridge resistance of $850\,\Omega$.

[c]Typical value for electro-magnetic feedback with a feedback resistor of $499\,\Omega$.

[d]$16 + \frac{1}{2}\log_2 N$ for $N = 3072$ samples. Resolution is limited by AMR noise density.

Appendix F

Magnetic Sources in LISA Pathfinder

A significant number of LISA Pathfinder units were characterized by using a mobile coil facility (MCF) in order to identify their magnetic contributions to the local spacecraft field. A representative set of these subsystems was used with the purpose of mimicking the magnetic environment generated by the spacecraft (see Table F.1), where the dominant contributions are the cold gas latch valves. We remark that an important contribution to the total magnetic budget in LISA Pathfinder is due to the NTC temperature sensors positioned close to the TM. These magnetic sources are not considered here because temperature sensors with a lower intrinsic magnetic moment are expected to be used in eLISA.

Magnetic moment components and distributions of the dipole sources are known. However, only magnitudes and locations were used and considered fixed for our particular analysis. The dipole orientations of the different magnetic sources were randomly set in order to generate different magnetic scenarios and thus verify the efficiency of the interpolation method.

Table F.1: Positions and magnetic dipole moments of the 29 LISA Pathfinder subsystems considered for the evaluation of the interpolation approach described in Chapter 5. The measurements of the dipolar magnetic sources in LISA Pathfinder were carried out by Airbus DS [186].

	Dipole location			$|\mathbf{m}|$
	x [m]	y [m]	z [m]	[mA m^2]
Caging Mechanism Control Unit				
Dipole 1	-0.2570	-0.6247	0.5904	261.969
Continue on next page...				

Table F.1 — Continued

Data Management Unit				
Dipole 1	-0.4238	-0.6285	0.5989	38.033
Dipole 2	-0.3814	-0.5029	0.5750	9.504
IS FEE PCU				
Dipole 1	-0.2506	-0.3325	0.4139	0.200
Dipole 2	-0.3838	-0.5211	0.2869	19.119
Dipole 3	-0.4111	-0.5804	0.3019	6.235
Dipole 4	-0.3021	-0.6456	0.2539	7.063
IS FEE SAU		1		
Dipole 1	-0.5037	0.6208	0.6973	5.633
Dipole 2	-0.4579	0.4856	0.4502	12.001
IS FEE SAU 2				
Dipole 1	-0.2675	0.7150	0.4536	5.633
Dipole 2	-0.1732	0.6076	0.7005	12.001
Laser Assembly				
Dipole 1	0.7873	-0.7460	0.0618	6.512
Dipole 2	0.5140	-0.7826	0.1578	8.958
Dipole 3	0.6049	-0.6400	0.2089	17.295
Dipole 4	0.5659	-0.6025	0.0169	1.459
Laser Modulation Unit				
Dipole 1	0.6486	-0.6908	0.5478	3.362
Dipole 2	0.6777	-0.6984	0.5218	3.977
Phasemeter Unit				
Dipole 1	0.5660	-0.2188	0.5488	77.455
Dipole 2	0.5890	-0.2998	0.6338	60.814
Radiation Monitor				
Dipole 1	-0.5517	-0.1842	0.3591	20.151
Reference Laser Unit				
Dipole 1	0.6366	-0.7295	0.2679	4.236
Dipole 2	0.5960	-0.7419	0.3069	6.129
Sun Sensor 1				
Dipole 1	-0.3887	-0.8187	1.0107	1.158
Sun Sensor 2				
Dipole 1	0.3906	0.9740	1.0507	0.592
Sun Sensor 3				
Dipole 1	0.5106	0.8577	1.0107	1.225
Ultra-Violet Lamp Unit				
Dipole 1	-0.4258	-0.3368	0.5475	35.157

Continue on next page...

Cold gas latch valves				
Dipole 1	-0.2170	-0.8650	0.5560	824.621
Dipole 2	-0.7620	0.4120	0.5200	824.621
Dipole 3	0.6330	0.6240	0.5590	824.621

Bibliography

[1] Abbott B. P., Abbott R., Adhikari R., et al., 2009. LIGO: the Laser Interferometer Gravitational-Wave Observatory. *Rep. Prog. Phys.*, **72**(7), 076901.

[2] Abramovici A., Althouse W. E., Drever R. W. P., et al., 1992. LIGO - The Laser Interferometer Gravitational-Wave Observatory. *Science*, **256**, 325–333.

[3] Accadia T., Acernese F., Alshourbagy M., et al., 2012. Virgo: a laser interferometer to detect gravitational waves. *J. Instrum.*, **7**, 3012.

[4] Acernese F., Agathos M., Agatsuma K., et al., 2015. Advanced Virgo: a second-generation interferometric gravitational wave detector. *Class. Quantum Grav.*, **32**(2), 024001.

[5] Acernese F., Amico P., Alshourbagy M., et al., 2007. Status of Virgo detector. *Class. Quantum Grav.*, **24**, 381–392.

[6] Acosta V., Ledbetter M. P., Rochester S. M., et al., 2006. Nonlinear magneto-optical rotation with frequency-modulated light in the geophysical field range. *Phys. Rev. A*, **73**(5), 053404.

[7] Acuña M. H., 2002. Space-based magnetometers. *Rev. of Sci. Instruments.*, **73**, 3717–3736.

[8] Aguiar O. D., Andrade L. A., Camargo Filho L., et al., 2002. The Gravitational Wave Detector "Mario Schenberg": Status of the Project. *Brazilian J. of Phys.*, **32**, 866–868.

[9] Aguilera D. N., Ahlers H., Battelier B., et al., 2014. STE-QUEST–test of the universality of free fall using cold atom interferometry. *Class. Quantum Grav.*, **31**(11), 115010.

[10] Alexandrov E. B., Chaika M., and Kvostenko G., 1993. *Interference of Atomic States*. Springer-Verlag.

[11] Antonucci F., Armano M., Audley H., et al., 2011. From laboratory experiments to LISA Pathfinder: achieving LISA geodesic motion. *Class. Quantum Grav.*, **28**, 094002.

[12] Anza S., Armano M., Balaguer E., et al., 2005. The LTP experiment on the LISA Pathfinder mission. *Class. Quantum Grav.*, **22**, 125–148.

[13] Araújo H., Boatella C., Chmeissani M., et al., 2007. LISA and LISA PathFinder, the endeavour to detect low frequency GWs. *J. Phys. Conf. Ser.*, **66**, 012003.

[14] Araújo H. M., Howard A., Shaul D. N. A., and Sumner T. J., 2003. Electrostatic charging of cubic test masses in the LISA mission. *Class. Quantum Grav.*, **20**, 311.

[15] Araya A., Mio N., Tsubono K., et al., 1997. Optical mode cleaner with suspended mirrors. *Appl. Opt.*, **36**(7), 1446–1453.

[16] Armano M., Audley H., Auger G., et al., 2015. Disentangling the magnetic force noise contribution in LISA Pathfinder. *J. Phys. Conf. Ser.*, **610**(1), 012024.

[17] Armano M., Audley H., Auger G., et al., 2015. The LISA Pathfinder Mission. *J. Phys. Conf. Ser.*, **610**(1), 012005.

[18] Astone P., Baggio L., Bassan M., et al., 2010. IGEC2: A 17-month search for gravitational wave bursts in 2005-2007. *Phys. Rev. D*, **82**(2), 022003.

[19] Astone P., Bassan M., Bonifazi P., et al., 2002. The EXPLORER gravitational wave antenna: recent improvements and performances. *Class. Quantum Grav.*, **19**, 1905–1910.

[20] Astone P., Bassan M., Bonifazi P., et al., 1997. The gravitational wave detector NAUTILUS operating at T = 0.1 K. *Astroparticle Phys.*, **7**, 231–243.

[21] Audley H., Danzmann K., García Marín A., et al., 2011. The LISA Pathfinder interferometry-hardware and system testing. *Class. Quantum Grav.*, **28**, 094003.

[22] Auzinsh M., Budker D., and Rochester S., 2010. *Optically Polarized Atoms: Understanding Light-Atom Interactions*. Oxford University Press, Oxford.

[23] Baker C. A., Doyle D. D., Geltenbort P., et al., 2006. Improved Experimental Limit on the Electric Dipole Moment of the Neutron. *Phys. Rev. Lett.*, **97**(13), 131801.

166

[24] Balabas M. V., Budker D., Kitching J., Schwindt P. D. D., and Stalnaker J. E., 2006. Magnetometry with millimeter-scale antirelaxation-coated alkali-metal vapor cells. *J. Opt. Soc. Am. B*, **23**, 1001–1006.

[25] Balogh A., Beek T. J., Forsyth R. J., et al., 1992. The magnetic field investigation on the ULYSSES mission - Instrumentation and preliminary scientific results. *A&AS*, **92**, 221–236.

[26] Beker M., 2013. *Low-frequency Sensitivity of Next Generation Gravitational Wave Detectors*. Ph.D. thesis, Vrije Universiteit.

[27] Bender P. and the LISA Study Team, 1998. LISA for the Detection and Observation of Gravitational Waves. Pre-phase A. Tech. Rep. MPQ 233, Max-Planck-Institut für Quantenoptik.

[28] Bender P. L., 2014. Comparison of atom interferometry with laser interferometry for gravitational wave observations in space. *Phys. Rev. D*, **89**(6), 062004.

[29] Bennett W. R., 1948. Spectra of Quantized Signals. *Bell Syst. Tech. J.*, **27**(3), 446–472.

[30] Billingsley Aerospace & Defense, 2007. Spaceflight Magnetometer Acceptance Router: TFM100G4. Tech. Rep. SN 114-118, Billingsley.

[31] Blair D. G., Ivanov E. N., Tobar M. E., Turner P. J., van Kann F., and Heng I. S., 1995. High Sensitivity Gravitational Wave Antenna with Parametric Transducer Readout. *Phys. Rev. Lett.*, **74**, 1908–1911.

[32] Bonnin A., Zahzam N., Bidel Y., and Bresson A., 2013. Simultaneous Dual-Species Matter-Wave Accelerometer. *Phys. Rev. A*, **88**, 043615.

[33] Brown P., Whiteside B. J., Beek T. J., et al., 2014. Space magnetometer based on an anisotropic magnetoresistive hybrid sensor. *Rev. of Sci. Instruments*, **85**(12), 125117.

[34] Bubeck K., 2011. Magnetic Sniff Test of LTP EM Magnetometer. Tech. Rep. S2-ASD-TR-3130, Astrium.

[35] Budker D., Gawlik W., Kimball D. F., Rochester S. M., Yashchuk V. V., and Weis A., 2002. Resonant nonlinear magneto-optical effects in atoms. *Rev. Mod. Phys.*, **74**, 1153–1201.

[36] Budker D. and Kimball D. F. J., 2013. *Optical Magnetometry*. Cambridge University Press, New York.

[37] Canizares P., Chmeissani M., Conchillo A., et al., 2011. The LISA Pathfinder DMU and Radiation Monitor. *Class. Quantum Grav.*, **28**, 094004.

[38] Chong L., Jian L., Zhen Y., and Yong Z., 2013. Improved micro fluxgate sensor with double-layer Fe-based amorphous core. *Microsys. Technol.*, **19**(2), 167–172.

[39] Ciofi C., Cannatà G., Scandurra G., and Merlino R., 2007. A very low noise voltage reference for high sensitivity noise measurements. In *SPIE Conf. Ser.*, vol. 6600.

[40] Ciofi C., Giannetti R., Dattilo V., and Neri B., 1998. Ultra low-noise current sources. *IEEE Trans. Instrum. Meas.*, **47**(1), 78–81.

[41] Cohen-Tannoudji C. and Dupont-Roc J., 1972. Experimental Study of Zeeman Light Shifts in Weak Magnetic Fields. *Phys. Rev. A*, **5**, 968–984.

[42] Constable C. G. and Constable S. C., 2013. *Satellite Magnetic Field Measurements: Applications in Studying the Deep Earth*. American Geophysical Union.

[43] Danzmann K., 1992. Interferometric gravitational wave detectors become reality. In *Astronomische Gesellschaft Abstract Series*, vol. 7, 58–78.

[44] de Carvalho Benyosef L. C., Stael G. C., and Bochner M., 2008. Optimization of the magnetic properties of materials for fluxgate sensors. *Mater. Res.*, **11**, 145–149.

[45] Díaz–Aguiló M., García-Berro E., and Lobo A., 2009. Magnetic Experiments on Board the LTP. Tech. Rep. S2-IEC-TN-3044, IEEC.

[46] Diáz-Aguiló M., 2011. *Magnetic Diagnostics Algorithms for LISA Pathfinder: System Identification and Data Analysis*. Ph.D. thesis, Universitat Politècnica de Catalunya.

[47] Diaz-Aguiló M., García-Berro E., and Lobo A., 2012. Inflight magnetic characterization of the test masses onboard LISA Pathfinder. *Phys. Rev. D*, **85**(4), 042004.

[48] Diaz-Aguiló M., Lobo A., and García-Berro E., 2011. Neural network interpolation of the magnetic field for the LISA Pathfinder Diagnostics Subsystem. *Exp. Astron.*, **30**, 1–21.

[49] Diaz-Aguiló M., Mateos I., Ramos-Castro J., Lobo A., and García-Berro E., 2013. Design of the magnetic diagnostics unit onboard LISA Pathfinder. *Aerosp. Sci. Technol.*, **26**, 53–59.

[50] Díaz-Michelena M., 2009. Small Magnetic Sensors for Space Applications. *Sensors*, **9**(4), 2271.

[51] Dimopoulos S., Graham P. W., Hogan J. M., and Kasevich M. A., 2007. Testing General Relativity with Atom Interferometry. *Phys. Rev. Lett.*, **98**, 111102.

[52] Dimopoulos S., Graham P. W., Hogan J. M., Kasevich M. A., and Rajendran S., 2008. Atomic gravitational wave interferometric sensor. *Phys. Rev. D*, **78**, 122002.

[53] Dubetsky B. and Berman P. R., 2002. $\lambda/8$-period optical potentials. *Phys. Rev. A*, **66**(4), 045402.

[54] Dufay B., Saez S., Dolabdjian C., Yelon A., and Menard D., 2013. Development of a High Sensitivity Giant Magneto-Impedance Magnetometer: Comparison With a Commercial Flux-Gate. *IEEE Trans. on Magnetics*, **49**, 85–88.

[55] Eagleyard Photonics, 2010. Distributed Feedback Laser Data Sheet. Tech. Rep. EYF-DFB-0852-00150-1500-TOC03-000x Version 0.93, Eagleyard Photonics.

[56] Einstein A., 1916. Die Grundlage der allgemeinen Relativitätstheorie. *Annalen der Physik*, **354**, 769–822.

[57] eLISA Consortium, 2013. The Gravitational Universe. arXiv: 1305.5720.

[58] Fafone V., 2004. Resonant-mass detectors: status and perspectives. *Class. Quantum Grav.*, **21**, 377–386.

[59] Fertin D. and Trougnou L., 2007. LisaPF Test Masses Acceleration Noise due to Eddy Currents. Tech. Rep. S2-EST-TN-2016, ESTEC.

[60] Fertin D. and Trougnou L., 2010. Low Frequency Force due to Amplitude Modulated AC magnetic field. Tech. Rep. S2-EST-TN-3044, ESTEC.

[61] Folkner W. M., Buchman S., Byer R. L., et al., 2003. Disturbance reduction system: testing technology for precision formation control. In *SPIE Conf. Ser.*, vol. 4860, 221–228.

[62] Franco S., 2002. *Design with operational amplifiers and analog integrated circuits*. McGraw-Hill.

[63] Fray S., Diez C., Hänsch T. W., and Weitz M., 2004. Atomic Interferometer with Amplitude Gratings of Light and Its Applications to Atom Based Tests of the Equivalence Principle. *Phys. Rev. Lett.*, **93**, 240404.

[64] Freitas P. P., Ferreira R., Cardoso S., and Cardoso F., 2007. Magnetoresistive sensors. *J. Phys. Condens. Matter*, **19**(16), 165221.

[65] Gibert F., Nofrarias M., Karnesis N., et al., 2015. Thermo-elastic induced phase noise in the LISA Pathfinder spacecraft. *Class. Quantum Grav.*, **32**(4), 045014.

[66] Gordon D. and Brown R. E., 1972. Recent advances in fluxgate magnetometry. *IEEE Trans. on Magnetics*, **8**, 76–82.

[67] Graham P. W., Hogan J. M., Kasevich M. A., and Rajendran S., 2013. New Method for Gravitational Wave Detection with Atomic Sensors. *Phys. Rev. Lett.*, **110**(17), 171102.

[68] Grote H. and LIGO Scientific Collaboration, 2010. The GEO 600 status. *Class. Quantum Grav.*, **27**(8), 084003.

[69] Guzmán F., Flatscher R., Gerardi D., et al., 2013. LISA Technology package flight hardware test campaign. vol. 467 of *ASP Conf. Ser.*, 341.

[70] Hamilton P., Barter T., Kim G., Mukherjee B., and Müller H., 2012. Progress towards a test of the universality of free fall using a ^{6}Li-^{7}Li atom interferometer. In *APS Division of Atomic, Molecular and Optical Physics Meeting*, 5004.

[71] Harry G. M. and the LIGO Scientific Collaboration, 2010. Advanced LIGO: the next generation of gravitational wave detectors. *Class. Quantum Grav.*, **27**(8), 084006.

[72] Hauser H., Fulmek P., Haumer P., Vopalensky M., and Ripka P., 2003. Flipping field and stability in anisotropic magnetoresistive sensors. *Sens. Actuators A*, **106**(1-3), 121–125.

[73] Hauser H., Stangl G., Fallmann W., Chabicovsky R., and Riedling K., 2000. Magnetoresistive sensors. In *Proceedings of a Workshop at the Vienna University of Technology*, Preparation, Properties, and Applications of Thin Ferromagnetic Films.

[74] Heng I. S., Daw E., Giaime J., Hamilton W. O., Mchugh M. P., and Johnson W. W., 2002. Allegro: noise performance and the ongoing search for gravitational waves. *Class. Quantum Grav.*, **19**, 1889–1895.

[75] Hobbs G., 2013. The Parkes Pulsar Timing Array. *Class. Quantum Grav.*, **30**(22), 224007.

[76] Hogan J. M., Johnson D. M. S., Dickerson S., et al., 2011. An atomic gravitational wave interferometric sensor in low earth orbit (AGIS-LEO). *Gen. Relat. Gravit.*, **43**, 1953–2009.

[77] Honeywell, 2008. 1- and 2-Axis Magnetic Sensors HMC1001/1002/1021/1022. Tech. Rep. 900248 Rev C, Honeywell.

170

[78] Hooge F. N., 1994. 1/f noise sources. *IEEE Trans. Electron. Devices*, **41**, 1926–1935.

[79] Hooge F. N. and Hoppenbrouwers A. M. H., 1969. 1/f noise in continuous thin gold films. *Physica*, **45**, 386–392.

[80] Hueller M., Armano M., Carbone L., et al., 2005. Measuring the LISA test mass magnetic properties with a torsion pendulum. *Class. Quantum Grav.*, **22**(10), S521.

[81] Hughes S. A., 2003. Listening to the universe with gravitational-wave astronomy. *Ann. Phys.*, **303**, 142–178.

[82] Hulse R. A. and Taylor J. H., 1975. Discovery of a pulsar in a binary system. *ApJ*, **195**, L51–L53.

[83] Jackson J. D., 1999. *Classical Electrodynamics*. John Wiley & Sons.

[84] Janosek M. and Ripka P., 2009. PCB sensors in fluxgate magnetometer with controlled excitation. *Sens. Actuators A*, **151**(2), 141–144.

[85] Jensen K., Acosta V. M., Higbie J. M., Ledbetter M. P., Rochester S. M., and Budker D., 2009. Cancellation of nonlinear Zeeman shifts with light shifts. *Phys. Rev. A*, **79**(2), 023406.

[86] Jimenez-Martinez R., Griffith W., Wang Y.-J., et al., 2010. Sensitivity Comparison of Mx and Frequency-Modulated Bell Bloom Cs Magnetometers in a Microfabricated Cell. *IEEE Trans. Instrum. Meas.*, **59**(2), 372–378.

[87] Joint Committee for Guides in Metrology/WG1, 2008. Evaluation of measurement data - Guide to the expression of uncertainty in measurement.

[88] Kahl G., 2007. DDS Subsystem Specification. Tech. Rep. S2-ASD-RS-3004, ASD.

[89] Karnesis N., 2014. *Bayesian Data Analysis for LISA Pathfinder*. Ph.D. thesis, Universitat Autònoma de Barcelona.

[90] Karnesis N., Nofrarias M., Sopuerta C. F., et al., 2014. Bayesian model selection for LISA pathfinder. *Phys. Rev. D*, **89**(6), 062001.

[91] Kiefer C., 2012. *Quantum Gravity*. Oxford University Press.

[92] Kornack T. W., Smullin S. J., Lee S.-K., and Romalis M. V., 2007. A low-noise ferrite magnetic shield. *Appl. Phys. Lett.*, **90**(22), 223501.

[93] Kostinski N., Olsen B. A., Marsland R., McGuyer B. H., and Happer W., 2011. Temperature-insensitive laser frequency locking near absorption lines. *Rev. Sci. Instrum.*, **82**(3), 033114.

[94] Kramer M. and Champion D. J., 2013. The European Pulsar Timing Array and the Large European Array for Pulsars. *Class. Quantum Grav.*, **30**(22), 224009.

[95] Lämmerzahl C., 2011. *Testing Basic Laws of Gravitation - Are Our Postulates on Dynamics and Gravitation Supported by Experimental Evidence?*. Springer Science+Business Media.

[96] Laneve G. and Curti F., 1997. An orbit determination approach for small satellites. In *Space Flight Dynamics*, vol. 403 of *ESA Special Publication*.

[97] Laurent P., Abgrall M., Jentsch C., et al., 2006. Design of the cold atom PHARAO space clock and initial test results. *Appl. Phys. B*, **84**(4), 683–690.

[98] Lazio T. J. W., 2013. The Square Kilometre Array pulsar timing array. *Class. Quantum Grav.*, **30**(22), 224011.

[99] Le Gouët J., Mehlstäubler T. E., Kim J., et al., 2008. Limits to the sensitivity of a low noise compact atomic gravimeter. *Appl. Phys. B*, **92**, 133.

[100] Lee S.-K. and Romalis M. V., 2008. Calculation of magnetic field noise from high-permeability magnetic shields and conducting objects with simple geometry. *J. Appl. Phys*, **103**(8), 084904.

[101] Lévèque T., Gauguet A., Michaud F., Pereira Dos Santos F., and Landragin A., 2009. Enhancing the Area of a Raman Atom Interferometer Using a Versatile Double-Diffraction Technique. *Phys. Rev. Lett.*, **103**, 080405.

[102] Lobo A. and Mateos I., 2007. Test Plan for LTP Magnetic Diagnostics. Tech. Rep. S2-IEC-TP-3004, ICE (CSIC-IEEC).

[103] Lobo A. and Mateos I., 2008. Test Plan for the FM Magnetic Diagnostics Subsystem. Tech. Rep. S2-IEC-TP-3031, ICE (CSIC-IEEC).

[104] Lobo A. and Mateos I., 2008. Test Report for LTP Magnetic Diagnostics. Tech. Rep. S2-IEC-TR-3065, ICE (CSIC-IEEC).

[105] Lobo A. and Mateos I., 2009. Test Report for LTP FM Diagnostics. Tech. Rep. S2-IEC-TR-3067, ICE (CSIC-IEEC).

[106] Lobo A. and Mateos I., 2009. Test Specification for the FM Magnetic Diagnostics Subsystem. Tech. Rep. S2-IEC-TS-3046, ICE (CSIC-IEEC).

[107] Lobo A. and Mateos I., 2009. TR for LTP FM Magnetic DIs after DMU Faulty Capacitor Replacement. Tech. Rep. S2-IEC-TR-3092, ICE (CSIC-IEEC).

[108] Lobo A., Nofrarias M., Ramos-Castro J., and Sanjuán J., 2006. On-ground tests of the LISAPathFinder thermal diagnostics system. *Class. Quantum Grav.*, **23**, 5177–5193.

[109] Lu C.-C., Liu Y.-T., Jhao F.-Y., and Jeng J.-T., 2012. Responsivity and noise of a wire-bonded CMOS micro-fluxgate sensor. *Sens. Actuators A*, **179**, 39–43.

[110] Lück H., Hewitson M., Ajith P., et al., 2006. Status of the GEO600 detector. *Class. Quantum Grav.*, **23**, 71–92.

[111] Luong V., Chang C., Jeng J., Lu C., Hsu J., and Chang C., 2014. Reduction of Low-frequency Noise in Tunneling-magnetoresistance Sensors with a Modulated Magnetic Shielding. *IEEE Trans. on Magnetics*, **50**(11), 1–4.

[112] Magnetic Shield Corp., 2013. Zero Gauss Chambers. Tech. Rep. Catalog ZG-3, Magnetic Shield Corporation.

[113] Malátek M., Ripka P., and Kraus L., 2008. Temperature offset drift of GMI sensors. *Sens. Actuators A*, **147**(2), 415–418.

[114] Maroto O., 2008. DDS Serial Channel ICD. Tech. Rep. S2-NTE-ICD-3012, NTE.

[115] Maroto O., 2010. Acceptance Vibration Test Specification for the Magnetometer. Tech. Rep. S2-NTE-TS-3044, NTE.

[116] Masaki A. and the TAMA collaboration, 2002. Current status of TAMA. *Class. Quantum Grav.*, **19**(7), 1409.

[117] Mateos I., 2011. FM 3AM Noise Test Report. Tech. Rep. S2-IEC-TR-3126, ICE (CSIC-IEEC).

[118] Mateos I., 2011. FM 3AM Noise Test Specification. Tech. Rep. S2-IEC-TS-3048, ICE (CSIC-IEEC).

[119] Mateos I., 2011. Linearity and Degaussing of FM 3AM after Vibration Test Failure. Tech. Rep. S2-IEC-RP-3218, ICE (CSIC-IEEC).

[120] Mateos I., Diaz-Aguiló M., Gibert F., et al., 2012. Temperature coefficient improvement for low noise magnetic measurements in LISA. *J. Phys. Conf. Ser.*, **363**(1), 012051.

[121] Mateos I., Diaz-Aguiló M., Gibert F., et al., 2013. Magnetic Back Action Effect of Magnetic Sensors for eLISA/NGO. vol. 467 of *ASP Conf. Ser.*, 341.

[122] Mateos I., Díaz-Aguiló M., Ramos-Castro J., García-Berro E., and Lobo A., 2015. Interpolation of the magnetic field at the test masses in eLISA. *Class. Quantum Grav.*, **32**(16), 165003.

[123] Mateos I., Patton B., Zhivun E., Budker D., Wurm D., and Ramos-Castro J., 2015. Noise characterization of an atomic magnetometer at sub-millihertz frequencies. *Sens. Actuators A*, **224**, 147–155.

[124] Mateos I., Ramos-Castro J., and Lobo A., 2015. Low-frequency noise characterization of a magnetic field monitoring system using an anisotropic magnetoresistance. *Sens. Actuators A*, **235**, 57–63.

[125] Mathur B. S., Tang H., and Happer W., 1968. Light Shifts in the Alkali Atoms. *Phys. Rev.*, **171**, 11–19.

[126] Mattia B., Ripka P., and L. K., 2015. Effect of Stress-Induced Anisotropy on the Noise of Ring-Core Fluxgate. *IEEE Trans. on Magnetics*, **51**, 1–4.

[127] McLaughlin M. A., 2013. The North American Nanohertz Observatory for Gravitational Waves. *Class. Quantum Grav.*, **30**(22), 224008.

[128] Meers B. J., 1988. Recycling in laser-interferometric gravitational-wave detectors. *Phys. Rev. D*, **38**, 2317–2326.

[129] Mhaskar R., Knappe S., and Kitching J., 2010. Low-frequency characterization of MEMS-based portable atomic magnetometer. In *Frequency Control Symposium (FCS), 2010 IEEE International*, 376–379.

[130] Michelena M., Arruego I., Oter J., and Guerrero H., 2010. COTS-based Wireless Magnetic Sensor for Small Satellites. *IEEE Trans. Aerosp. Electron. Syst.*, **46**(2), 542–557.

[131] Michelson A. A. and Morley E. W., 1887. On the Relative Motion of the Earth and of the Luminiferous Ether. *Sidereal Messenger*, **6**, 306–310.

[132] Moodera J. S., Kinder L. R., Wong T. M., and Meservey R., 1995. Large Magnetoresistance at Room Temperature in Ferromagnetic Thin Film Tunnel Junctions. *Phys. Rev. Lett.*, **74**, 3273–3276.

[133] Moore C. J., Cole R. H., and Berry C. P. L., 2015. Gravitational-wave sensitivity curves. *Class. Quantum Grav.*, **32**(1), 015014.

[134] Moroni A., 2014. ISH/CVM FM01 Alignment Verification Report. Tech. Rep. S2-CGS-TR-3119, OHB-CGS.

[135] Moroni A., 2014. ISH/CVM FM01 Alignment Verification Report. Tech. Rep. S2-CGS-TR-3120, OHB-CGS.

[136] Motchenbacher C. D., 1993. *Low-Noise Electronic System Design*. John Wiley & Sons.

[137] MultiDimension Technology Co., 2015. MMLP57F TMR Linear Sensor. Tech. Rep. 1.3, MultiDimension Technology Co.

[138] Narod B. B., Bennest J. R., Strom-Olsen J. O., Nezil F., and Dunlap R. A., 1985. An evaluation of the noise performance of Fe, Co, Si, and B amorphous alloys in ring-core fluxgate magnetometers. *Can. J. Phys.*, **63**, 1468.

[139] Nielsen O. V., Petersen J. R., Fernandez A., et al., 1991. Analysis of a fluxgate magnetometer based on metallic glass sensors. *Meas. Sci. Technol.*, **2**, 435–440.

[140] Nobili A. M., Shao M., Pegna R., et al., 2012. 'Galileo Galilei' (GG): space test of the weak equivalence principle to 10^{-17} and laboratory demonstrations. *Class. Quantum Grav.*, **29**, 184011.

[141] Nofrarias M., 2007. *Thermal Diagnostics in the LISA Technology Package Experiment*. Ph.D. thesis, Universitat de Barcelona.

[142] Nofrarias M., Röver C., Hewitson M., et al., 2010. Bayesian parameter estimation in the second LISA Pathfinder mock data challenge. *Phys. Rev. D*, **82**, 122002.

[143] Overduin J., Everitt F., Worden P., and Mester J., 2012. STEP and fundamental physics. *Class. Quantum Grav.*, **29**, 184012.

[144] Pallás R. W. J., 2000. *Sensors and Signal Conditioning*. New York: Wiley-Interscience.

[145] Patton B., Zhivun E., Hovde D. C., and Budker D., 2014. All-Optical Vector Atomic Magnetometer. *Phys. Rev. Lett.*, **113**(1), 013001.

[146] Peters A., Chung K. Y., and Chu S., 1999. Measurement of gravitational acceleration by dropping atoms. *Nature*, **400**, 849.

[147] Primdahl F., 1970. The fluxgate mechanism, part I: The gating curves of parallel and orthogonal fluxgates . *IEEE Trans. on Magnetics*, **6**, 376–383.

[148] Primdahl F., Hernando B., Nielsen O. V., and Petersen J. R., 1989. Demagnetising factor and noise in the fluxgate ring-core sensor. *J. Phys. E: Sci. Instrum.*, **22**(12), 1004.

[149] Primdahl F., Hernando B., Nielsen O. V., and Petersen J. R., 1989. Demagnetising factor and noise in the fluxgate ring-core sensor. *J. Phys. E*, **22**, 1004–1008.

[150] Primdahl F., Risbo T., Merayo J. M. G., Brauer P., and Tøffner Clausen L., 2006. In-flight spacecraft magnetic field monitoring using scalar/vector gradiometry. *Meas. Sci. Technol.*, **17**, 1563–1569.

[151] Reig C., Cardoso de Freitas S., and Mukhopadhyay S. C., 2013. *Giant Magnetoresistance (GMR). From Basis to State-of-the-Art Applications*. Springer.

[152] Rikitake T., 1987. *Magnetic and Electromagnetic Shielding*. TERRAPUB and D. Reidel.

[153] Ripka P., 2003. Advances in fluxgate sensors. *Sens. Actuators A*, **106**(1-3).

[154] Ripka P. and Janosek M., 2010. Advances in Magnetic Field Sensors. *IEEE Sensors J.*, **10**(6), 1108–1116.

[155] Robertson N. A., 2000. Laser interferometric gravitational wave detectors. *Class. Quantum Grav.*, **17**(15).

[156] Rudolph J., Herr W., Grzeschik C., et al., 2015. A high-flux BEC source for mobile atom interferometers. *New J. Phys.*, **17**(6), 065001.

[157] Russell B., Clement L., Hernandez J., Byagowi A., Schor D., and Kinsner W., 2013. Implementation of a nanosatellite attitude determination and control system for the T-Sat1 mission. In *26th Annual IEEE CCECE*, 1–5.

[158] Salomon G., Fouché L., Lepoutre S., Aspect A., and Bourdel T., 2014. All-optical cooling of K39 to Bose-Einstein condensation. *Phys. Rev. A*, **90**(3), 033405.

[159] Sanjuán J., 2009. Bitrate Reduction in the DDS. Tech. Rep. S2-IEC-TN-3051, ICE (CSIC-IEEC).

[160] Sanjuán J., 2009. *Development and Validation of the Thermal Diagnostics Instrumentation in LISA Pathfinder*. Ph.D. thesis, Universitat Politècnica de Catalunya.

[161] Sanjuán J., Lobo A., Nofrarias M., et al., 2008. Magnetic polarization effects of temperature sensors and heaters in LISA Pathfinder. *Rev. of Sci. Instruments*, **79**, 084503.

[162] Sathyaprakash B., Abernathy M., Acernese F., et al., 2012. Scientific objectives of Einstein Telescope. *Class. Quantum Grav.*, **29**(12), 124013.

[163] Saulson P. R., 1994. *Fundamentals of interferometric gravitational wave detectors*. Singapore: World Scientific Publishers.

[164] Schlamminger S., Choi K.-Y., Wagner T. A., Gundlach J. H., and Adelberger E. G., 2008. Test of the Equivalence Principle Using a Rotating Torsion Balance. *Phys. Rev. Lett.*, **100**, 041101.

[165] Schlippert D., Hartwig J., Albers H., et al., 2014. Quantum Test of the Universality of Free Fall. *Phys. Rev. Lett.*, **112**(20), 203002.

[166] Schuldt T., Schubert C., Krutzik M., et al., 2015. Design of a dual species atom interferometer for space. *Exp. Astron.*, **39**(2).

[167] Schumaker B. L., 2003. Disturbance reduction requirements for LISA. *Class. Quantum Grav.*, **20**, 239–245.

[168] Schutz B. F., 1984. Gravitational waves on the back of an envelope. *Amer. J. of Phys.*, **52**, 412–419.

[169] Schwindt P. D. D., Lindseth B., Knappe S., Shah V., Kitching J., and Liew L.-A., 2007. Chip-scale atomic magnetometer with improved sensitivity by use of the M_x technique. *Appl. Phys. Lett.*, **90**(8), 081102.

[170] Scouten D. C., 1972. Sensor noise in low-level flux-gate magnetometers. *IEEE Trans. on Magnetics*, **8**, 223–231.

[171] Shah V., Knappe S., Schwindt P. D. D., and Kitching J., 2007. Subpicotesla atomic magnetometry with a microfabricated vapour cell. *Nat. Photonics*, **1**, 649–652.

[172] Somiya K., 2012. Detector configuration of KAGRA - the Japanese cryogenic gravitational-wave detector. *Class. Quantum Grav.*, **29**(12), 124007.

[173] STE-QUEST Study Science Team, 2013. STE-QUEST Science Requirements Document, FPM-SA-Dc-00001, issue 1, revision 5.

[174] Stutzke N. A., Russek S. E., Pappas D. P., and Tondra M., 2005. Low-frequency noise measurements on commercial magnetoresistive magnetic field sensors. *J. Appl. Phys*, **97**(10Q107).

[175] Sumner T. J., Pendlebury J. M., and Smith K. F., 1987. Convectional magnetic shielding. *J. Phys. D: Appl. Phys.*, **20**, 1095–1101.

[176] Tarallo M. G., Mazzoni T., Poli N., Sutyrin D. V., Zhang X., and Tino G. M., 2014. Test of Einstein Equivalence Principle for 0-Spin and Half-Integer-Spin Atoms: Search for Spin-Gravity Coupling Effects. *Phys. Rev. Lett.*, **113**(2), 023005.

177

[177] Taylor J. H., Fowler L. A., and McCulloch P. M., 1979. Measurements of general relativistic effects in the binary pulsar PSR 1913+16. *Nature*, **277**, 437–440.

[178] Touboul P., Métris G., Lebat V., and Robert A., 2012. The MICROSCOPE experiment, ready for the in-orbit test of the equivalence principle. *Class. Quantum Grav.*, **29**, 184010.

[179] Trougnou L., 2007. AC Magnetic Susceptibility of LisaPF Test Masses. Tech. Rep. S2-EST-TN-3013, ESTEC.

[180] Trougnou L., 2008. Impact of LTP Thermal Diagnostics on Magnetic Acceleration Budget. Tech. Rep. S2-EST-TN-3026, ESA-ESTEC.

[181] Uchiyama T., Hamada N., and Cai C., 2013. Development of multicore magneto-impedance sensor for stable pico-Tesla resolution. In *Seventh International Conference on Sensing Technology*, 573–577.

[182] van de Veerdonk R. J. M., Beliën P. J. L., Schep K. M., et al., 1997. 1/f noise in anisotropic and giant magnetoresistive elements. *J. Appl. Phys*, **82**, 6152–6164.

[183] Vitale S., 2005. Science Requirements and Top-level Architecture Definition for the Lisa Technology Package (LTP) on Board LISA Pathfinder (SMART-2). Tech. Rep. LTPA-UTN-ScRD-Iss003-Rev1, Department of Physics, University of Trento, Italy.

[184] Vitale S., 2007. Effect of Eddy Currents on Down-conversion of Magnetic Noise. Tech. Rep. Memo, LISA Technology Package, Department of Physics, University of Trento.

[185] Vitale S., 2014. Space-borne gravitational wave observatories. *Gen. Relat. Gravit.*, **46**, 1730.

[186] Wealthy D. and Trenkel C., 2010. Prediction of Spacecraft Magnetic Field Based on Recent Testing. Tech. Rep. S2-ASU-TN-2523 Issue 3, Astrium Gmbh. Germany.

[187] Weber J., 1960. Detection and Generation of Gravitational Waves. *Phys. Rev. D*, **117**, 306–313.

[188] Weber J., 1969. Evidence for Discovery of Gravitational Radiation. *Phys. Rev. Lett.*, **22**, 1320–1324.

[189] Willke B., Ajith P., Allen B., et al., 2006. The GEO-HF project. *Class. Quantum Grav.*, **23**(8), S207.

178

[190] Wolf, P. and STE-QUEST core science team, 2015. STE-QUEST: ESA Cosmic Vision M4. Tech. rep., Observatoire de Paris, CNRS, UPMC, LNE.

[191] Wu C.-C. and Chen A., 1978. Effect of nonparabolicity on transverse magnetoresistance of semiconductors in strong magnetic fields. *Phys. Rev. B*, **18**, 1916–1922.

[192] Xu S., Rochester S. M., Yashchuk V. V., Donaldson M. H., and Budker D., 2006. Construction and applications of an atomic magnetic gradiometer based on nonlinear magneto-optical rotation. *Rev. Sci. Instrum.*, **77**(8), 083106.

[193] Yashchuk V. V., Budker D., and Davis J. R., 2000. Laser frequency stabilization using linear magneto-optics. *Rev. Sci. Instrum.*, **71**, 341–346.

[194] Zendri J., Baggio L., Bignotto M., et al., 2002. Status report and near future prospects for the gravitational wave detector AURIGA. *Class. Quantum Grav.*, **19**, 1925–1933.